



**NATIONAL TECHNICAL UNIVERSITY OF ATHENS  
SCHOOL OF CIVIL ENGINEERING**

**STABILITY CRITERIA FOR HOLLOW-SECTION  
STEEL ARCHES**

DOCTORAL THESIS OF  
**ILIAS D. THANASOULAS**

Supervised by  
**CHARIS J. GANTES**  
Professor NTUA

Athens, January 2020





**ΕΘΝΙΚΟ ΜΕΤΣΟΒΙΟ ΠΟΛΥΤΕΧΝΕΙΟ**  
**ΣΧΟΛΗ ΠΟΛΙΤΙΚΩΝ ΜΗΧΑΝΙΚΩΝ**

**ΚΡΙΤΗΡΙΑ ΕΥΣΤΑΘΕΙΑΣ ΧΑΛΥΒΔΙΝΩΝ ΤΟΞΩΝ**  
**ΚΟΙΛΗΣ ΔΙΑΤΟΜΗΣ**

**ΔΙΔΑΚΤΟΡΙΚΗ ΔΙΑΤΡΙΒΗ**  
**ΗΛΙΑ Δ. ΘΑΝΑΣΟΥΛΑ**

Επιβλέπων  
**ΧΑΡΗΣ Ι. ΓΑΝΤΕΣ**  
Καθηγητής ΕΜΠ

Αθήνα, Ιανουάριος 2020







**NATIONAL TECHNICAL UNIVERSITY OF ATHENS  
SCHOOL OF CIVIL ENGINEERING**

# **STABILITY CRITERIA FOR HOLLOW-SECTION STEEL ARCHES**

DOCTORAL THESIS OF

**ILIAS D. THANASOULAS**

Diploma in Civil Engineering, NTUA (2011)

MSc in Analysis and Design of Earthquake Resistant Structures, NTUA (2014)

The thesis is submitted to the School of Civil Engineering  
of the National Technical University of Athens  
in fulfilment of the requirements for the Degree of Doctor of Philosophy

**ADVISORY COMMITTEE:**

1. C. GANTES, Professor NTUA (supervisor)
2. I. VAYAS, Professor NTUA
3. V. KOUMOUSIS, Professor NTUA

**EXAMINATION COMMITTEE:**

1. C. GANTES, Professor NTUA (supervisor)
2. I. VAYAS, Professor NTUA
3. V. KOUMOUSIS, Professor NTUA
4. S. KARAMANOS, Professor UTh
5. N. LAGAROS, Associate Professor NTUA
6. D. LIGNOS, Associate Professor EPFL
7. P. THANOPOULOS, Lecturer NTUA

Athens, January 2020

© Copyright 2020 by Ilias D. Thanasoulas  
All Rights Reserved

Neither the whole nor any part of this doctoral thesis may be copied, stored in a retrieval system, distributed, reproduced, translated, or transmitted for commercial purposes, in any form or by any means now or hereafter known, electronic or mechanical, without the written permission from the author. Reproducing, storing and distributing this doctoral thesis for non-profitable, educational or research purposes is allowed, without prejudice to reference to its source and to inclusion of the present text. Any queries in relation to the use of the present doctoral thesis for commercial purposes must be addressed to its author.

Approval of this doctoral thesis by the School of Civil Engineering of the National Technical University of Athens (NTUA) does not constitute in any way an acceptance of the views of the author contained herein by the said academic organization (L. 5343/1932, art. 202).



**ΕΘΝΙΚΟ ΜΕΤΣΟΒΙΟ ΠΟΛΥΤΕΧΝΕΙΟ**  
**ΣΧΟΛΗ ΠΟΛΙΤΙΚΩΝ ΜΗΧΑΝΙΚΩΝ**

## **ΚΡΙΤΗΡΙΑ ΕΥΣΤΑΘΕΙΑΣ ΧΑΛΥΒΔΙΝΩΝ ΤΟΞΩΝ ΚΟΙΛΗΣ ΔΙΑΤΟΜΗΣ**

**ΔΙΔΑΚΤΟΡΙΚΗ ΔΙΑΤΡΙΒΗ**

**ΗΛΙΑ Δ. ΘΑΝΑΣΟΥΛΑ**

Δίπλωμα Πολιτικού Μηχανικού Ε.Μ.Π. (2011)

Μεταπτυχιακό Δίπλωμα Ειδίκευσης Ε.Μ.Π. (2014)

«Δομοστατικός Σχεδιασμός και Ανάλυση Κατασκευών»

Η διατριβή υποβλήθηκε στη Σχολή Πολιτικών Μηχανικών του Εθνικού Μετσοβίου Πολυτεχνείου προς εκπλήρωση των προϋποθέσεων του τίτλου του Διδάκτορος Μηχανικού

**ΤΡΙΜΕΛΗΣ ΣΥΜΒΟΥΛΕΥΤΙΚΗ ΕΠΙΤΡΟΠΗ:**

1. Χ. ΓΑΝΤΕΣ, Καθηγητής ΕΜΠ (επιβλέπων)
2. Ι. ΒΑΓΙΑΣ, Καθηγητής ΕΜΠ
3. Β. ΚΟΥΜΟΥΣΗΣ, Καθηγητής ΕΜΠ

**ΕΠΤΑΜΕΛΗΣ ΕΞΕΤΑΣΤΙΚΗ ΕΠΙΤΡΟΠΗ:**

1. Χ. ΓΑΝΤΕΣ, Καθηγητής ΕΜΠ (επιβλέπων)
2. Ι. ΒΑΓΙΑΣ, Καθηγητής ΕΜΠ
3. Β. ΚΟΥΜΟΥΣΗΣ, Καθηγητής ΕΜΠ
4. Σ. ΚΑΡΑΜΑΝΟΣ, Καθηγητής ΠΘ
5. Ν. ΛΑΓΑΡΟΣ, Αν. Καθηγητής ΕΜΠ
6. Δ. ΛΙΓΝΟΣ, Αν. Καθηγητής ΕΡΦΛ
7. Π. ΘΑΝΟΠΟΥΛΟΣ, Λέκτορας ΕΜΠ

Αθήνα, Ιανουάριος 2020

© Copyright 2020 by Ηλίας Δ. Θανάσουλας  
Με επιφύλαξη παντός δικαιώματος

Απαγορεύεται η αντιγραφή, αποθήκευση σε αρχείο πληροφοριών, διανομή, αναπαραγωγή, μετάφραση ή μετάδοση της παρούσας εργασίας, εξ ολοκλήρου ή τμήματος αυτής, για εμπορικό σκοπό, υπό οποιαδήποτε μορφή και με οποιοδήποτε μέσο επικοινωνίας, ηλεκτρονικό ή μηχανικό, χωρίς την προηγούμενη έγγραφη άδεια του συγγραφέα. Επιτρέπεται η αναπαραγωγή, αποθήκευση και διανομή για σκοπό μη κερδοσκοπικό, εκπαιδευτικής ή ερευνητικής φύσης, υπό την προϋπόθεση να αναφέρεται η πηγή προέλευσης και να διατηρείται το παρόν μήνυμα. Ερωτήματα που αφορούν στη χρήση της εργασίας για κερδοσκοπικό σκοπό πρέπει να απευθύνονται προς το συγγραφέα.

Η έγκριση της διδακτορικής διατριβής από την Ανώτατη Σχολή Πολιτικών Μηχανικών του Εθνικού Μετσοβίου Πολυτεχνείου δεν υποδηλώνει αποδοχή των απόψεων του συγγραφέως (Ν. 5343/1932, Άρθρο 202).

# ACKNOWLEDGMENTS

I would like to express my gratitude to my thesis advisor, Professor Charis Gantes, for his continuous guidance and support all these years. The personal interaction with him was always inspirational. Thanks to his knowledge, experience, ideas, and mainly his own, unique way of transmitting all of them, this doctoral thesis was successfully completed – Professor Gantes, thanks for everything.

My sincere appreciation is also expressed to the other members of my doctoral thesis committee. Many thanks are addressed to Professor Ioannis Vayas and Professor Vlasios Koumoussis for their constructive advice.

Special thanks are addressed to Dr. Cyril Douthe, for laying the foundation of this research through his former experimental work. His work motivated me to begin dealing with the topic of steel arches. Our common efforts in publishing the test results, comprised an important milestone of the present dissertation.

My sincere appreciation is expressed to Professor Emeritus Georgios Ioannidis, who first introduced me into the world of steel structures, as an undergraduate student. Moreover, influences from Andreas Spiliopoulos, who advised me during my undergraduate diploma thesis, have been more than important. Both contributed in convincing me to follow this direction.

Many thanks are due to all members of the Institute of Steel Structures. I will not forget our long conversations with Dr. Xenofon Lignos, about technical or other issues, and of course, the celebrations we were organizing occasionally or not.

During my PhD studies, I had the opportunity to collaborate with excellent students in the School of Civil Engineering. The high level of students at NTUA, helps the academic staff to become better. Special thanks to Iason Vardakoulis, Spyros Kalyvas, Maria Kalafati, Sofia Korlou, Antonia Nousiou, and Spyros Venetis, for their hard efforts and the passion they showed in our common work.

The work presented here was mainly supported by the State Scholarships Foundation of Greece (IKY), under Grant No. 23485. Funding was also awarded from IKY during my first year of M.Sc. studies, under the Grant No. 2012-ΠΕ3-292. The financial support of the State Scholarships Foundation is gratefully acknowledged.

During my years at NTUA, I was very fortunate to meet many good friends. In particular, I would like to thank my colleagues Yiannis Kalogeris, Christos Sofianos, Dimitris Billionis, Zaharias Fasoulakis, Maria-Eleni Dasiou, Stella Avgerinou, Konstantina Koulatsou, Maria Livanou, Aggelos Karvelis, as well as, the newer members of the lab, Kostas Vlachakis, Akrivi Chatzidaki, Sofia Antonodimitraki, Orestis Ioannou, Christos Lachanas, Panagiotis Tsarpalis and Dimitris Tsarpalis, for the nice environment in the department. Many thanks go to my closest people in the lab, Stelios Vernardos, Vasilis Melissianos, and Dinos Bakalis, not only for sharing the same space, but more importantly, for sharing our common hopes and concerns all these years. Special thanks to Liesbeth Arnouts for her pleasant stay here during the last months. Finally, I would like to thank my best friends from the beginning of this journey, Andreas Koutras, Panos Kounis, George Manos, Nikos Mastrantonas, Akis Gkamarazis, Christos Levantis, Dimitris Tsalpatouros, Nasos Leventis, Dinos Pesinis and Giannis Spyropoulos, for the countless moments we have shared together in the School of Civil Engineering and beyond.

Last but certainly not least, my wholehearted gratitude goes to my family, who made it all possible. Their unconditional love and support are essential to continue...

Ilias D. Thanasoulas  
Athens, December 2019

*to my Parents,  
Dionysis and Sotiria*







National Technical University of Athens  
School of Civil Engineering

**Doctoral Thesis of Ilias D. Thanasoulas**  
**Stability Criteria for Hollow-Section Steel Arches**

Supervisor: Professor Charis J. Gantes  
Athens, January 2020

**Abstract**

Objective of the dissertation is to gain insight into the structural stability of steel arches comprising hollow cross-sections. Steel arches are typically manufactured from initially straight members, which are subjected to bending in order to meet the desired curvature. The roller-bending process is the most commonly used method for curving constructional steel members in the fabrication industry. It is a cold-forming process, in which a workpiece is passed iteratively through a three-roller-bending machine. Residual stresses, or commonly called "locked-in" stresses, along with significant plastic deformations, are induced to steel members during cold-forming, affecting their structural behavior. The present doctoral thesis aims at assessing the effects of residual stresses and geometric imperfections on the inelastic stability of steel arches.

In this context, a combined experimental, numerical and analytical investigation is implemented. A state-of-the-art experimental study is presented, regarding the in-plane behavior of roller-bent arches. Detailed finite element simulations of pertinent experimental tests are carried out, aiming at validating the developed numerical models. The roller-bending process is explicitly simulated, accounting for the real contact interaction between the bending machine and the steel workpiece. Experimental and numerical results are compared in terms of load-displacement equilibrium paths, strain-gauge measurements and deformed shapes, providing good quantitative and qualitative agreement. Following validation of the developed numerical models, the influence of the main roller-bending characteristics on the residual stress/strain formations of roller-bent hollow sections are assessed, on the basis of comprehensive parametric studies. The effects of residuals stresses on the elastic domain of hollow sections, as well as on the critical loads of steel arches, are investigated next, using analytical expressions that rely on linear analysis. The results are compared between various hollow sections, providing qualitative conclusions. Subsequently, the inelastic stability of arches is accurately assessed by means of Geometry and Material Nonlinear Analyses, incorporating reliable locked-in stress distributions and appropriate geometric imperfections.

The contribution of the present dissertation to the advancement of engineering science and design practice includes, mainly among others, the development of sophisticated numerical simulations of the cold-curving process, the presentation and interpretation of experimental and numerical results on roller-bent arches, the development of residual stress models for roller-bent hollow sections, and the proposal of appropriate buckling curves for hollow-section steel arches. The experimental and numerical results highlight the presence of the "Bauschinger" and "strain aging" effects on the roller-bent arches. The proposed residual stress distributions can be efficiently exploited from analysts to develop new design recommendations. Finally, the proposed buckling curves can be reliably implemented in the structural design practice, according to modern structural design standards.





Εθνικό Μετσόβιο Πολυτεχνείο  
Σχολή Πολιτικών Μηχανικών

**Διδακτορική Διατριβή Ηλία Δ. Θανάσουλα**  
**Κριτήρια Ευστάθειας Χαλύβδινων Τόξων Κοίλης Διατομής**

Επιβλέπων: Καθηγητής Χάρης Ι. Γαντές  
Αθήνα, Ιανουάριος 2020

**Περίληψη**

Αντικείμενο της διδακτορικής διατριβής αποτελεί η διερεύνηση της ευστάθειας χαλύβδινων τόξων κοίλης διατομής. Τα μεταλλικά τόξα κατασκευάζονται από κατεργασία ευθύγραμμων μελών με διάφορες μεθόδους. Η πιο διαδεδομένη μέθοδος για την καμπύλωση μελών δομικού χάλυβα είναι η εν ψυχρώ διαμόρφωση με χρήση τυμπάνων (roller-bending). Στην περίπτωση αυτή, το ευθύγραμμο μέλος διέρχεται από τη μηχανή καμπύλωσης που αποτελείται από τύμπανα, ενώ η επιθυμητή καμπυλότητα επιτυγχάνεται μέσω της κάμψης τριών σημείων που προκαλεί πλαστικές παραμορφώσεις. Η εν ψυχρώ διαμόρφωση εισάγει σημαντικές παραμένουσες τάσεις και παραμορφώσεις στα τόξα, επηρεάζοντας την μηχανική τους συμπεριφορά. Στόχος της παρούσας διατριβής είναι η αποτίμηση της επιρροής των παραμενουσών τάσεων και των γεωμετρικών ατελειών στην ευστάθεια των χαλύβδινων τόξων.

Στο πλαίσιο της διατριβής εφαρμόζεται ένας συνδυασμός πειραματικών, αριθμητικών και αναλυτικών μεθόδων έρευνας. Τα αποτελέσματα πειραματικών δοκιμών σε χαλύβδινα τόξα, καμπυλωμένα εν ψυχρώ, συγκρίνονται με τα αντίστοιχα αριθμητικά αποτελέσματα, στοχεύοντας στην πιστοποίηση των αριθμητικών προσομοιωμάτων. Η διαδικασία καμπύλωσης των τόξων προσομοιώνεται λεπτομερώς, λαμβάνοντας υπόψη την αλληλεπίδραση που αναπτύσσεται μέσω επαφής του μέλους με τα τύμπανα της μηχανής. Διαπιστώνεται ικανοποιητική σύγκλιση μεταξύ των αριθμητικών και των πειραματικών αποτελεσμάτων σε όρους αντοχής, μετατοπίσεων και αναπτυσσόμενων παραμορφώσεων. Πραγματοποιείται μια εκτεταμένη αριθμητική διερεύνηση των παραμέτρων που επηρεάζουν τις κατανομές παραμενουσών τάσεων σε κοίλες τετραγωνικές, ορθογωνικές και κυκλικές διατομές. Κατόπιν, διερευνάται η επιρροή των παραμενουσών τάσεων στην ελαστοπλαστική συμπεριφορά της διατομής και στο κρίσιμο φορτίο λυγισμού του τόξου, με χρήση αναλυτικών μεθόδων. Η ευστάθεια των τόξων από χάλυβα αποτιμάται με ακρίβεια μέσω μη γραμμικών αριθμητικών αναλύσεων υλικού και γεωμετρίας, που περιλαμβάνουν αξιόπιστα μεγέθη γεωμετρικών ατελειών και κατανομών παραμενουσών τάσεων.

Η πρωτοτυπία της διατριβής και η συμβολή της στην έρευνα και στην πράξη του μηχανικού συνοψίζονται, κυρίως, στην ανάπτυξη λεπτομερών αριθμητικών προσομοιωμάτων της διαδικασίας καμπύλωσης, στην παρουσίαση και ερμηνεία πειραματικών και αριθμητικών αποτελεσμάτων σε χαλύβδινα τόξα, στη δημιουργία μοντέλων παραμενουσών τάσεων για καμπυλωμένα εν ψυχρώ μέλη κοίλης διατομής, και στη διατύπωση κατάλληλων οδηγιών σχεδιασμού υπό τη μορφή καμπυλών λυγισμού. Τα πειραματικά και αριθμητικά αποτελέσματα, αναδεικνύουν σημαντικά φαινόμενα που πηγάζουν από τη διαδικασία της εν ψυχρώ καμπύλωσης. Οι προτεινόμενες κατανομές παραμενουσών τάσεων είναι πολύ χρήσιμες στην ανάλυση των τοξωτών φορέων. Τέλος, οι προτεινόμενες καμπύλες λυγισμού μπορούν να εφαρμοσθούν αξιόπιστα στο σχεδιασμό χαλύβδινων τόξων, όπου μέχρι τώρα χρησιμοποιούνται καμπύλες λυγισμού για ευθύγραμμα μέλη.

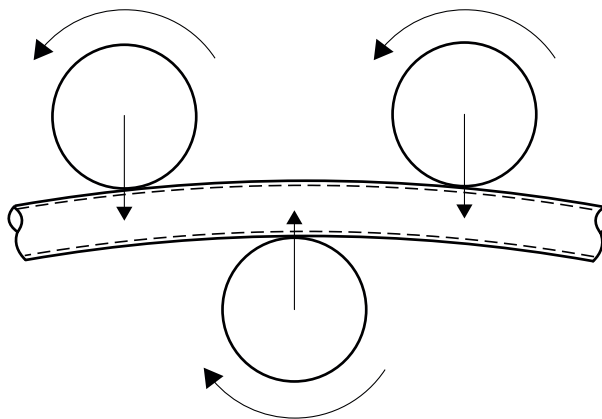


# ΕΚΤΕΝΗΣ ΠΕΡΙΛΗΨΗ (EXTENDED SUMMARY)

## 1. ΕΙΣΑΓΩΓΗ

Οι τοξωτοί φορείς από δομικό χάλυβα είναι ιδιαίτερα δημοφιλείς στις κατασκευές, εξαιτίας της καλής μηχανικής συμπεριφοράς και των αισθητικών πλεονεκτημάτων που προσφέρουν [1]. Τα καμπύλα μέλη δομικού χάλυβα κατασκευάζονται από την κατεργασία ευθύγραμμων μελών, ενώ υπάρχουν διάφορες μέθοδοι για το σκοπό αυτό [2]. Η πιο διαδεδομένη και οικονομική μέθοδος για την καμπύλωση χαλύβδινων μελών είναι η εν ψυχρώ καμπύλωση με χρήση τυμπάνων (roller-bending). Στην περίπτωση αυτή, το υπό διαμόρφωση ευθύγραμμο μέλος διέρχεται από κατάλληλη μηχανή καμπύλωσης που αποτελείται από τύμπανα (Σχήμα 1), ενώ η επιθυμητή καμπυλότητα επιτυγχάνεται μέσω κάμψης τριών σημείων που προκαλεί πλαστικές παραμορφώσεις [3]. Σημαντικές παραμένουσες τάσεις και παραμορφώσεις εισάγονται από την εν ψυχρώ καμπύλωση. Οι παραμένουσες τάσεις και οι γεωμετρικές ατέλειες επηρεάζουν τη μηχανική συμπεριφορά των μελών, μειώνοντας σημαντικά την αντοχή τους σε λυγισμό [4]. Κρίνεται επομένως σκόπιμο να διερευνηθούν οι τάσεις/παραμορφώσεις που εισάγονται κατά την εν ψυχρώ διαμόρφωση των τόξων από χάλυβα, καθώς και η επιρροή τους στην μηχανική συμπεριφορά των τοξωτών φορέων.

Ο σύγχρονος σχεδιασμός των τοξωτών φορέων βασίζεται στην εφαρμογή καμπυλών λυγισμού που προορίζονται για ευθύγραμμα μέλη και ως εκ τούτου θεωρούν διαφορετικές κατανομές παραμενουσών τάσεων από αυτές των καμπύλων μελών, ή στην εκτέλεση μη-γραμμικών αναλύσεων γεωμετρίας και υλικού που λαμβάνουν έμμεσα υπόψη την επιρροή των παραμενουσών τάσεων στην οριακή αντοχή [5-6]. Η συγκεκριμένη πρακτική σχεδιασμού δεν έχει σαφή στάθμη αξιοπιστίας. Αντικείμενο της διδακτορικής διατριβής είναι (α) ο προσδιορισμός των παραμενουσών τάσεων και παραμορφώσεων χαλύβδινων τόξων κοίλης διατομής, (β) η διερεύνηση της επιρροής τους στη μηχανική συμπεριφορά των φορέων, και (γ) η διατύπωση κατάλληλων οδηγιών σχεδιασμού για τόξα. Στο πλαίσιο της διατριβής, παρουσιάζεται μια πειραματική, αριθμητική και αναλυτική διερεύνηση της συμπεριφοράς των χαλύβδινων τόξων κοίλης διατομής. Τα πειραματικά αποτελέσματα χρησιμοποιούνται για την πιστοποίηση των αριθμητικών προσομοιωμάτων. Αριθμητικές και αναλυτικές μέθοδοι εφαρμόζονται για την αποτίμηση της συμπεριφοράς των χαλύβδινων τόξων εξετάζοντας ένα μεγάλο πλήθος παραμέτρων. Τέλος, προτείνονται κατάλληλες καμπύλες λυγισμού, οι οποίες μπορούν να χρησιμοποιηθούν αξιόπιστα για τη μελέτη και τον σχεδιασμό τοξωτών φορέων από χάλυβα.



Σχήμα 1: Καμπύλωση μέσω κάμψης τριών σημείων.

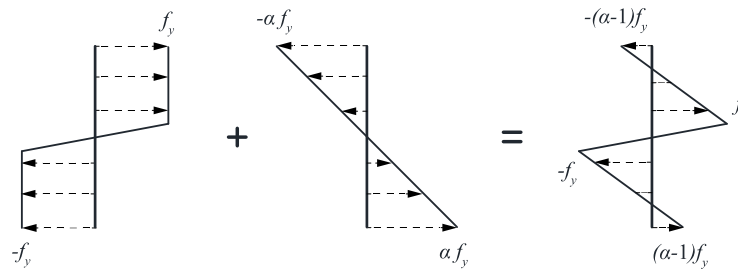
## 2. ΣΥΝΤΟΜΗ ΒΙΒΛΙΟΓΡΑΦΙΚΗ ΑΝΑΣΚΟΠΗΣΗ

Οι παραμένουσες τάσεις από την εν ψυχρώ καμπύλωση διερευνήθηκαν αρχικά από τον Timoshenko [7]. Για την εκτίμηση των παραμενουσών τάσεων χρησιμοποιήθηκε ένα αδρομερές προσομοίωμα εφαρμόζοντας τη θεωρία δοκού Euler-Bernoulli. Θεωρώντας ισορροπία των αναπτυσσόμενων ροπών στη διατομή (Εξ. 1-3), οι παραμένουσες τάσεις προκύπτουν από επαλληλία των ορθών τάσεων λόγω ανελαστικής φόρτισης και ελαστικής αποφόρτισης, ως συνάρτηση του συντελεστή σχήματος  $a$  (λόγος της πλαστικής  $W_{pl}$  προς την ελαστική  $W_{el}$  ροπής αντίστασης) και της τάσης διαρροής του χάλυβα  $f_y$ , όπως παρουσιάζεται στο Σχήμα 2. Σύμφωνα με τις παραδοχές του θεωρητικού μοντέλου, οι διατμητικές τάσεις αμελούνται, και οι ορθές τάσεις λαμβάνονται ομοιόμορφες στο πλάτος της διατομής θεωρώντας συνθήκες επίπεδης έντασης. Το θεωρητικό μοντέλο παραμενουσών τάσεων είναι ανεξάρτητο από το σχήμα της διατομής.

$$M_{pl} + M_{sb} = 0 \quad (\text{Εξ. 1})$$

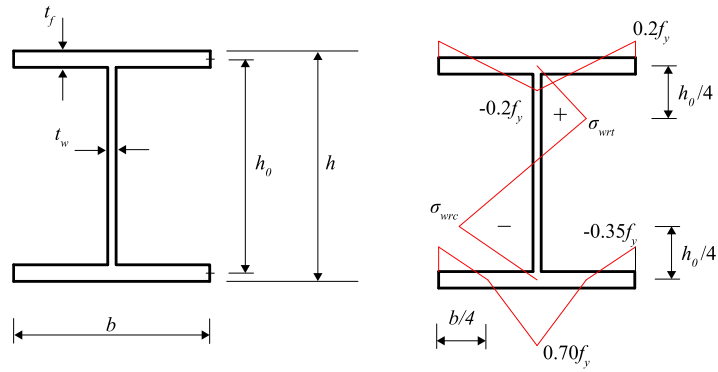
$$M_{pl} = -W_{pl} \cdot f_y \quad (\text{Εξ. 2})$$

$$\sigma_{sb} = \frac{M_{sb}}{W_{el}} = -\frac{W_{pl}}{W_{el}} \cdot f_y, \sigma_{res} = f_y \cdot (1 - a), \quad \text{όπου } a = \frac{W_{pl}}{W_{el}} \quad (\text{Εξ. 3})$$



Σχήμα 2: Ορθές παραμένουσες τάσεις από ανελαστική κάμψη και ελαστική επαναφορά.

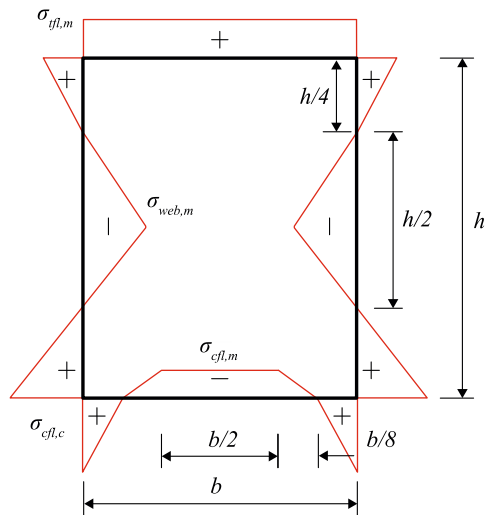
Η διεθνής έρευνα σχετικά με τις παραμένουσες τάσεις σε τόξα που έχουν καμπυλωθεί εν ψυχρώ είναι περιορισμένη. Οι παραμένουσες τάσεις σε χαλύβδινα τόξα που αποτελούνται από διατομές HEA, HEB και IPE, προσδιορίστηκαν πειραματικά [8], χρησιμοποιώντας τη μέθοδο των τομών (sectioning method). Από τις εργαστηριακές μετρήσεις προέκυψε ότι η κατανομή των παραμενουσών τάσεων μεταβάλλεται μετά την καμπύλωση, ενώ διαφοροποιείται σημαντικά από τη θεωρητική κατανομή Timoshenko. Επιπλέον, παρατηρήθηκαν σημαντικές διακυμάνσεις των τάσεων κατά το πλάτος των πελμάτων, και συγκεντρώσεις τάσεων στις ενώσεις κορμού-πελμάτων. Οι αποκλίσεις από τη θεωρητική κατανομή αποδίδονται στην ύπαρξη διάτμησης και στην παραμορφωσιμότητα της διατομής από την κάμψη τριών σημείων. Λεπτομερείς αριθμητικές προσομοιώσεις της διαδικασίας καμπύλωσης πραγματοποιήθηκαν σε τόξα που αποτελούνται από διατομές HEA, HEB, και IPE, χρησιμοποιώντας τη μέθοδο των πεπερασμένων στοιχείων [9]. Στο πλαίσιο της έρευνας αυτής, προσομοιώθηκε η αλληλεπίδραση του μέλους με τα τύμπανα της μηχανής και υπολογίστηκαν αριθμητικά οι παραμένουσες τάσεις. Από τη σύγκριση πειραματικών και αριθμητικών αποτελεσμάτων διαπιστώθηκε ικανοποιητική σύγκλιση, και ως εκ τούτου, πιστοποιήθηκε η ακρίβεια του αριθμητικού προσομοιώματος. Έτσι, προτάθηκε κατάλληλο αναλυτικό μοντέλο για τον προσδιορισμό των παραμενουσών τάσεων στις διατομές που εξετάστηκαν [10]. Η προτεινόμενη κατανομή παραμενουσών τάσεων παρουσιάζεται στο Σχήμα 3. Οι τιμές των παραμενουσών τάσεων υπολογίζονται αναλυτικά σύμφωνα με την Εξ. 4.



Σχήμα 3: Προτεινόμενο μοντέλο παραμενουσών τάσεων σε διατομές HEA, HEB και IPE [10].

$$\sigma_{wrt} = \frac{7bt_f}{30h_0t_w}f_y, \quad \sigma_{wrc} = -\frac{14bt_f}{30h_0t_w}f_y \quad (\text{Εξ. 4})$$

Επιπρόσθετα, αριθμητικές προσομοιώσεις της διαδικασίας καμπύλωσης πραγματοποιήθηκαν σε τόξα που αποτελούνται από κοίλες ορθογωνικές διατομές [11]. Στο πλαίσιο της έρευνας, διερευνήθηκε η επιρροή διαφόρων παραμέτρων στην κατανομή των παραμενουσών τάσεων, όπως οι συννοριακές συνθήκες, οι διαστάσεις της διατομής, η ακτίνα καμπυλότητας και η ποιότητα του χάλυβα. Με βάση τα αποτελέσματα που προέκυψαν, προτάθηκε κατάλληλο μοντέλο παραμενουσών τάσεων για κοίλες ορθογωνικές διατομές καμπυλωμένες εν ψυχρώ (Σχήμα 4). Οι τιμές των παραμενουσών τάσεων προσδιορίζονται σύμφωνα με τις Εξ. 5-8.



Σχήμα 4: Προτεινόμενο μοντέλο παραμενουσών τάσεων σε κοίλες ορθογωνικές διατομές [11].

Για  $20 \leq R/h \leq 150$ ,  $1 \leq h/b \leq 2$ ,  $20 \leq h/t \leq 50$  και  $235\text{MPa} \leq f_y \leq 450\text{MPa}$ :

$$\sigma_{cfl,c}/f_y = \varepsilon[0.81 - 0.0028(R/h) - 0.09(h/b) + 0.008(h/t)] \quad (\text{Εξ. 5})$$

Για  $1 \leq h/b \leq 2$ ,  $20 \leq h/t \leq 50$  και  $235\text{MPa} \leq f_y \leq 450\text{MPa}$ :

- $20 \leq R/h \leq 150$

$$\sigma_{web,m}/f_y = \varepsilon[-0.28 - 0.0034(R/h) - 0.05(h/b) - 0.01(h/t)] \quad (\text{Εξ. 6})$$

- $75 \leq R/h \leq 150$

$$\sigma_{web,m}/f_y = \varepsilon[-0.73 + 0.0026(R/h) - 0.05(h/b) - 0.01(h/t)] \quad (\text{Εξ. 7})$$

Όπου,  $\varepsilon = \sqrt{f_y/350}$

$$\sigma_{cfl,m}/f_y = -[\sigma_{cfl,m}(1.6 + 0.4(h/b)) + 0.8\sigma_{web,m}(h/b) + \sigma_{cfl,c}(0.2 + 0.4(h/b))] \quad (\text{Εξ. 8})$$

Όπου,  $\sigma_{tf,m} = 0.15f_y$

Οι μηχανικές ιδιότητες του χάλυβα μεταβάλλονται εξαιτίας των πλαστικών παραμορφώσεων από την εν ψυχρώ καμπύλωση. Η μεταβολή του μέτρου ελαστικότητας και των ορίων αναλογίας, διαρροής, και θραύσης, προσδιορίστηκε πειραματικά για χαλύβδινα τόξα διατομής HEA, HEB, και IPE [12]. Στο πλαίσιο της έρευνας, πραγματοποιήθηκαν δοκιμές θλίψης και εφελκυσμού σε κατάλληλα δοκίμια (coupon tests) που διαμορφώθηκαν πριν/μετά τη διαδικασία καμπύλωσης. Από την πειραματική διερεύνηση προέκυψε σημαντική διαφοροποίηση της συμπεριφοράς του υλικού μετά την καμπύλωση, η οποία εξαρτάται κυρίως από τη θέση του δοκιμίου στη διατομή και από τη διεύθυνση της φόρτισης. Με βάση τα αποτελέσματα της πειραματικής διερεύνησης, διατυπώθηκαν αναλυτικές σχέσεις για τον προσδιορισμό των μηχανικών ιδιοτήτων μετά την εν ψυχρώ καμπύλωση [13].

Η ευστάθεια των τόξων, αναφορικά με τον λυγισμό εντός και εκτός επιπέδου, έχει εξετασθεί πειραματικά σε πλήθος ερευνητικών εργασιών [14-19]. Επιπλέον, αριθμητικές προσομοιώσεις της μηχανικής συμπεριφοράς των τόξων έχουν δημοσιευθεί σε αρκετές εργασίες [20-23]. Εκτός των προηγούμενων, αναλυτικές σχέσεις για τον ορθό σχεδιασμό των τόξων έχουν διατυπωθεί στη βιβλιογραφία [24-27], οι οποίες βασίζονται στα αποτελέσματα εκτενών αριθμητικών αναλύσεων, χρησιμοποιώντας ακριβή προσομοιώματα πεπερασμένων στοιχείων που έχουν πιστοποιηθεί με πειραματικές μεθόδους. Ωστόσο, στην πλειοψηφία των αριθμητικών προσομοιώσεων, οι παραμένουσες τάσεις που εφαρμόζονται αφορούν είτε ευθύγραμμα μέλη, είτε ακολουθούν την θεωρητική κατανομή [7], οι οποίες δεν είναι ακριβείς στην περίπτωση τόξων καμπυλωμένων εν ψυχρώ. Κατάλληλες οδηγίες σχεδιασμού [28], υπό τη μορφή κανονιστικών καμπυλών λυγισμού, έχουν διατυπωθεί αποκλειστικά για τόξα διατομής HEA, HEB και IPE, χρησιμοποιώντας ακριβείς κατανομές παραμενουσών τάσεων που προέκυψαν από πειραματικές μετρήσεις και αριθμητικές αναλύσεις (Σχήμα 3).

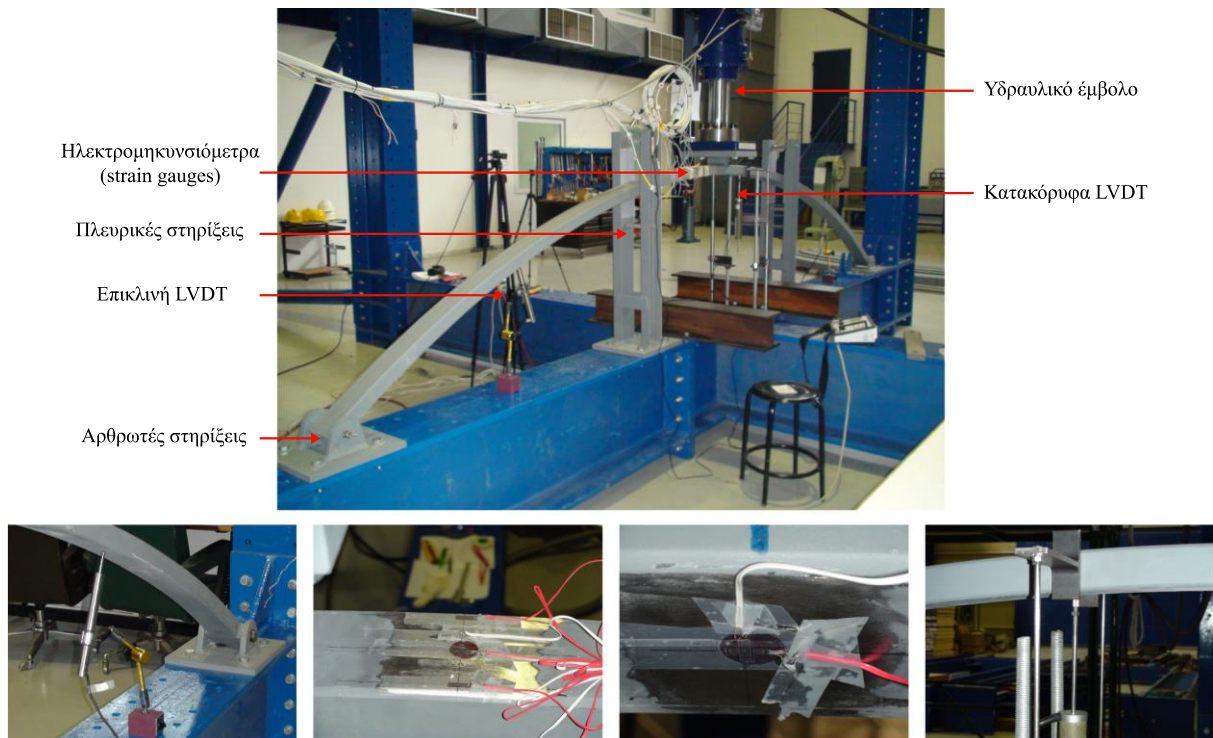
Η ερευνητική κοινότητα έχει ασχοληθεί εκτενώς με το θέμα της ευστάθειας τόξων από χάλυβα, και έχουν γραφεί εξαιρετικά βιβλία στο αντικείμενο αυτό. Οι σχετικές ερευνητικές εργασίες που πραγματοποιήθηκαν πριν το 1970, συνοψίζονται στο βιβλίο "*Handbook of Structural Stability*" [29]. Στο βιβλίο "*Stability of Metal Structures, a World View*" [30], πραγματοποιείται απευθείας σύγκριση μεταξύ διαφορετικών κανονιστικών οδηγιών για μεταλλικά τόξα. Αρκετές πειραματικές δοκιμές που έχουν πραγματοποιηθεί σε τόξα συνοψίζονται σε ένα κεφάλαιο του βιβλίου "*Buckling Experiments*" [31]. Στο βιβλίο "*Design of curved steel*" [32] παρουσιάζεται μια εφαρμοσμένη προσέγγιση για την ανάλυση και το σχεδιασμό τόξων φορέων, αναλύοντας διάφορα κατασκευαστικά θέματα. Το θέμα της ευστάθειας των χαλύβδινων τόξων αναλύεται λεπτομερώς σε ένα κεφάλαιο του βιβλίου "*Guide to Stability Design Criteria for Metal Structures*" [33]. Τέλος, η πιο σύγχρονη (state-of-the-art) προσέγγιση θεμάτων που αφορούν την κατασκευή, την ανάλυση και το σχεδιασμό καμπύλων μελών από χάλυβα, παρουσιάζεται στο βιβλίο "*Curved Member Design*" [34].



### 3. ΠΕΙΡΑΜΑΤΙΚΗ ΚΑΙ ΑΡΙΘΜΗΤΙΚΗ ΔΙΕΡΕΥΝΗΣΗ

Στο πλαίσιο της διατριβής παρουσιάζονται οι εργαστηριακές δοκιμές σε τοξωτούς φορείς που πραγματοποιήθηκαν στο Εργαστήριο Μεταλλικών Κατασκευών ΕΜΠ, από τους Δρ. Cyril Douthe και Δρ. Ξενοφών Λιγνό υπό την επίβλεψη του Καθ. Χάρη Γαντέ. Οι πειραματικές δοκιμές αφορούν δώδεκα τόξα κοίλης ορθογωνικής διατομής RHS 50x100x5, χάλυβα S355, καμπυλωμένα εν ψυχρώ περί τον ασθενή άξονα. Το διάγραμμα τάσεων–παραμορφώσεων του χάλυβα προσδιορίζεται από δοκιμές μονοαξονικού εφελκυσμού [35] σε κατάλληλα διαμορφωμένα δοκίμια που λήφθηκαν πριν τη διαδικασία καμπύλωσης των δοκιμίων. Τα τόξα ομαδοποιούνται σε δυο κατηγορίες καμπυλότητας, αποτελούμενα από ακτίνες 3.71m (ψηλά τόξα) και 4.10m (ρηχά τόξα). Το θεωρητικό οριζόντιο άνοιγμα των τόξων είναι ίσο με 4.725 m. Ωστόσο, μετρήσεις των γεωμετρικών διαστάσεων των τόξων έδειξαν την ύπαρξη σημαντικών γεωμετρικών ατελειών εξαιτίας της διαδικασίας καμπύλωσης. Οι γεωμετρικές ατέλειες αφορούν την ακτίνα καμπυλότητας, το μήκος του τόξου, καθώς και ασυμμετρίες περί το μέσον.

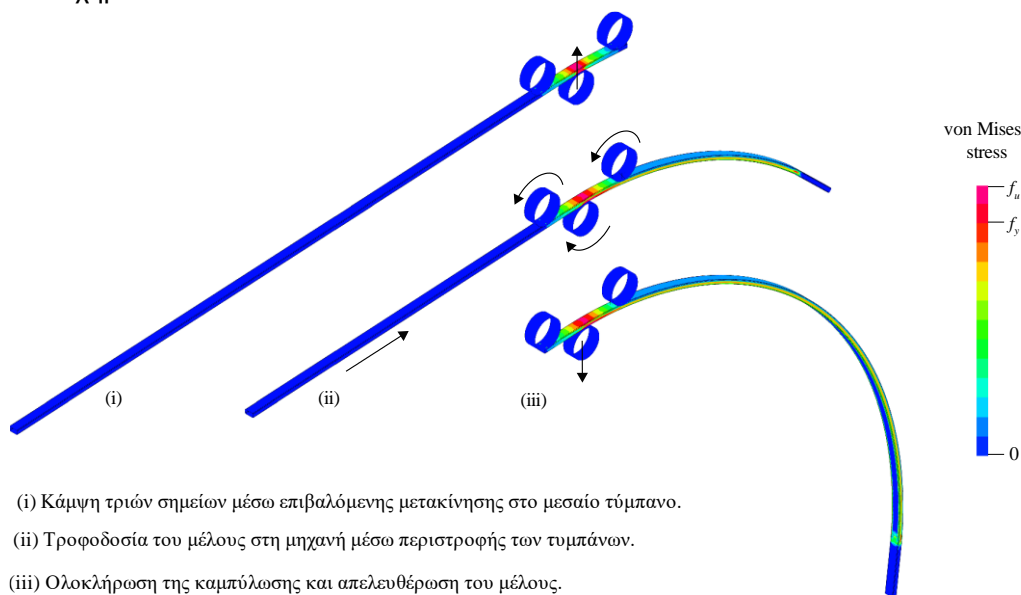
Τα τόξα δοκιμάζονται υπό θλιπτικό ή εφελκυστικό συγκεντρωμένο φορτίο στην κορυφή, μέσω κατάλληλου υδραυλικού εμβόλου. Αρθρωτές στηρίξεις χρησιμοποιούνται στα άκρα των τόξων, ενώ πλευρικές στηρίξεις τοποθετούνται σε κατάλληλες θέσεις του ανοίγματος για την εξασφάλιση των τόξων από λυγισμό εκτός επιπέδου. Για την καταγραφή και αποτύπωση της καθολικής και τοπικής συμπεριφοράς των δοκιμίων χρησιμοποιούνται τα ακόλουθα μετρητικά όργανα: (α) ηλεκτρομηκυσσιόμετρα (strain gauges), τοποθετημένα 150mm δεξιά από την κορυφή του τόξου στο άνω και κάτω πέλμα, για τη μέτρηση των διαμηκών και εγκάρσιων ανηγμένων παραμορφώσεων, (β) ηλεκτρονικά αποστασιόμετρα (LVDT), τοποθετημένα 150mm αριστερά από την κορυφή του τόξου, για τη μέτρηση των κατακόρυφων μετακινήσεων ή πιθανής στροφής, και (γ) επικλινή ηλεκτρονικά αποστασιόμετρα (LVDT), εγκατεστημένα 700mm από τα άκρα του τόξου, για τη μέτρηση των εγκαρσίων μετακινήσεων. Οι πειραματικές δοκιμές εκτελούνται με έλεγχο μετακίνησης. Ένας σύντομος κύκλος φόρτισης-αποφόρτισης εφαρμόζεται αρχικά ώστε να εξαλειφθεί η επιρροή τυχών γεωμετρικών ανοχών στην συμπεριφορά. Η πειραματική διάταξη και οι λεπτομέρειες των μετρητικών συσκευών παρουσιάζονται στο Σχήμα 5.



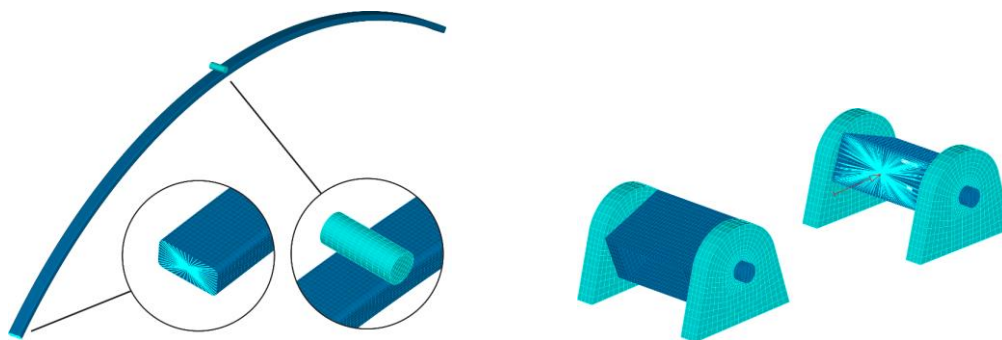
Σχήμα 5: Πειραματική διάταξη και λεπτομέρειες μετρητικών οργάνων.

Στη συνέχεια πραγματοποιείται λεπτομερής προσομοίωση της συμπεριφοράς των εξεταζόμενων τόξων με τη μέθοδο των πεπερασμένων στοιχείων [36]. Οι αριθμητικές αναλύσεις εκτελούνται στο πρόγραμμα πεπερασμένων στοιχείων ADINA [37]. Για το ορθό προσδιορισμό των παραμενουσών τάσεων προσομοιώνεται ο ακριβής τρόπος καμπύλωσης των τόξων, μέσω της αλληλεπίδρασης του μέλους με τα τύμπανα της μηχανής. Τα υπό διαμόρφωση μέλη προσομοιώνονται με επιφανειακά πεπερασμένα στοιχεία (shell elements), και κατάλληλα στοιχεία επαφής εισάγονται στις διεπιφάνειες επαφής. Η αριθμητική προσομοίωση εκτελείται σε τρία διαδοχικά βήματα, όπως φαίνεται στο Σχήμα 6. Η κατανομή των παραμενουσών τάσεων που προκύπτει είναι μη συμμετρική και διαφέρει από την θεωρητική κατανομή Timoshenko, εμφανίζοντας συγκεντρώσεις τάσεων στις γωνίες πελμάτων-κορμού της κοίλης ορθογωνικής διατομής.

Στη συνέχεια, μη γραμμικές αναλύσεις υλικού και γεωμετρίας [38] πραγματοποιούνται για την προσομοίωση των πειραματικών δοκιμών θλίψης/εφελκυσμού στα τόξα. Στο πλαίσιο αυτό, χρησιμοποιούνται οι κατανομές παραμενουσών τάσεων που υπολογίστηκαν από την προσομοίωση της διαδικασίας καμπύλωσης. Επιπλέον, μορφώνονται λεπτομερή προσομοιώματα των αρθρωτών στηρίξεων με χωρικά πεπερασμένα στοιχεία και προσδιορίζεται η δυσκαμψία τους με ακρίβεια. Άκαμπτα στοιχεία (rigid links) εφαρμόζονται στα άκρα του τόξου, συνδέοντας τους κόμβους της ακραίας διατομής με το κέντρο βάρους τους. Μη γραμμικά ελατήρια εισάγονται στους κεντροβαρικούς κόμβους των άκρων, χρησιμοποιώντας την ισοδύναμη δυσκαμψία των στηρίξεων. Ο τρόπος φόρτισης των τόξων προσομοιώνεται λεπτομερώς, μέσω επαφής με κύλινδρο φόρτισης. Τα αριθμητικά προσομοιώματα των πειραματικών δοκιμών απεικονίζονται στο Σχήμα 7.

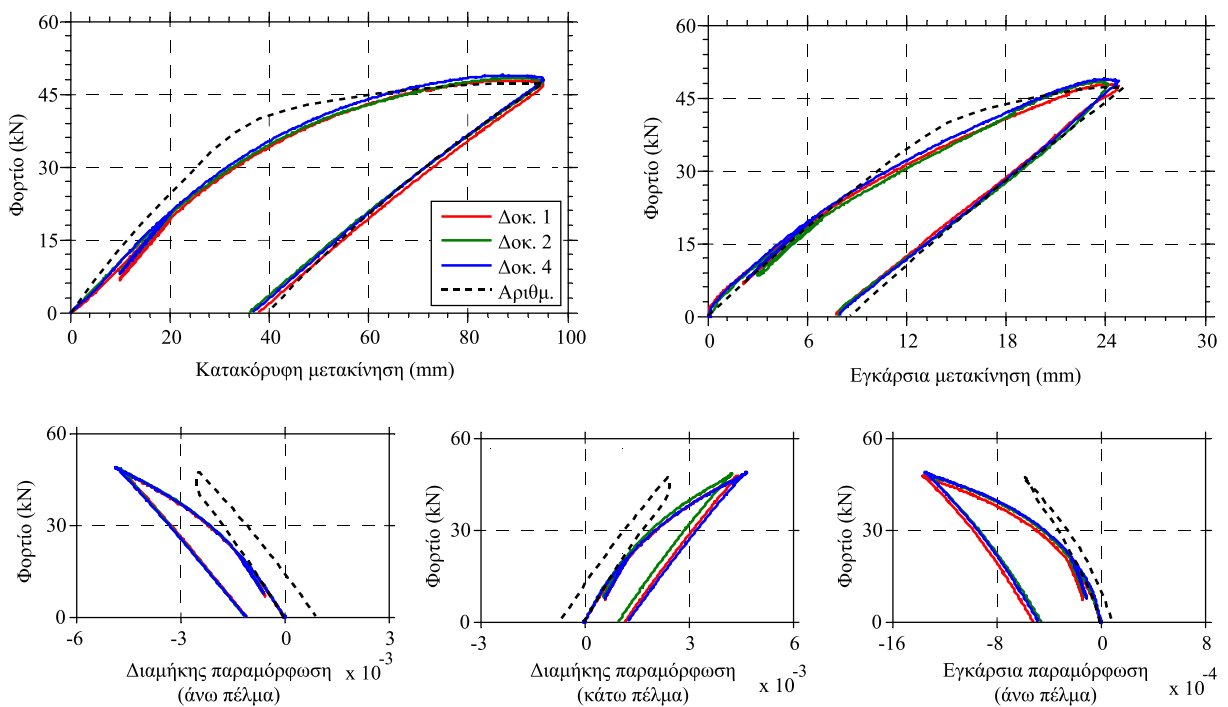


Σχήμα 6: Προσομοίωση της διαδικασίας εν ψυχρώ καμπύλωσης των τόξων.

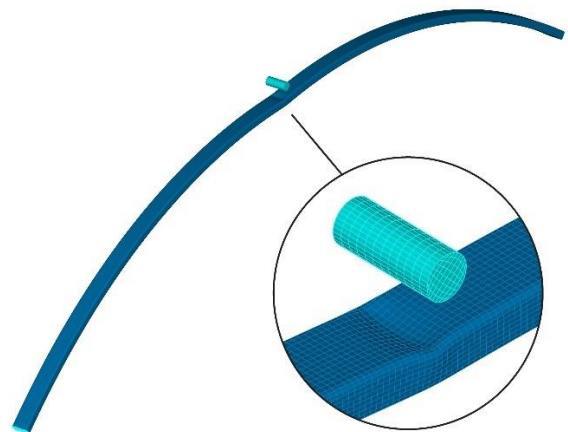


Σχήμα 7: Αριθμητικά προσομοιώματα των πειραματικών δοκιμών.

Η σύγκριση μεταξύ αριθμητικών και πειραματικών αποτελεσμάτων ελέγχεται μέσω σύγκρισης δρόμων ισορροπίας φορτίου-μετακίνησης, φορτίου-παραμορφώσεων, καθώς επίσης και μορφών παραμόρφωσης κατά την αστοχία. Η σύγκριση των δρόμων ισορροπίας για τα ψηλά τόξα υπό θλίψη παρουσιάζεται στο Σχήμα 8. Παρατηρείται εξαιρετική επαναληψιμότητα μεταξύ των πειραματικών δοκιμών. Από τον σύντομο κύκλο φόρτισης-αποφόρτισης που πραγματοποιήθηκε σε χαμηλό επίπεδο φορτίου, παρατηρείται πρόωρη πλαστικοποίηση του υλικού. Η κλίση του κύκλου αποφόρτισης συμπίπτει με την αρχική δυσκαμψία του αριθμητικού προσομοιώματος. Έτσι συνεπάγεται ότι η πρόωρη διαρροή οφείλεται στη μεταβολή των ιδιοτήτων του υλικού από την εν ψυχρώ διαμόρφωση, εξαιτίας του φαινομένου Bauschinger [39]. Κρίσιμος παράγοντας για το οριακό φορτίο είναι η καμπτική διαρροή στην κορυφή του τόξου, η οποία συνοδεύεται από τοπικό λυγισμό στο σημείο επαφής με τον κύλινδρο φόρτισης στο άνω πέλμα. Χαρακτηριστικές εικόνες του φορέα στο τέλος των πειραματικών δοκιμών και την αριθμητική προσομοίωση, παρουσιάζονται στο Σχήμα 9.

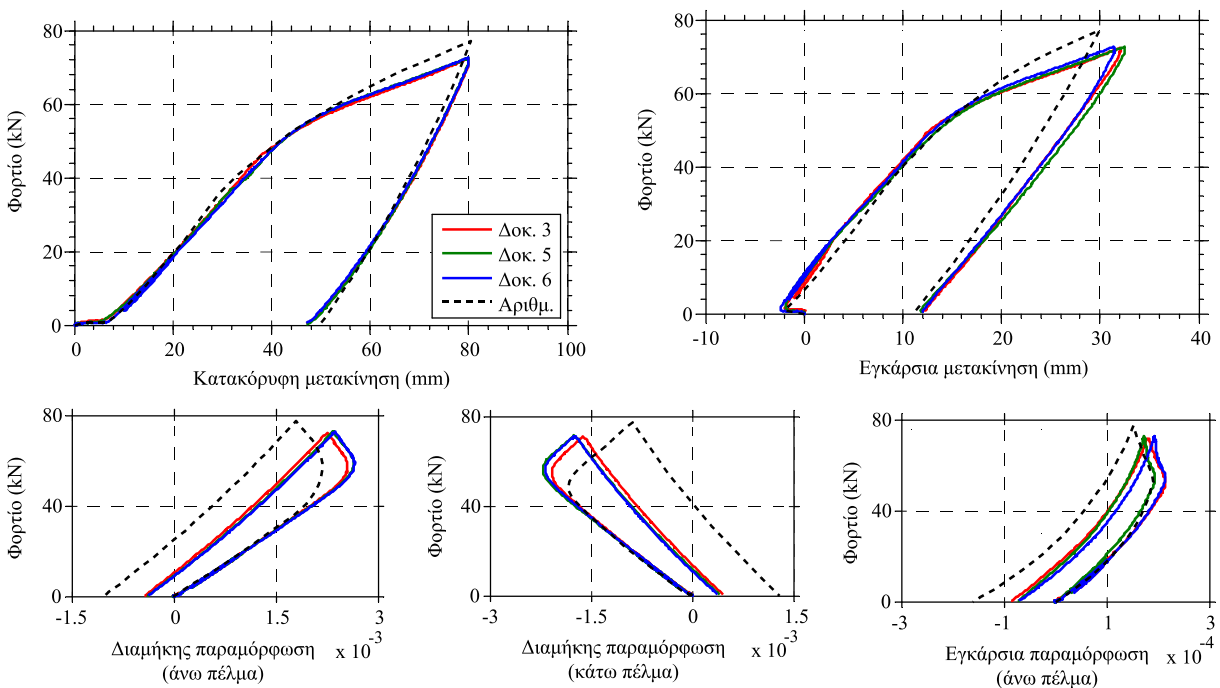


Σχήμα 8: Σύγκριση δρόμων ισορροπίας ψηλών τόξων υπό θλίψη.

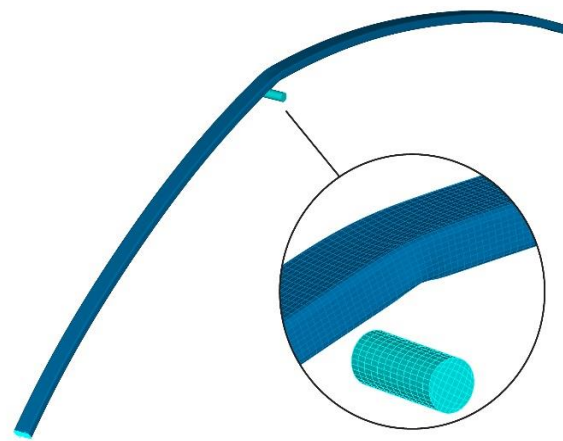


Σχήμα 9: Χαρακτηριστικά στιγμιότυπα παραμόρφωσης τόξων υπό θλίψη.

Η σύγκριση των δρόμων ισορροπίας αναφορικά με τα ψηλά τόξα υπό εφελκυσμό παρουσιάζεται στο Σχήμα 10. Και σε αυτή την περίπτωση παρατηρείται πολύ καλή επαναληψιμότητα μεταξύ των πειραματικών δοκιμών. Οι δρόμοι ισορροπίας φορτίου-μετακίνησης παρουσιάζουν έναν αρχικό κλάδο μηδενικής δυσκαμψίας εξαιτίας των γεωμετρικών ανοχών στις στηρίξεις. Η πρόωρη διαρροή που παρατηρήθηκε στον κύκλο φόρτισης-αποφόρτισης των τόξων υπό θλιπτικό φορτίο, δεν εμφανίζεται στην περίπτωση των τόξων υπό εφελκυσμό. Η ροπή κάμψης στην κορυφή είναι ομόρροπη με τη ροπή πλαστικοποίησης κατά την εν ψυχρώ διαμόρφωση, και ως εκ τούτου δεν εμφανίζεται το φαινόμενο Bauschinger. Η ροπή πλήρους πλαστικοποίησης είναι υψηλότερη πειραματικά σε σχέση με το αριθμητικό προσομοίωμα. Η αύξηση της πλαστικής αντοχής αποδίδεται στην ύπαρξη του φαινομένου strain aging [40], σύμφωνα με το οποίο αυξάνεται το όριο διαρροής του χάλυβα ύστερα από ορισμένο χρονικό διάστημα, όταν υποστεί πλαστικές παραμορφώσεις. Τα τόξα υπό εφελκυσμό παρουσιάζουν ανοδικό δρόμο ισορροπίας εξαιτίας της κράτυνσης του χάλυβα. Χαρακτηριστικά στιγμιότυπα των τόξων κατά τέλος των πειραματικών δοκιμών και της αριθμητικής προσομοίωσης παρουσιάζονται στο Σχήμα 11.



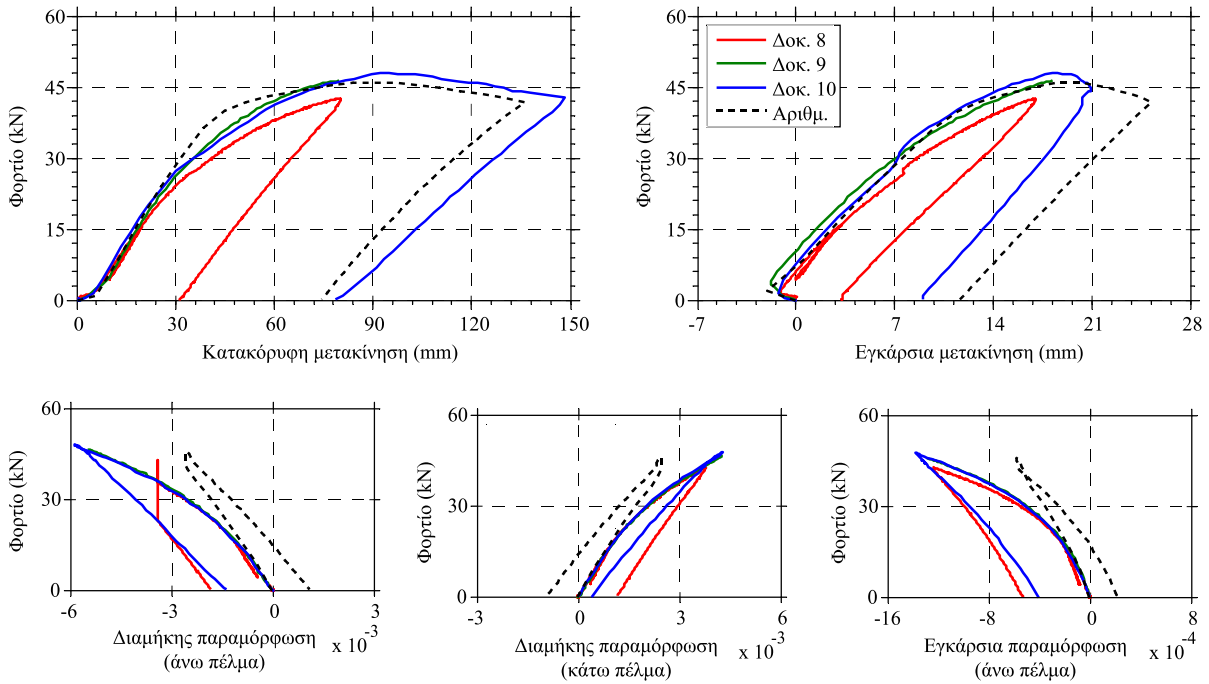
Σχήμα 10: Σύγκριση δρόμων ισορροπίας ψηλών τόξων υπό εφελκυσμό.



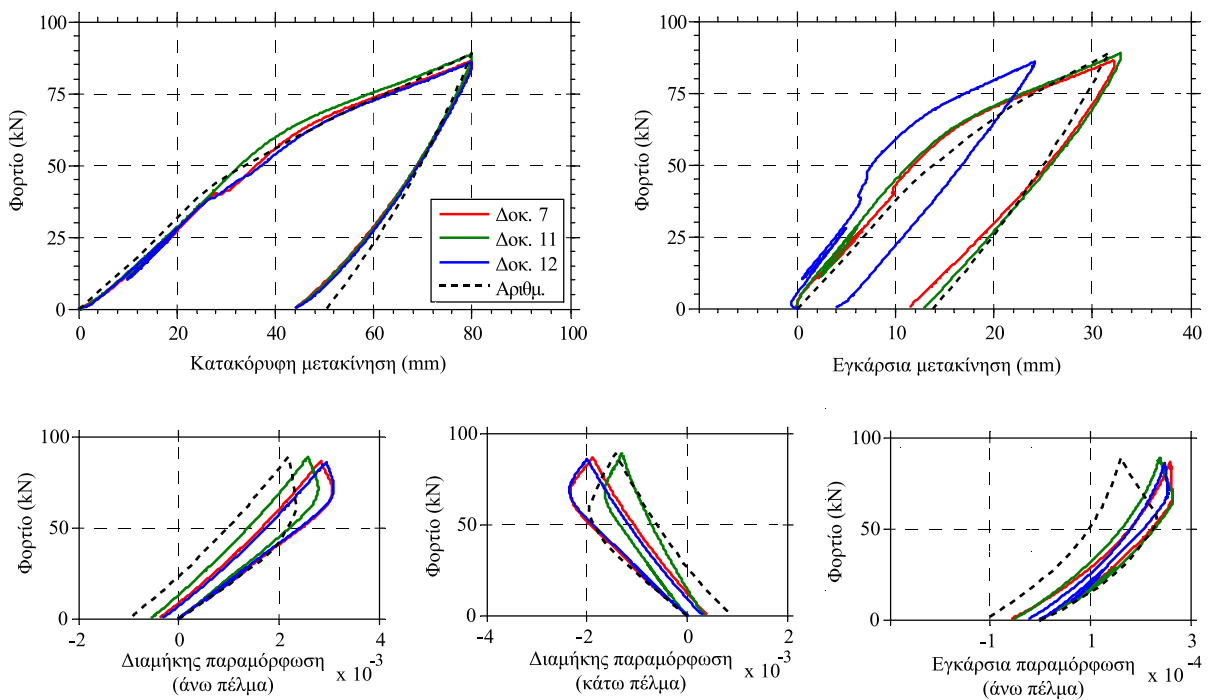
Σχήμα 11: Χαρακτηριστικά στιγμιότυπα παραμόρφωσης τόξων υπό εφελκυσμό.



Οι δρόμοι ισορροπίας των χαμηλών τόξων υπό θλίψη και εφελκυσμό παρουσιάζονται στο Σχήμα 12 και Σχήμα 13, αντίστοιχα. Τα αποτελέσματα και οι μορφές αστοχίας είναι παρόμοια με τα αντίστοιχα των ψηλών τόξων. Τέλος, πραγματοποιήθηκαν συγκρίσεις σε πανομοιότυπα αριθμητικά προσομοιώματα με/χωρίς παραμένουσες τάσεις. Για το σκοπό αυτό, χρησιμοποιήθηκαν οι γεωμετρίες των ψηλών και χαμηλών τόξων υπό διάφορες περιπτώσεις φορτίσεων. Από τις συγκρίσεις διαπιστώθηκε ότι η επιρροή των παραμενουσών τάσεων είναι σχετικά μικρή για τα εξεταζόμενα τόξα.



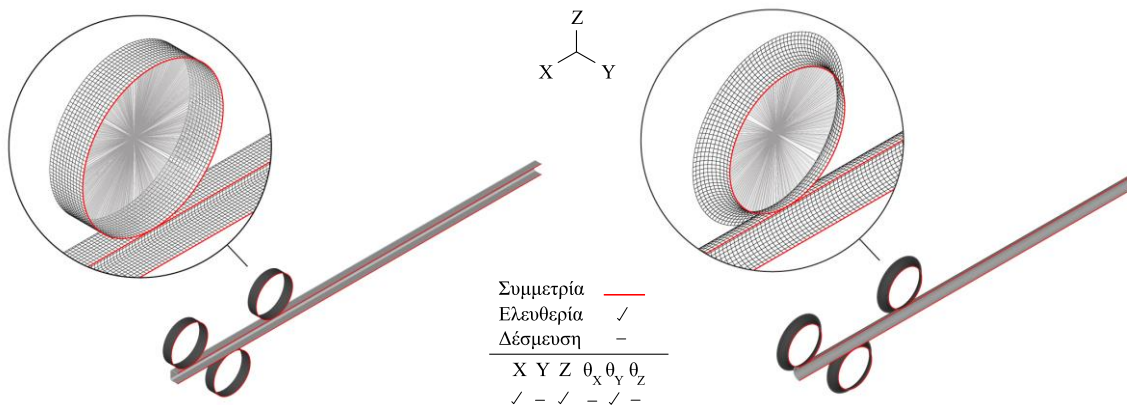
Σχήμα 12: Σύγκριση δρόμων ισορροπίας χαμηλών τόξων υπό θλίψη.



Σχήμα 13: Σύγκριση δρόμων ισορροπίας χαμηλών τόξων υπό εφελκυσμό.

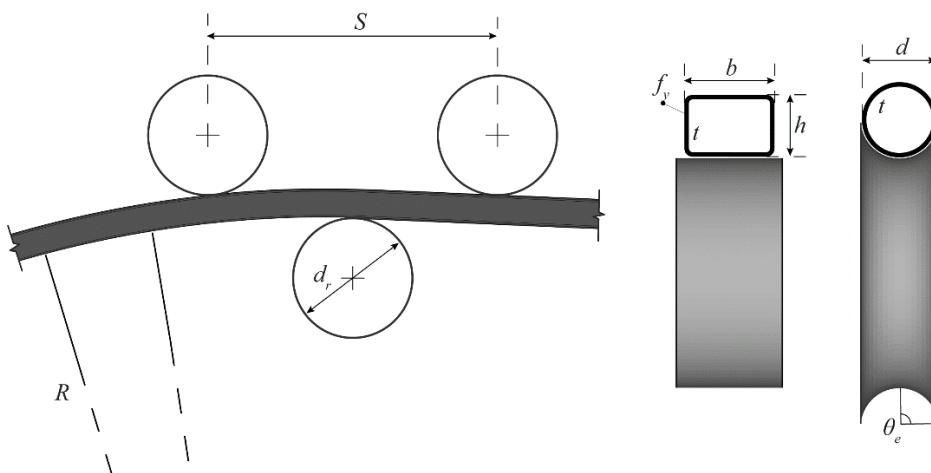
#### 4. ΠΑΡΑΜΕΤΡΙΚΕΣ ΑΝΑΛΥΣΕΙΣ ΚΑΜΠΥΛΩΣΗΣ ΤΟΞΩΝ ΚΟΙΛΗΣ ΔΙΑΤΟΜΗΣ

Οι παράγοντες που επηρεάζουν την κατανομή και το μέγεθος των παραμενουσών τάσεων εξαιτίας της εν ψυχρώ καμπύλωσης, εξετάζονται μέσω παραμετρικών αναλύσεων με πεπερασμένα στοιχεία. Για το σκοπό αυτό προσομοιώνεται λεπτομερώς η διαδικασία καμπύλωσης μελών που αποτελούνται από κοίλες κυκλικές, τετραγωνικές και ορθογωνικές διατομές. Τα υπό διαμόρφωση μέλη προσομοιώνονται σύμφωνα με τη μεθοδολογία που παρουσιάστηκε στο Κεφάλαιο 3. Αναλύσεις ευαισθησίας πραγματοποιούνται για τον έλεγχο σύγκλισης σχετικά με τον τύπο και το μέγεθος των στοιχείων. Για τη μείωση του υπολογιστικού φόρτου μορφώνεται το ήμισυ του αριθμητικού προσομοιώματος, αξιοποιώντας τις συνθήκες συμμετρίας του προβλήματος. Ενδεικτικά αριθμητικά προσομοιώματα της διαδικασίας καμπύλωσης κοίλων διατομών παρουσιάζονται στο Σχήμα 14.



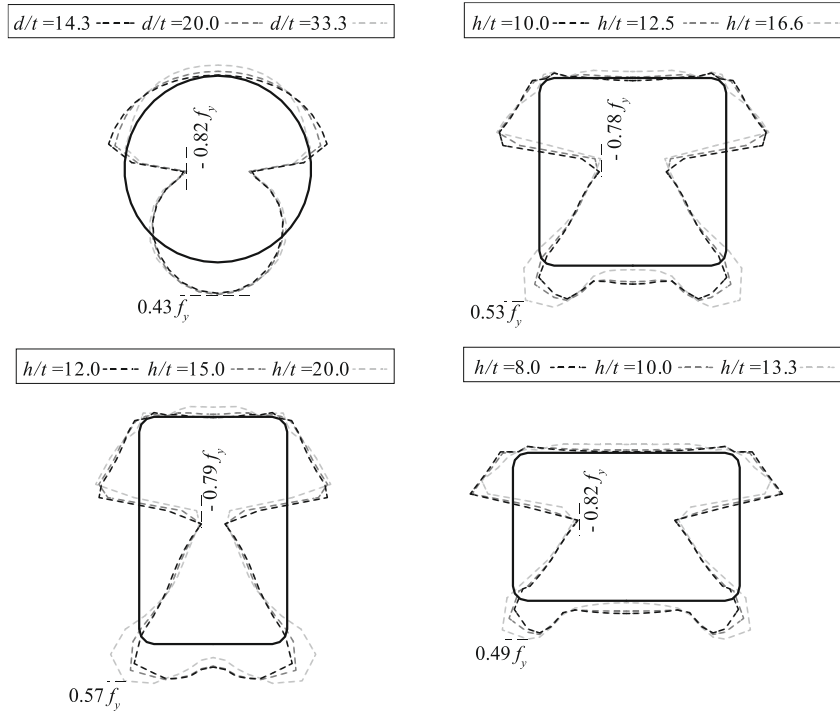
Σχήμα 14: Αριθμητικά προσομοιώματα καμπύλωσης SHS/RHS (αριστερά) και CHS (δεξιά).

Οι αριθμητικές αναλύσεις πραγματοποιούνται, εξετάζοντας ένα πλήθος παραμέτρων που αφορούν τις εξωτερικές διαστάσεις  $b$ ,  $h$ ,  $d$  και τα πάχη  $t$  των διατομών, την ακτίνα καμπυλότητας  $R$ , την ποιότητα του χάλυβα  $f_y$ , το μήκος κάμψης τριών σημείων  $S$ , τη διάμετρο των τυμπάνων  $d_r$  και τη γωνία επικάλυψης  $\theta_e$  στην περίπτωση των κοίλων κυκλικών διατομών. Για τις παραμετρικές αναλύσεις χρησιμοποιούνται οι διατομές RHS 80x120, SHS 100x100, RHS 120x80 και CHS 100. Τα αποτελέσματα παρουσιάζονται κατάλληλα αδιαστατοποιημένα, και ως εκ τούτου είναι ανεξάρτητα από την επιλογή των διατομών.

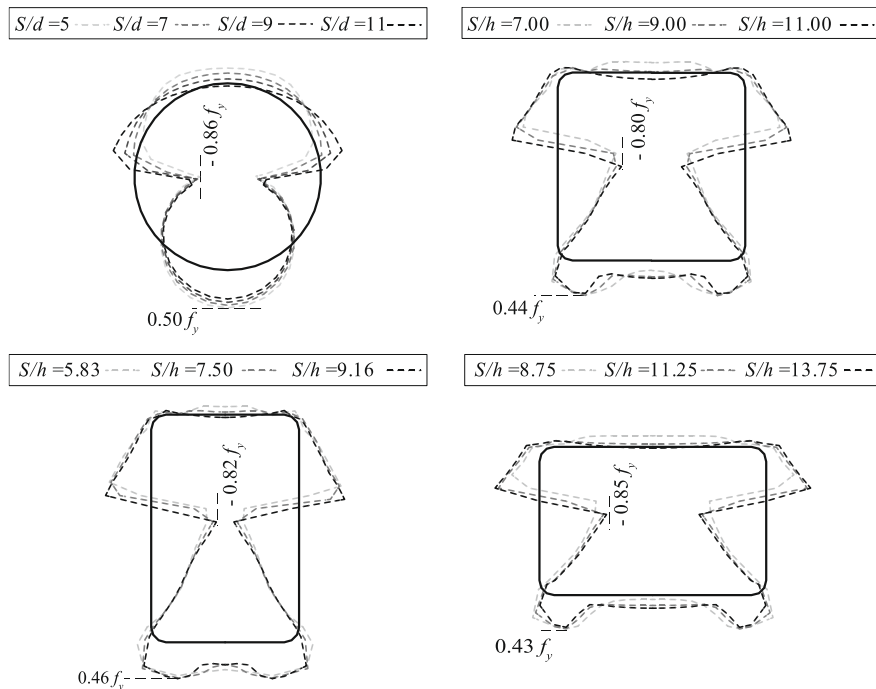


Σχήμα 15: Αριθμητικά προσομοιώματα καμπύλωσης μελών κοίλης διατομής.

Από τις παραμετρικές αναλύσεις προκύπτει πως οι λόγοι (α) ύψους προς πάχος της διατομής και (β) του μήκους κάμψης προς το ύψος της διατομής, επηρεάζουν κυρίως τις αναπτυσσόμενες παραμένουσες τάσεις. Στην περίπτωση διατομών μικρής λυγηρότητας, οι οποίες καμπυλώνονται εφαρμόζοντας μεγάλο μήκος κάμψης, οι παραμένουσες τάσεις προσεγγίζουν τη θεωρητική κατανομή Timoshenko. Οι παραμένουσες τάσεις παρουσιάζονται στο Σχήμα 16 και Σχήμα 17, ως συνάρτηση του λόγου ύψος προς πάχος και μήκος κάμψης προς ύψος της διατομής αντίστοιχα.

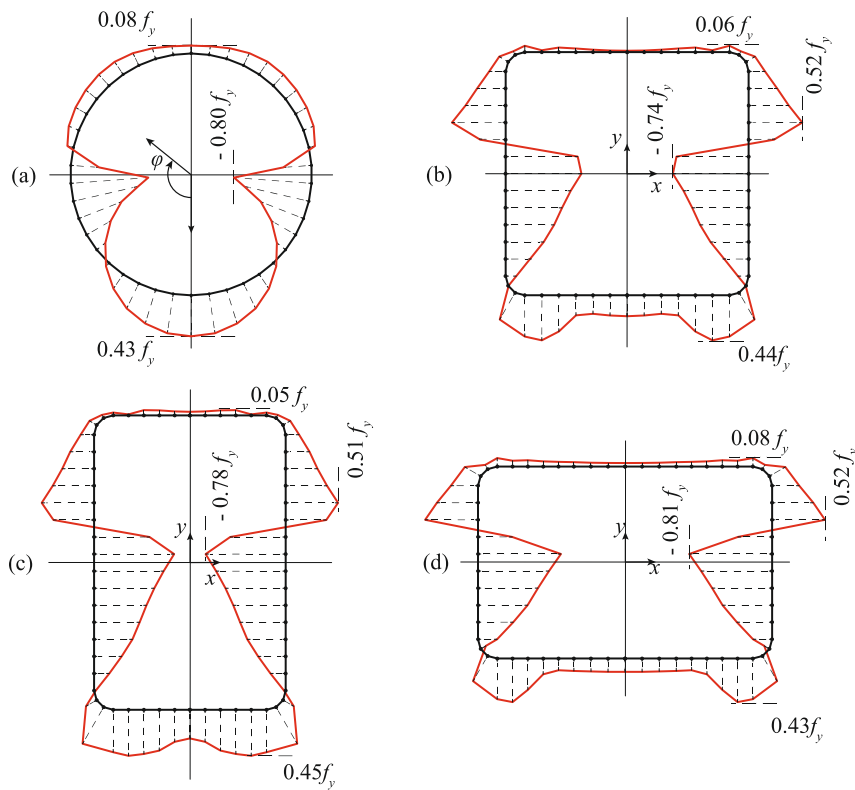


Σχήμα 16: Επιρροή του λόγου ύψος προς πάχος κοίλης διατομής στις παραμένουσες τάσεις.



Σχήμα 17: Επιρροή του λόγου μήκος κάμψης προς ύψος κοίλης διατομής στις παραμένουσες τάσεις.

Με βάση τα αποτελέσματα των παραμετρικών αναλύσεων, προτείνονται χαρακτηριστικές κατανομές παραμενουσών τάσεων για κοίλες διατομές καμπυλωμένες εν ψυχρώ. Οι κατανομές ικανοποιούν τις συνθήκες εσωτερικής ισορροπίας σε όρους δυνάμεων και ροπών. Οι προτεινόμενες κατανομές για κοίλες κυκλικές, τετραγωνικές, και ορθογωνικές διατομές ( $h/b = 0.66$ ,  $h/b = 1.50$ ) παρουσιάζονται στο Σχήμα 18. Οι τιμές των παραμενουσών τάσεων δίνονται στους Πίνακες 1 έως 4.



Σχήμα 18: Προτεινόμενες κατανομές παραμενουσών τάσεων λόγω εν ψυχρώ καμπύλωσης σε κοίλες διατομές.

Πίνακας 1: Παραμένουσες τάσεις κοίλων κυκλικών διατομών.

$\varphi$ (rad)	Τάση ( $f_y$ )	$\varphi$ (rad)	Τάση ( $f_y$ )
0.00	0.43	1.65	-0.29
0.15	0.41	1.80	0.07
0.30	0.36	1.94	0.11
0.45	0.29	2.09	0.13
0.60	0.18	2.24	0.15
0.75	0.05	2.39	0.16
0.90	-0.11	2.54	0.16
1.05	-0.29	2.69	0.14
1.20	-0.48	2.84	0.11
1.35	-0.68	2.99	0.09
1.50	-0.80	3.14	0.08



Πίνακας 2: Παραμένουσες τάσεις κοίλων τετραγωνικών διατομών.

A/A	Θέση $x(b)$	Θέση $y(h)$	Τάση ( $f_i$ )	A/A	Θέση $x(b)$	Θέση $y(h)$	Τάση ( $f_i$ )
1	0.00	-0.50	0.20	17	0.50	0.07	-0.71
2	0.07	-0.50	0.20	18	0.50	0.14	0.25
3	0.14	-0.50	0.18	19	0.50	0.21	0.52
4	0.21	-0.50	0.20	20	0.50	0.28	0.39
5	0.28	-0.50	0.35	21	0.50	0.35	0.28
6	0.35	-0.50	0.44	22	0.50	0.42	0.16
7	0.42	-0.50	0.40	23	0.49	0.46	0.10
8	0.46	-0.49	0.30	24	0.46	0.49	0.04
9	0.49	-0.46	-0.01	25	0.42	0.50	0.06
10	0.50	-0.42	-0.11	26	0.35	0.50	0.02
11	0.50	-0.35	-0.24	27	0.28	0.50	0.05
12	0.50	-0.28	-0.37	28	0.21	0.50	0.04
13	0.50	-0.21	-0.47	29	0.14	0.50	0.02
14	0.50	-0.14	-0.55	30	0.07	0.50	0.02
15	0.50	-0.07	-0.64	31	0.00	0.50	0.01
16	0.50	0.00	-0.74				

Πίνακας 3: Παραμένουσες τάσεις κοίλων ορθογωνικών διατομών ( $h/b = 1.50$ ).

A/A	Θέση $x(b)$	Θέση $y(h)$	Τάση ( $f_i$ )	A/A	Θέση $x(b)$	Θέση $y(h)$	Τάση ( $f_i$ )
1	0.00	-0.50	0.28	17	0.50	0.03	-0.78
2	0.08	-0.50	0.31	18	0.50	0.09	-0.54
3	0.16	-0.50	0.40	19	0.50	0.14	0.40
4	0.24	-0.50	0.43	20	0.50	0.20	0.51
5	0.32	-0.50	0.45	21	0.50	0.26	0.40
6	0.40	-0.50	0.41	22	0.50	0.32	0.31
7	0.45	-0.49	0.41	23	0.50	0.38	0.23
8	0.49	-0.47	0.12	24	0.50	0.43	0.13
9	0.50	-0.43	-0.02	25	0.49	0.47	0.08
10	0.50	-0.38	-0.15	26	0.45	0.49	0.03
11	0.50	-0.32	-0.27	27	0.40	0.50	0.03
12	0.50	-0.26	-0.37	28	0.32	0.50	0.01
13	0.50	-0.20	-0.45	29	0.24	0.50	0.05
14	0.50	-0.14	-0.51	30	0.16	0.50	0.05
15	0.50	-0.09	-0.59	31	0.08	0.50	0.04
16	0.50	-0.03	-0.68	32	0.00	0.50	0.03

Πίνακας 4: Παραμένουσες τάσεις κοίλων ορθογωνικών διατομών ( $h/b = 0.66$ ).

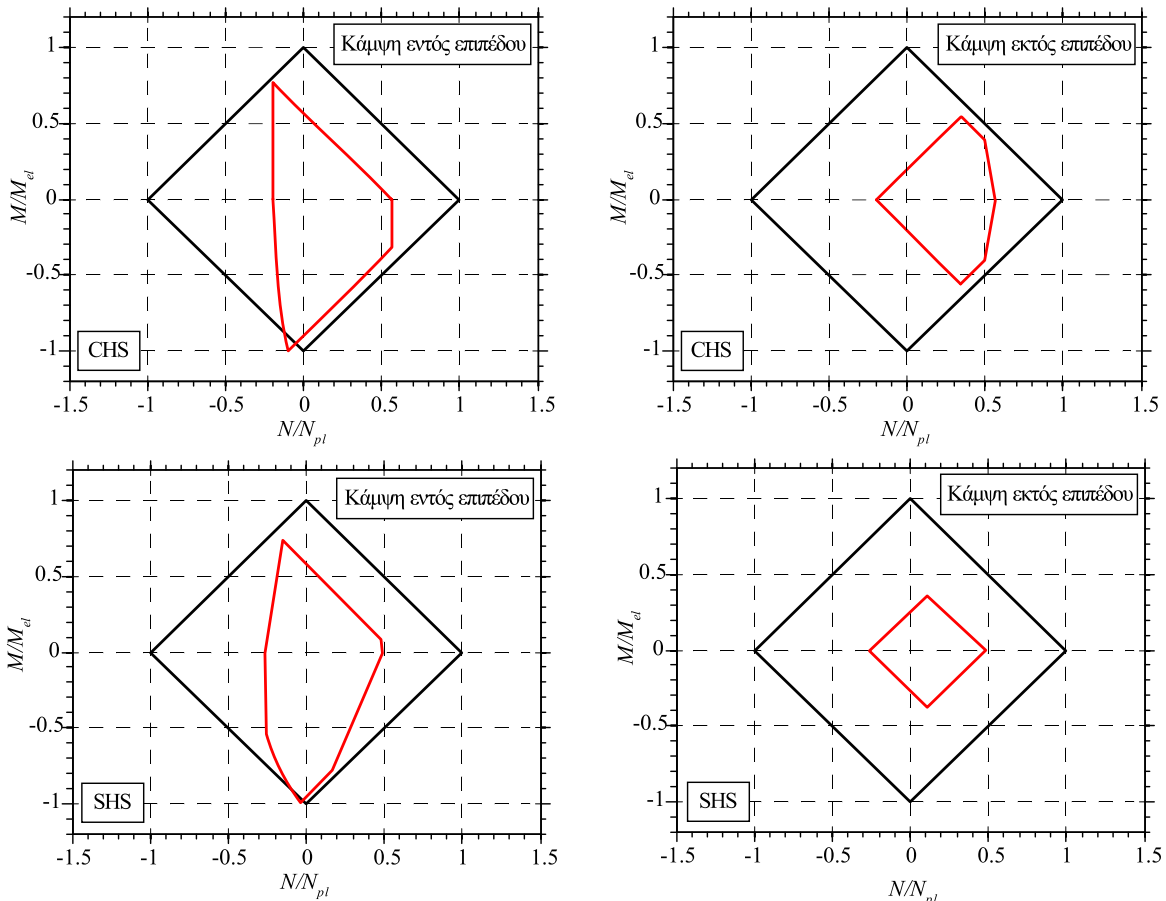
A/A	Θέση $x(b)$	Θέση $y(h)$	Τάση ( $f_i$ )	A/A	Θέση $x(b)$	Θέση $y(h)$	Τάση ( $f_i$ )
1	0.00	-0.50	0.13	17	0.50	0.04	-0.81
2	0.06	-0.50	0.13	18	0.50	0.13	-0.33
3	0.12	-0.50	0.13	19	0.50	0.22	0.52
4	0.17	-0.50	0.12	20	0.50	0.31	0.40
5	0.23	-0.50	0.11	21	0.50	0.40	0.27
6	0.28	-0.50	0.15	22	0.49	0.45	0.18
7	0.33	-0.50	0.31	23	0.47	0.49	0.05
8	0.38	-0.50	0.43	24	0.43	0.50	0.08
9	0.43	-0.50	0.40	25	0.38	0.50	0.06
10	0.47	-0.49	0.28	26	0.33	0.50	0.06
11	0.49	-0.45	-0.06	27	0.28	0.50	0.05
12	0.50	-0.40	-0.19	28	0.23	0.50	0.05
13	0.50	-0.31	-0.35	29	0.17	0.50	0.04
14	0.50	-0.22	-0.48	30	0.12	0.50	0.04
15	0.50	-0.13	-0.59	31	0.06	0.50	0.03
16	0.50	-0.04	-0.69	32	0.00	0.50	0.03

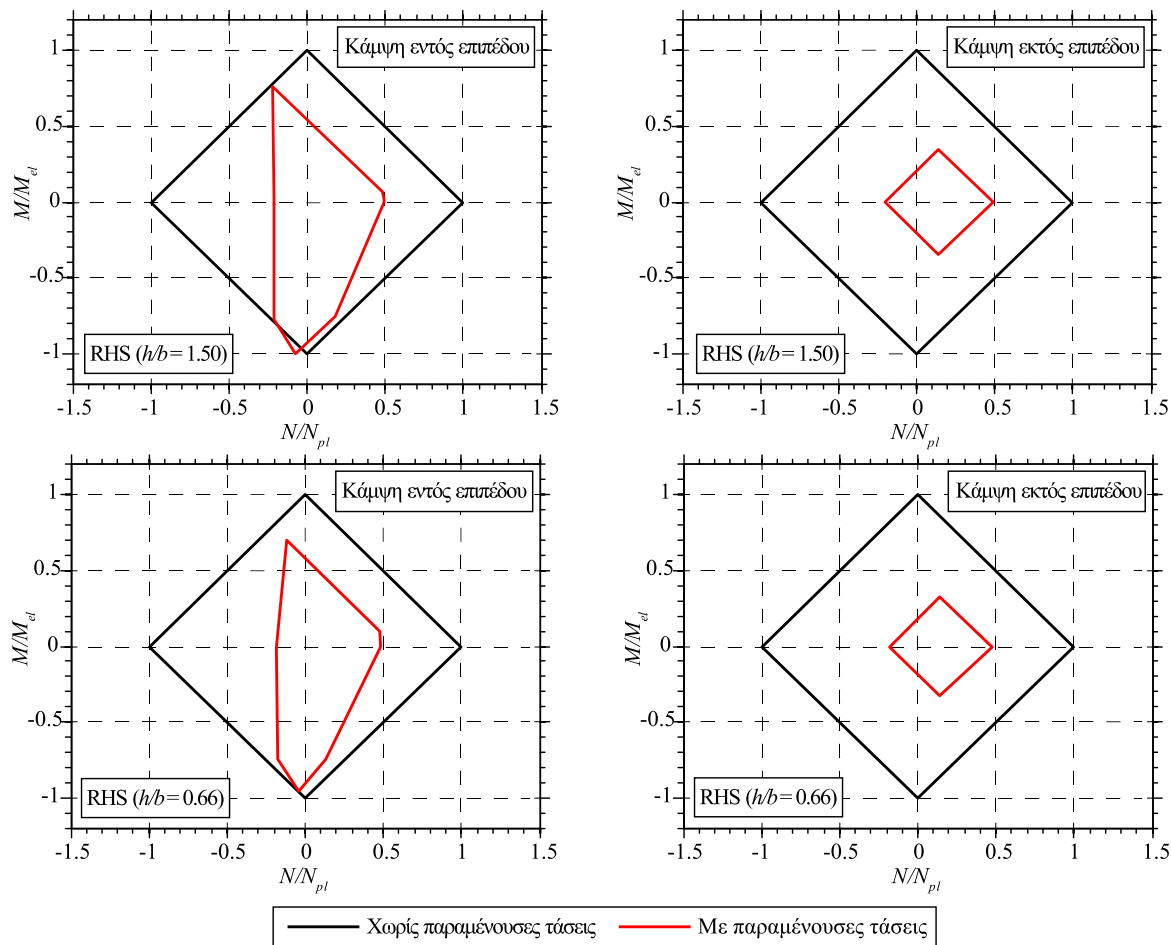
## 5. ΕΠΙΡΡΟΗ ΠΑΡΑΜΕΝΟΥΣΩΝ ΤΑΣΕΩΝ ΛΟΓΩ ΚΑΜΠΥΛΩΣΗΣ

Η παρουσία παραμενουσών τάσεων στις διατομές από χάλυβα επηρεάζει τη συνολική συμπεριφορά των μελών, προκαλώντας είτε (α) έναρξη της διαδικασίας πλαστικοποίησης για τιμές της εξωτερικής φόρτισης μικρότερες από την τιμή που αντιστοιχεί στο όριο αναλογίας του υλικού ή (β) μείωση της αντοχής όταν η αστοχία οφείλεται σε λυγισμό. Η έναρξη της διαρροής σε κοίλες διατομές καμπυλωμένες εν ψυχρώ προσδιορίζεται υπολογίζοντας την αναλυτική έκφραση της εξίσωσης αλληλεπίδρασης για συνδυασμένη φόρτιση αξονικής δύναμης και καμπτικής ροπής σύμφωνα με την Εξ. 9, όπου  $A$  το εμβαδόν της διατομής,  $I$  η καμπτική ροπή αδρανείας,  $z$  η απόσταση από τον ουδέτερο άξονα, και  $\sigma_{rs}$  η τιμή παραμένουσας τάσης στη θέση  $z$ .

$$\frac{N}{A} + \frac{M}{I}z + \sigma_{rs} \leq f_y \quad (\text{Εξ. 9})$$

Διαγράμματα αλληλεπίδρασης  $M-N$  για κοίλες κυκλικές, τετραγωνικές και ορθογωνικές διατομές παρουσιάζονται στο Σχ. 19. Οι υπολογισμοί πραγματοποιήθηκαν σε διατομές CHS 100x5, SHS 100x100x8, RHS 120x80x8, και RHS 80x120x8, χρησιμοποιώντας τις προτεινόμενες κατανομές παραμενουσών τάσεων που υπολογίστηκαν στο Κεφάλαιο 4. Τα διαγράμματα παρουσιάζονται αδιαστατοποιημένα με την ελαστική αντοχή των διατομών, και ως εκ τούτου τα αποτελέσματα δεν εξαρτώνται από την επιλογή των διατομών. Η θεωρητική κατανομή Timoshenko περιλαμβάνει μέγιστη τιμή παραμενουσών τάσεων ίση με το όριο διαρροής, και επομένως στην περίπτωση αυτή δεν υπάρχει ελαστικό όριο αντοχής. Εφελκυστικές δυνάμεις και καμπτικές ροπές που τείνουν να ανοίξουν το τόξο έχουν συμβατικά θετικό πρόσημο. Παρατηρείται πιο μεγάλη μείωση της ελαστικής αντοχής για κάμψη εκτός επιπέδου, καθώς οι μέγιστες τιμές παραμενουσών τάσεων συναντώνται περί το μέσο των κοίλων διατομών. Συνολικά, τα αποτελέσματα είναι παρόμοια στις κοίλες κυκλικές, τετραγωνικές και ορθογωνικές διατομές. Τα διαγράμματα αλληλεπίδρασης μπορούν να χρησιμοποιηθούν στον ελαστικό σχεδιασμό των τόξων από χάλυβα.





Σχήμα 19: Διαγράμματα αλληλεπίδρασης  $M-N$  για κοίλες κυκλικές, τετραγωνικές και ορθογωνικές διατομές.

Η επιρροή των παραμενουσών τάσεων στο κρίσιμο φορτίο λυγισμού των τόξων υπολογίζεται με βάση αναλυτικές εκφράσεις. Η μεθοδολογία υπολογισμού [41] βασίζεται στον προσδιορισμό της ενεργούς καμπτικής δυσκαμψίας μιας διατομής, θεωρώντας ότι για δεδομένη αξονική ένταση τμήμα της διατομής έχει πλαστικοποιηθεί λόγω των παραμενουσών τάσεων, και επομένως δεν συνεισφέρει στην καμπτική αντίσταση. Τα κρίσιμα φορτία λυγισμού εντός και εκτός επιπέδου των τόξων με απλές στρεπτικές στηρίξεις και υπό ομοιόμορφο ακτινικά κατανομημένο φορτίο, δίνονται από τις Εξ. 10 και Εξ. 11 [42].

$$N_{cr}^{in-plane} = \frac{EI_{yy}}{R^2} \left( \frac{\pi^2}{(a/2)^2} - 1 \right) \quad (\text{Εξ. 10})$$

$$N_{cr}^{out-of-plane} = \frac{EI_{zz}}{R^2} \cdot \frac{(\pi^2 - \alpha^2)^2}{\alpha^2[\pi^2 + \alpha^2(EI_{zz}/C)]} \quad (\text{Εξ. 11})$$

όπου,  $EI_{yy}$  η καμπτική δυσκαμψία εντός επιπέδου,  $EI_{zz}$  η καμπτική δυσκαμψία εκτός επιπέδου,  $C$  η στρεπτική δυσκαμψία,  $R$  η ακτίνα του κυκλικού τόξου,  $a$  η γωνία του κυκλικού τόξου.

Η ενεργός θλιπτική τάση  $\sigma_{eff}$  που αναπτύσσεται σε μια διατομή με παραμένουσες  $\sigma_{rs}$ , για δεδομένη αντίστοιχη τιμή τάσης  $\sigma_u$  χωρίς παραμένουσες, υπολογίζεται από την Εξ. 12.

$$\begin{aligned} \sigma_{eff} &= f_y, & \text{όταν } \sigma_{rs} + \sigma_u &\geq f_y \\ \sigma_{eff} &= \sigma_{rs} + \sigma_u, & \text{όταν } \sigma_{rs} + \sigma_u &< f_y \end{aligned} \quad (\text{Εξ. 12})$$

Ολοκληρώνοντας τις τιμές της ενεργούς τάσης στο εμβαδόν της διατομής υπολογίζεται η ενεργός αξονική δύναμη  $N_{eff}$ , σύμφωνα με την Εξ. 13.

$$N_{eff} = \int_A \sigma_{eff} dA \quad (\text{Εξ. 13})$$

Η ενεργός ροπή αδράνειας της διατομής  $I_{eff}$  υπολογίζεται συναρτήσει της ενεργούς τάσης που αναπτύσσεται στη διατομή, θεωρώντας μηδενική αντίσταση στις περιοχές που έχουν πλαστικοποιηθεί (Εξ. 14).

$$I_{eff}^{yy} = \int_{A_{el}} z^2 dydz, \text{ για } \sigma_{eff}(y, z) \leq f_y \quad (\text{Εξ. 14})$$

$$I_{eff}^{zz} = \int_{A_{el}} y^2 dydz, \text{ για } \sigma_{eff}(y, z) \leq f_y$$

Με αντικατάσταση των τιμών ενεργούς ροπής αδράνειας στις Εξ. 10 και Εξ. 11 υπολογίζεται το κρίσιμο φορτίο του τόξου με παραμένουσες τάσεις  $N_{cr,eff}$ . Η ανηγμένη λυγηρότητα  $\bar{\lambda}$  του τόξου υπολογίζεται από την τετραγωνική ρίζα της πλαστικής αντοχής προς το κρίσιμο φορτίο λυγισμού (Εξ. 15). Έτσι, βρίσκεται η ζητούμενη τιμή της λυγηρότητας για την οποία το  $N_{cr,eff}$  ισούται με το  $N_{eff}$ .

$$\bar{\lambda} = \sqrt{\frac{N_{pl}}{N_{cr}}} \quad (\text{Εξ. 15})$$

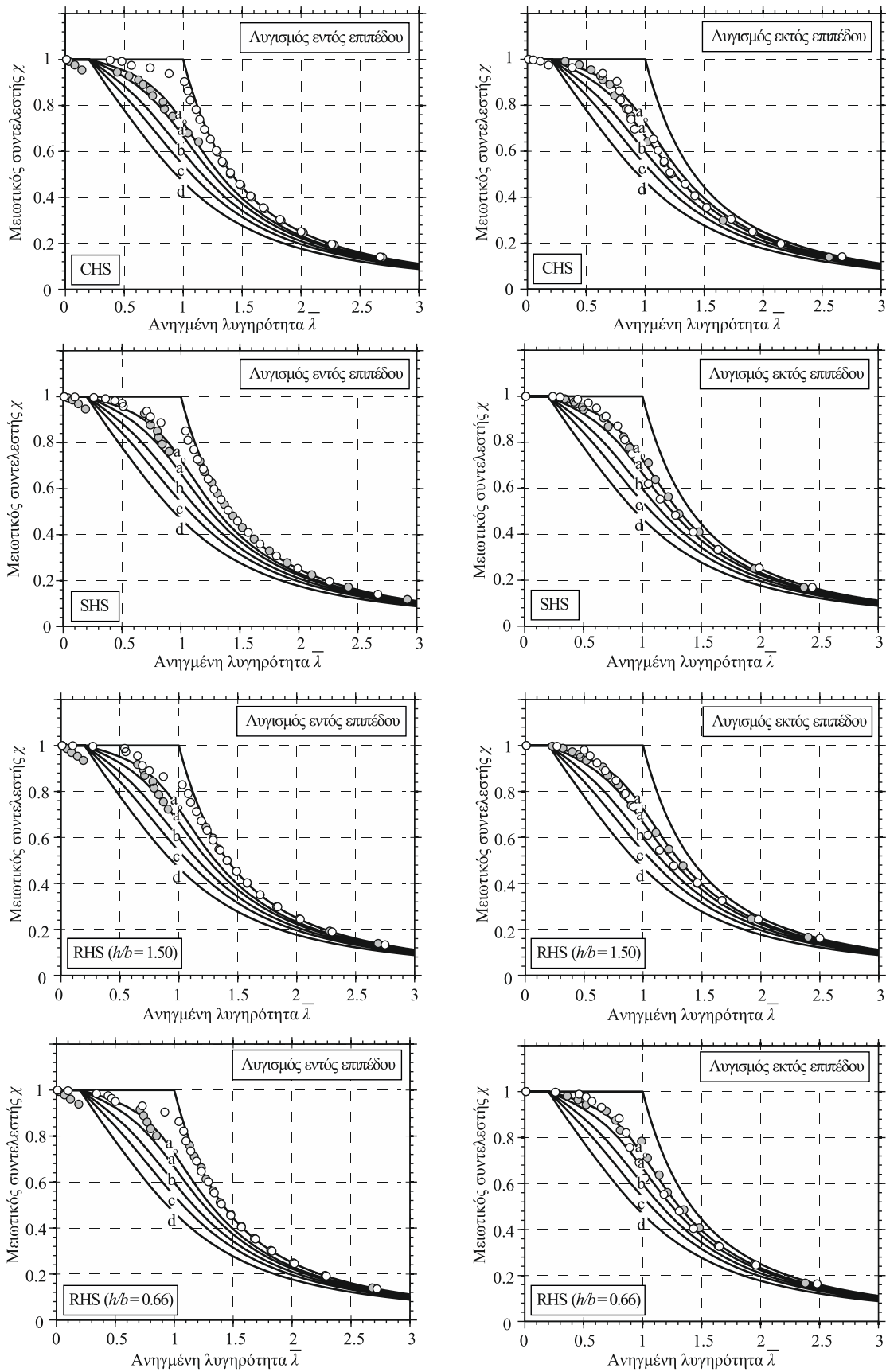
Η μέση αναπτυσσόμενη τάση στη διατομή  $\sigma_{avg}$  υπολογίζεται από την Εξ. 16. Ο μειωτικός συντελεστής  $\chi$  υπολογίζεται για την συγκεκριμένη ανηγμένη λυγηρότητα από την Εξ. 17.

$$\sigma_{avg} = \frac{N_{eff}}{A} \quad (\text{Εξ. 16})$$

$$\chi = \frac{\sigma_{avg}}{f_y} \quad (\text{Εξ. 17})$$

Η διαδικασία επαναλαμβάνεται για ολόκληρο το εύρος τάσης  $\sigma_u \leq f_y$ .

Τα κρίσιμα φορτία λυγισμού για τόξα κοίλης κυκλικής, τετραγωνικής και ορθογωνικής διατομής παρουσιάζονται στο Σχ. Α-20. Τα αποτελέσματα συγκρίνονται με τις καμπύλες λυγισμού ( $a_0, a, b, c, d$ ) του Ευρωκώδικα 3 [6]. Οι υπολογισμοί πραγματοποιήθηκαν σε διατομές CHS 100x5, SHS 100x100x8, RHS 120x80x8, RHS 80x120x8, ορίου διαρροής 355MPa, και συνολική γωνία τόξου  $\pi/8$ . Σχετικές αναλύσεις έδειξαν ότι οι παράμετροι έχουν αμελητέα επιρροή στα αδιαστατοποιημένα αποτελέσματα υπό μορφής καμπυλών λυγισμού. Για κάθε σχήμα διατομής χρησιμοποιήθηκαν δύο διαφορετικές κατανομές τάσεων, η θεωρητική κατανομή Timoshenko [7] και η προτεινόμενη κατανομή που προέκυψε από τις αριθμητικές αναλύσεις του Κεφ. 4. Η θεωρητική κατανομή παρουσιάζει θλιπτικές παραμένουσες τάσεις στο άνω τμήμα της διατομής, και επομένως προκαλεί πιο σημαντική μείωση στα κρίσιμα φορτία λυγισμού εντός επιπέδου σε σχέση με την αριθμητική κατανομή. Η απότομη μείωση του κρίσιμου φορτίου για μικρή αλλαγή της ανηγμένης λυγηρότητας, που συναντάται χρησιμοποιώντας την θεωρητική κατανομή, οφείλεται στην ταυτόχρονη πλαστικοποίηση μεγάλου τμήματος της διατομής, εξαιτίας της σταθερής τάσης κατά μήκος των πελμάτων. Η μείωση του κρίσιμου φορτίου λυγισμού είναι πιο μεγάλη για τον εκτός επιπέδου σε σχέση με τον εντός επιπέδου λυγισμό, καθώς οι μέγιστες τιμές παραμενουσών τάσεων συναντώνται περί το μέσο των κοίλων διατομών, έχοντας σημαντική επιρροή στην καμπική δυσκαμψία εκτός επιπέδου. Η επιρροή των παραμενουσών τάσεων σε πολύ λυγηρά τόξα είναι αμελητέα. Συνολικά, τα αποτελέσματα είναι σχεδόν παρόμοια για τις κοίλες κυκλικές, τετραγωνικές και ορθογωνικές διατομές. Κλείνοντας, τα κρίσιμα φορτία λυγισμού είναι χρήσιμα για την ποιοτική αξιολόγηση της επιρροής των παραμενουσών τάσεων μεταξύ διαφόρων τύπων διατομών, αλλά δεν μπορούν να χρησιμοποιηθούν κατευθείαν στον σχεδιασμό των τόξων, καθώς δεν περιλαμβάνουν την επιρροή των γεωμετρικών ατελειών.



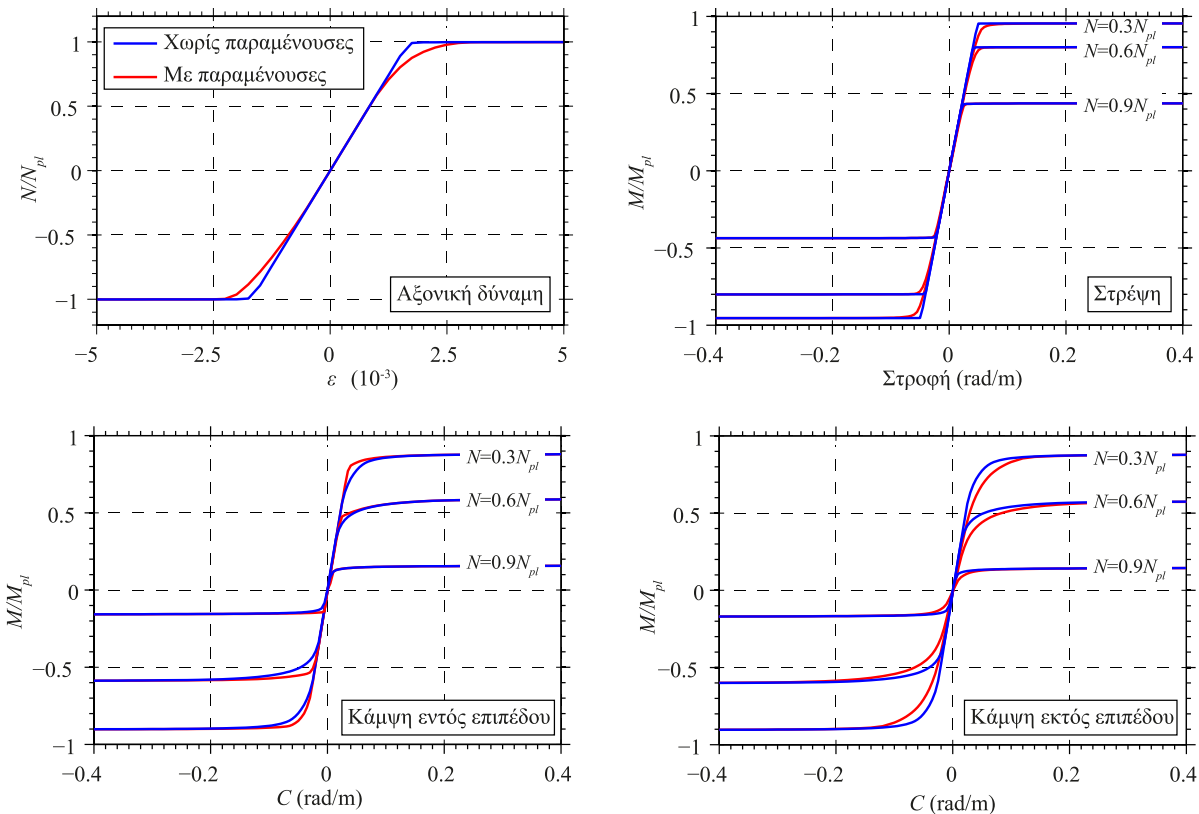
Παραμένουσες τάσεις: ○ Αριθμητική κατανομή ○ Θεωρητική κατανομή

Σχήμα 20: Κρίσιμα φορτία λυγισμού για τόξα κοίλης κυκλικής, τετραγωνικής και ορθογωνικής διατομής.

## 6. ΕΥΣΤΑΘΕΙΑ ΤΟΞΩΝ ΚΑΙ ΚΡΙΤΗΡΙΑ ΣΧΕΔΙΑΣΜΟΥ

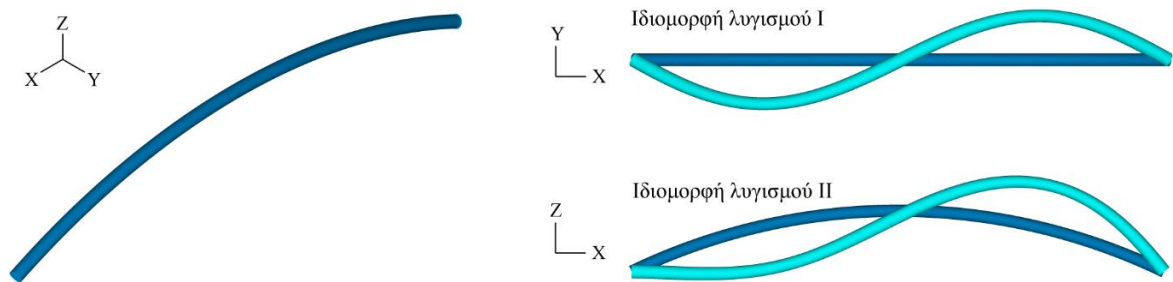
Οι παραμένουσες τάσεις και οι γεωμετρικές ατέλειες επηρεάζουν σημαντικά την αντοχή σε λυγισμό μελών από χάλυβα. Εκτεταμένη έρευνα έχει πραγματοποιηθεί διεθνώς για την εκτίμηση της οριακής αντοχής ευθύγραμμων μελών υπό θλίψη μέσω της διατύπωσης κατάλληλων καμπυλών λυγισμού [33]. Οι καμπύλες λυγισμού βασίζονται στην εκτέλεση μεγάλου πλήθους αριθμητικών αναλύσεων που περιλαμβάνουν παραμένουσες τάσεις και γεωμετρικές ατέλειες, χρησιμοποιώντας αξιόπιστα προσομοιώματα πεπερασμένων στοιχείων που έχουν πιστοποιηθεί μέσω πειραματικών δοκιμών. Κατάλληλες καμπύλες λυγισμού για καμπύλα μέλη δεν υπάρχουν διαθέσιμες στη βιβλιογραφία, εκτός από την περίπτωση κυκλικών τόξων διατομής HEA, HEB και IPE [28]. Έτσι, στον σύγχρονο σχεδιασμό τοξωτών φορέων χρησιμοποιούνται οι καμπύλες λυγισμού που προορίζονται για ευθύγραμμα μέλη, οι οποίες περιλαμβάνουν διαφορετικές κατανομές παραμενουσών τάσεων. Στο πλαίσιο της παρούσας διατριβής προτείνεται η δημιουργία καμπυλών λυγισμού για χαλύβδινα κυκλικά τόξα κοίλης διατομής.

Για το σκοπό αυτό, τόξα κοίλης κυκλικής διατομής προσομοιώνονται με πεπερασμένα στοιχεία δοκού (beam elements), χρησιμοποιώντας κατάλληλα διαγράμματα αξονικής δύναμης-παραμόρφωσης, καμπτικής ροπής-καμπυλότητας και στρεπτικής ροπής-στροφής. Τα διαγράμματα αναφέρονται στις μηχανικές ιδιότητες διατομής CHS 100x5, ποιότητας χάλυβα S355, και παράγονται μέσω μη γραμμικών αναλύσεων υλικού σε κατάλληλα προσομοιώματα με ή χωρίς παραμένουσες τάσεις. Για τον έλεγχο της προτεινόμενης προσομοίωσης, πραγματοποιήθηκαν αναλύσεις ευαισθησίας σε μία περίπτωση τόξου με ακτίνα καμπυλότητας  $R = 5.09\text{m}$  και λόγο ύψους προς άνοιγμα  $f/l = 0.11$  (benchmark case), συγκρίνοντας τα αριθμητικά αποτελέσματα στοιχείων δοκού και επιφανειακών στοιχείων. Από τη σύγκριση προέκυψε ότι ο προτεινόμενος τρόπος προσομοίωσης είναι ακριβής. Τα διαγράμματα αξονικής δύναμης-παραμόρφωσης, καμπτικής ροπής-καμπυλότητας και στρεπτικής ροπής-στροφής, για ενδεικτικά επίπεδα αξονικής θλιπτικής δύναμης  $0.3N_{pl}$ ,  $0.6N_{pl}$ , και  $0.9N_{pl}$ , παρουσιάζονται στο Σχήμα 21. Οι εφελκυστικές δυνάμεις και οι καμπτικές ροπές που τείνουν να ανοίξουν το τόξο έχουν συμβατικά θετικό πρόσημο.



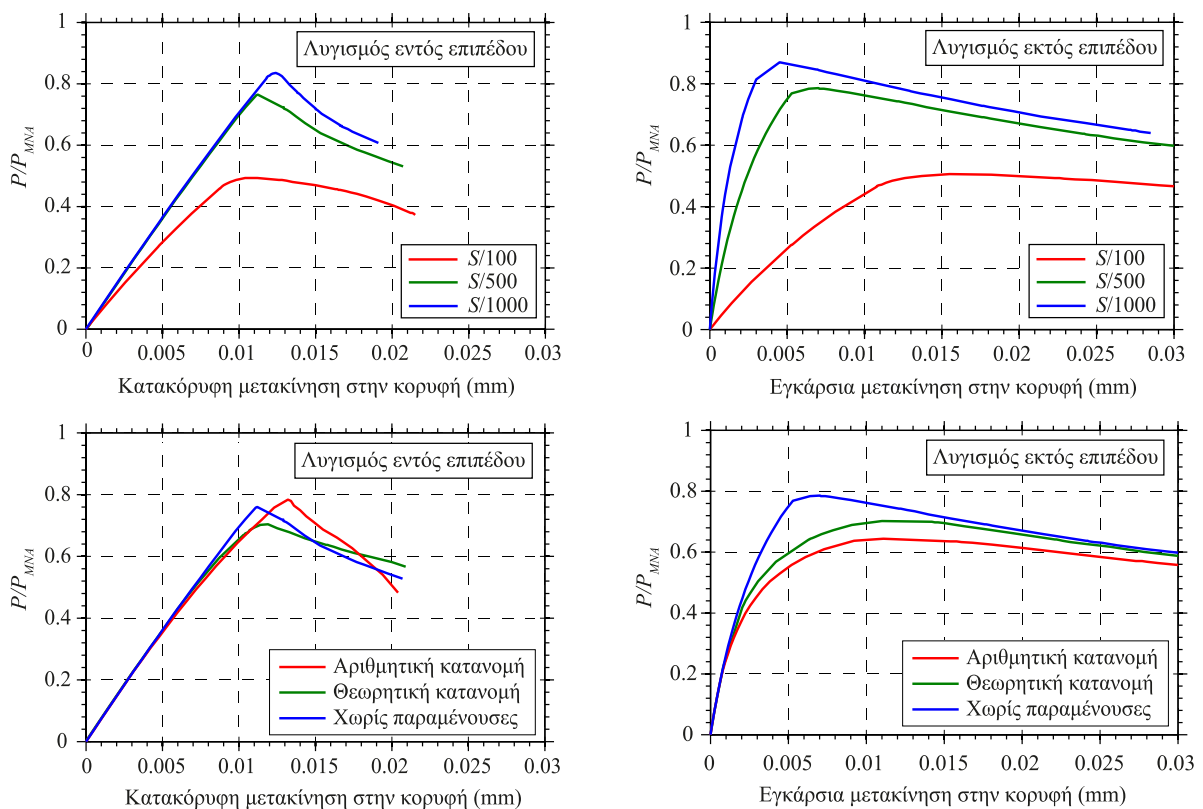
Σχήμα 21: Διαγράμματα δύναμης-παραμόρφωσης, ροπής-καμπυλότητας και ροπής-στροφής.

Στη συνέχεια εκτελούνται μη γραμμικές αναλύσεις υλικού και γεωμετρίας, προκειμένου να εξετασθεί η επιρροή του μεγέθους των γεωμετρικών ατελειών και της κατανομής των παραμενουσών τάσεων στην οριακή αντοχή. Οι αναλύσεις πραγματοποιούνται για την ίδια περίπτωση τόξου που χρησιμοποιήθηκε κατά την πιστοποίηση της προτεινόμενης προσομοίωσης. Απλές στρεπτικές στηρίξεις εφαρμόζονται στα άκρα του τόξου, ενώ χρησιμοποιείται μια πλευρική στήριξη στην κορυφή του, ώστε το μήκος λυγισμού εντός και εκτός επιπέδου να είναι ίσο. Οι δύο πρώτες ιδιομορφές λυγισμού, για ομοιόμορφο καταναμημένο φορτίο στην κατακόρυφη διεύθυνση, παρουσιάζονται στο Σχήμα 22.



Σχήμα 22: Ιδιομορφές για εκτός (I) και εντός επιπέδου (II) λυγισμό του τόξου.

Αρχικά, εξετάζονται τα τόξα χωρίς παραμένουσες τάσεις, με μεγέθη γεωμετρικών ατελειών  $S/100$ ,  $S/500$  και  $S/1000$ , όπου  $S$  το μήκος λυγισμού (μισό μήκος τόξου), σύμφωνα με τα σχήματα των δύο πρώτων ιδιομορφών (Σχήμα 22). Στη συνέχεια, εξετάζεται η επιρροή των παραμενουσών τάσεων, σε τόξα με μέγεθος ατελειών  $S/500$ . Οι δρόμοι ισορροπίας φορτίου-μετακίνησης για τις περιπτώσεις που αναφέρθηκαν παρουσιάζονται στο Σχήμα 23. Παρατηρείται σημαντική επιρροή του μεγέθους αρχικών ατελειών και της κατανομής παραμενουσών τάσεων στο οριακό φορτίο λυγισμού των τόξων.



Σχήμα 23: Δρόμοι ισορροπίας φορτίου μετακίνησης για λυγισμό εντός (αριστερά) και εκτός επιπέδου (δεξιά).

Για τη διατύπωση καμπυλών λυγισμού χρησιμοποιείται μια συστηματική μεθοδολογία που περιλαμβάνει την εκτέλεση μη γραμμικών αναλύσεων υλικού (MNA), γραμμικοποιημένων αναλύσεων λυγισμού (LBA), και μη γραμμικών αναλύσεων υλικού και γεωμετρίας με ατέλειες και παραμένουσες τάσεις (GMNIA). Η ανηγμένη λυγηρότητα των τόξων υπολογίζεται σύμφωνα με την Εξ. 18.

$$\bar{\lambda} = \sqrt{\frac{P_{MNA}}{P_{LBA}}} \quad (\text{Εξ. 18})$$

Ο μειωτικός συντελεστής  $\chi$  υπολογίζεται σύμφωνα με την Εξ. 19.

$$\chi = \frac{P_{GMNIA}}{P_{MNA}} \quad (\text{Εξ. 19})$$

Τα αριθμητικά αποτελέσματα χρησιμοποιούνται για τον υπολογισμό της γενικευμένης ατέλειας  $n$  (generalized imperfection) και του συντελεστή ατελειών  $a$  (imperfection factor), σύμφωνα με τις εξισώσεις του Ευρωκώδικα 3, μέρος 1-1 [6].

Η τιμή του μειωτικού συντελεστή  $\chi$  καθορίζεται σύμφωνα με τις Εξ. 20 και Εξ. 21.

$$\chi = \frac{1}{\phi + \sqrt{\phi^2 - \bar{\lambda}^2}} \text{ αλλά } \chi \leq 1.0 \quad (\text{Εξ. 20})$$

$$\phi = 0.5(1 + n + \bar{\lambda}^2) \quad (\text{Εξ. 21})$$

Επομένως η γενικευμένη ατέλεια  $n$  υπολογίζεται σύμφωνα με την Εξ. 22.

$$n = \chi \left( \frac{1}{\chi^2} + \bar{\lambda}^2 \right) - 1 - \bar{\lambda}^2 \quad (\text{Εξ. 22})$$

Συνδυάζοντας τις Εξ. 18, Εξ. 19, Εξ. 22, προκύπτει η Εξ. 23, από την οποία υπολογίζεται η γενικευμένη ατέλεια με βάση τα αποτελέσματα των αναλύσεων πεπερασμένων στοιχείων.

$$n = \frac{P_{GMNIA}}{P_{MNA}} \left( \left( \frac{P_{MNA}}{P_{GMNIA}} \right)^2 + \frac{P_{MNA}}{P_{LBA}} \right) - 1 - \frac{P_{MNA}}{P_{LBA}} \quad (\text{Εξ. 23})$$

Λόγω του ότι η επιρροή των αρχικών ατελειών συσχετίζεται με το μήκος του μέλους έχει καθιερωθεί το  $n$  να εκφράζεται ως συνάρτηση της ανηγμένης λυγηρότητας. Η συσχέτιση μπορεί να είναι είτε γραμμική (Εξ. 24), όπως στις εξισώσεις που ορίζουν τις καμπύλες λυγισμού του Ευρωκώδικα, είτε μεγαλύτερου βαθμού (Εξ. 25), όπως σε πιο σύνθετα προβλήματα ευστάθειας.

$$n = \alpha(\bar{\lambda} - \bar{\lambda}_0) \geq 0 \quad (\text{Εξ. 24})$$

$$n = \alpha[(\bar{\lambda} - \bar{\lambda}_1)^\beta - \bar{\lambda}_0] \geq 0 \quad (\text{Εξ. 25})$$

Ο συντελεστής ατελειών  $a$  εξαρτάται από τον τύπο της διατομής. Οι τιμές λυγηρότητας  $\bar{\lambda}_0$  και  $\bar{\lambda}_1$  χρησιμοποιούνται για τον ορισμό των καμπυλών λυγισμού.

Σύμφωνα με το EN1993-1-1 [6], η τιμή του  $\bar{\lambda}_0$  λαμβάνεται ίση με 0.2, και ο συντελεστής ατελειών  $\alpha$  που αντιστοιχεί σε κάθε καμπύλη λυγισμού λαμβάνεται από τον Πίνακα 5.

Πίνακας 5: Συντελεστές ατελειών για καμπύλες λυγισμού EN1993-1-1 [6].

Καμπύλη λυγισμού	$a_0$	$a$	$b$	$c$	$d$
Συντελεστής ατελειών $a$	0.13	0.21	0.34	0.49	0.76

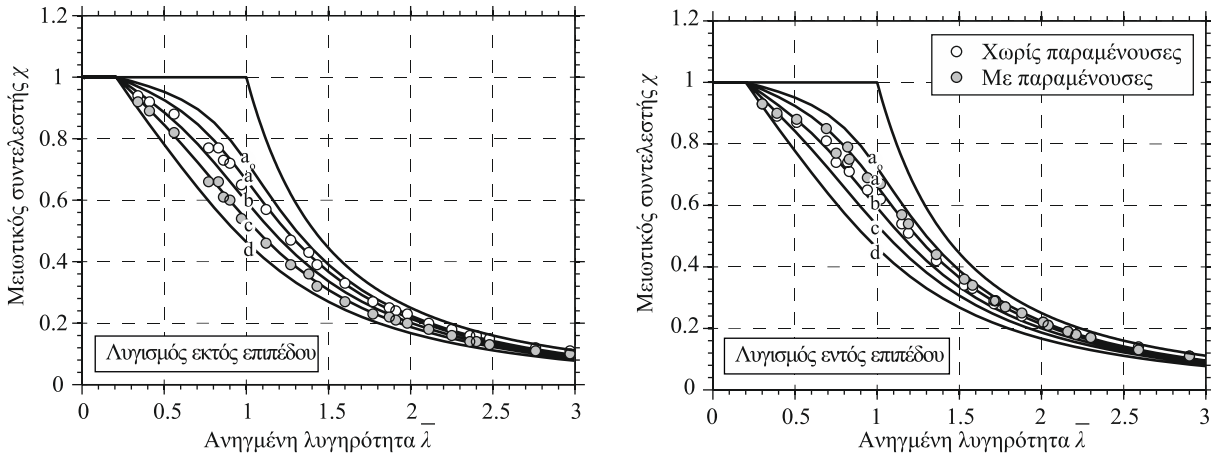


Αναλύσεις πεπερασμένων στοιχείων πραγματοποιούνται σε χαλύβδινα τόξα κοίλης κυκλικής διατομής, ακολουθώντας τη συστηματική προσέγγιση που παρουσιάστηκε. Οι μηχανικές ιδιότητες της διατομής CHS 100x5 παραμένουν σταθερές, ενώ το άνοιγμα  $l$  και το ύψος  $f$  των τόξων μεταβάλλονται κατάλληλα, καλύπτοντας μεγάλο εύρος ανηγμένης λυγηρότητας. Ο λόγος του ύψους  $f$  προς το άνοιγμα  $l$  κυμαίνεται στο εύρος  $0.10 \leq f/l \leq 0.30$ , ενώ ο λόγος της ακτίνας καμπυλότητας  $R$  προς τη διάμετρο της διατομής  $d$  κυμαίνεται στο εύρος  $10.9 \leq R/d \leq 106.3$ , όπως φαίνεται στον Πίνακα 6. Οι αριθμητικές αναλύσεις πραγματοποιούνται για τα τόξα με ή χωρίς παραμένουσες τάσεις. Για τις μη γραμμικές αναλύσεις χρησιμοποιείται μέγεθος αρχικών ατελειών  $S/500$ , το οποίο ισούται με το μέγιστο επιτρεπόμενο μέγεθος γεωμετρικών ανοχών σε καμπύλα μέλη [32]. Οι αρχικές ατέλειες ακολουθούν τις ιδιομορφές λυγισμού του σχήματος 22, που αντιστοιχούν σε λυγισμό εντός και εκτός επιπέδου των τόξων. Απλές στρεπτικές στηρίξεις εφαρμόζονται στα άκρα των τόξων, ενώ χρησιμοποιείται μια πλευρική στηρίξη στην κορυφή, ώστε το μήκος λυγισμού εντός και εκτός επιπέδου να είναι ίσο. Τα τόξα εξετάζονται για ομοιόμορφα κατανεμημένο φορτίο στην ακτινική διεύθυνση. Οι κοίλες κυκλικές διατομές δεν είναι ευπαθείς σε στρεπτοκαμπτικό λυγισμό, και επομένως η συγκεκριμένη φόρτιση, από την οποία αναπτύσσεται προέχουσα θλίψη, θεωρείται επαρκής.

Πίνακας 6: Γεωμετρία εξεταζόμενων τόξων.

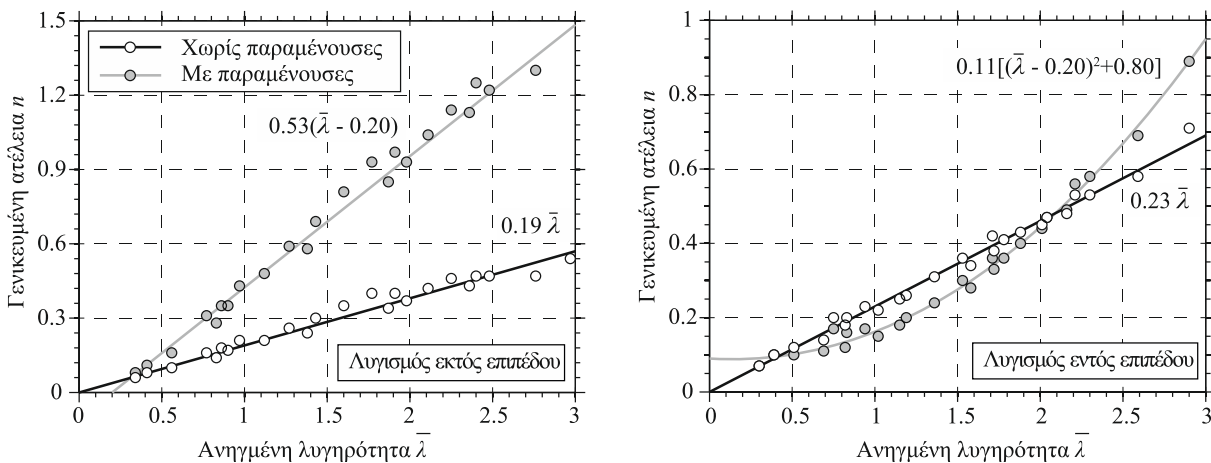
No.	$f$ (m)	$l$ (m)	$R$ (m)	$f/l$	$R/d$
1	3.00	14.00	9.67	0.21	96.7
2	3.00	12.00	7.50	0.25	75.0
3	2.00	11.00	8.56	0.18	85.6
4	2.00	10.00	7.25	0.20	72.5
5	2.50	10.00	6.25	0.25	62.5
6	3.00	10.00	5.67	0.30	56.7
7	1.00	9.00	10.63	0.11	106.3
8	1.50	9.00	7.50	0.17	75.0
9	2.00	9.00	6.06	0.22	60.6
10	2.50	9.00	5.30	0.28	53.0
11	2.00	8.00	5.00	0.25	50.0
12	1.00	8.00	8.50	0.13	85.0
13	2.00	7.00	4.06	0.29	40.6
14	1.00	7.00	6.63	0.14	66.3
15	1.00	6.00	5.00	0.17	50.0
16	1.50	5.00	2.83	0.30	28.3
17	1.00	5.00	3.63	0.20	36.3
18	0.50	5.00	6.50	0.10	65.0
19	0.80	4.00	2.90	0.20	29.0
20	0.49	4.36	5.09	0.11	50.9
21	0.40	4.00	5.20	0.10	52.0
22	0.90	3.00	1.70	0.30	17.0
23	0.50	2.50	1.81	0.20	18.1
24	0.30	2.00	1.82	0.15	18.2
25	0.30	1.50	1.09	0.20	10.9

Η αντοχή των τόξων για λυγισμό εντός και εκτός επιπέδου, συγκρίνεται με τις καμπύλες λυγισμού του EN1993-1-1, όπως παρουσιάζεται στο Σχήμα 24. Η μείωση της αντοχής λυγισμού είναι πιο σημαντική για τον εκτός επιπέδου σε σχέση με τον εντός επιπέδου λυγισμό, καθώς οι μέγιστες τιμές παραμενουσών τάσεων συναντώνται περί το μέσο των κοίλων διατομών, έχοντας σημαντική επιρροή στην καμπτική δυσκαμψία εκτός επιπέδου. Για τον εκτός επιπέδου λυγισμό, η παρουσία των γεωμετρικών ατελειών και των παραμενουσών τάσεων προκαλεί μείωση της αντοχής ( $\bar{\lambda} = 1$ ) έως 38% και 12% αντίστοιχα. Για τον εντός επιπέδου λυγισμό των τόξων, η παρουσία των γεωμετρικών ατελειών προκαλεί μείωση ( $\bar{\lambda} = 1$ ) της αντοχής έως περίπου 38%, ενώ η επιρροή των παραμενουσών τάσεων είναι αμελητέα.



Σχήμα 24: Μειωτικός συντελεστής αντοχής για λυγισμό εντός και εκτός επιπέδου.

Με βάση τα αριθμητικά αποτελέσματα υπολογίζεται ο συντελεστής γενικευμένης ατέλειας  $n$ . Χρησιμοποιώντας αναλύσεις παλινδρόμησης, προκύπτουν οι εξισώσεις υπολογισμού της γενικευμένης ατέλειας. Η γενικευμένη ατέλεια για τον εκτός επιπέδου λυγισμό των τόξων, με ή χωρίς παραμένουσες τάσεις, προσεγγίζεται επαρκώς χρησιμοποιώντας γραμμική παλινδρόμηση. Για τον εντός επιπέδου λυγισμό, η γενικευμένη ατέλεια προσεγγίζεται χρησιμοποιώντας γραμμική παλινδρόμηση στην περίπτωση τόξων χωρίς παραμένουσες τάσεις, ενώ στην περίπτωση τόξων με παραμένουσες τάσεις χρησιμοποιείται παλινδρόμηση δεύτερου βαθμού. Η διαφορά οφείλεται στην πρόσθετη κάμψη εντός επιπέδου που προκαλείται από την αξονική βράχυνση του τόξου στις μικρές τιμές λυγηρότητας, εξαιτίας της πρόωρης διαρροής λόγω παραμενουσών τάσεων. Τα διαγράμματα του συντελεστή γενικευμένων ατελειών και της ανηγμένης λυγηρότητας, για λυγισμό εντός και εκτός επιπέδου, παρουσιάζονται στο Σχήμα 25.



Σχήμα 25: Συντελεστής γενικευμένων ατελειών για λυγισμό εντός και εκτός επιπέδου.

Οι εξισώσεις υπολογισμού του συντελεστή γενικευμένων ατελειών για τον εντός ή εκτός επιπέδου λυγισμό τόξων με ή χωρίς παραμένουσες τάσεις, παρουσιάζονται στον Πίνακα 7.

Πίνακας 7: Εξισώσεις υπολογισμού του συντελεστή γενικευμένων ατελειών  $n$ .

Διατομή	Εκτός επιπέδου λυγισμός	Εντός επιπέδου λυγισμός
Με παραμένουσες τάσεις	$0.53(\bar{\lambda} - 0.20) \geq 0$	$0.11[(\bar{\lambda} - 0.20)^2 + 0.80] \geq 0$
Χωρίς παραμένουσες τάσεις	$0.19\bar{\lambda} \geq 0$	$0.23\bar{\lambda} \geq 0$

## 7. ΣΥΝΟΨΗ ΚΑΙ ΣΥΜΠΕΡΑΣΜΑΤΑ

Αντικείμενο της παρούσας διδακτορικής διατριβής αποτελεί η διερεύνηση της ευστάθειας χαλύβδινων τόξων κοίλης διατομής. Τα τόξα από χάλυβα διαμορφώνονται από την κατεργασία ευθύγραμμων μελών, ενώ υπάρχουν διάφορες κατασκευαστικές μέθοδοι για το σκοπό αυτό. Η πιο διαδεδομένη μέθοδος για την καμπύλωση μελών δομικού χάλυβα είναι η εν ψυχρώ διαμόρφωση με χρήση τυμπάνων (roller-bending). Στην περίπτωση αυτή, το υπό διαμόρφωση ευθύγραμμο μέλος διέρχεται από κατάλληλη μηχανή καμπύλωσης που αποτελείται από τύμπανα, ενώ η επιθυμητή καμπυλότητα επιτυγχάνεται μέσω κάμψης τριών σημείων που προκαλεί πλαστικές παραμορφώσεις. Η εν ψυχρώ διαμόρφωση εισάγει σημαντικές παραμένουσες τάσεις και παραμορφώσεις, επηρεάζοντας την μηχανική συμπεριφορά των τόξων. Στόχος της παρούσας διατριβής είναι η αποτίμηση της επιρροής των παραμενουσών τάσεων και των γεωμετρικών ατελειών στην ευστάθεια τοξωτών φορέων από χάλυβα. Στο πλαίσιο αυτό εφαρμόζεται ένας συνδυασμός πειραματικών, αριθμητικών και αναλυτικών μεθόδων έρευνας. Τα αποτελέσματα εργαστηριακών δοκιμών σε τόξα κοίλης ορθογωνικής διατομής συγκρίνονται με τα αντίστοιχα αριθμητικά αποτελέσματα πεπερασμένων στοιχείων. Η διαδικασία καμπύλωσης των τόξων προσομοιώνεται ακριβώς, λαμβάνοντας υπόψη την αλληλεπίδραση που αναπτύσσεται μέσω επαφής του μέλους με τα τύμπανα της μηχανής. Διαπιστώνεται ικανοποιητική σύγκλιση μεταξύ των αριθμητικών και των πειραματικών αποτελεσμάτων σε όρους αντοχής, μετατοπίσεων και αναπτυσσόμενων παραμορφώσεων. Πραγματοποιείται μια εκτεταμένη αριθμητική διερεύνηση των παραμέτρων που επηρεάζουν τις κατανομές παραμενουσών τάσεων σε κοίλες τετραγωνικές, ορθογωνικές και κυκλικές διατομές. Κατόπιν, με χρήση αναλυτικών μεθόδων διερευνάται η επιρροή των παραμενουσών τάσεων στην ελαστοπλαστική συμπεριφορά και στο κρίσιμο φορτίο λυγισμού των τόξων. Η οριακή αντοχή έναντι ευστάθειας αποτιμάται τελικά μέσω μη γραμμικών αριθμητικών αναλύσεων υλικού και γεωμετρίας, που περιλαμβάνουν αξιόπιστα μεγέθη γεωμετρικών ατελειών και κατανομών παραμενουσών τάσεων.

Τα βασικά συμπεράσματα που προκύπτουν από την παρούσα διατριβή συνοψίζονται ακολούθως:

- Η έρευνα που έχει πραγματοποιηθεί διεθνώς αναφορικά με τις παραμένουσες τάσεις, τις μηχανικές ιδιότητες, και την ευστάθεια τόξων που έχουν καμπυλωθεί εν ψυχρώ είναι πολύ περιορισμένη.
- Τα καμπυλωμένα εν ψυχρώ τόξα εκδηλώνουν πρόωρη πλαστικοποίηση η οποία εξαρτάται από τη φορά της καμπτικής καταπόνησης λόγω του φαινομένου Bauschinger.
- Τα καμπυλωμένα εν ψυχρώ τόξα παρουσιάζουν αυξημένο όριο διαρροής και μειωμένη πλαστιμότητα εξαιτίας του φαινομένου strain aging, που εκδηλώνεται από την πλαστική κατεργασία του χάλυβα.
- Οι παραμένουσες τάσεις των καμπυλωμένων εν ψυχρώ τόξων διαφέρουν σημαντικά από τη θεωρητική κατανομή Timoshenko, η οποία θεωρεί συνθήκες επίπεδης έντασης χωρίς διάτμηση.
- Εφελκυστικές παραμένουσες τάσεις συναντώνται στην άνω και κάτω ίνα των κοίλων διατομών, και σημαντικές συγκεντρώσεις τάσεων παρατηρούνται στις γωνίες κορμών-πελμάτων.
- Η παρουσία παραμενουσών τάσεων προκαλεί μείωση της ελαστικής αντοχής της διατομής και του κρίσιμου φορτίου λυγισμού των τόξων.
- Η επιρροή των παραμενουσών τάσεων είναι πιο σημαντική στην περίπτωση κάμψης ή λυγισμού εκτός επιπέδου, καθώς οι μέγιστες τιμές τάσεων βρίσκονται περί το μέσον του ύψους της διατομής.
- Καμπύλες λυγισμού για τόξα μπορούν να δημιουργηθούν μέσω αριθμητικών αναλύσεων, λαμβάνοντας υπόψη ακριβείς κατανομές παραμενουσών τάσεων και αξιόπιστα μεγέθη γεωμετρικών ατελειών.
- Για τον εκτός επιπέδου λυγισμό των τόξων, η παρουσία των γεωμετρικών ατελειών και των παραμενουσών τάσεων προκαλεί μείωση της αντοχής έως περίπου 38% και 12% αντίστοιχα.
- Για τον εντός επιπέδου λυγισμό των τόξων, η παρουσία των γεωμετρικών ατελειών προκαλεί μείωση της αντοχής έως περίπου 38%, ενώ η επιρροή των παραμενουσών τάσεων είναι αμελητέα.

## 8. ΠΡΩΤΟΤΥΠΗ ΣΥΜΒΟΛΗ ΚΑΙ ΠΡΟΤΑΣΕΙΣ ΓΙΑ ΠΕΡΑΙΤΕΡΩ ΕΡΕΥΝΑ

Η πρωτότυπη συμβολή της διατριβής στην επιστήμη και πράξη του μηχανικού συνοψίζεται στα εξής:

- Πραγματοποιήθηκαν συγκρίσεις αποτελεσμάτων από πειραματικές δοκιμές και αριθμητικές αναλύσεις σε χαλύβδινα τόξα καμπυλωμένα εν ψυχρώ. Τα αποτελέσματα συμβάλουν στην ποιοτική ερμηνεία και ποσοτική επαλήθευση της μηχανικής συμπεριφοράς των τόξων [43].
- Προσδιορίστηκαν οι παράμετροι που επηρεάζουν την κατανομή και το μέγεθος των παραμενουσών τάσεων από την εν ψυχρώ καμπύλωση τόξων. Τα αποτελέσματα μπορούν να αξιοποιηθούν ερευνητικά για τη διενέργεια μετρήσεων παραμενουσών τάσεων [44-45].
- Προτάθηκαν κατανομές παραμενουσών τάσεων για καμπυλωμένα εν ψυχρώ μέλη κοίλης διατομής. Οι κατανομές παραμενουσών τάσεων είναι χρήσιμες στην ερευνητική κοινότητα για τη διατύπωση κατάλληλων κανόνων σχεδιασμού [44-45].
- Δημιουργήθηκαν διαγράμματα αλληλεπίδρασης για κοίλες κυκλικές, τετραγωνικές και ορθογωνικές διατομές με παραμένουσες τάσεις. Τα διαγράμματα αλληλεπίδρασης είναι χρήσιμα στην μελετητική πρακτική για τον ελαστικό σχεδιασμό των τόξων από χάλυβα.
- Υπολογίσθηκαν αναλυτικά τα κρίσιμα φορτία λυγισμού για χαλύβδινα τόξα με παραμένουσες τάσεις. Τα κρίσιμα φορτία προσφέρουν μια συγκριτική και ποιοτική εκτίμηση της επιρροής των παραμενουσών τάσεων μεταξύ διαφόρων διατομών και κατανομών παραμενουσών τάσεων.
- Διατυπώθηκαν αξιόπιστες καμπύλες λυγισμού για χαλύβδινα τόξα κοίλης διατομής. Οι καμπύλες λυγισμού είναι πολύ χρήσιμες στη μελετητική πρακτική για το σχεδιασμό τοξωτών φορέων σύμφωνα με τους ισχύοντες κανονισμούς [46].

Με βάση τα αποτελέσματα της παρούσας διατριβής, προτείνεται περαιτέρω:

- Διενέργεια εργαστηριακών δοκιμών για τη μέτρηση των παραμενουσών τάσεων που προέρχονται από την εν ψυχρώ καμπύλωση χαλύβδινων τόξων κοίλης διατομής. Τα πειραματικά αποτελέσματα μπορούν να συγκριθούν με αντίστοιχα αριθμητικά αποτελέσματα που παρουσιάστηκαν.
- Εφαρμογή προχωρημένων νόμων υλικού στην προσομοίωση των τόξων, λαμβάνοντας υπόψη τη παρουσία του φαινομένου Bauschinger. Ωστόσο, τέτοια υλικά συνήθως δεν είναι συμβατά με την εισαγωγή παραμενουσών τάσεων στα πεπερασμένα στοιχεία.
- Πειραματική διερεύνηση της συμπεριφοράς του χάλυβα μετά την εν ψυχρώ διαμόρφωση. Η μειωμένη δυσκαμψία των τόξων λόγω του φαινομένου Bauschinger θα πρέπει να ενσωματωθεί στο σχεδιασμό μέσω κατάλληλων εξισώσεων προσδιορισμού την ενεργής ανηγμένης λυγηρότητας.
- Αξιολόγηση του σχεδιασμού τοξωτών φορέων χρησιμοποιώντας εξισώσεις που προορίζονται για ευθύγραμμα μέλη. Αποτελέσματα αριθμητικών αναλύσεων και πειραματικών δοκιμών σε τοξωτούς φορείς μπορούν να χρησιμοποιηθούν για τον έλεγχο των εξισώσεων σχεδιασμού.
- Διατύπωση κριτηρίων ευστάθειας σε χαλύβδινα τόξα που διαμορφώνονται μέσω καμπύλωσης εν θερμώ ή συγκολλήσεων. Οι σχετικές παραμένουσες τάσεις μπορούν να προσδιορισθούν μέσω θερμομηχανικών αναλύσεων σύμφωνα με μεθοδολογίες που έχουν διατυπωθεί στη βιβλιογραφία [47-50].

## BIBΛΙΟΓΡΑΦΙΑ

- [1] Bjorhovde, R. (2006). "Cold Bending of Wide-Flange Shapes for Construction." *Engineering Journal*, vol. 4, pp. 271–286.
- [2] Alwood, T. (2006). "What Engineers Should Know About Bending Steel." *Modern Steel Construction magazine*, (May).
- [3] Packer, J. A. (2013). "Bending of Hollow Structural Sections." *Steel Tube Institute*.
- [4] ECCS (1976). *Manual on Stability of Steel Structures*. European Convention for Constructional Steelwork, Liege, Belgium.
- [5] AISC (2016). *Specification for Structural Steel Buildings*. American Institute of Steel Construction, Chicago, IL.
- [6] CEN (2005). *Eurocode 3: Design of Steel Structures, Part 1-1: General Rules and Rules for Buildings, EN 1993-1-1*. Comité Européen de Normalisation (CEN), European Committee for Standardization Brussels, Belgium.
- [7] Timoshenko, S. P. (1956). *Strength of Materials Part II - Advanced Theory and Problems*, 3<sup>rd</sup> Ed., D. Van Nostrand Company, New York, NY.
- [8] Spoorenberg, R. C., Snijder, H. H., and Hoenderkamp, J. C. D. (2010). "Experimental investigation of residual stresses in roller bent wide flange steel sections." *Journal of Constructional Steel Research*, vol. 66, pp. 737–747.
- [9] Spoorenberg, R. C., Snijder, H. H., and Hoenderkamp, J. C. D. (2011). "Finite element simulations of residual stresses in roller bent wide flange sections." *Journal of Constructional Steel Research*, vol. 67, pp. 39–50.
- [10] Spoorenberg, R. C., Snijder, H. H., and Hoenderkamp, J. C. D. (2011). "Proposed Residual Stress Model for Roller Bent Steel Wide Flange Sections," *Journal of Constructional Steel Research*, vol. 67, pp. 992–1000.
- [11] Chiew, S.P., Jin, Y.F. and Lee, C.K. (2016). "Residual Stress Distribution of Roller Bending of Steel Rectangular Structural Hollow Sections." *Journal of Constructional Steel Research*, vol. 119, pp. 85–97.
- [12] Spoorenberg, R. C., Snijder, H. H., and Hoenderkamp, J. C. D. (2012). "Mechanical Properties of Roller Bent Wide Flange Sections—Part 1: Experimental Investigation," *Journal of Constructional Steel Research*, vol. 68, pp. 51–62.
- [13] Spoorenberg, R. C., Snijder, H. H., and Hoenderkamp, J. C. D. (2012). "Mechanical Properties of Roller Bent Wide Flange Sections - Part 2: Prediction Model." *Journal of Constructional Steel Research*, vol. 68, pp. 63–77.
- [14] Tokarz, F. J. (1971). "Experimental Study of Lateral Buckling of Arches." *ASCE J. Struct. Div.*, vol. 97, pp. 545–559.
- [15] Sakimoto, T., Yamao, T., and Komatsu, S. (1979). "Experimental Study on the Ultimate Strength of Steel Arches." *Proc. Jpn. Soc. Civ. Eng.*, No. 286, pp. 139–149.
- [16] Tokarz, F. J. (1971). "Experimental Study of Lateral Buckling of Arches." *ASCE J. Struct. Div.*, vol. 97, pp. 545–559.
- [17] Papangelis, J. P., and Trahair, N. S. (1987). "Flexural–Torsional Buckling of Arches." *ASCE J. Struct. Eng.*, vol. 113, pp. 889–906.
- [18] Guo, Y., Zhao, S., Pi, Y., Andrew, M., and Dou, C. (2015). "An experimental study on out-of-plane inelastic buckling strength of fixed steel arches." *Engineering Structures*, vol. 98, pp. 118–127.

- [19] La Poutré, D. B. La, Spoorenberg, R. C., Snijder, H. H., and Hoenderkamp, J. C. D. (2013). "Out-of-plane stability of roller bent steel arches — An experimental investigation." *Journal of Constructional Steel Research*, vol. 81, pp. 20–34.
- [20] Komatsu, S., and Sakimoto, T. (1977). "Ultimate Load Carrying Capacity of Steel Arches." *ASCE J. Struct. Div.*, vol. 103, pp. 2323–2336.
- [21] Pi, Y., Trahair, N.S. (1996). "Three-dimensional nonlinear analysis of elastic arches." *Engineering Structures*, vol. 18, pp. 49–63.
- [22] Guo, Y., Chen, H., Pi, Y., and Andrew, M. (2016). "In-plane strength of steel arches with a sinusoidal corrugated web under a full-span uniform vertical load: Experimental and numerical investigations." *Engineering Structures*, vol. 110, pp. 105–115.
- [23] Huang, Y., Liu, A., Zhu, C., Lu, H., and Gao, W. (2019). "Experimental and numerical investigations on out-of-plane ultimate resistance of parallel twin-arch under uniform radial load." *Thin Walled Structures*, vol. 135, pp. 147–159.
- [24] Pi, Y.-L., and Bradford, M. A. (2004). "In-Plane Strength and Design of Fixed Steel I-Section Arches." *Eng. Struct.*, vol. 26, pp. 291–301.
- [25] Pi, Y.-L., and Bradford, M. A. (2005). "Out-of-Plane Strength Design of Fixed Steel I-Section Arches." *ASCE J. Struct. Eng.*, vol. 131, pp. 560–568.
- [26] Pi, Y.-L., and Trahair, N. S. (1998), "Out-of-Plane Inelastic Buckling and Strength of Steel Arches," *ASCE J. Struct. Eng.*, vol. 124, pp. 174–183.
- [27] Pi, Y.-L., and Trahair, N. S. (1999). "In-Plane Buckling and Design of Steel Arches." *ASCE J. Struct. Eng.*, vol. 125, pp. 1291–1298.
- [28] Spoorenberg, R. C., Snijder, H. H., Hoenderkamp, J. C. D., and Beg, D. (2012). "Design rules for out-of-plane stability of roller bent steel arches with FEM." *Journal of Constructional Steel Research*, vol. 79, pp. 9–21.
- [29] Hayashi, T. (Ed.) (1971). *Handbook of Structural Stability*. Corona Publishing, Tokyo.
- [30] Beedle, L. S. (Ed.) (1991). *Stability of Metal Structures, a World View*. 2<sup>nd</sup> ed., Structural Stability Research Council, Bethlehem, PA.
- [31] Singer, J., Arbocz, J., and Weller, T. (1998). *Buckling Experiments: Experimental Methods in Buckling of Thin-Walled Structures*. J Wiley, New York.
- [32] King, C., and Brown, D. (2001). *Design of Curved Steel*. The Steel Construction Institute, Berkshire, UK.
- [33] Ziemian, R. D. (Ed.) (2010). *Guide to Stability Design Criteria for Metal Structures*. John Wiley & Sons, Inc., United States of America.
- [34] Dowswell, B. (2018). *Curved Member Design*. American Institute of Steel Construction, Chicago, IL.
- [35] International Organization for Standardization. (2010). *EN ISO 6892.01 - Metallic materials - Tensile testing - Part 1: Method of test at room temperature*. Geneva, Switzerland.
- [36] Bathe, K.J. (2014). *Finite Element Procedures*. Prentice Hall, Pearson Education, Inc., Watertown, USA.
- [37] ADINA R&D Inc. (2017). *Theory and modeling guide*. Watertown, MA, USA.
- [38] Gantes, C. J., and Fragkopoulos, K. A. (2009). "Strategy for numerical verification of steel structures at the ultimate limit state." *Structure and Infrastructure Engineering*, vol. 6, pp. 1–31.

- [39] Lange, J. and Grages, H. (2009). "Influence of the Bauschinger Effect on the Deflection Behavior of Cambered Steel and Steel Concrete Composite Beams." *Structural Engineering International*, International Association of Bridge and Structural Engineers.
- [40] Chajes, A., Britvec, S.J. and Winter, G. (1963). "Effects of Cold-Straining on Structural Sheet Steels." *Journal of the Structural Division. ASCE*, vol. 89, pp. 1–32.
- [41] Beedle, L. S., and Tall, L. (1960), "Basic Column Strength." *ASCE J. Struct. Div.*, vol. 86, pp. 139–173.
- [42] Timoshenko, S. P., and Gere, J. M. (1961). *Theory of Elastic Stability*. 2<sup>nd</sup> ed., McGraw-Hill, New York.
- [43] Thanasoulas, I. D., Douthe, C. E., Gantes, C. J., and Lignos, X. A. (2018). "Influence of roller-bending on RHS steel arches: Experimental and numerical investigation." *Thin-Walled Structures*, vol. 131, pp. 668–680.
- [44] Thanasoulas, I. D., and Gantes, C. J. (2020a). "Numerical investigation on the residual stresses of roller-bent circular-hollow-sections." *Journal of Constructional Steel Research*, vol. 164, 105777.
- [45] Thanasoulas, I. D., and Gantes, C. J. (2018). "Effects of roller bending on curved constructional steels of rectangular hollow section." *Proceedings of the IASS Symposium 2018 Creativity in Structural Design*, Jul. 16-20, MIT, Boston, USA.
- [46] Thanasoulas, I. D., and Gantes, C. J. (2020). "Stability criteria for circular-hollow-section steel arches." Ready for submission in peer-reviewed scientific journal.
- [47] Thanasoulas, I. D., Vardakoulias, I. K., Kolaitis, D. I., Gantes, C. J., and Founti, M. A. (2015). "A preliminary thermal and mechanical simulation study of load-bearing cold-formed steel drywall systems exposed to fire", *2nd IAFSS European Symposium of Fire Safety Science*, Jun. 16-18, Nicosia, Cyprus.
- [48] Thanasoulas, I. D., Vardakoulias, I. K., Kolaitis, D. I., Gantes, C. J., and Founti, M. A. (2016). "Thermal and Mechanical Computational Study of Load-Bearing Cold-Formed Steel Drywall Systems Exposed to Fire." *Fire Technology*, vol. 52(6), pp. 2071–2092.
- [49] Thanasoulas, I. D., Vardakoulias, I. K., Kolaitis, D. I., Gantes, C. J., and Founti, M. A. (2017). "Nonlinear numerical simulation of fire-resistance tests for load-bearing cold-formed-steel dry-wall systems". *9th Greek National Steel Structures Conference*, 5-7 Oct., Larissa, Greece.
- [50] Thanasoulas, I. D., Vardakoulias, I. K., Kolaitis, D. I., Gantes, C. J., and Founti, M. A. (2018). "Coupled thermo-mechanical simulation for the performance-based fire design of CFS drywall systems." *Journal of Constructional Steel Research*, vol. 145, pp. 196–209.





## CONTENTS

<b>1</b>	<b>INTRODUCTION</b>	<b>1</b>
1.1	ARCHES IN CONSTRUCTION	1
1.2	MANUFACTURING PROCESS	3
1.3	ANALYSIS AND DESIGN	4
1.4	PROBLEM STATEMENT AND OBJECTIVE	6
1.5	OUTLINE OF THESIS	6
	REFERENCES	7
<b>2</b>	<b>LITERATURE REVIEW</b>	<b>9</b>
2.1	INTRODUCTION	9
2.2	ROLLER-BENDING OF ARCHES	9
2.2.1	General remarks	9
2.2.2	Residual stresses	11
2.2.3	Material properties	17
2.3	IN-PLANE BEHAVIOR OF ARCHES	19
2.3.1	Elastic stability and ultimate strength	19
2.3.2	Design recommendations	21
2.4	OUT-OF-PLANE BEHAVIOR OF ARCHES	21
2.4.1	Elastic stability and ultimate strength	21
2.4.2	Design recommendations	22
2.5	CONCLUSIONS	22
	REFERENCES	23
<b>3</b>	<b>EXPERIMENTAL TESTS</b>	<b>27</b>
3.1	INTRODUCTION	27
3.2	DESCRIPTION OF EXPERIMENTS	28
3.2.1	Test specimens	28
3.2.2	Experimental setup	30
3.2.3	Measuring devices	31
3.2.4	Testing procedure	33
3.3	MATERIAL PROPERTIES	33
3.4	EXPERIMENTAL RESULTS	34
3.4.1	High arches under compression	34
3.4.2	High arches under tension	36
3.4.3	Shallow arches under compression	38
3.4.4	Shallow arches under tension	40
3.5	CONCLUSIONS	42
	REFERENCES	42

<b>4</b>	<b>NUMERICAL SIMULATION OF EXPERIMENTS .....</b>	<b>45</b>
4.1	INTRODUCTION .....	45
4.2	NUMERICAL MODELING .....	46
4.3	COMPARISON OF EXPERIMENTAL AND NUMERICAL RESULTS.....	49
4.3.1	High arches under compression .....	50
4.3.2	High arches under tension .....	52
4.3.3	Shallow arches under compression .....	54
4.3.4	Shallow arches under tension.....	55
4.4	COMPARISON OF ROLLER-BENT AND STRESS-FREE MODELS .....	57
4.5	CONCLUSIONS .....	59
	REFERENCES.....	59
<b>5</b>	<b>ROLLER-BENDING SIMULATION OF SHS/RHS ARCHES .....</b>	<b>61</b>
5.1	INTRODUCTION .....	61
5.2	NUMERICAL MODELING .....	63
5.3	VALIDATION STUDY .....	65
5.4	PARAMETRIC ANALYSES .....	67
5.4.1	Thickness ratio $h/t$ .....	68
5.4.2	Bending ratio $R/h$ .....	69
5.4.3	Steel yield stress $f_y$ .....	70
5.4.4	Normalized bending length $S/h$ .....	71
5.4.5	Normalized roll diameter $d_r/h$ .....	72
5.5	RESIDUAL STRESS MODEL .....	73
5.6	CONCLUSIONS .....	77
	REFERENCES.....	77
<b>6</b>	<b>ROLLER-BENDING SIMULATION OF CHS ARCHES .....</b>	<b>79</b>
6.1	INTRODUCTION .....	79
6.2	NUMERICAL MODELING .....	81
6.3	VALIDATION STUDY .....	83
6.4	PARAMETRIC ANALYSES .....	85
6.4.1	Thickness ratio $d/t$ .....	86
6.4.2	Bending ratio $R/d$ .....	87
6.4.3	Steel yield stress $f_y$ .....	88
6.4.4	Normalized bending length $S/d$ .....	88
6.4.5	Normalized roll diameter $d_r/d$ .....	89
6.4.6	Encapsulating angle $\theta_e$ .....	90
6.5	RESIDUAL STRESS MODEL .....	91
6.6	CONCLUSIONS .....	93
	REFERENCES.....	94

<b>7</b>	<b>EFFECTS OF RESIDUAL STRESSES ON ROLLER-BENT SECTIONS.....</b>	<b>95</b>
7.1	INTRODUCTION .....	95
7.2	ANALYTICAL METHODOLOGY.....	97
7.3	EFFECT ON ELASTIC STRENGTH .....	99
7.3.1	Circular-Hollow-Sections.....	99
7.3.2	Square-Hollow-Sections .....	100
7.3.3	Rectangular-Hollow-Sections .....	101
7.4	EFFECT ON BUCKLING LOAD .....	103
7.4.1	Circular-Hollow-Sections.....	103
7.4.2	Square-Hollow-Sections .....	104
7.4.3	Rectangular-Hollow-Sections .....	105
7.5	CONCLUSIONS .....	107
	REFERENCES .....	107
<b>8</b>	<b>STRUCTURAL STABILITY OF ARCHES .....</b>	<b>109</b>
8.1	INTRODUCTION .....	109
8.2	NUMERICAL MODELING.....	111
8.3	VALIDATION STUDY .....	111
8.4	SENSITIVITY ANALYSES .....	114
8.4.1	Effect of geometric imperfections .....	114
8.4.2	Effect of residual stresses.....	116
8.5	PARAMETRIC ANALYSES .....	118
8.6	CONCLUSIONS .....	121
	REFERENCES .....	121
<b>9</b>	<b>DESIGN CRITERIA FOR THE STABILITY OF ARCHES .....</b>	<b>123</b>
9.1	INTRODUCTION .....	123
9.2	METHODOLOGY .....	124
9.3	BUCKLING CURVES.....	125
9.4	CONCLUSIONS .....	128
	REFERENCES .....	129
<b>10</b>	<b>SUMMARY AND CONCLUSIONS .....</b>	<b>131</b>
10.1	EXTENDED SUMMARY.....	131
10.2	CONCLUDING REMARKS .....	134
10.3	RESEARCH CONTRIBUTION AND INNOVATION .....	135
10.4	SUGGESTIONS FOR FUTURE RESEARCH .....	135
	REFERENCES .....	136
	<b>APPENDIX .....</b>	<b>137</b>



## List of Figures

Figure 1-1: Curved cast iron in roof trusses (King and Brown, 2001).....	1
Figure 1-2: Examples of steel arches in AESS applications. ....	2
Figure 1-3: Tsakona Bridge, Greece (left) and Sydney Harbor Bridge, Australia (right).....	2
Figure 1-4: Athens Olympic Stadium, Greece (left) and Wembley Stadium in London, United Kingdom (right). ....	3
Figure 1-5: Roller bending (top-left), incremental bending (top-right), rotary-draw bending (bottom-left) and induction-bending (bottom-right). ....	4
Figure 1-6: Main buckling modes of arches.....	4
Figure 1-7: Typical design for stability using buckling curves. ....	5
Figure 2-1: Roller-bending method. ....	10
Figure 2-2: Curving mechanics of roller-bending. ....	10
Figure 2-3: Residual stress distributions in literature. ....	11
Figure 2-4: Loading (a), unloading (b) and residual (c) stress distributions.....	12
Figure 2-5: Sectioning process of HE 100A and HE 360B (Spoorenberg et al., 2010).....	13
Figure 2-6: Residual stresses of straight and roller-bent HE 360B (Spoorenberg et al., 2010). ....	13
Figure 2-7: Roller-bending simulation (Spoorenberg et al., 2011a).....	14
Figure 2-8: Numerical, experimental and theoretical residual stresses of roller-bent HE 360B (Spoorenberg et al., 2011a).....	15
Figure 2-9: Proposed residual stress model for roller-bent wide-flange-sections (Spoorenberg et al., 2011b). ....	15
Figure 2-10: Proposed residual stress model for roller-bent RHS (Chiew et al., 2016).....	16
Figure 2-11: Cross-sectional zones Spoorenberg et al. (2012b).....	18
Figure 2-12: Typical fundamental buckling mode shapes.....	19
Figure 2-13: Experimental studies of (a) Guo et al (2016), (b) Lu et al. (2017), and (c) Afshan et al. (2019).....	20
Figure 2-14: Experimental studies of (a) La Poutré et al. (2013) and (b) Guo et al. (2015).....	22
Figure 3-1: Arch specimens. ....	28
Figure 3-2: Dimension measurements of test specimens. ....	29
Figure 3-3: Laboratory testing frame and test configuration. ....	30
Figure 3-4: Views of the hinge support (detail D1).....	31
Figure 3-5: Views of the loading plates (detail D2) for the tension (left) and compression (right) tests. ....	31
Figure 3-6: View of the experimental set-up and the measuring devices. ....	32
Figure 3-7: Detailed views of measuring devices.....	32
Figure 3-8: Views of the sectioned material's deflection (left) and the tensile coupon test (right).....	33
Figure 3-9: True stress-strain curves from tensile coupon tests. ....	34
Figure 3-10: Load-displacement curves at the crown of high arches under compression.....	34
Figure 3-11: Load-displacement curves at the position of inclined LVDT of high arches under compression. ....	35

Figure 3-12: Longitudinal strain at the top flange (top-left), the bottom flange (top-right) and transverse strain at the bottom flange (bottom) of high arches under compression. ....	35
Figure 3-13: Characteristic deformed shape of high arches under compression at the end of tests. ...	36
Figure 3-14: Load-displacement curves at the crown of high arches under tension.....	36
Figure 3-15: Load-displacement curves at the position of inclined LVDT of high arches under tension. ....	37
Figure 3-16: Longitudinal strain at the top flange (top-left), the bottom flange (top-right) and transverse strain at the bottom flange (bottom) of high arches under tension. ....	37
Figure 3-17: Characteristic deformed shape of high arches under tension at the end of tests.....	38
Figure 3-18: Load-displacement curves at the crown of shallow arches under compression. ....	38
Figure 3-19: Load-displacement curves at the inclined LVDT of shallow arches under compression. ..	39
Figure 3-20: Longitudinal strain at the top flange (top-left), the bottom flange (top-right) and transverse strain at the bottom flange (bottom) of shallow arches under compression. ....	39
Figure 3-21: Fracture at the top flange of Sp. 9. ....	40
Figure 3-22: Load-displacement curves at the crown of shallow arches under tension. ....	40
Figure 3-23: Load-displacement curves at the inclined LVDT of shallow arches under tension. ....	41
Figure 3-24: Longitudinal strain at the top flange (top-left), the bottom flange (top-right) and transverse strain at the bottom flange (bottom) of shallow arches under tension.....	41
Figure 4-1: Bilinear material model based on the tensile coupon tests. ....	46
Figure 4-2: Numerical simulation of the roller-bending process. ....	47
Figure 4-3: Longitudinal residual stresses (kPa), strains and accumulated plastic strains at the shell midsurface of the high (top) and shallow (bottom) arches. ....	47
Figure 4-4: Finite element model of hinged support. ....	48
Figure 4-5: Horizontal stiffness of hinged supports. ....	48
Figure 4-6: Finite element model of experimental tests.....	49
Figure 4-7: Load-displacement curves at the crown of high arches under compression. ....	50
Figure 4-8: Load-displacement curves at the position of inclined LVDT of high arches under compression. ....	50
Figure 4-9: Longitudinal strain at the top flange (top-left), the bottom flange (top-right) and transverse strain at the bottom flange (bottom) of high arches under compression. ....	51
Figure 4-10: Characteristic deformed shape of high arches under compression from tests (left) and GMNA (right). ....	51
Figure 4-11: Load-displacement curves at the crown of high arches under tension.....	52
Figure 4-12: Load-displacement curves at the position of inclined LVDT of high arches under tension. ....	52
Figure 4-13: Longitudinal strain at the top flange (top-left), the bottom flange (top-right) and transverse strain at the bottom flange (bottom) of high arches under tension. ....	53
Figure 4-14: Characteristic deformed shape of high arches under tension from tests (left) and GMNA (right).....	53
Figure 4-15: Load-displacement curves at the crown of shallow arches under compression. ....	54
Figure 4-16: Load-displacement curves at the inclined LVDT of shallow arches under compression. ..	54

Figure 4-17: Longitudinal strain at the top flange (top-left), the bottom flange (top-right) and transverse strain at the bottom flange (bottom) of shallow arches under compression. ....	55
Figure 4-18: Load-displacement curves at the crown of shallow arches under tension.....	55
Figure 4-19: Load-displacement curves at the inclined LVDT of shallow arches under tension.....	56
Figure 4-20: Longitudinal strain at the top flange (top-left), the bottom flange (top-right) and transverse strain at the bottom flange (bottom) of shallow arches under tension. ....	56
Figure 4-21: Comparison between roller-bent and stress-free model under compressive load.....	57
Figure 4-22: Comparison between roller-bent and stress-free model under tensile load.....	57
Figure 4-23: Comparison of load-displacement equilibrium paths and failure modes between roller-bent and stress-free arches under various loading conditions. ....	59
Figure 5-1: Roller-bending of SHS (left) and RHS bent the "hard way" (top-right) and "easy way" (bottom-right). ....	61
Figure 5-2: Example of SHS distortion due to roller-bending ( $\rho_w = 8\%$ and $\rho_f = 6\%$ ).....	62
Figure 5-3: Theoretical distribution of residual stresses. ....	63
Figure 5-4: Finite element model and boundary conditions. ....	64
Figure 5-5: Numerical simulation of the roller-bending process. ....	65
Figure 5-6: Numerical validation models.....	65
Figure 5-7: Membrane residual stresses (left) and strains (right) of the shell and solid element models. ....	66
Figure 5-8: Membrane residual stresses (left) and strains (right) of the initial and refined shell element models. ....	66
Figure 5-9: Main roller-bending parameters. ....	67
Figure 5-10: Membrane residual stresses (left) and strains (right), for $h/b = 0.66$ . ....	68
Figure 5-11: Membrane residual stresses (left) and strains (right), for $h/b = 1.00$ . ....	68
Figure 5-12: Membrane residual stresses (left) and strains (right), for $h/b = 1.50$ . ....	69
Figure 5-13: Membrane residual stresses (left) and strains (right), for $h/b = 1.00$ . ....	70
Figure 5-14: Membrane residual stresses (left) and strains (right), for $h/b = 1.00$ . ....	70
Figure 5-15: Membrane residual stresses (left) and strains (right), for $h/b = 0.66$ . ....	71
Figure 5-16: Membrane residual stresses (left) and strains (right), for $h/b = 1.00$ . ....	71
Figure 5-17: Membrane residual stresses (left) and strains (right), for $h/b = 1.50$ . ....	72
Figure 5-18: Membrane residual stresses (left) and strains (right), for $h/b = 1.00$ . ....	73
Figure 5-19: Proposed residual stress distribution of roller-bent RHS ( $h/b = 0.66$ ). ....	74
Figure 5-20: Proposed residual stress distribution of roller-bent SHS ( $h/b = 1.00$ ). ....	75
Figure 5-21: Proposed residual stress distribution of roller-bent RHS ( $h/b = 1.50$ ). ....	76
Figure 6-1: Example of roller-bending a CHS workpiece. ....	79
Figure 6-2: Example of CHS distortion due to roller-bending ( $\rho = 13\%$ ).....	80
Figure 6-3: Theoretical distribution of residual stresses. ....	81
Figure 6-4: Finite element model and boundary conditions. ....	82
Figure 6-5: Analysis sequence along with von Mises stress. ....	83
Figure 6-6: Numerical validation models.....	84

Figure 6-7: Membrane residual stresses (left) and strains (right) of the shell and solid element models. ....	84
Figure 6-8: Membrane residual stresses (left) and strains (right) of the initial and refined shell element models. ....	85
Figure 6-9: Main roller-bending parameters. ....	86
Figure 6-10: Membrane residual stresses (left) and strains (right), for various $d/t$ . ....	86
Figure 6-11: Membrane residual stresses (left) and strains (right), for various $R/d$ . ....	87
Figure 6-12: Membrane residual stresses (left) and strains (right), for various $f_y$ . ....	88
Figure 6-13: Membrane residual stresses (left) and strains (right), for various $S/d$ . ....	89
Figure 6-14: Membrane residual stresses (left) and strains (right), for various $d_i/d$ . ....	90
Figure 6-15: Bending dies of encapsulating angles $\theta_e$ equal to $\pi/6$ , $\pi/3$ and $\pi/2$ . ....	90
Figure 6-16: Membrane residual stresses (left) and strains (right), for various $\theta_e$ . ....	91
Figure 6-17: Expansion of residual stresses distributions. ....	92
Figure 6-18: Proposed residual stress distributions of roller-bent CHS. ....	93
Figure 7-1: Eurocode 3 multiple column curves (CEN, 2005). ....	96
Figure 7-2: Proposed residual stress distributions for roller-bent (a) CHS, (b) SHS, (c) RHS ( $h/b = 1.50$ ) and (d) RHS ( $h/b = 0.66$ ). ....	96
Figure 7-3: Axial force of circular arches under radial compression. ....	97
Figure 7-4: Interaction diagram $N-M$ for the in-plane response of CHS. ....	99
Figure 7-5: Interaction diagram $N-M$ for the out-of-plane response of CHS. ....	99
Figure 7-6: Interaction diagram $N-M$ for the in-plane response of SHS. ....	100
Figure 7-7: Interaction diagram $N-M$ for the out-of-plane response of SHS. ....	100
Figure 7-8: Interaction diagram $N-M$ for the in-plane response of RHS ( $h/b = 1.50$ ). ....	101
Figure 7-9: Interaction diagram $N-M$ for the out-of-plane response of RHS ( $h/b = 1.50$ ). ....	101
Figure 7-10: Interaction diagram $N-M$ for the in-plane response of RHS ( $h/b = 0.66$ ). ....	102
Figure 7-11: Interaction diagram $N-M$ for the out-of-plane response of RHS ( $h/b = 0.66$ ). ....	102
Figure 7-12: In-plane buckling resistance of roller-bent CHS arches. ....	103
Figure 7-13: Out-of-plane buckling resistance of roller-bent CHS arches. ....	103
Figure 7-14: In-plane buckling resistance of roller-bent SHS arches. ....	104
Figure 7-15: Out-of-plane buckling resistance of roller-bent SHS arches. ....	104
Figure 7-16: In-plane buckling resistance of roller-bent RHS arches ( $h/b = 1.50$ ). ....	105
Figure 7-17: Out-of-plane buckling resistance of roller-bent RHS arches ( $h/b = 1.50$ ). ....	105
Figure 7-18: In-plane buckling resistance of roller-bent RHS arches ( $h/b = 0.66$ ). ....	106
Figure 7-19: Out-of-plane buckling resistance of roller-bent RHS arches ( $h/b = 0.66$ ). ....	106
Figure 8-1: Residual stress distributions of steel arches. ....	110
Figure 8-2: Beam element model of arch and $N-\varepsilon$ diagram of CHS 100x5. ....	111
Figure 8-3: Shell element model along with details of the rigid links and the residual stresses. ....	112
Figure 8-4: Buckling eigenmodes of beam (left) and shell (right) element models. ....	112
Figure 8-5: Comparison of the out-of-plane buckling response between shell and beam elements...	113
Figure 8-6: Comparison of the out-of-plane buckling response between shell and beam elements...	113
Figure 8-7: Comparison of the in-plane buckling response between shell and beam elements. ....	114



Figure 8-8: Out-of-plane buckling response for various imperfection magnitudes.....	115
Figure 8-9: Out-of-plane buckling response for various imperfection magnitudes.....	115
Figure 8-10: In-plane buckling response for various imperfection magnitudes. ....	116
Figure 8-11: Out-of-plane buckling response for various residual stresses. ....	116
Figure 8-12: Out-of-plane buckling response for various residual stresses. ....	117
Figure 8-13: In-plane buckling response for various residual stresses. ....	117
Figure 8-14: Out-of-plane buckling resistance of roller-bent and stress-free CHS.....	119
Figure 8-15: In-plane buckling resistance of roller-bent and stress-free CHS.....	120
Figure 9-1: Generalized imperfection curves for the out-of-plane buckling.....	126
Figure 9-2: Generalized imperfection curves for the in-plane buckling .....	127
Figure 9-3: Proposed imperfection diagrams for out-of-plane (left) and in-plane (right) buckling. ....	128
Figure 9-4: Proposed design buckling curves for out-of-plane (left) and in-plane (right) buckling.....	128
Figure A-1: Finite element model with employed residual stresses. ....	137
Figure A-2: Axial force-strain response of roller-bent and stress-free CHS. ....	137
Figure A-3: Moment-curvature diagrams for in-plane bending. ....	139
Figure A-4: Moment-curvature diagrams for out-of-plane bending. ....	142
Figure A-5: Torsion-twist diagrams. ....	144



## List of Tables

Table 2-1: Experimental tests on roller-bent wide flange sections (Spoorenberg et al., 2010). .....	12
Table 2-2: Workpiece parameters. ....	14
Table 2-3: Roller-bending arrangement parameters. ....	15
Table 2-4: Roller-bending arrangement (Chiew et al., 2016). ....	16
Table 2-5: Coupon tests on roller-bent wide-flange-sections (Spoorenberg et al., 2012a). ....	17
Table 2-6: Values of $C$ parameter. ....	18
Table 2-7: Critical load and horizontal reaction for circular arches under pure compression. ....	19
Table 3-1: Experimental tests. ....	28
Table 3-2: High arches dimensions. ....	29
Table 3-3: Shallow arches dimensions. ....	29
Table 3-4: Best fitting radii and deviations of high arches. ....	29
Table 3-5: Best fitting radii and deviations of shallow arches. ....	30
Table 5-1: General guidelines for minimum cold-bending radii of SHS/RHS (Dowswell, 2018). ....	62
Table 5-2: Developed strains in the compression and tension zones of the cross-section. ....	70
Table 5-3: Proposed residual stresses along the semi-perimeter of RHS ( $h/b = 0.66$ ). ....	74
Table 5-4: Proposed residual stresses along the semi-perimeter of SHS ( $h/b = 1.00$ ). ....	75
Table 5-5: Proposed residual stresses along the semi-perimeter of RHS ( $h/b = 1.50$ ). ....	76
Table 6-1: General guidelines for minimum cold-bending radii of CHS (Dowswell, 2018). ....	80
Table 6-2: Membrane residual stresses of CHS for various $d/t$ . ....	87
Table 6-3: Developed strains of CHS for various $R/d$ . ....	87
Table 6-4: Membrane residual stresses of CHS for various $S/d$ . ....	89
Table 6-5: Membrane residual stresses (with respect to $f_y$ ) for various $S/d$ and $d/t$ . ....	92
Table 6-6: Proposed residual stresses along the semi-perimeter of CHS. ....	93
Table 8-1: Examined arch configurations. ....	118
Table 8-2: Out-of-plane buckling of roller-bent and stress-free arches under uniform radial load. ....	119
Table 8-3: In-plane buckling of roller-bent and stress-free arches under uniform radial load. ....	120
Table 9-1: Imperfection factor $\alpha$ for column curves according to EN1993-1-1. ....	124
Table 9-2: Out-of-plane buckling of roller-bent and stress-free arches under uniform radial load. ....	125
Table 9-3: In-plane buckling of roller-bent and stress-free arches under uniform radial load. ....	126
Table 9-4: Proposed imperfection parameter $\eta$ . ....	127
Table A-1: Axial force-strain values of roller-bent and stress-free CHS 100x5. ....	138
Table A-2: Moment-Curvature values for roller-bent CHS 100x5. ....	140
Table A-3: Moment-Curvature values for stress-free CHS 100x5. ....	141
Table A-4: Moment-Curvature values for roller-bent CHS 100x5. ....	143
Table A-5: Torsion-Twist values for roller-bent CHS 100x5. ....	145
Table A-6: Torsion-Twist values for stress-free CHS 100x5. ....	146



# 1 INTRODUCTION

## 1.1 ARCHES IN CONSTRUCTION

Early arch structures were built from stone or masonry thousands of years ago, comprising mainly bridges, aqueducts and gates. Before steel came into general use during the latter part of the 19th Century, curved structures were constructed from iron, which was cast in liquid form in a curved profile or built up from wrought iron components, either with shaped web plates or in the form of lattice trusses (King and Brown, 2001). Because wrought iron was very soft and exhibited low tensile strength, blacksmiths could easily curve small components by hot forging. The main applications of iron comprised bridges as well as roof trusses for various exhibit halls, attracting the interest of engineers and architects as expressions of structural function and artistic endeavor (Figure 1-1). In the second half of the 19th century, the development of constructional steel introduced new concepts in structural engineering, as both tensile and compressive loads could be carried effectively. Nonetheless, a limited number of steel buildings comprising curved elements had been constructed until the late 1970s.



Figure 1-1: Curved cast iron in roof trusses (King and Brown, 2001).

During the last few decades, demands for curved steel members increased rapidly. Curved constructional steels constituted an attractive solution due to their aesthetic appeal and the wide variety of forms that can be created. Their use was further facilitated by the technological progress regarding the steelmaking and forming techniques, as well as the advances in computational tools employed in engineering analysis. Architecturally Exposed Structural Steel (AESS) has become more popular worldwide, as a way of expressing the structural integrity of a building and at the same time putting the structural system at the aesthetic forefront. Curved constructional steel members started to be used in many AESS applications (AISC, 2003), providing the users with natural light and a sense of spaciousness and grandeur in public facilities such as airports, stations, shopping malls and leisure centers (Figure 1-2).

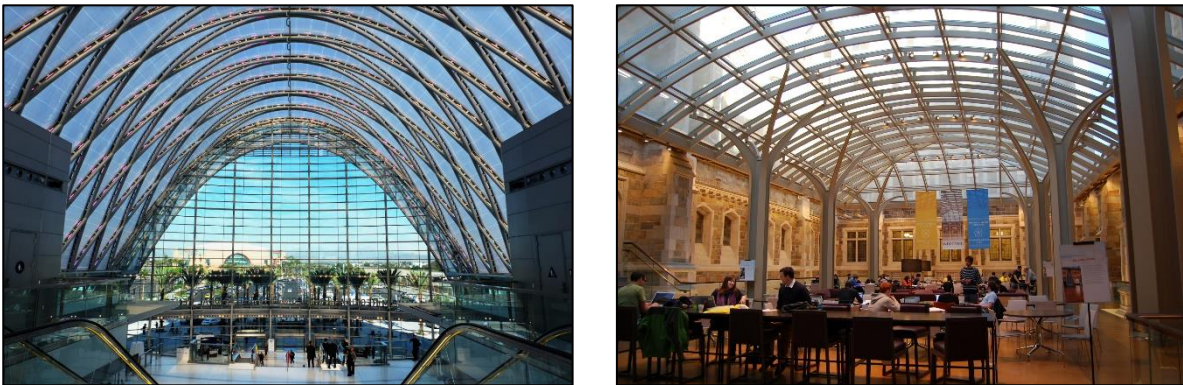


Figure 1-2: Examples of steel arches in AESS applications.

From the structural point of view, arches are able to cover long spans without intermediate supports, as loads are carried largely in compression rather than bending action (Bjorhovde, 2006). For certain arch curvatures, boundary conditions and loading distributions, where the funicular curve of load coincides with the centroidal axis of the rib, pure axial compression is developed along the entire arch length. Because of their beneficial behavior, arches are commonly used as the primary load-bearing components in large structural and infrastructural engineering applications, such as bridges, stadiums, buildings, etc. In these cases, arches are constructed in stages, consisting of smaller curved or straight steel segments that are connected (bolted or welded) on site and loads are transferred by means of cables. Typical examples of steel arches in civil engineering infrastructures are shown in Figure 1-3 and Figure 1-4, including the Tsakona bridge (Greece), the Sydney Harbor Bridge (Australia), the Athens Olympic Stadium (Greece), and the new Wembley Stadium in London (United Kingdom).



Figure 1-3: Tsakona Bridge, Greece (left) and Sydney Harbor Bridge, Australia (right).

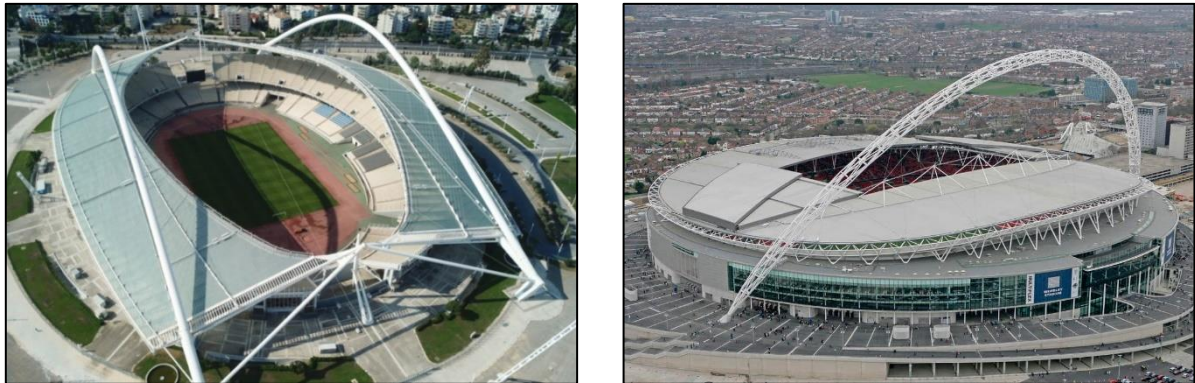


Figure 1-4: Athens Olympic Stadium, Greece (left) and Wembley Stadium in London, United Kingdom (right).

## 1.2 MANUFACTURING PROCESS

Curved steel members are typically manufactured from initially straight members which are subjected to bending in order to meet the desired curvature (Alwood, 2006; Smith, 2008; Packer, 2013). Several manufacturing methods are available in industry, including the roller bending, incremental bending, rotary-draw bending, and induction bending processes (Figure 1-5). Some of them are more common in the steel construction industry, while others are employed in the automobile, piping or other industries. A brief description of the main curving methods is presented next.

- The roller-bending process is the most common and economical method for curving constructional steel members. It is a cold-forming process, where a workpiece is passed iteratively through a three-roller-bending machine. In each subsequent pass, the bending rolls are manipulated in an appropriate manner that involves local plastification of steel, until the desired curvature is reached. The method is also called “pyramid roll bending” because of the three-roller pyramid arrangement.
- The incremental bending process is a cold-forming method, in which hydraulic rams are used to apply bending forces at several discrete, closely spaced locations along the member. Additional supports are typically employed on the workpiece, aiming at reducing distortions during the bending operation. This method is usually applied for curving of large-section beams into small-radii of curvature with minimal distortions.
- The rotary-draw bending is a cold-forming process, where a steel member is clamped and drawn around a rotating die. Special draw-bending equipment is usually required to eliminate cross-sectional distortions during the bending process, including appropriate mandrels and die sets. This method is commonly used in the automobile, mechanical and piping industry for curving workpieces of small hollow sections into tight radii.
- The induction bending process is a hot-bending method, in which an electric coil is used to heat (1500°C - 1900°C) a narrow band of the workpiece (50mm - 150mm), while the member is rotated around a fixed-radius pivot arm. Sprayed water or forced air is used to cool down the material adjacent to the heated zone, after passing through the coil. Although induction bending is more expensive than other processes, it provides higher dimensional accuracy and smaller cross-sectional distortions. Moreover, smaller radii can be achieved, and lighter sections can be curved compared to cold-formed processes.





Figure 1-5: Roller bending (top-left), incremental bending (top-right), rotary-draw bending (bottom-left) and induction-bending (bottom-right).

### 1.3 ANALYSIS AND DESIGN

Analysis and design methods of steel arches are based on the evaluation of their structural adequacy, considering the nonlinear effects due to material yielding and elastic/inelastic instabilities. Instabilities of arches can be characterized by snap-through, in-plane, and out-of-plane buckling (Figure 1-6). Snap-through buckling is usually the prevailing buckling mode in cases of shallow arches (low height to span ratio), which are restrained against out-of-plane displacements. In this context, the arch stiffness is gradually reduced due to the induced axial shortening, resulting to a limit point in which transition from compressive to tensile action occurs suddenly. In-plane buckling is predominant in cases of non-shallow arches, which are adequately braced against out-of-plane displacements. In this case, either symmetric or antisymmetric mode shapes can be developed. Out-of-plane buckling occurs in cases of arches exhibiting significant free-standing portions. This type of buckling comprises a combination of flexural and lateral-torsional buckling, and therefore is also denoted as flexural-torsional buckling.

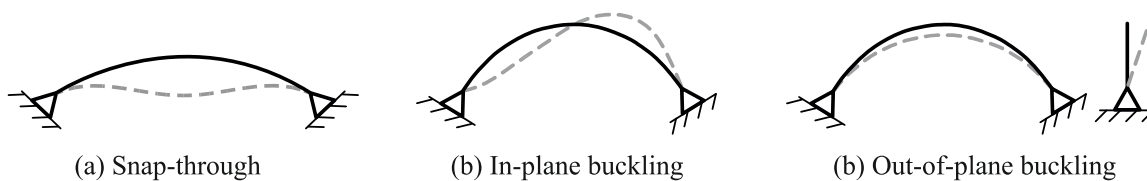


Figure 1-6: Main buckling modes of arches.



Generally, structural analyses are classified in two main categories, namely 1<sup>st</sup> and 2<sup>nd</sup> order analyses. The appropriate analysis type is determined based on the characteristics of the examined structural system. In 1<sup>st</sup> order analyses, relatively small deformations are considered to be developed in the structure, which do not influence the equilibrium equations. Thus, the equilibrium equations are formulated with respect to the undeformed geometry. In this case, the principle of superposition regarding the loads holds, and loads are linearly related with deformations. Although the 1<sup>st</sup> order analysis is a fast and inexpensive type of analysis, it may be inaccurate when developed deformations become large, which should then be considered by implementing 2<sup>nd</sup> order analyses. In 2<sup>nd</sup> order analyses, the equilibrium equations are formulated in the deformed state of the structure. This type of analysis is employed in cases of flexible structural systems, or when instability phenomena dominate the structural response. Advances in computational engineering have facilitated the use of the Finite Element Method (FEM) in the analysis and design of structures. Numerical analyses, based on FEM, are commonly employed for the verification of steel structures (Gantes and Fragkopoulos, 2009). Starting from setting up an appropriate finite element model, Linear Analyses (LA) are able to provide the developed actions and displacements with respect to the undeformed geometry. Linearized Buckling Analyses (LBA) are aimed at providing the buckling modes and corresponding critical loads of structures. The effects of material yielding are effectively considered by performing Material Nonlinear Analysis (MNA), while the effects of geometrical nonlinearities can be assessed by carrying out Geometrical Nonlinear Analysis (GNA). A combination of Geometrical and Material Nonlinear Analysis (GMNA) is able to account for the possible interaction of both nonlinearities. Finally, the buckling behavior of steel structures can be accurately derived from Geometrical and Material Nonlinear Imperfection Analysis (GMNIA), including appropriate shapes and values of initial imperfections and residual stresses.

At this time, the concept of limit states is adopted in modern structural steel design standards (CEN, 2005; AISC, 2018). In this context, 1<sup>st</sup> order or 2<sup>nd</sup> order analyses are employed to obtain the developed actions of structures under design loads, which are compared to strength resistances accounting for material failure or local/global buckling. For common cases both material nonlinearities as well as geometric nonlinearities are calculated using closed-form equations. More specifically, the steel yield/ultimate point is considered for calculation of the cross-sectional strength capacity. Local buckling is taken into account by classifying cross-sections into appropriate classes based on their wall slenderness, in which the plastic, elastic, or reduced (effective) cross-section resistance is used. Global buckling is considered by implementing reduction factors according to relevant buckling curves, which are related to the member slenderness incorporating the effects of geometric imperfections and residual stresses. Buckling curves are available for steel beams and columns, given in the form of Figure 1-7.

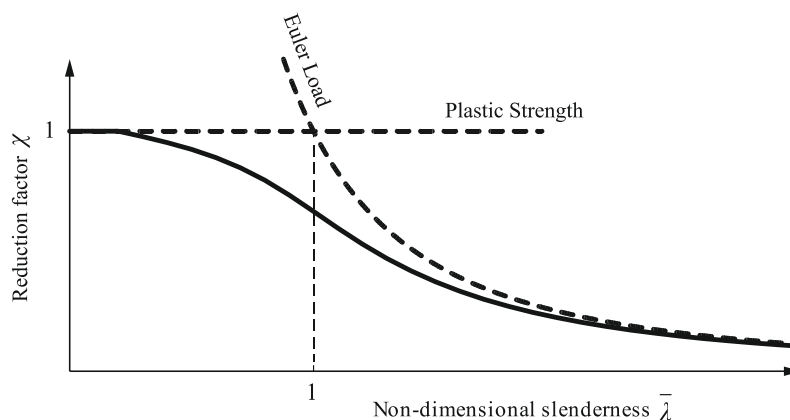


Figure 1-7: Typical design for stability using buckling curves.

## 1.4 PROBLEM STATEMENT AND OBJECTIVE

Geometric imperfections and residual stresses affect the elastic domain of the material, causing premature yielding of the cross-section and having considerable effect on the brittle fracture, fatigue and buckling strength of steel members (ECCS, 1976). Aberrations of the theoretical geometry as well as self-equilibrating locked-in stresses, are induced to steel arches after the roller-bending manufacturing process, which is typically employed in the steel construction industry. Limited studies are found in the literature regarding the distribution and magnitude of imperfections and residual stresses of roller-bent hollow sections (Dowswell, 2018), while their influence on the structural response of arches has not been properly assessed. Therefore, in many cases structural engineers have to carry out non-linear finite element simulations, which are cost- and time-consuming, incorporating indirectly these effects in the developed numerical models, in order to evaluate the structural adequacy of arches. This practice usually results in over-dimensioned structures with questionable reliability, due to the lack of knowledge on the inelastic stability of roller-bent arches.

Scope of the present dissertation is to offer insight in the structural behavior of steel arches comprising hollow sections, by (a) quantifying (in terms of distribution and amplitude) the residual stresses and geometrical imperfections encountered in roller-bent members, (b) assessing their influence on the structural behavior of arches, and (c) providing design guidelines in terms of pertinent buckling curves, in which the effects of the roller-bending process are taken into account. To that effect, a combined experimental, numerical and analytical investigation is implemented during the whole research work, aiming at evaluating reliably the structural behavior of hollow-section steel arches. Experimental results are used to validate the developed numerical models, while extensive numerical simulations along with analytical calculations are employed to investigate parametrically the structural behavior of hollow-section arches. The contribution of this dissertation in the engineering science and practice, is considered to be significant, as the structural design of arches, which until now is either relying on arbitrary and often erroneous simplifying assumptions, or is otherwise based on highly demanding nonlinear simulations, can be facilitated by implementing the proposed design guidelines.

## 1.5 OUTLINE OF THESIS

The present dissertation is divided into ten chapters. A brief introduction to the constructional issues of steel arches, analysis and design practices, along with the problem statement have been presented in this first chapter. In Chapter 2, literature findings on the structural behavior of steel arches are summarized, with emphasis on roller-bent residual stresses and material properties, elastic and inelastic stability issues, along with pertinent design recommendations. In Chapter 3, original experimental tests on the in-plane behavior of roller-bent arches are presented, which were carried out in the Institute of Steel Structures at the National Technical University of Athens. Finite element simulations of the aforementioned experiments are performed in Chapter 4, aiming at comparing experimental and numerical results for the calibration of numerical models. In Chapter 5, an extensive parametric study is carried out, examining the effects of the main roller-bending characteristics on the developed stress/strain distributions of square- and rectangular- hollow-sections. A pertinent parametric study regarding roller-bent circular-hollow-sections is presented in Chapter 6. An analytical investigation of the effects of residual stresses on roller-bent hollow sections is presented in Chapter 7. In Chapter 8, the structural stability of hollow-section arches is assessed using finite element analyses, and pertinent design stability criteria are proposed in Chapter 9. Finally, the conclusions and contributions of this dissertation as well as recommendations for further research are given in Chapter 10.

## REFERENCES

- AISC (2003). "Architecturally Exposed Structural Steel." AESS Supplement, *Modern Steel Construction*, American Institute of Steel Construction, May.
- AISC (2016). *Specification for Structural Steel Buildings*. American Institute of Steel Construction, Chicago, IL.
- Alwood, T. (2006). "What Engineers Should Know About Bending Steel." *Modern Steel Construction magazine*, May.
- Bjorhovde, R. (2006). "Cold Bending of Wide-Flange Shapes for Construction." *Engineering Journal*, vol. 4, pp. 271–286.
- CEN (2005). *Eurocode 3: Design of Steel Structures, Part 1-1: General Rules and Rules for Buildings, EN 1993-1-1*. Comité Européen de Normalisation (CEN), European Committee for Standardization Brussels, Belgium.
- Dowswell, B. (2018). *Curved Member Design*. American Institute of Steel Construction, Chicago, IL.
- ECCS (1976). *Manual on Stability of Steel Structures*. European Convention for Constructional Steelwork, Liege, Belgium.
- Gantes, C. J., and Fragkopoulos, K. A. (2009). "Strategy for numerical verification of steel structures at the ultimate limit state." *Structure and Infrastructure Engineering*, vol. 6, pp. 1–31.
- King, C., and Brown, D. (2001). *Design of Curved Steel*. The Steel Construction Institute, Berkshire, UK.
- Packer, J. A. (2013). "Bending of Hollow Structural Sections." *Steel Tube Institute*.
- Smith, B. (2008). "A Conversation with a Bender." *Modern Steel Construction magazine*, July.



## 2 LITERATURE REVIEW

### 2.1 INTRODUCTION

The structural behavior of arches with emphasis on stability is presented in several literature findings. Because it is not feasible to provide a complete overview of all research studies within a single chapter of the present dissertation, the more important and relevant findings will be presented. It should be noted that excellent sources on the topic can be found in the bibliography. An overview of the research studies prior to 1970 is given in the "*Handbook of Structural Stability*" by Hayashi (1971). In the "*Stability of Metal Structures, a World View*" (Beedle, 1991), a comparison between building standards and provisions for the spatial stability of arches is attempted. The arch elastic and inelastic stability are discussed in a book chapter of the "*Structural Stability Design, Steel and Composite Structures*" (Fukumoto, 1996). A summation of pertinent experimental studies is presented in the "*Buckling Experiments*" by Singer et al. (1998). In the "*Design of curved steel*" (King and Brown, 2001), a comprehensive study for the practical design of curved members is presented, including practical worked examples. The spatial stability of arches, the pertinent design criteria and several bracing recommendations, are thoroughly presented in a book chapter of the "*Guide to Stability Design Criteria for Metal Structures*" (Ziemian, 2010). Finally, a design guide of curved steel members, including the state-of-the-art literature findings on fabrication, analysis and design issues, is given in the "*Curved Member Design*", by Bo Dowswell (2018).

### 2.2 ROLLER-BENDING OF ARCHES

#### 2.2.1 General remarks

The roller-bending process, or alternatively "pyramid roll bending", is the most common and cost-effective method for producing circular arches in the steel constructional industry. It is a cold-formed process, where the workpiece is passed iteratively through three rollers (Figure 2-1). In each subsequent pass, the bending rolls are manipulated in an appropriate manner that involves local plastification of steel, until the desired curvature is reached. Steel members of any cross-sectional shape can typically be curved, including open or closed profiles. Nevertheless, cross-sectional distortions are inevitably induced during the roller-bending process. The minimum achieved arc radius is usually limited by the maximum magnitude of cross-sectional distortion which is allowed to take place. Special techniques are used to minimize the encountered distortions, such as filling hollow sections with sand or utilizing auxiliary rolls on the tension flanges of open profiles in order to provide additional restraints to the flanges and web. Practical information on the manufacturing processes can be found from bend/fabricator companies.

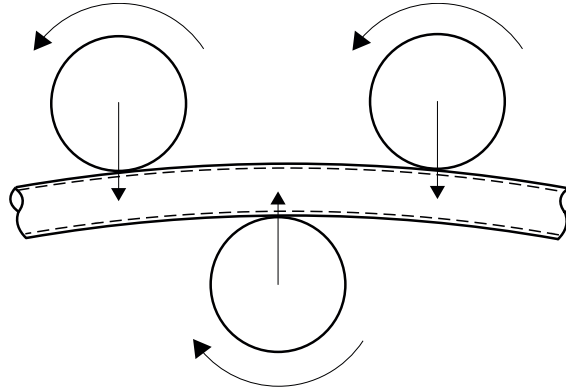


Figure 2-1: Roller-bending method.

Early studies on cold-curving were carried out by Hansen & Jannerup (1979), investigating analytically the resulting geometry of solid bars after roller-bending. Kennedy et al. (1986) and Kennedy (1988) investigated the induced deformations and cross-sectional distortions of roller-bent Hollow-Structural-Sections (HSS). A detailed description of the roller-bending process along with the associated curving mechanics have been presented by Bjorhovde (2006). The curving mechanism is based on steel yielding in order to meet a certain radius of curvature, as shown in Figure 2-2. During multi-pass roller-bending, the obtained curvature is determined by measuring the span length and the rise of the workpiece. The radius of curvature  $R$  for a circular arch of span length (chord length)  $l$  and rise  $f$  is given by Eq. (2-1). The curvature  $k$  is defined as the inverse of radius  $R$ , according to Eq. (2-2). The longitudinal strains at the top and bottom height of the cross-section depend on the member's curvature and the cross-sectional depth  $d$ , according to the fundamental strain-curvature relationship of Eq. (2-3). Geometric imperfections, residual stresses and alteration of the mechanical properties are induced in roller-bent members from the cold-forming process. Pertinent research studies regarding the effects of roller-bending will be presented next.

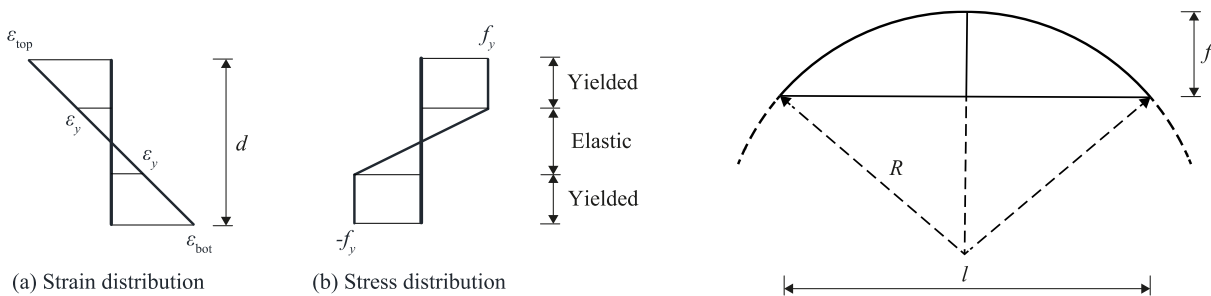


Figure 2-2: Curving mechanics of roller-bending.

$$R = \frac{4f^2 + l^2}{8f} \quad (2-1)$$

$$k = \frac{1}{R} \quad (2-2)$$

$$\frac{1}{R} = \frac{\varepsilon_{top} - \varepsilon_{bot}}{d} \quad (2-3)$$

### 2.2.2 Residual stresses

Residual stresses, or commonly called "locked-in" stresses, are induced to steel profiles after fabrication processes. Locked-in stress distributions are self-equilibrated within the cross-section, emanating from cross-sectional uneven cooling after hot-rolling, welding or cutting operations, as well as from plastic deformations caused by cold-forming, cold-straightening or cambering processes. These stresses are considered to have a significant effect on the brittle fracture, fatigue, stress corrosion, buckling and post-buckling strength of steel members (ECCS, 1976). Locked-in stresses are usually decomposed into the longitudinal and transverse components. In the case of thin-walled sections, residual stresses are commonly idealized as a summation of two types: membrane and flexural. The former are more prevalent in roll-formed members, while the latter dominate in the press-braked ones (Schafer, 1998). Indicative longitudinal residual stress distributions from studies of Komatsu and Sakimoto (1977), and ECCS (1976, 1984) are depicted in Figure 2-3.

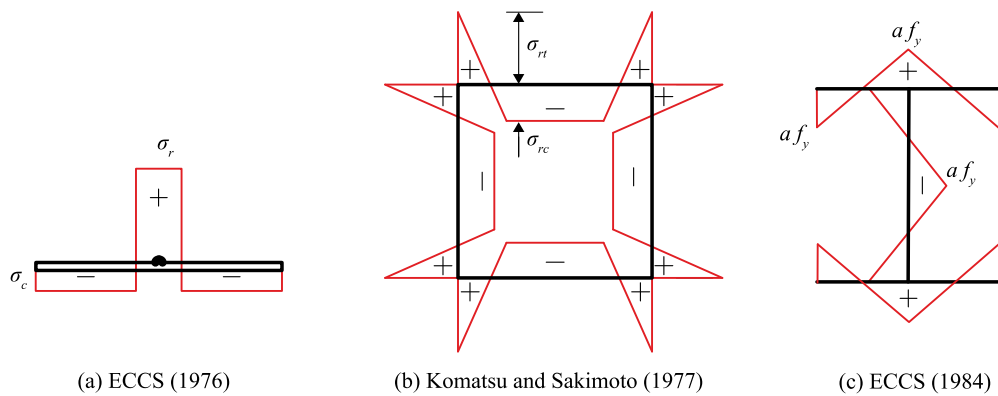


Figure 2-3: Residual stress distributions in literature.

The locked-in formations resulting from the cross-sectioning process have been thoroughly investigated in the literature. However, when the straight workpiece is bent into the desired shape, most of the section exhibits anew yielding. Thus, the previous residual stress pattern from the sectioning process is replaced by a new pattern due to curving. A theoretical distribution of the residual stresses emanating from the inelastic bending of beams is given by Timoshenko (1956), as function of the steel's yield stress  $f_y$  and the ratio  $a$  between the plastic and elastic section modulus. By aggregating the bending stresses due to inelastic  $M_{pl}$  (Figure 2-4a) and elastic "spring-back"  $M_{sb}$  (Figure 2-4b) moments, the self-equilibrated locked-in distribution (Figure 2-4c) is obtained. The theoretical distribution exhibits an anti-symmetrical layout about the neutral axis, which does not differentiate between cross-sectional shapes. Based on the assumptions of the simplified model, the theoretical distribution is generally valid for bending beams exhibiting small shear stresses relative to the bending stresses (Euler-Bernoulli theory), as well as uniform bending stresses across the cross-sectional width (plane stress conditions).

$$M_{pl} + M_{sb} = 0 \quad (2-4)$$

$$M_{pl} = -W_{pl} \cdot f_y \quad (2-5)$$

$$\sigma_{sb} = \frac{M_{sb}}{W_{el}} = -\frac{W_{pl}}{W_{el}} \cdot f_y, \quad \sigma_{res} = f_y \cdot (1 - a), \quad \text{where } a = \frac{W_{pl}}{W_{el}} \quad (2-6)$$

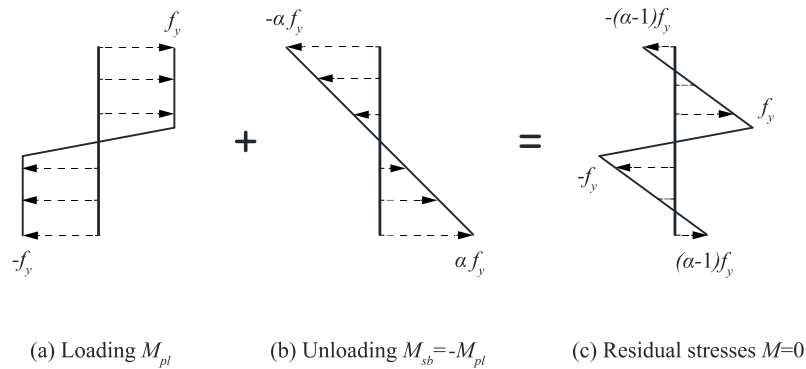


Figure 2-4: Loading (a), unloading (b) and residual (c) stress distributions.

The residual stress distributions resulting from the roller-bending process have been investigated in a limited number of studies. Residual stress measurements on roller-bent specimens comprising wide flange sections, were carried out by Spoorenberg et al. (2010), using the sectioning method. Previous measurements, employing the hole-drilling method, yielded unsatisfactory results (La Poutre, 2005). Electrical strain gauges were implemented on the surfaces of specimens, in order to measure the longitudinal strains that were released after carrying out longitudinal saw cuts. A total number of 18 roller-bent specimens were examined, comprising various steel grades and radii curvature, as shown in Table 2-1. For comparison purposes, the electrical discharging machining (EDM) technique and the conventional saw cutting procedure were used to measure residual stresses. It was evidenced that both techniques yield almost identical residual stress patterns. Strain release was recorded during the entire saw cutting procedure, until approximately 30 minutes after the end of cutting. The corresponding stress values were calculated by multiplying the strain measurements with the Young modulus obtained from the tensile coupon tests, prior to curving process. The membrane stresses were determined by averaging stresses from the opposite faces of steel plates. The sectioning process of HE 100A and HE 360B specimens, is shown indicatively in Figure 2-5.

Table 2-1: Experimental tests on roller-bent wide flange sections (Spoorenberg et al., 2010).

No.	Cross-section	Mechanical properties prior to curving process		Steel Grade	Bending radius R (mm)
		$f_y$ (Mpa)	$f_t$ (Mpa)		
1	HE 100A	322	433	S235	1910
2	HE 100A	279	418	S235	2546
3	HE 100A	279	418	S235	3820
4	HE 100A	364	566	S355	1910
5	HE 100A	364	566	S355	2546
6	HE 100A	364	566	S355	3820
7	HE 100B	248	411	S235	1910
8	HE 100B	285	412	S235	2546
9	HE 100B	285	412	S235	3820
10	HE 100B	386	492	S355	1910
11	HE 100B	390	495	S355	2546
12	HE 100B	390	495	S355	3820
13	HE 360B	269	389	S235	8000
14	HE 360B	357	534	S355	8000
15	IPE 360	297	414	S235	4500
16	IPE 360	297	414	S235	8000
17	IPE 360	361	528	S355	4500
18	IPE 360	361	528	S355	8000



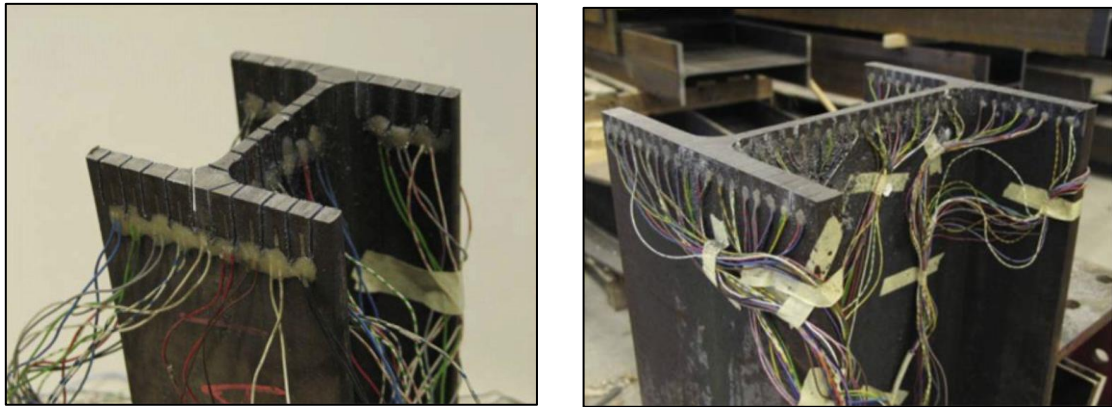


Figure 2-5: Sectioning process of HE 100A and HE 360B (Spoorenberg et al., 2010).

Overall, the measured residual stresses exhibited similar distributions in all cases. A comparison of the locked-in stress formations between straight and roller-bent HE 360B specimens is shown in Figure 2-6. The residual stresses of straight specimens were found in agreement with theoretical predictions of hot-rolled sections. However, the locked-in stresses of roller-bent specimens differed from their straight counterparts, indicating that roller-bending has a significant effect on the longitudinal residual stress distributions. The roller-bent formations varied also from the Timoshenko distribution, exhibiting stress concentrations at the web-to-flange junctions. Furthermore, it was shown that there is no clear correlation between curving radii and residual stresses. It was observed that decrease of bending radii results in increase of compressive stresses at the web, while stresses at the top and bottom flange remain unaffected. Residual stresses at the bottom web-to-flange junction were found to exceed the yield stress of the material prior to curving process, as a result of strain hardening due to the induced cold-working. Finally, significant stress gradients were observed through the wall thickness of flanges in the roller-bent specimens.

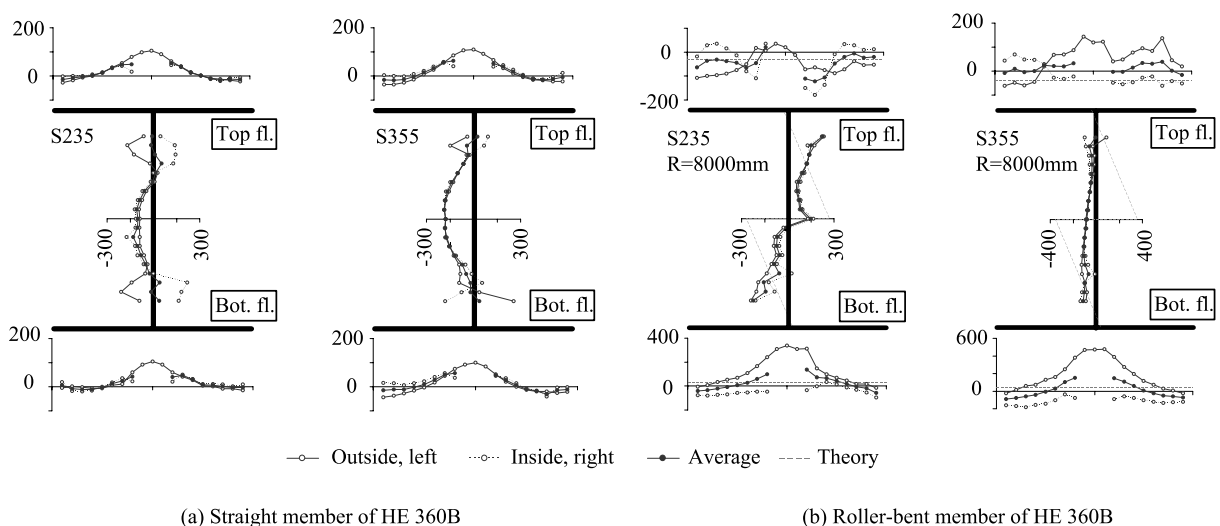


Figure 2-6: Residual stresses of straight and roller-bent HE 360B (Spoorenberg et al., 2010).

Finite element simulations of the roller-bending process were performed next by the same research team (Spoorenberg et al., 2011a). Scope of the numerical study was the validation of the developed numerical models against the experimental results of Spoorenberg et al. (2010). The full interaction between bending rollers and workpieces was considered in the employed finite element models, as

shown in Figure 2-7. Parameters of the workpiece and roller-bending arrangement are summarized in Table 2-2 and Table 2-3, respectively. Aiming at reducing the computational effort, only half of the I-section was modeled, taking advantage of symmetry conditions. Workpieces were meshed using solid elements, since preliminary analyses using shell or beam elements provided large discrepancies with respect to the experimental results. A material model, based on the true stress/strain results of the tensile coupon tests prior to curving process, was employed in the numerical simulations. The material plasticity was characterized by the von Mises yield criterion and the Prandtl-Reuss flow rule using an isotropic hardening law. Implicit static analyses were carried out in the general-purpose finite element software ANSYS.

Membrane residual stresses were extracted by averaging the locked-in stress values over the integration points in the thickness direction. The preexisting locked-in stress formations from the sectioning process were found to have an insignificant effect on the final distributions. A comparison between numerical, experimental and theoretical residual stresses of roller-bent HE 360B is shown in Figure 2-8. The numerical and experimental results provided good agreement regarding the top and bottom flanges, while moderate agreement was obtained at the web of wide-flange-sections. The encountered discrepancies were attributed to the presence of the flange support roller, which was found to affect considerably the developed locked-in formations. Both experimental and numerical distributions differed significantly from the theoretical (anti-symmetrical) distribution of Timoshenko. Taking into consideration the model's simplifications, as well as the accuracy with which residual stresses can be measured, it was concluded that the proposed finite element model was capable to provide the residual stresses of roller-bent wide-flange-sections with sufficient accuracy for design purposes.

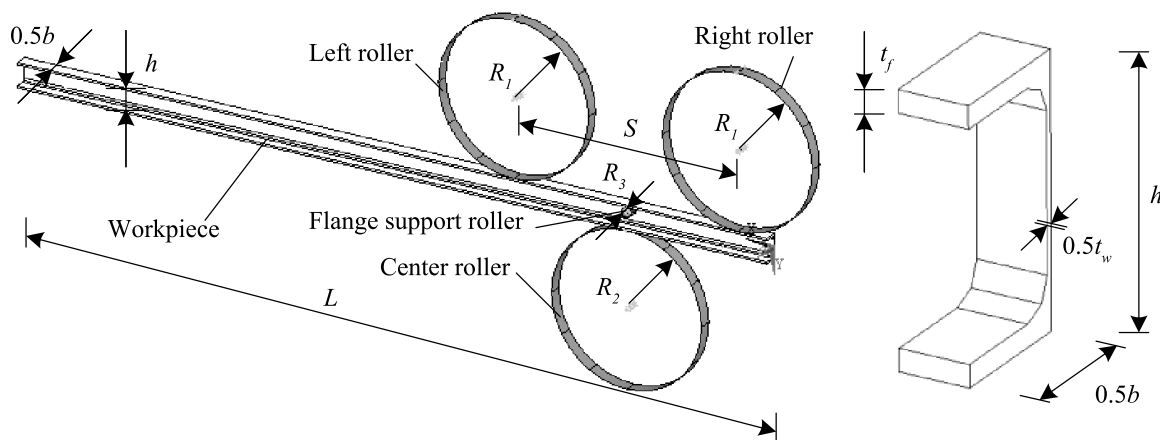


Figure 2-7: Roller-bending simulation (Spoorenberg et al., 2011a).

Table 2-2: Workpiece parameters.

No.	Cross-Section	Steel grade	Bending radius (mm)
1	HE 100A	S235	1910
2	HE 100A	S235	2546
3	HE 100A	S235	3820
4	HE 100A	S355	1910
5	HE 100A	S355	2546
6	HE 100A	S355	3820
13	HE 360B	S235	8000
14	HE 360B	S235	8000

Table 2-3: Roller-bending arrangement parameters.

Roller-bending arrangement	HE 100A	HE 100B
Distance between outer rolls, $S$ (mm)	900	2500
Modeled beam length, $L$ (mm)	3000	10800
Radius of left and right roll, $R_1$ (mm)	300	325
Radius of center roll, $R_2$ (mm)	300	325
Radius of flange support roll, $R_3$ (mm)	20	80

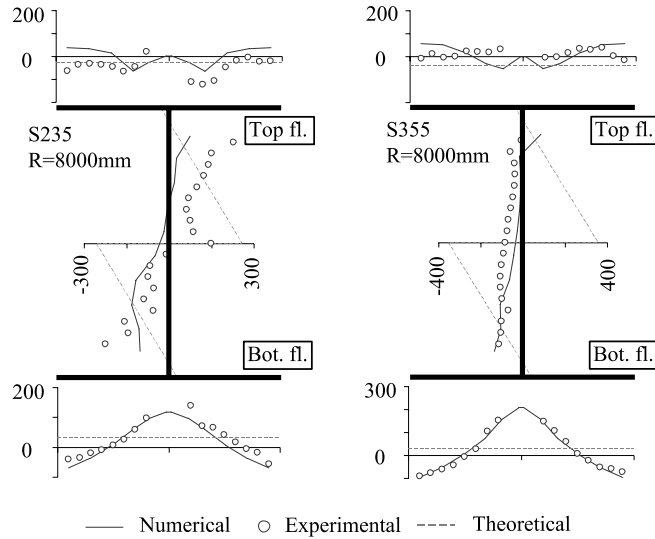


Figure 2-8: Numerical, experimental and theoretical residual stresses of roller-bent HE 360B (Spoorenberg et al., 2011a).

Based on the results of finite element analyses, a residual stress model suitable for roller-bent wide-flange-sections was proposed (Spoorenberg et al., 2011b). The model was considered generally applicable within the examined range of curving radii  $R$  over cross-sectional height  $h$ , namely  $10 \leq R/h \leq 40$ . The proposed model is depicted in Figure 2-9. Pertinent residual stress values can be calculated according to Eq. (2-7). The residual stress model was compared to experimental and numerical residual stress measurements and good agreement was observed.

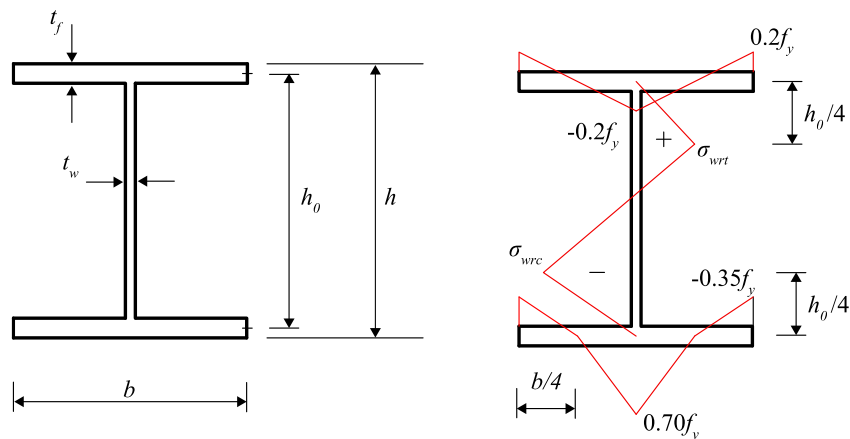


Figure 2-9: Proposed residual stress model for roller-bent wide-flange-sections (Spoorenberg et al., 2011b).

$$\sigma_{wrt} = \frac{7bt_f}{30h_0t_w} f_y, \quad \sigma_{wrc} = -\frac{14bt_f}{30h_0t_w} f_y \tag{2-7}$$

The residual stress formations of roller-bent Rectangular-Hollow-Sections (RHS) have been investigated by Chiew et al. (2016). In this context, detailed roller-bending simulations of RHS steel workpieces were carried out in the general-purpose finite element software ABAQUS. The full interaction between the bending rollers and workpieces was considered, employing various roller-bending arrangements, as shown in Table 2-4. Moreover, different boundary conditions, bending curvatures, and steel grades were examined. The workpieces were modelled using solid elements associated with an isotropic trilinear hardening model. The obtained residual stress formations differed from the theoretical distribution of Timoshenko, exhibiting stress concentrations at the web-to flange junctions. Residual stresses were found to be affected by the cross-sectional aspect ratio and thickness ratio, as well as the bending radii. Based on the results of parametric analyses, a residual stress model suitable for roller-bent RHS was proposed, satisfying the cross-sectional equilibrium requirements. The proposed model is given in Figure 2-10, and pertinent residual stress values can be calculated according to Eq. (2-8) to (2-11).

Table 2-4: Roller-bending arrangement (Chiew et al., 2016).

No.	Cross-sectional dimensions (mm)	Diameter (mm)		Roller distance (mm)
		Outer rollers	Middle roller	
1	101.6 × 76.2 × 6.35	385	430	710
2	101.6 × 101.6 × 4.78	385	430	710
3	127.0 × 127.0 × 4.78	385	430	710
4	127.0 × 127.0 × 4.78	385	430	710
5	152.4 × 101.6 × 4.78	385	430	710
6	152.4 × 152.4 × 6.35	385	430	710
7	177.8 × 127.0 × 6.35	460	515	1015
8	177.8 × 177.8 × 7.95	460	515	1015
9	203.2 × 101.6 × 9.53	460	515	1015
10	203.2 × 203.2 × 6.35	460	515	1015
11	254.0 × 152.4 × 6.35	460	515	1015
12	254.0 × 254.0 × 9.53	460	515	1015

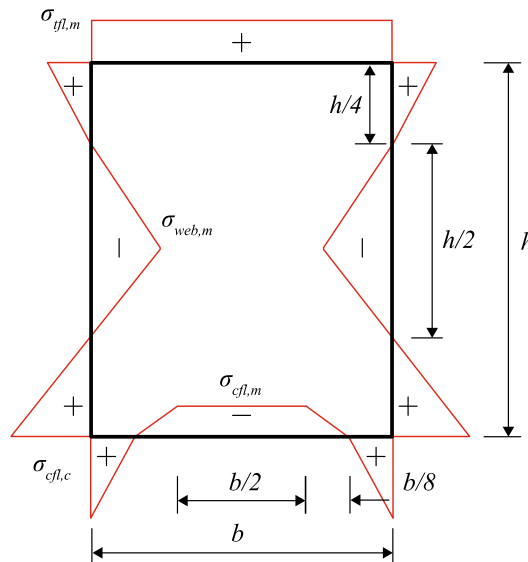


Figure 2-10: Proposed residual stress model for roller-bent RHS (Chiew et al., 2016).

For  $20 \leq R/h \leq 150$ ,  $1 \leq h/b \leq 2$ ,  $20 \leq h/t \leq 50$  and  $235\text{MPa} \leq f_y \leq 450\text{MPa}$ :

$$\sigma_{cfl,c}/f_y = \varepsilon[0.81 - 0.0028(R/h) - 0.09(h/b) + 0.008(h/t)] \quad (2-8)$$

For  $1 \leq h/b \leq 2$ ,  $20 \leq h/t \leq 50$  and  $235\text{MPa} \leq f_y \leq 450\text{MPa}$ :

- $20 \leq R/h \leq 150$

$$\sigma_{web,m}/f_y = \varepsilon[-0.28 - 0.0034(R/h) - 0.05(h/b) - 0.01(h/t)] \quad (2-9)$$

- $75 \leq R/h \leq 150$

$$\sigma_{web,m}/f_y = \varepsilon[-0.73 + 0.0026(R/h) - 0.05(h/b) - 0.01(h/t)] \quad (2-10)$$

Where,  $\varepsilon = \sqrt{f_y/350}$

$$\sigma_{cfl,m}/f_y = -[\sigma_{cfl,m}(1.6 + 0.4(h/b)) + 0.8\sigma_{web,m}(h/b) + \sigma_{cfl,c}(0.2 + 0.4(h/b))] \quad (2-11)$$

Where,  $\sigma_{tfl,m} = 0.15f_y$

### 2.2.3 Material properties

The material properties of roller-bent sections are affected by the induced plastification due to cold-working. The changes are primarily attributed to the Bauschinger effect, which causes a gradually softening response of steel, as well as the strain hardening and strain aging effects, which cause increase of yield stress, ultimate stress and hardness, as well as decrease of ductility and toughness. An experimental investigation on the mechanical properties of roller-bent wide-flange-sections has been performed by Spoorenberg et al. (2012a). Tensile and compressive coupon tests were carried out, on specimens machined from the web and flanges of roller-bent sections and their initial straight counterparts. Specimens of various steel grades, sections and bending radii, were examined (Table 2-5). The specimens were loaded until fracture in the tensile tests, whereas they were loaded up to approximately 2% strain in the compression tests due to the absence of necking phenomenon.

Table 2-5: Coupon tests on roller-bent wide-flange-sections (Spoorenberg et al., 2012a).

Cross-section	Steel grade	Radius (mm)	Bending ratio $R/h$
HE 100A	S235	1910	19.89
HE 100A	S355	1910	19.89
HE 100A	S235	2546	26.52
HE 100A	S355	2546	26.52
HE 100A	S235	3820	39.79
HE 100A	S355	3820	39.79
HE 100B	S235	1910	19.10
HE 100B	S355	1910	19.10
HE 100B	S235	2546	2.55
HE 100B	S355	2546	2.55
HE 100B	S235	3820	3.82
HE 100B	S355	3820	3.82
HE 360B	S235	8000	22.22
HE 360B	S355	8000	22.22
IPE 360	S235	4500	12.50
IPE 360	S355	4500	12.50
IPE 360	S235	8000	22.22
IPE 360	S355	8000	22.22

Overall, non-uniform properties were obtained over the cross-sections of examined specimens. Moreover, it was found that the obtained response was significantly affected by the curving radius and steel grade. The sharp yield point in the stress-strain curve of the straight material was replaced by a gradually softening response due to the Bauschinger effect. Based on the results of coupon tests, an analytical model for estimating the modified mechanical properties of roller-bent wide-flange-sections, was proposed by Spoorenberg et al. (2012b). In this context, a series of equations was developed to estimate the proportional limit, the yield stress, the ultimate tensile stress, as well as the strain at the ultimate tensile stress and at fracture, for the cross-sectional zones shown in Figure 2-11. A parameter  $C$  was introduced, which was calibrated on the experimental data and reflected the relative variation of the yield and ultimate tensile stress within the roller-bent cross-section.

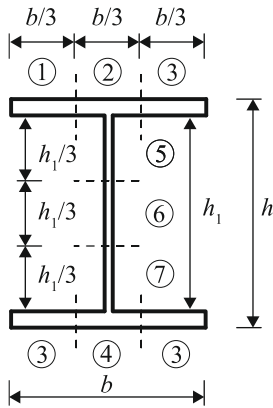


Figure 2-11: Cross-sectional zones  
Spoorenberg et al. (2012b).

Table 2-6: Values of  $C$  parameter.

No.	Cross-sectional zone	S235	S355
1	Top flange tips	0.912	2.75
2	Top flange center	2.98	4.01
3	Bottom flange tips	-1.18	-4.74
4	Bottom flange center	2.23	4.34
5	Top web	1.02	1.52
6	Center web	0	0
7	Bottom web	1.93	0.619

The yield stress  $f_{y,r}$  of roller-bent sections is given as function of the yield stress  $f_{y,s}$  prior to roller-bending, the bending ratio  $R/h$ , and the  $C$  parameter, according to Eq. (2-12).

$$f_{y,r} = \frac{0.559f_{y,s}}{0.559 - C/(R/h)}, \quad \text{for S235 steel grade.} \quad (2-12)$$

$$f_{y,r} = \frac{0.886f_{y,s}}{0.886 - C/(R/h)}, \quad \text{for S355 steel grade.}$$

The proportional limit  $f_{p,r}$  of roller-bent sections can be calculated as function of the yield stress  $f_{y,r}$  and the modulus of elasticity  $E$  according to Eq. (2-13).

$$f_{p,r}/f_{y,r} = -0.701 + 815f_{y,r}/E \leq 1.0, \quad \text{for S235 steel grade.} \quad (2-13)$$

$$f_{p,r}/f_{y,r} = -0.468 + 519f_{y,r}/E \leq 1.0, \quad \text{for S355 steel grade.}$$

The ultimate tensile stress  $f_t$  of both roller-bent and straight members can be calculated as function of the yield stress  $f_y$  and the modulus of elasticity  $E$ , according to Eq. (2-14).

$$f_y/f_t = 0.347 + 234f_y/E \leq 1.0, \quad \text{for S235 steel grade.} \quad (2-14)$$

$$f_y/f_t = 0.121 + 313f_y/E \leq 1.0, \quad \text{for S355 steel grade.}$$

The strain  $\varepsilon_t$  at the ultimate tensile stress of both roller-bent and straight members is given by Eq. (2-15).

$$\varepsilon_t = 0.404 - 160f_y/E, \text{ for S235 steel grade.} \quad (2-15)$$

$$\varepsilon_t = 0.282 - 79.3f_y/E, \text{ for S355 steel grade.}$$

The strain  $\varepsilon_u$  at fracture of both roller-bent and straight members is given by Eq. (2-16).

$$\varepsilon_u = 0.612 - 208f_y/E \geq \varepsilon_t, \text{ for S235 steel grade.} \quad (2-16)$$

$$\varepsilon_u = 0.409 - 70.7f_y/E \geq \varepsilon_t, \text{ for S355 steel grade.}$$

## 2.3 IN-PLANE BEHAVIOR OF ARCHES

### 2.3.1 Elastic stability and ultimate strength

Early studies on the in-plane stability of arches were performed by Timoshenko and Gere (1961) and Austin (1971). In this context, analytical solutions were derived, providing the critical loads for the in-plane buckling of arches comprising various boundary conditions and types of loading. Indicative values of distributed loads and horizontal reactions of three-hinged, two-hinged and fixed symmetric arches are given in Table 2-7 (Timoshenko and Gere, 1961). The critical values refer to circular arches of rise-to-span ratios from 0.10 to 0.50 under pure axial compression load. The fundamental buckling modes of the examined cases are depicted in Figure 2-12. In the case of three-hinged arches, the critical buckling mode is typically symmetric, while buckling of fixed and two-hinged arches is typically dominated by an anti-symmetrical mode in which the arch sways laterally.

Table 2-7: Critical load and horizontal reaction for circular arches under pure compression.

$h/L$	Three-Hinged Arch		Two-Hinged Arch		Fixed Arch	
	$qL^3/EI$	$HL^2/EI$	$qL^3/EI$	$HL^2/EI$	$qL^3/EI$	$HL^2/EI$
0.10	22.2	26.7	28.4	34.1	58.9	70.7
0.20	33.5	17.6	39.3	20.6	90.4	47.5
0.30	34.9	9.3	40.9	10.9	93.4	24.9
0.40	30.2	3.4	32.8	3.7	80.7	9.1
0.50	24.0	0.0	24.0	0.0	64.0	0.0

where:  $h$ , rise;  $L$ , span;  $q$ , critical load;  $H$ , critical horizontal reaction at supports;  $E$ , Young's modulus of elasticity;  $I$ , cross-sectional moment of inertia.

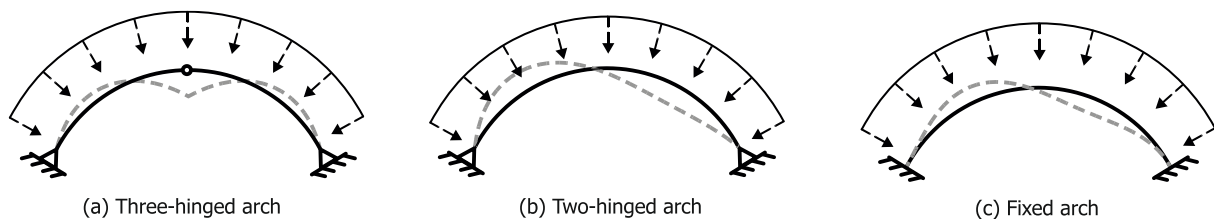


Figure 2-12: Typical fundamental buckling mode shapes.



Research on the in-plane stability of arches has been extensive during the last few decades (Harries, 1970; Kuranishi and Lu, 1972; Kuranishi et al., 1980; Jukes et al., 1983; Yabuki and Vinnakota, 1984; Rajasekaran and Padmanabhan, 1989; Mitri and Hassani, 1990; Khan et al., 1996; Pi and Trahair, 1999). Pi et al. (2002) studied the in-plane non-linear buckling of circular arches of arbitrary cross-section that are subjected to a radial load distributed uniformly around the arch axis. Bradford et al. (2002) investigated the in-plane non-linear buckling of circular arches of arbitrary cross-section that are subjected to a central concentrated radial load. Moreover, Pi et al. (2007) investigated the in-plane non-linear elastic behavior and stability of elastically supported shallow circular arches that are subjected to a radial uniform load. Dimopoulos and Gantes (2008) studied the in-plane behavior of circular arches with circular-hollow-sections, examining the effects of a number of design parameters, such as the boundary conditions, the rise-to-span ratio, and the included angle. Pi et al. (2008) investigated the non-linear in-plane analysis and buckling of arches with elastic rotational end restraints under a central concentrated load. Pi and Bradford (2009) derived analytical solutions for the non-linear post-buckling of these arches under uniform radial loading. These investigations were focused on arches having symmetrical boundary conditions. Pi and Bradford (2012) studied the non-linear elastic in-plane buckling and post-buckling behavior of pin-ended shallow circular arches with various boundary conditions under radial and central concentrated loads. Analytical solutions for the non-linear in-plane buckling and post-buckling behavior and for the buckling loads were derived. The in-plane ultimate resistance of steel arches with sinusoidal corrugated webs, under a full-span uniform vertical load was examined by Guo et al. (2016), by means of experimental tests and numerical simulations. An integral equation solution to the linear and geometrically nonlinear problem of non-uniform in-plane shallow arches under a central concentrated force was presented by Tsiatas and Babouskos (2017). An experimental and numerical investigation into the in-plane buckling and ultimate resistance of circular steel arches was performed by Lu et al. (2017). The collapse behavior of a non-uniform circular shallow arch was analytically studied for both fixed and pinned boundary conditions by Yan et al. (2018). The behavior of prestressed high strength steel arched trusses was evaluated by Afshan et al. (2019) by means of experimental tests and numerical simulations, resulting in the development of design recommendations.

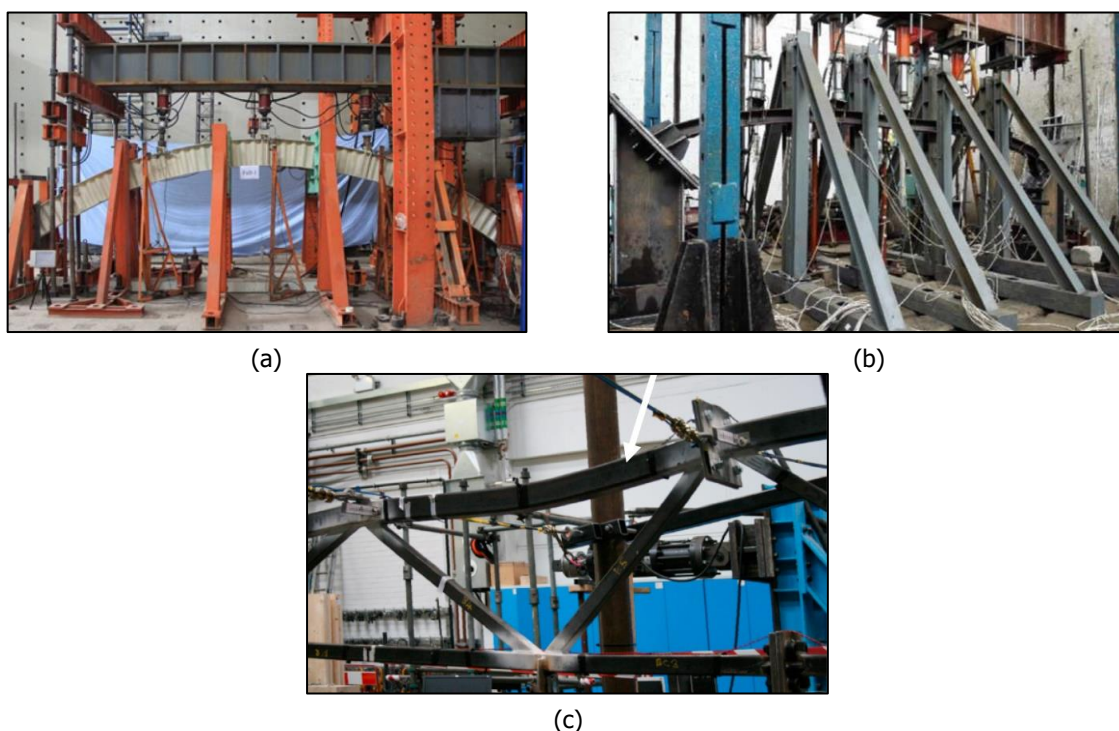


Figure 2-13: Experimental studies of (a) Guo et al (2016), (b) Lu et al. (2017), and (c) Afshan et al. (2019).



### 2.3.2 Design recommendations

Design procedures for arches based on the ultimate inelastic strength studies have been proposed by Kuranishi (1973), Komatsu and Shinke (1977), and Kuranishi and Yabuki (1984). Kuranishi (1973) proposed an interaction-type formula similar to beam-column formulas for two-hinged parabolic arches under unsymmetrical loading. Komatsu and Shinke (1977) presented practical formulas for the planar ultimate-load intensity of two-hinged and fixed parabolic steel arches that are a function of the normal thrust calculated at a quarter point of the arch rib by first-order elastic analysis. They also recommended that the ultimate load capacity of arch ribs with varying and/or hybrid cross section can be evaluated accurately by using mean values of the cross-sectional area and/or yield-stress level of the material, which would be calculated by averaging along the entire axial length of the rib. Kuranishi and Yabuki (1984) also presented accurate practical formulas for the in-plane ultimate strength of parabolic two-hinged steel arch ribs and steel arch bridge structures with a stiffening girder. Sakimoto and Watanabe (1995) proposed a design procedure based on nonlinear analysis that proportions each member automatically, so as to meet the ultimate-strength requirements of the complete structural system. The procedure is based on the tangent-modulus method and eigenvalue analysis. Pi and Trahair (1999) and Pi and Bradford (2004) proposed interaction equations for the design of hinged and fixed circular arches with I-shape cross sections, considering the presence of initial geometric imperfections and residual stresses. Dimopoulos and Gantes (2008) proposed a series of appropriate modification factors for the design of circular steel arches of circular-hollow-sections, that could be included in the Eurocode interaction equations in order to improve their accuracy.

## 2.4 OUT-OF-PLANE BEHAVIOR OF ARCHES

### 2.4.1 Elastic stability and ultimate strength

Early studies on the out-of-plane stability of arches were performed by Timoshenko & Gere (1961), providing the critical loads of arches comprising various boundary conditions and types of loading. The closed-form solutions were extended by Vlasov (1963) in order to include the warping rigidity in the case of double symmetric cross sections. The elastic buckling of freestanding arches subjected to a uniformly distributed load was further investigated by Namita (1968). Finite element analyses on both free-standing and braced arches subjected to a uniformly distributed vertical load were performed by Komatsu and Sakimoto (1977), Sakimoto and Komatsu (1983). Numerical results were compared to relevant experimental results carried out by Sakimoto et al. (1979). Analytical solutions for the out-of-plane buckling loads of arches were obtained by Papangelis and Trahair (1987), Rajasekaran and Padmanabhan (1989), Yang and Kuo (1986, 1987, 1991), Pi and Trahair (1998) and Pi and Bradford (2005). Bradford and Pi (2006) investigated the elastic buckling of laterally fixed steel arches under uniform bending. Pi et al. (2010), obtained the analytical solutions for the lateral-torsional buckling load of circular steel pin-ended arches subjected to a central concentrated load. An experimental investigation of the elastic-plastic out-of-plane buckling response of roller-bent circular steel arches comprising wide-flange-sections and subjected to a single force applied to the crown, was carried out by La Poutré et al. (2013). Finite element simulations of pertinent tests were performed by Spoorenberg et al. (2012c), considering reliably the effects of roller-bending on the residual stresses, geometric imperfections and the change in the material properties. An experimental study on the out-of-plane inelastic buckling behavior of fixed circular steel I-section arches under symmetric three-point loading and non-symmetric two-point loading was carried out by Guo et al. (2015). In this context, a pertinent numerical model was developed and validated against the test results. Experimental and numerical investigations on the out-of-plane ultimate resistance of parallel twin-arch under uniform radial load were performed by Huang et al. (2019).

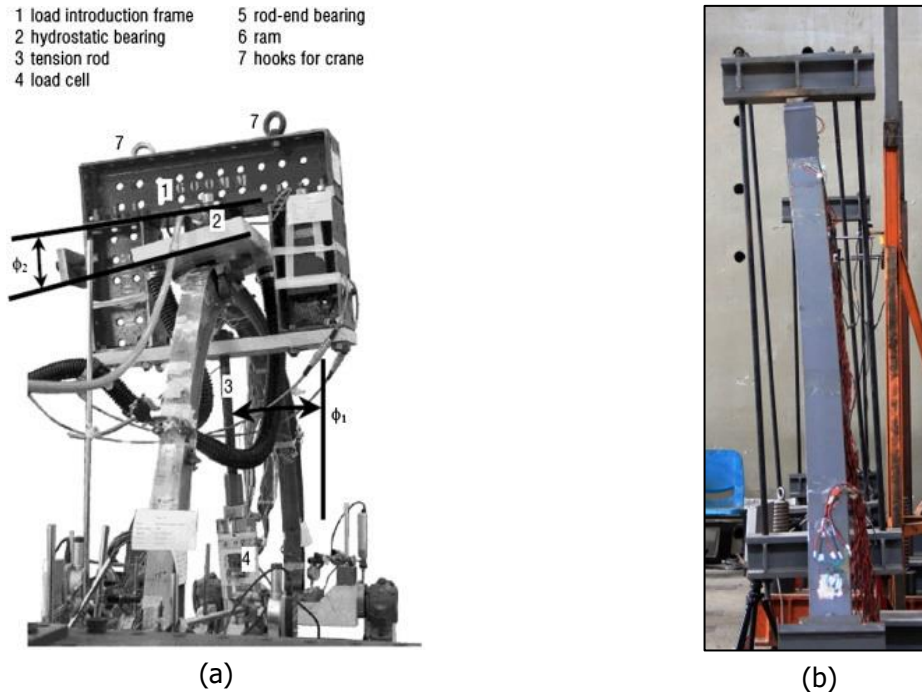


Figure 2-14: Experimental studies of (a) La Poutré et al. (2013) and (b) Guo et al. (2015).

### 2.4.2 Design recommendations

Design recommendations for the out-of-plane stability of freestanding circular arches of I-sections were provided by Pi and Trahair (1998) and Pi and Bradford (2005). In this context, appropriate interaction equations were proposed, including the effects of imperfections and residual stresses. La Poutré (2005) investigated the inelastic out-of-plane stability of roller-bent arches, comprising wide-flange-sections. It was shown that the general method of Eurocode 3 part 1-1 (CEN, 2005), is an accurate method for assessing the inelastic stability of arches in case that no closed-form buckling equations are available. Design rules for roller-bent arches comprising wide-flange-sections were proposed by Spoorenberg et al. (2012c). Appropriate column curve diagrams associated with suitable imperfection parameters were derived to check the out-of-plane buckling response of a roller-bent steel arches.

## 2.5 CONCLUSIONS

An overview of the existing literature regarding the structural behavior of steel arches was presented in this section, with emphasis on the residual stresses and material properties of roller-bent members, elastic and inelastic stability issues, along with pertinent design recommendations. Even though the spatial stability of arches has been investigated thoroughly in the literature, limited research work is found on the residual stresses and the mechanical properties emanating from the fabrication process, as well as their influence on the buckling resistance. Pertinent research studies are available only for wide-flange-section arches, in which the importance of such parameters is highlighted. The present doctoral thesis aims at bridging this gap, by investigating the structural behavior of roller-bent arches comprising hollow sections. In this way, it intends to provide guidance for the analysis and design of arches by (a) quantifying the residual stresses and deformations encountered in roller-bent hollow sections in terms of their distribution and amplitude, and (b) assessing the influence of such imperfections on their structural behavior. In order to achieve this goal, a combined experimental, numerical and analytical methodology is implemented.

**REFERENCES**

- Afshan, S., Theofanous, M., Wang, J., Gkantou, M., and Gardner, L. (2019). "Testing, numerical simulation and design of prestressed high strength steel arched trusses." *Engineering Structures*, vol. 183, pp. 510–522.
- Austin, W. J. (1971). "In-Plane Bending and Buckling of Arches." *ASCE J. Struct. Div.*, vol. 97, pp. 1575–1592.
- Beedle, L. S. (Ed.) (1991). *Stability of Metal Structures, a World View*. 2<sup>nd</sup> ed., Structural Stability Research Council, Bethlehem, PA.
- Bjorhovde, R. (2006). "Cold Bending of Wide-Flange Shapes for Construction." *Engineering Journal*, vol. 4, pp. 271–286.
- Bradford, M. A., and Pi, Y. (2002). "Elastic Flexural-Torsional Buckling of Discretely Restrained Arches." *ASCE J. Struct. Eng.*, vol. 128, pp. 719–727.
- Bradford, M. A., and Pi, Y. (2006). "Flexural – torsional buckling of fixed steel arches under uniform bending." *Journal of Constructional Steel Research*, vol. 62, pp. 20–26.
- CEN (2005). *Eurocode 3: Design of Steel Structures, Part 1-1: General Rules and Rules for Buildings, EN 1993-1-1*. Comité Européen de Normalisation (CEN), European Committee for Standardization Brussels, Belgium.
- Chiew, S.P., Jin, Y.F. and Lee, C.K. (2016). "Residual Stress Distribution of Roller Bending of Steel Rectangular Structural Hollow Sections." *Journal of Constructional Steel Research*, vol. 119, pp. 85–97.
- Dimopoulos, C. A., and Gantes, C. J. (2008). "Nonlinear in-plane behavior of circular steel arches with hollow circular." *Journal of Constructional Steel Research*, vol. 64, pp. 1436–1445.
- Dowswell, B. (2018). *Curved Member Design*. American Institute of Steel Construction, Chicago, IL.
- ECCS (1976). *Manual on Stability of Steel Structures*. European Convention for Constructional Steelwork, Liege, Belgium.
- ECCS (1984). *Ultimate limit state calculation of sway frames with rigid joints*. Technical Committee 8 – Structural Stability Technical Working Group 8.2, Publication No. 33, Paris.
- Fukumoto, Y. (1996). *Structural Stability Design, Steel and Composite Structures*. Pergamon, Amsterdam.
- Guo, Y., Chen, H., Pi, Y., and Andrew, M. (2016). "In-plane strength of steel arches with a sinusoidal corrugated web under a full-span uniform vertical load: Experimental and numerical investigations." *Engineering Structures*, vol. 110, pp. 105–115.
- Guo, Y., Zhao, S., Pi, Y., Andrew, M., and Dou, C. (2015). "An experimental study on out-of-plane inelastic buckling strength of fixed steel arches." *Engineering Structures*, vol. 98, pp. 118–127.
- Hansen, N.E. and Jannerup, O. (1979). "Modeling of elastic-plastic bending of beams using a roller bending machine." *Journal of Engineering for Industry Transactions of ASME*, vol. 101, pp. 304–310.
- Harries, H. (1970). "Traglast stahlerner Zweigelenkbogen mit ausgebreiteten Fließzonen." *Stahlbau*, Vol. 6, pp. 170–177; vol. 8, pp. 2.
- Hayashi, T. (Ed.) (1971). *Handbook of Structural Stability*. Corona Publishing, Tokyo.

- Huang, Y., Liu, A., Zhu, C., Lu, H., and Gao, W. (2019). "Experimental and numerical investigations on out-of-plane ultimate resistance of parallel twin-arch under uniform radial load." *Thin Walled Structures*, vol. 135, pp. 147–159.
- Jukes, S. G., Hassani, F. P., and Whittaker, B. N. (1983). "Characteristics of Steel Arch Support Systems for the Mine Roadway, Part I, Modelling Theory, Instrumentation and Preliminary Results." *Mining Sci. Technol.*, vol. 1, pp. 43–58.
- Kennedy, J.B, Seddeik, M. and Brady, F. (1986). "Deformations in Cold-Bent HSS Members." *Engineering AISC*, vol. 23, pp. 117–123.
- Kennedy, J.B. (1988). *Design Aids - Minimum Bending Radii for Square and Rectangular Hollow Structural Sections Subjected to Cold Bending*. CIDECT Report 11C-88-14-E, CIDECT.
- Khan, U. H., Mitri, H. S., and Jones, D. (1996). "Full Scale Testing of Steel Arch Tunnel Supports." *Int. J. Rock Mech. Min.*, vol. 33, pp. 219–232.
- King, C., and Brown, D. (2001). *Design of Curved Steel*. The Steel Construction Institute, Berkshire, UK.
- Komatsu, S., and Sakimoto, T. (1977). "Ultimate Load Carrying Capacity of Steel Arches." *ASCE J. Struct. Div.*, vol. 103, pp. 2323–2336.
- Komatsu, S., and Shinke, T. (1977). "Practical Formulas for In-Plane Load Carrying Capacity of Arches." *Proc. Jpn. Soc. Civ. Eng.*, No. 267, pp. 39–51 (in Japanese).
- Kuranishi, S. (1973). "Allowable Stress for Two-Hinged Steel Arch." *Proc. Jpn. Soc. Civ. Eng.*, No. 213, pp. 71–75.
- Kuranishi, S., and Lu, L. W. (1972). "Load Carrying Capacity of Two-Hinged Steel Arches." *Proc. Jpn. Soc. Civ. Eng.*, No. 204, pp. 129–140 (in English).
- Kuranishi, S., and Yabuki, T. (1984). "Lateral Load Effect on Arch Bridge Design." *ASCE J. Struct. Eng.*, Vol. 110, No. 9, pp. 2263–2274.
- Kuranishi, S., Sato, T., and Otsuki, M. (1980). "Load Carrying Capacity of Two-Hinged Steel Arch Bridges with Stiffening Deck." *Proc. Jpn. Soc. Civ. Eng.*, No. 300, pp. 121–130.
- La Poutré, D. B. (2005). "*Inelastic Spatial Stability of Circular Steel Wide Flange Arches*." Ph.D. thesis, Technische Universiteit Eindhoven, Eindhoven, The Netherlands.
- La Poutré, D. B. La, Spoorenberg, R. C., Snijder, H. H., and Hoenderkamp, J. C. D. (2013). "Out-of-plane stability of roller bent steel arches - An experimental investigation." *Journal of Constructional Steel Research*, vol. 81, pp. 20–34.
- Lu, Y., Cheng, Y., and Han, Q. (2017). "Experimental investigation into the in-plane buckling and ultimate resistance of circular steel arches with elastic horizontal and rotational end restraints." *Thin Walled Structures*, vol. 118, pp. 164–180.
- Mitri, H. S., and Hassani, F. P. (1990). "Structural Characteristics of Coal Mine Steel Arch Supports," *Int. J. Rock Mech. Min.*, vol. 27, pp. 121–127.
- Namita, Y. (1968). "Second Order Theory of Curved Bars and Its Use in the Buckling Problem of Arches," *Trans. Jpn. Soc. Civ. Eng.*, No. 155, pp. 32–41 (in German).
- Papangelis, J. P., and Trahair, N. S. (1987). "Flexural-Torsional Buckling of Arches," *ASCE J. Struct. Eng.*, vol. 113, pp. 889–906.

- Pi, Y., and Bradford, M. A. (2009). "Non-linear in-plane postbuckling of arches with rotational end restraints under uniform radial loading." *International Journal of Non-Linear Mechanics*, vol. 44, pp. 975–989.
- Pi, Y., and Bradford, M. A. (2012). "Non-linear buckling and postbuckling analysis of arches with unequal rotational end restraints under a central concentrated load." *International Journal of Solids and Structures*, vol. 49, pp. 3762–3773.
- Pi, Y., Bradford, M. A., and Tin-loi, F. (2007). "Nonlinear analysis and buckling of elastically supported circular shallow arches." *International Journal of Solids and Structures*, vol. 44, pp. 2401–2425.
- Pi, Y., Bradford, M. A., and Tin-loi, F. (2008). "Non-linear in-plane buckling of rotationally restrained shallow arches under a central concentrated load." *International Journal of Non-Linear Mechanics*, vol. 43, pp. 1–17.
- Pi, Y., Bradford, M. A., and Tong, G. (2010). "Elastic lateral – torsional buckling of circular arches subjected to a central concentrated load." *International Journal of Mechanical Sciences*, vol. 52, pp. 847–862.
- Pi, Y., Bradford, M. A., and Uy, B. (2002). "In-plane stability of arches." *International Journal of Solids and Structures*, vol. 39, pp. 105–125.
- Pi, Y.-L., and Bradford, M. A. (2004). "In-Plane Strength and Design of Fixed Steel I-Section Arches." *Eng. Struct.*, vol. 26, pp. 291–301.
- Pi, Y.-L., and Bradford, M. A. (2005). "Out-of-Plane Strength Design of Fixed Steel I-Section Arches." *ASCE J. Struct. Eng.*, vol. 131, pp. 560–568.
- Pi, Y.-L., and Trahair, N. S. (1998). "Out-of-Plane Inelastic Buckling and Strength of Steel Arches," *ASCE J. Struct. Eng.*, vol. 124, pp. 174–183.
- Pi, Y.-L., and Trahair, N. S. (1999). "In-Plane Buckling and Design of Steel Arches." *ASCE J. Struct. Eng.*, vol. 125, pp. 1291–1298.
- Rajasekaran, S., and Padmanabhan, S. (1989). "Equations of Curved Beams." *ASCE J. Eng. Mech.*, vol. 115, pp. 1094–1110.
- Sakimoto, T., and Komatsu, S. (1983). "Ultimate Strength Formula for Steel Arches." *ASCE J. Struct. Div.*, vol. 109, pp. 613–627.
- Sakimoto, T., and Watanabe, H. (1995). "A New Procedure for Frame Design." *Proc. SSRC Annual Tech. Session*, Pittsburgh, PA, pp. 23–31.
- Sakimoto, T., Yamao, T., and Komatsu, S. (1979). "Experimental Study on the Ultimate Strength of Steel Arches." *Proc. Jpn. Soc. Civ. Eng.*, No. 286, pp. 139–149.
- Schafer, B. W., and Pekoz, T. (1998). "Computational Modeling of Cold-Formed Steel: Characterizing Geometric Imperfections and Residual Stresses." *J. Constr. Steel Res.*, vol. 47, pp. 193–210.
- Singer, J., Arbocz, J., and Weller, T. (1998). *Buckling Experiments: Experimental Methods in Buckling of Thin-Walled Structures*. J Wiley, New York.
- Spoorenberg, R. C., Snijder, H. H., and Hoenderkamp, J. C. D. (2010). "Experimental investigation of residual stresses in roller bent wide flange steel sections." *Journal of Constructional Steel Research*, vol. 66, pp. 737–747.

- Spoorenberg, R. C., Snijder, H. H., and Hoenderkamp, J. C. D. (2011a). "Finite element simulations of residual stresses in roller bent wide flange sections." *Journal of Constructional Steel Research*, vol. 67, pp. 39–50.
- Spoorenberg, R. C., Snijder, H. H., and Hoenderkamp, J. C. D. (2011b). "Proposed Residual Stress Model for Roller Bent Steel Wide Flange Sections," *Journal of Constructional Steel Research*, vol. 67, pp. 992–1000.
- Spoorenberg, R. C., Snijder, H. H., and Hoenderkamp, J. C. D. (2012a). "Mechanical Properties of Roller Bent Wide Flange Sections—Part 1: Experimental Investigation," *Journal of Constructional Steel Research*, vol. 68, pp. 51–62.
- Spoorenberg, R. C., Snijder, H. H., and Hoenderkamp, J. C. D. (2012b). "Mechanical Properties of Roller Bent Wide Flange Sections - Part 2: Prediction Model." *Journal of Constructional Steel Research*, vol. 68, pp. 63–77.
- Spoorenberg, R. C., Snijder, H. H., Hoenderkamp, J. C. D., and Beg, D. (2012c). "Design rules for out-of-plane stability of roller bent steel arches with FEM." *Journal of Constructional Steel Research*, vol. 79, pp. 9–21.
- Timoshenko, S. P. (1956). *Strength of Materials Part II - Advanced Theory and Problems*, 3<sup>rd</sup> Ed., D. Van Nostrand Company, New York, NY.
- Timoshenko, S. P., and Gere, J. M. (1961). *Theory of Elastic Stability*. 2<sup>nd</sup> ed., McGraw-Hill, New York.
- Tsiatas, G. C., and Babouskos, N. G. (2017). "Linear and geometrically nonlinear analysis of non-uniform shallow arches under a central concentrated force." *International Journal of Non-Linear Mechanics*, vol. 92, pp. 92–101.
- Vlasov, V. Z. (1963). *Thin Walled Elastic Beams*, 2<sup>nd</sup> ed., Israel Program for Scientific Translations, Jerusalem.
- Yabuki, T., and Vinnakota, S. (1984). "Stability of Steel Arch-Bridges, A State-of-the-Art Report." *Solid Mech. Arch.*, Vol. 9, No. 2, Martinus Nijhoff Publishers, The Hague, The Netherlands.
- Yan, S., Shen, X., Chen, Z., and Jin, Z. (2018). "Collapse behavior of non-uniform shallow arch under a concentrated load for fixed and pinned boundary conditions." *International Journal of Mechanical Sciences*, vol. 137, pp. 46–67.
- Yang, Y. B., and Kuo, S. R. (1986). "Static Stability of Curved Thin-Walled Beams," *ASCE J. Eng. Mech*, vol. 112, pp. 821–841.
- Yang, Y. B., and Kuo, S. R. (1987). "Effect of Curvature on Stability of Curved Beams." *ASCE J. Struct. Eng.*, vol. 113, pp. 1185–1202.
- Yang, Y. B., and Kuo, S. R. (1991). "Use of Straight-Beam Approach to Study Buckling of Curved Beams." *ASCE J. Struct. Eng.*, vol. 117, pp. 1963–1978.
- Ziemian, R. D. (Ed.) (2010). *Guide to Stability Design Criteria for Metal Structures*. John Wiley & Sons, Inc., United States of America.

## 3 EXPERIMENTAL TESTS

### 3.1 INTRODUCTION

Several experimental studies regarding the spatial stability of arches are reported in the literature. Early experiments on aluminum arches were carried out by Stüssi (1944), Kee (1961), Tokarz (1971), as well as Di Tommaso and Viola (1976), aiming at verifying theoretical solutions based on the linear buckling theory. Papangelis and Trahair (1987) performed flexural-torsional buckling tests on roller-bent arches of aluminum I-sections, and pertinent results were compared to previous analytical solutions. An experimental study on the spatial stability of arches comprising twin-arch ribs of welded box-sections was carried out by Sakimoto et al. (1979). Sakata and Sakimoto (1990) investigated experimentally the out-of-plane buckling resistance of twin-arch ribs comprising welded I-sections. Out-of-plane buckling tests on steel arches of roller-bent and welded I-sections were carried out by La Poutré et al. (2013) and Guo et al. (2015), respectively. Furthermore, Guo et al. (2016) tested the in-plane stability of steel arches comprising welded I-section with corrugated webs. Lu et al. (2017) carried out experimental tests to study the in-plane buckling resistance of roller-bent I-section arches. Recent experimental investigations on the out-of-plane buckling of twin-arch ribs of roller-bent Circular-Hollow-Sections were carried out by Huang et al. (2019).

In this chapter, a state-of-the-art experimental study on the in-plane behavior of roller-bent arches comprising Rectangular-Hollow-Sections (RHS) is presented. Scope of the experimental tests was to investigate the effects of roller-bending on the structural behavior of RHS arches, as well as to employ the experimental results as basis for calibration of pertinent numerical models (c.f. Chapter 4). Twelve roller-bent specimens, grouped in two sets of curvatures, were examined under compression and tension loading. Appropriate dimension measurements were undertaken, aiming at evaluating the encountered geometric imperfections of specimens due to roller-bending. The material properties were obtained through tensile coupon tests, machined prior to the curving process, in order to exclude the effects of roller-bending on steel properties. An appropriate layout was employed for the execution of the experimental tests, including configurations for the support and loading of arches. Measuring devices were installed on each specimen, in order to capture the developed displacements and deformations during the testing procedure. The experimental tests were carried out at the Institute of Steel Structures in the National Technical University of Athens by Dr. Cyril E. Douthe and Dr. Xenofon A. Lignos under the supervision of Prof. Charis J. Gantes.

## 3.2 DESCRIPTION OF EXPERIMENTS

### 3.2.1 Test specimens

A total number of 12 circular steel arches (Figure 3-1) were tested at the Institute of Steel Structures in the School of Civil Engineering of the National Technical University of Athens. The curving process was carried out at EMEK SA facilities, using a roller-bending machine of roller diameter equal to 300mm and distance of the outer-roller centers equal to 900mm. Cold-formed RHS 50x100x5mm sections of S355 steel quality were employed in all specimens, exhibiting the longitudinal weld at the bottom wide-flange. The arches were curved about their weak axis in order to exhibit high out-of-plane stiffness. The first set of six arches were designed with radii of curvature equal to 3.71m (referred thereafter as high arches), while the second set of six arches were designed with radii of curvature equal to 4.10m (referred thereafter as shallow arches). Both high and shallow arches were designed to cover the same horizontal span of 4725mm. Three compression and three tension tests were performed for each set, as summarized in Table 3-1.



Figure 3-1: Arch specimens.

Table 3-1: Experimental tests.

No.	Arch	Test
Sp. 1	High	Compression
Sp. 2	High	Compression
Sp. 3	High	Tension
Sp. 4	High	Compression
Sp. 5	High	Tension
Sp. 6	High	Tension
Sp. 7	Shallow	Tension
Sp. 8	Shallow	Compression
Sp. 9	Shallow	Compression
Sp. 10	Shallow	Compression
Sp. 11	Shallow	Tension
Sp. 12	Shallow	Tension

Steel arches manufactured by the roller-bending method usually exhibit large geometric imperfections and a non-ideally uniform curvature. Six measurements were undertaken in each arch in order to evaluate the exact dimensions of the specimens, including the length of the horizontal span ( $L$ ), as well as the height at five locations along the member ( $h_1-h_5$ ), as is shown in Figure 3-2. The measured dimensions of the high and shallow arches are summarized in Table 3-2 and Table 3-3 along with the corresponding theoretical dimensions. The mean horizontal span was found approximately 7mm longer for the high arches and 13mm shorter for the shallow arches, compared to the theoretical one, while the mean middle-height was found 3mm larger and 13mm shorter for the high and shallow arches respectively. A maximum difference of approximately 9mm between the heights of the first and second semi-span of the arches was also observed, demonstrating a loss of symmetry. The best fitting radius and the deriving deviations of each specimen's curvature are presented in Table 3-4 and Table 3-5, by employing the least square method. The average fitting radii of the high and shallow arches were estimated equal to 3.73m and 4.03m, respectively.



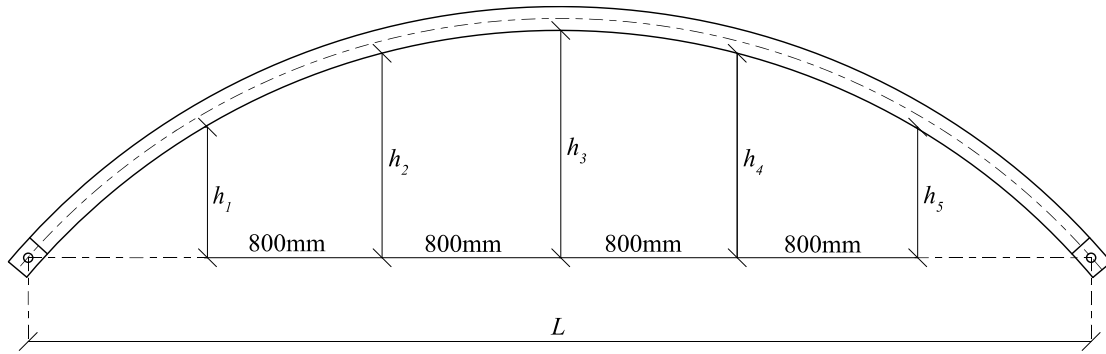


Figure 3-2: Dimension measurements of test specimens.

Table 3-2: High arches dimensions.

Arch	$L$ (mm)	$h_1$ (mm)	$h_2$ (mm)	$h_3$ (mm)	$h_4$ (mm)	$h_5$ (mm)
Sp. 1	4726	453	735	825	736	454
Sp. 2	4738	449	723	811	728	454
Sp. 3	4737	458	730	815	729	456
Sp. 4	4734	453	734	821	728	452
Sp. 5	4730	455	732	827	737	458
Sp. 6	4728	467	740	832	739	464
Average	4732	456	732	822	733	456
Theoretical	4725	459	737	825	737	459

Table 3-3: Shallow arches dimensions.

Arch	$L$ (mm)	$h_1$ (mm)	$h_2$ (mm)	$h_3$ (mm)	$h_4$ (mm)	$h_5$ (mm)
Sp. 7	4709	406	654	736	652	401
Sp. 8	4706	409	659	739	661	407
Sp. 9	4725	403	648	723	643	394
Sp. 10	4716	400	659	740	659	402
Sp. 11	4707	402	659	744	660	398
Sp. 12	4711	405	657	739	654	401
Average	4712	404	656	737	655	401
Theoretical	4725	397	645	724	645	397

Table 3-4: Best fitting radii and deviations of high arches.

Arch	Best fitting radius (mm)	St. deviation (mm)	Min. deviation (mm)	Max. deviation (mm)
Sp. 1	3708	2.6	-3.6	2.7
Sp. 2	3776	2.1	-2.7	3.3
Sp. 3	3761	1.1	-1.2	1.8
Sp. 4	3733	2.9	-3.0	3.0
Sp. 5	3700	3.0	-3.9	3.9
Sp. 6	3700	2.4	-2.9	3.6
Average	3730	2.4	-2.9	3.0

Table 3-5: Best fitting radii and deviations of shallow arches.

Arch	Best fitting radius (mm)	St. deviation (mm)	Min. deviation (mm)	Max. deviation (mm)
Sp. 7	4031	2.3	-2.4	4.3
Sp. 8	4007	2.3	-2.5	3.3
Sp. 9	4109	3.4	-2.6	5.6
Sp. 10	4014	1.9	-3.3	1.5
Sp. 11	3986	2.8	-4.7	2.9
Sp. 12	4022	1.8	-2.4	2.1
Average	4028	2.4	-3.0	3.3

### 3.2.2 Experimental setup

An appropriate layout was designed for the execution of the experimental tests, including configurations for the support and loading of the specimens. The arch specimens were hinged to the laboratory testing frame using pins at both ends. All arches were reinforced locally at their ends, by welding 10mm thick plates at the webs of RHS, in order to avoid local yielding in the vicinity of pivot axes. The distance between the hinges was designed to be 4725mm in all tests, but the actual span differed between specimens, as described in the previous section. Therefore, a suitable displacement was imposed at the one arch's end, through a temporary sliding system, in order to bring the hinge to the proper position before placement of pins. Lateral supports were placed at the thirds of the span in order to prevent the occurrence of out-of-plane buckling. Their inner face was covered by Teflon™ foils in order to reduce the friction between arches and lateral supports. The employed test configuration and the hinge assembly are shown in Figure 3-3 and Figure 3-4, respectively. Compression and tension tests were performed using a 300kN hydraulic actuator with a maximum stroke (STR) of 300mm. The load was imposed to the arch crown through a 30mm thick loading plate, on which half of a cylinder with diameter 48mm was welded (referred thereafter as loading cylinder). In the compression test configuration, the loading plate was fixed directly to the actuator by bolts, whereas in the tension test configuration, it was attached to the actuator through four rods. A view of the loading plates used in both cases is shown in Figure 3-5.

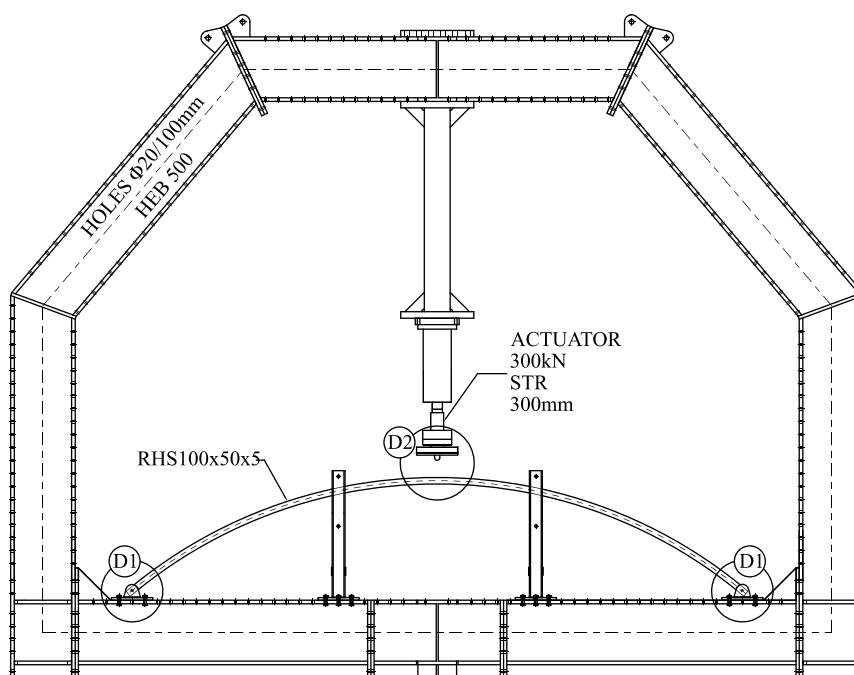


Figure 3-3: Laboratory testing frame and test configuration.

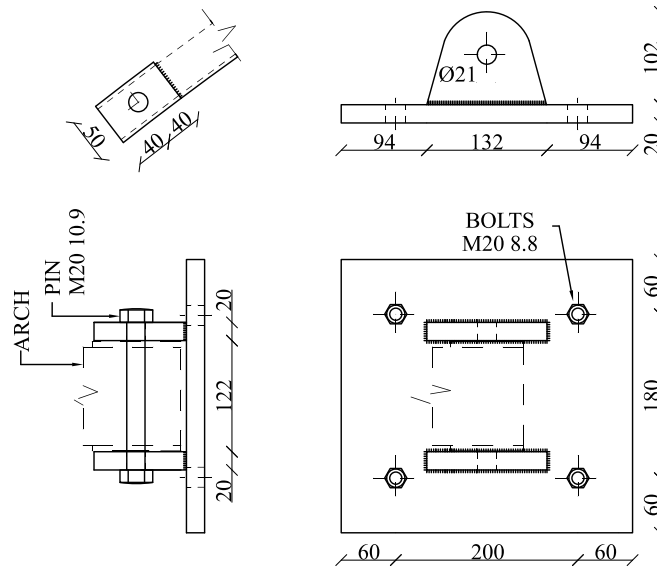


Figure 3-4: Views of the hinge support (detail D1).

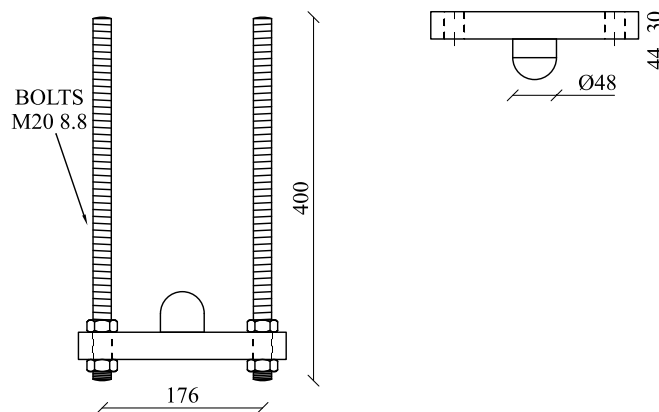


Figure 3-5: Views of the loading plates (detail D2) for the tension (left) and compression (right) tests.

### 3.2.3 Measuring devices

The imposed displacement and reaction force were measured by a displacement-cell and a load-cell respectively, mounted on the actuator's head. Three Individual Linear Variable Differential Transformers (LVDTs) were installed in each specimen to measure the vertical displacement at a distance of 150mm on the left of the crown and capture any possible torsional rotation. Two inclined LVDTs, located at a horizontal distance of 700mm from both arch's ends, were also employed to measure deflections (perpendicular to the cross-section) in the opposite direction of that at crown. Four Strain Gauges (SGs) consisting of two 90° tee rosettes and two linear gauges, were set on each specimen in order to measure the developed longitudinal and transverse strains at a cross-section located 150mm on the right of the crown. The two rosettes were placed in the middle of the top and bottom flanges, while the two linear gauges were placed on the top flange edges, in order to assess the uniformity of the stress distribution. The experimental set-up and the employed measuring devices are depicted in Figure 3-6 and Figure 3-7, respectively.

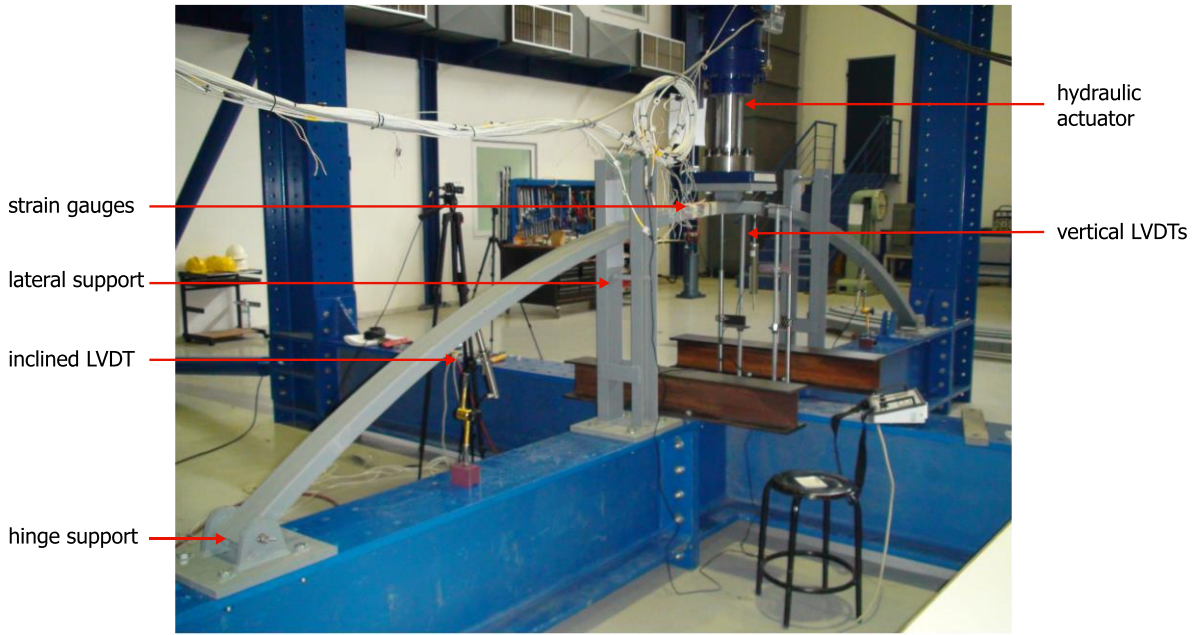
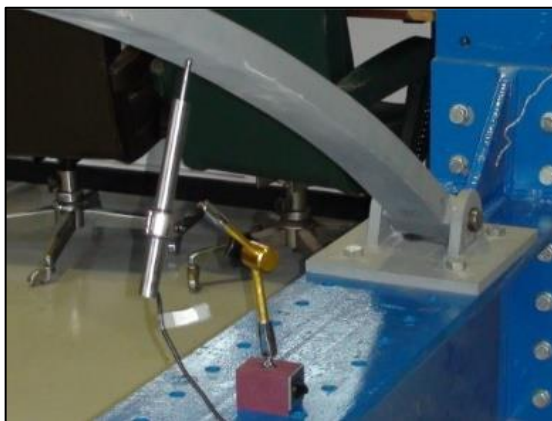
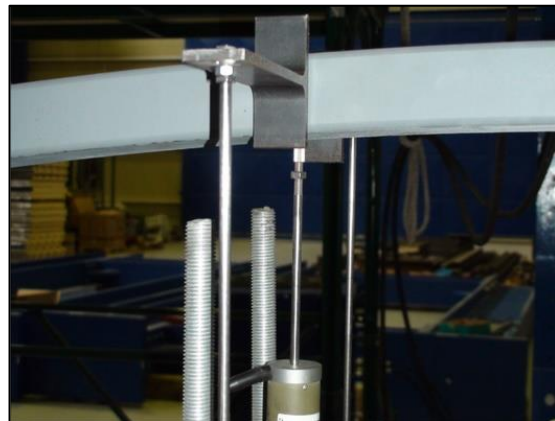


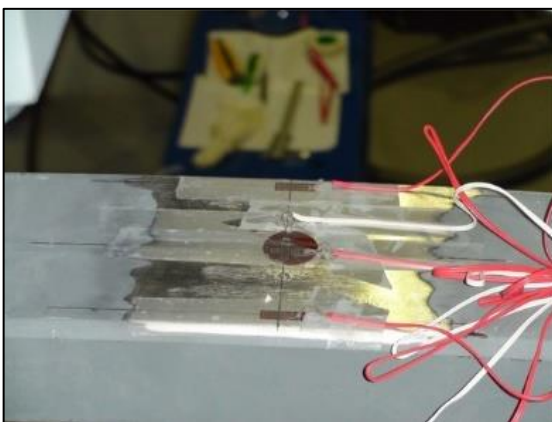
Figure 3-6: View of the experimental set-up and the measuring devices.



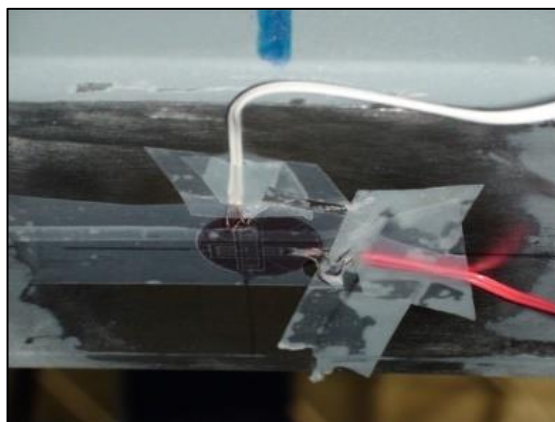
(a) Inclined LVDT



(b) Vertical LVDTs



(c) Top-flange strain gauge



(c) Bottom-flange strain gauge

Figure 3-7: Detailed views of measuring devices.

### 3.2.4 Testing procedure

The forthcoming loading protocol was implemented in the displacement-controlled tests: a first loading step up to 20mm followed by an unloading step back to 10mm were performed before the final loading up to 80mm and 95mm for the tension and the compression tests, respectively. The magnitude of the maximum displacement was sufficient for reaching the ultimate bearing capacity of the arches, while the small cycle between 10mm and 20mm was aimed at remaining in the domain that clearances do not influence the experimental results.

### 3.3 MATERIAL PROPERTIES

The material properties of the test specimens were obtained through tensile coupon tests conducted according to ISO 6892-1:2009 (International Organization for Standardization, 2010). The coupons were machined from three initially straight specimens (Sp. 2, 4 and 10), prior to the curving process, in order to avoid the effects of roller-bending on the steel properties. Following the sectioning process, each coupon was machined from the middle of the RHS wide flange opposite to the weld, aiming at avoiding the localized effects at the corners due to the section forming as well as the influence of the heat affected zone. The released tensile coupons were observed to curve from their initial flat geometry, indicating the presence of high through-thickness flexural residual stresses, typical of cold-formed hollow sections which are not subjected to post-forming heat treatment. The flexural residual stresses showed a tendency of tension on the outer surface and compression on the inner surface of the sections. Views of the sectioned material's deflection and the tensile coupon test are illustrated in Figure 3-8.

Tensile coupon tests provide forces and displacements which are used to compute engineering stresses ( $\sigma_e$ ) and engineering strains ( $\varepsilon_e$ ). However, it is necessary to convert engineering stress-strain data to true stress-strain data before employing them in a large-strain finite-element-analysis [30]. The corresponding true stress ( $\sigma_t$ ) and true strain ( $\varepsilon_t$ ) can be calculated according to Eq. (3-1) and Eq. (3-2). Good agreement was found between the true stress - strain curves of the tensile coupon tests (Sp. 2, 4 and 10), shown in Figure 3-9. The modulus of elasticity was found equal to 205GPa. The yield stress occurred equal to 470MPa, taken as the 0.2% proof stress since the transition between the elastic and the plastic domains was very smooth, which is typical of cold-formed sections in contrast to the hot-rolled (Gardner et al., 2010). The ultimate tensile stress occurred approximately 550MPa at a strain of 10.1%. The limited ductility encountered in the tensile tests, is considered to be consequence of the RHS cold forming.

$$\sigma_t = \sigma_e(1 + \varepsilon_e) \quad (3-1)$$

$$\varepsilon_t = \ln(1 + \varepsilon_e) \quad (3-2)$$

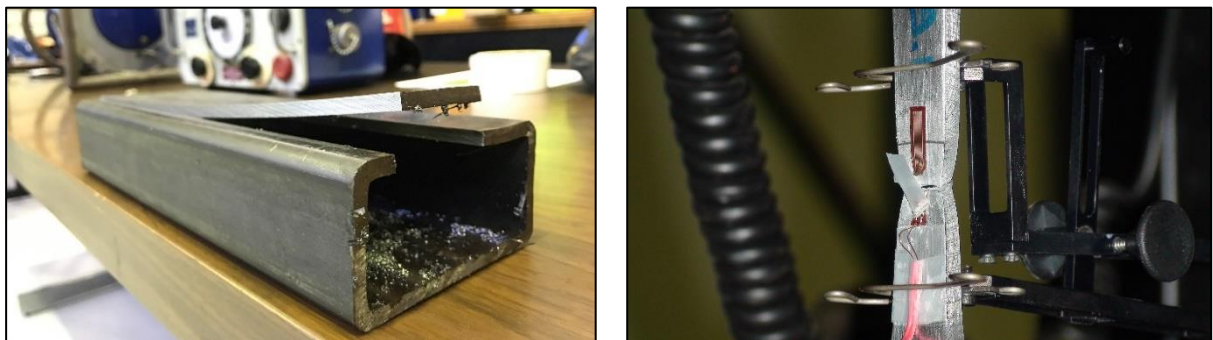


Figure 3-8: Views of the sectioned material's deflection (left) and the tensile coupon test (right).

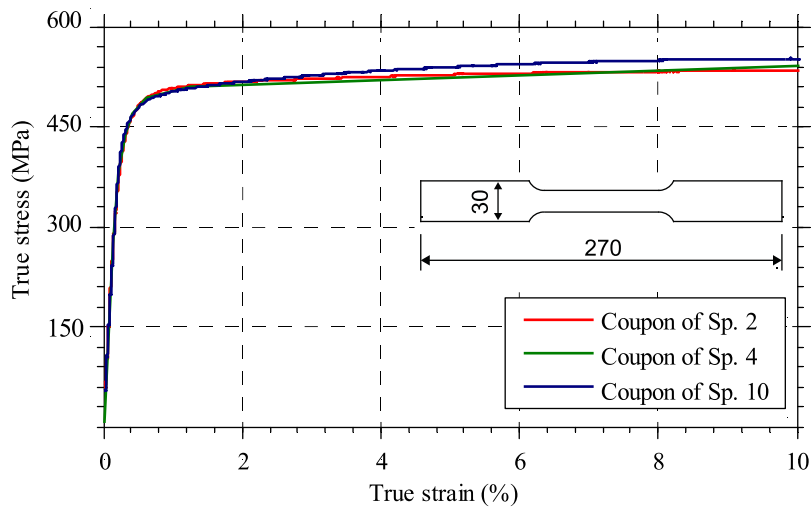


Figure 3-9: True stress-strain curves from tensile coupon tests.

### 3.4 EXPERIMENTAL RESULTS

#### 3.4.1 High arches under compression

Experimental results of the high arches under compressive loading are compared in terms of equilibrium paths of load with vertical displacement at the crown (Figure 3-10) and transverse displacement at the position of the inclined LVDT (Figure 3-11). Excellent repeatability is observed between the test results. The ultimate strength capacity of the arches is found approximately equal to 48kN. A softer response is noticed in the experimental load-displacement curves compared to the slope of the small unloading cycle, indicating that the specimens exhibited premature yielding. This behavior cannot be attributed to the initial imperfections of the specimens, since (a) imperfections are considered to affect the ultimate strength when buckling is involved as failure mode, but not the elastic part of the response, and (b) the softening response is shown consistent through all specimens. The roller-bending residual stresses probably could have caused premature yielding, but their effect on the initial stiffness of the arches is assessed later to be small (c.f. Section 4.4). The encountered premature yielding is attributed to the Bauschinger effect, since an opposite bending moment of the induced during roller-bending is developed at the crown under the compressive load.

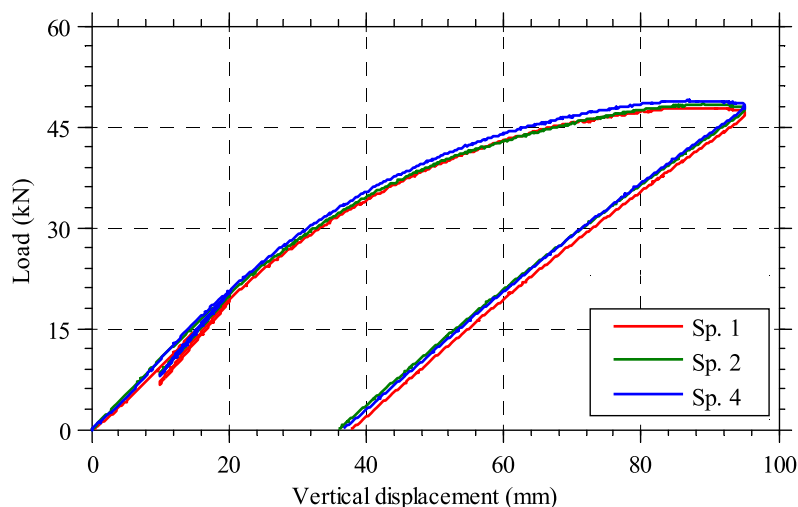


Figure 3-10: Load-displacement curves at the crown of high arches under compression.

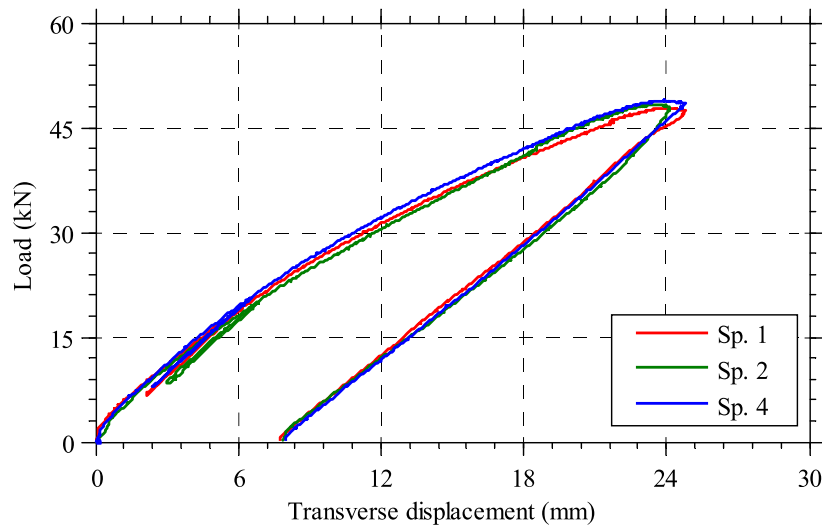


Figure 3-11: Load-displacement curves at the position of inclined LVDT of high arches under compression.

Characteristic strain gauge measurements, including the developed longitudinal strains at the top and bottom flange middles, along with the transverse strains at the bottom flange middle, are compared in Figure 3-12. The developed longitudinal strains at the top and bottom flange middles are of similar magnitude, while the transverse strains are also significant (one quarter of longitudinal strains), which is due to Poisson effect and transverse bending that is typical for curved members. The softening response is evidenced in all strain gauge measurements and the slope of the small unloading cycle is parallel to the unloading stiffness, supporting the case of premature yielding at the crown due to the Bauschinger effect. A characteristic deformed shape at the end of this set of tests (Sp. 1, 2 and 4) is presented in Figure 3-13. The failure mode in all cases is dominated by yielding at the crown accompanied by inelastic local buckling of the top flange.

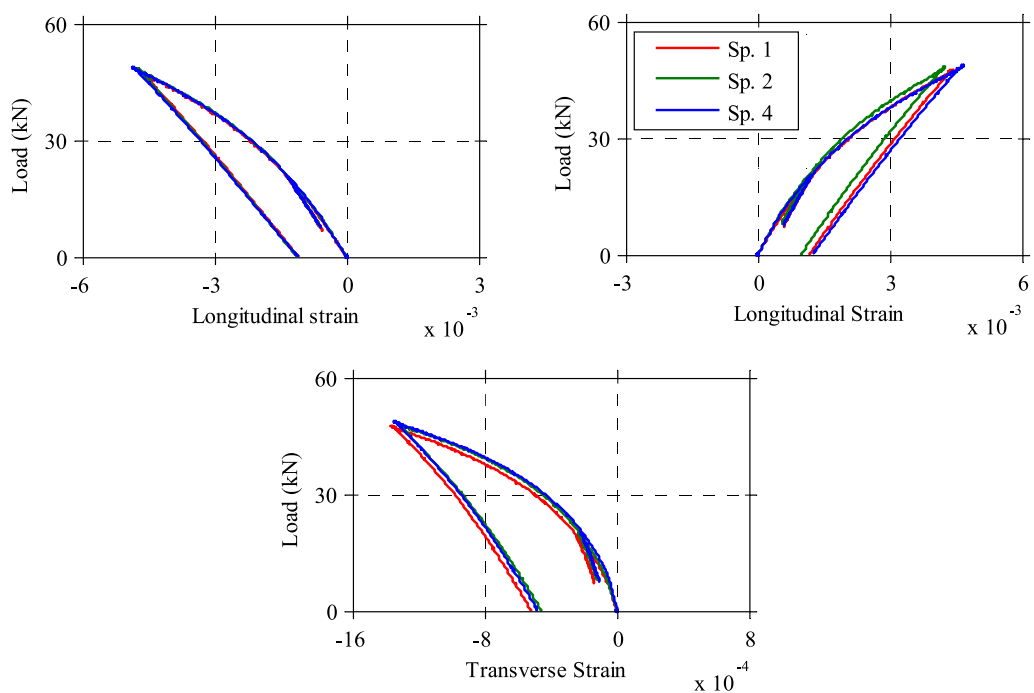


Figure 3-12: Longitudinal strain at the top flange (top-left), the bottom flange (top-right) and transverse strain at the bottom flange (bottom) of high arches under compression.





Figure 3-13: Characteristic deformed shape of high arches under compression at the end of tests.

### 3.4.2 High arches under tension

Experimental results of the high arches under tensile loading are compared in terms of equilibrium paths of load with vertical displacement at the crown (Figure 3-14) and transverse displacement at the position of the inclined LVDT (Figure 3-15). Excellent agreement is found between test results. The load-displacement curves present an initial part of increasing displacement with a small increase of load, attributed to the initial geometric clearances of the support assemblies. In Figure 3-14, an approximately linear behavior is encountered for imposed load up to 55kN, followed by a gradual diminishing of stiffness due to yielding at the crown before load is carried largely in tension. The small unloading cycle is almost coincident to the loading-one, demonstrating that initially the specimens were in the elastic domain. The Bauschinger effect is not encountered in this case, in which the developed bending moment at the crown is towards the same direction as the one induced during roller-bending.

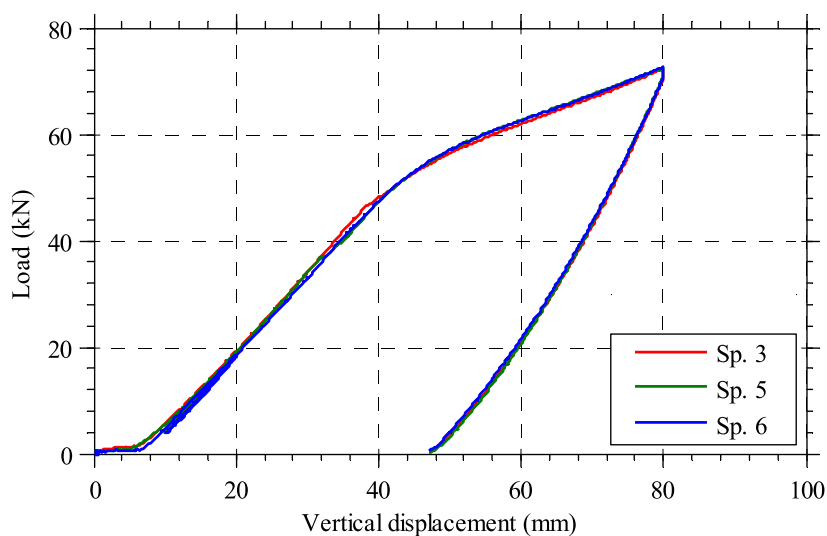


Figure 3-14: Load-displacement curves at the crown of high arches under tension.



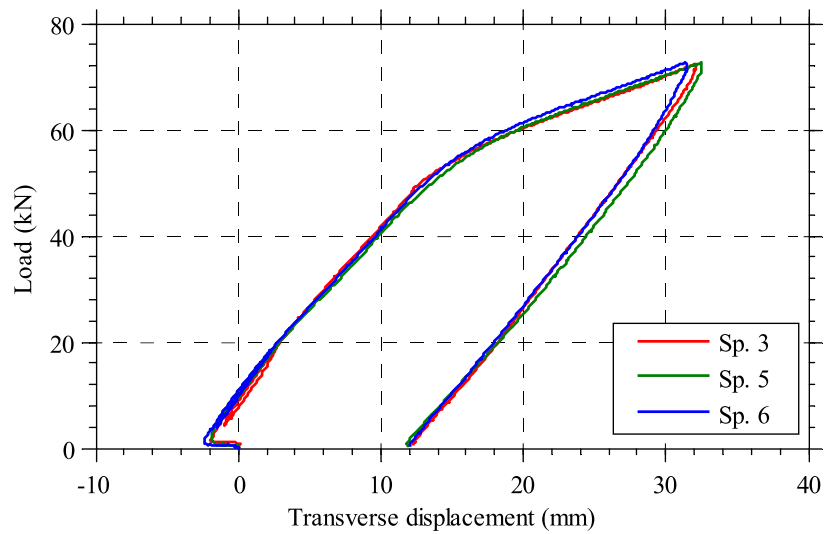


Figure 3-15: Load-displacement curves at the position of inclined LVDT of high arches under tension.

Characteristic strain gauge measurements including the developed longitudinal strains at the top and bottom flange middles along with the transverse strains at the bottom flange middle are compared in Figure 3-16. Excellent agreement is observed in the strain-gauge results, which present an initially linear elastic response. Thus, it is confirmed that the loading direction significantly affects the stress–strain response of the material and the premature yielding is due to the Bauschinger effect. The developed longitudinal strains at the top and bottom flange middles are found to exhibit similar magnitudes, while transverse strains are also significant. A characteristic deformed shape at the end of tests (Sp. 3, 5 and 6), is presented in Figure 3-17.

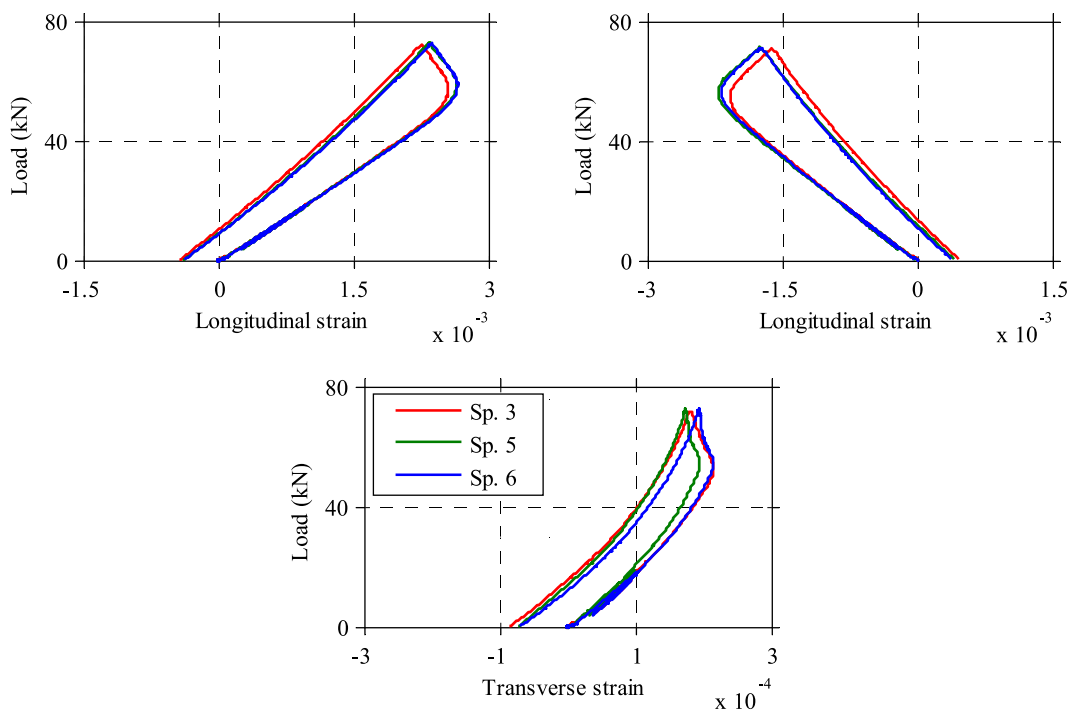


Figure 3-16: Longitudinal strain at the top flange (top-left), the bottom flange (top-right) and transverse strain at the bottom flange (bottom) of high arches under tension.

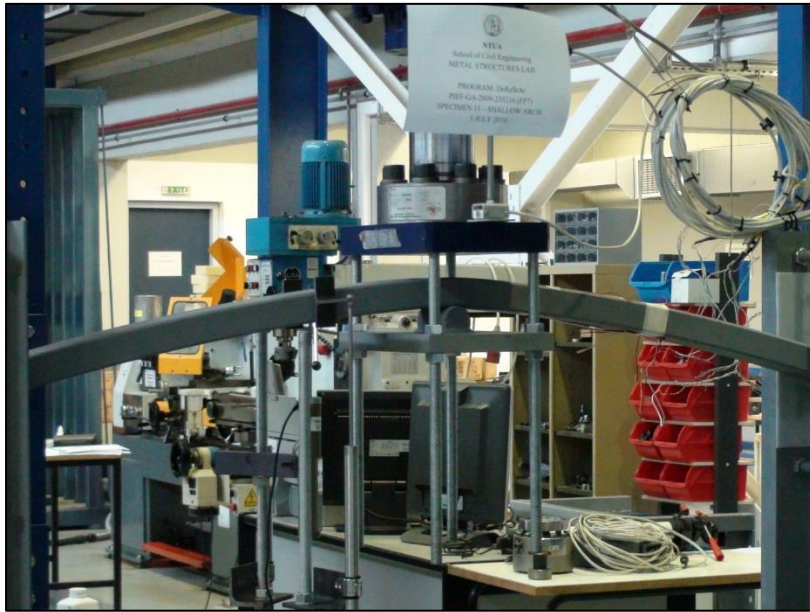


Figure 3-17: Characteristic deformed shape of high arches under tension at the end of tests.

### 3.4.3 Shallow arches under compression

Experimental results of the shallow arches under compressive loading are compared in terms of equilibrium paths of load with vertical displacement at the crown (Figure 3-18) and transverse displacement at the position of the inclined LVDT (Figure 3-19). Aiming at assessing the structural response to a greater extent, a total displacement of 150mm was imposed in Sp. 10. The load-displacement curves present an initial part of increasing displacement with a small increase of load, typically attributed to the initial geometric tolerances of the hinge supports. The overall response is almost similar between the shallow and high arches under compression and the softening response is evidenced here as well. Shallow arches under compression develop higher axial forces and lower bending moments than high arches and therefore the softening response due to the Bauschinger effect may be less prevalent.

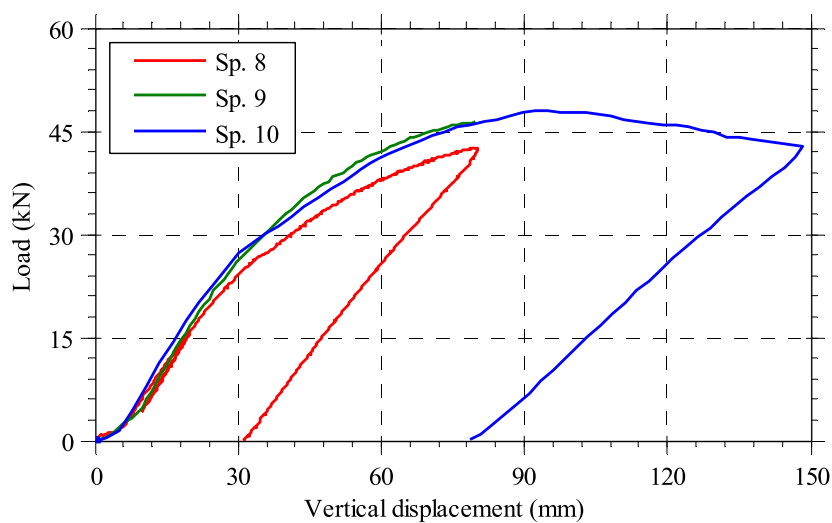


Figure 3-18: Load-displacement curves at the crown of shallow arches under compression.

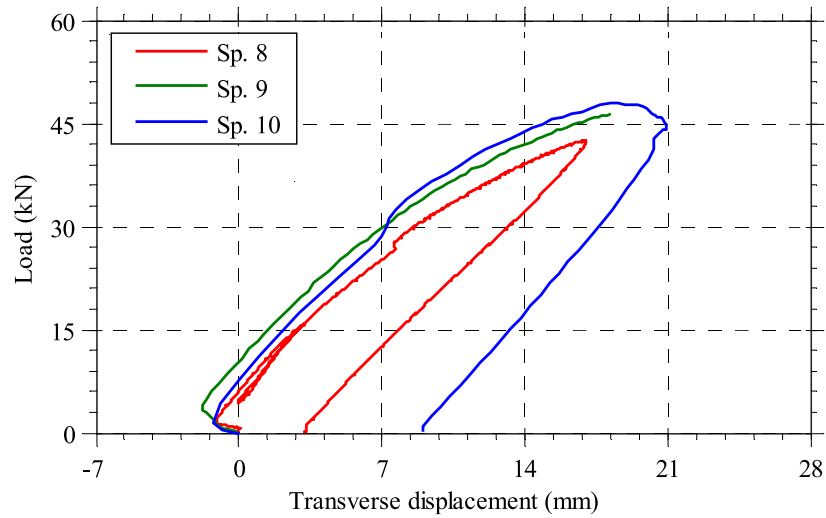


Figure 3-19: Load-displacement curves at the inclined LVDT of shallow arches under compression.

Characteristic strain gauge measurements, including the developed longitudinal strains at the top and bottom flange middles, along with the transverse strains at the bottom flange middle, are compared in Figure 3-20. The strain gauge measuring longitudinal strains at the top-flange middle of specimen 8, failed during the test. The failure modes of specimens 8 and 10 are similar to the one depicted in Figure 3-13. Testing of specimen 9 was stopped prematurely due to material fracture at the arch’s crown (Figure 3-21), demonstrating the limited ductility of the specimens as a result of the induced section-forming and roller-bending cold-work.

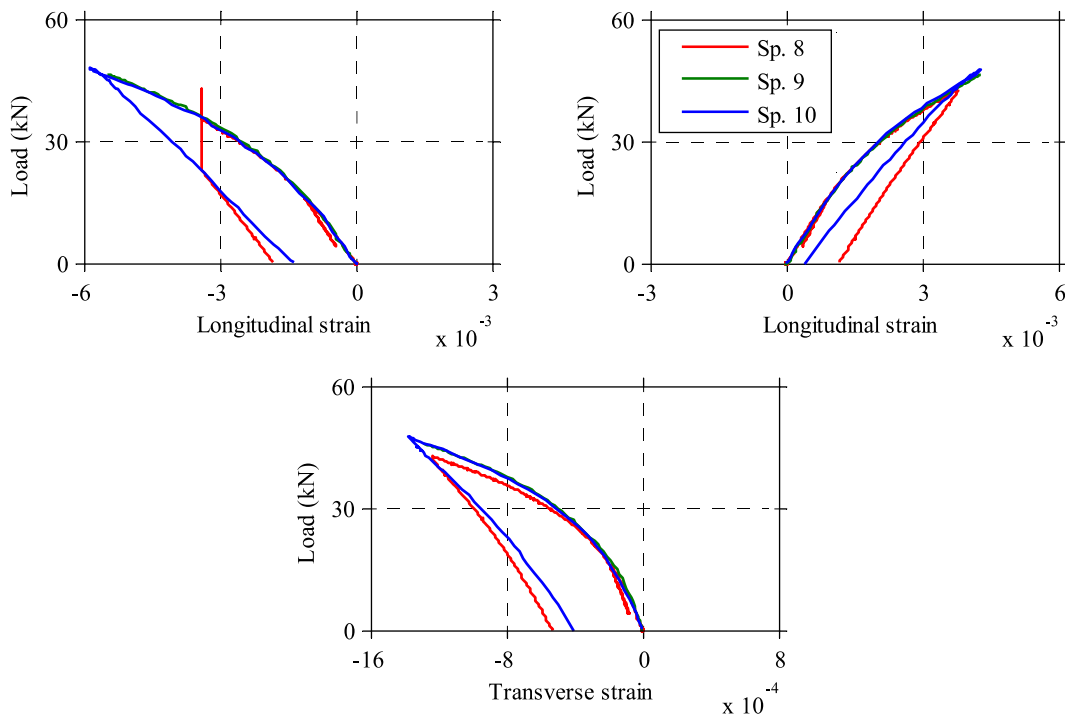


Figure 3-20: Longitudinal strain at the top flange (top-left), the bottom flange (top-right) and transverse strain at the bottom flange (bottom) of shallow arches under compression.

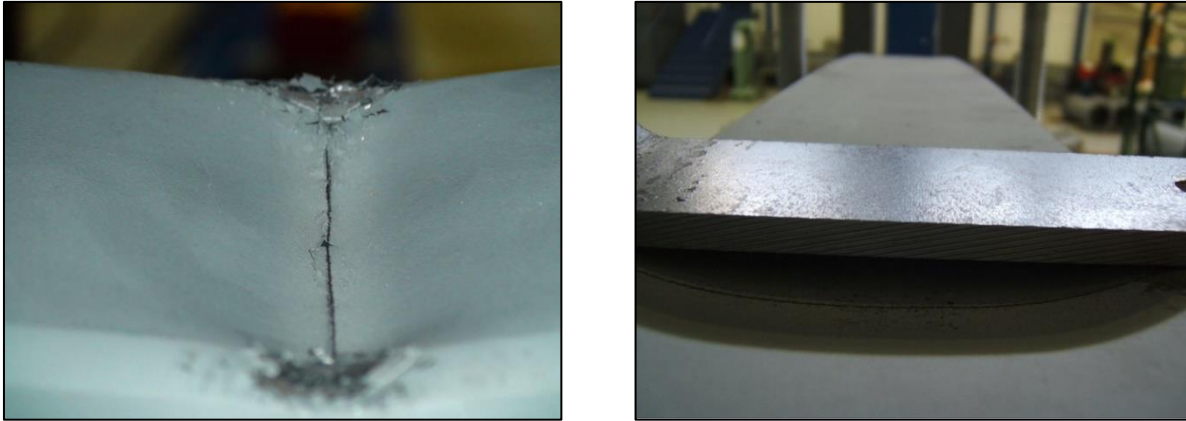


Figure 3-21: Fracture at the top flange of Sp. 9.

#### 3.4.4 Shallow arches under tension

Experimental results of the shallow arches under tensile loading are compared in terms of equilibrium paths of load with vertical displacement at the crown (Figure 3-22) and transverse displacement at the position of the inclined LVDT (Figure 3-23). Once again, very good agreement is observed between test results. The inclined LVDT of specimen 12 failed to measure accurately the transverse displacement, as friction between the bottom flange and the LVDT introduced large error. The overall response is similar between shallow and high arches under tension. Characteristic strain gauge measurements, including the developed longitudinal strains at the top and bottom flange middles, along with the transverse strains at the bottom flange middle, are compared in Figure 3-24. The deformed shape at the end of this set of tests (Sp. 7, 11 and 12) is similar to the one depicted in Figure 3-17.

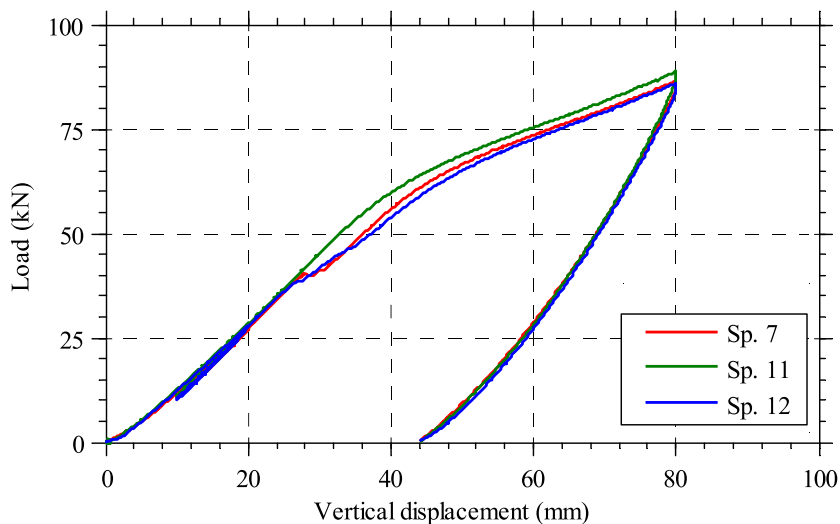


Figure 3-22: Load-displacement curves at the crown of shallow arches under tension.

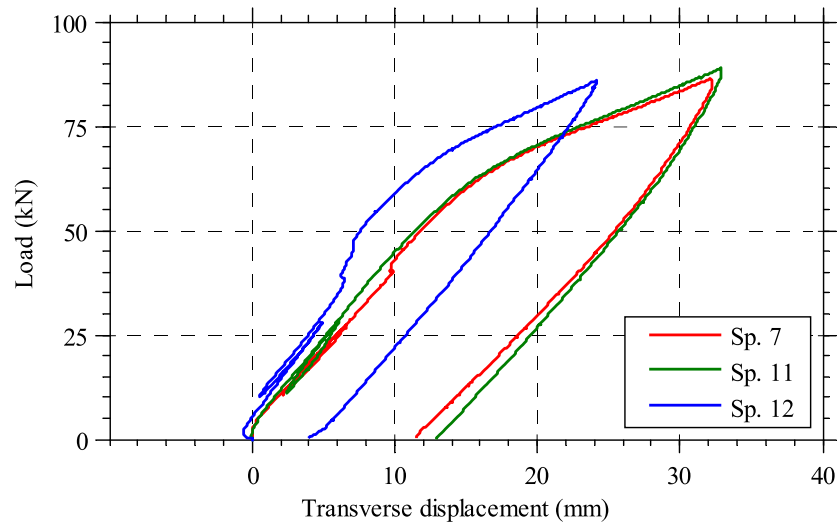


Figure 3-23: Load-displacement curves at the inclined LVDT of shallow arches under tension.

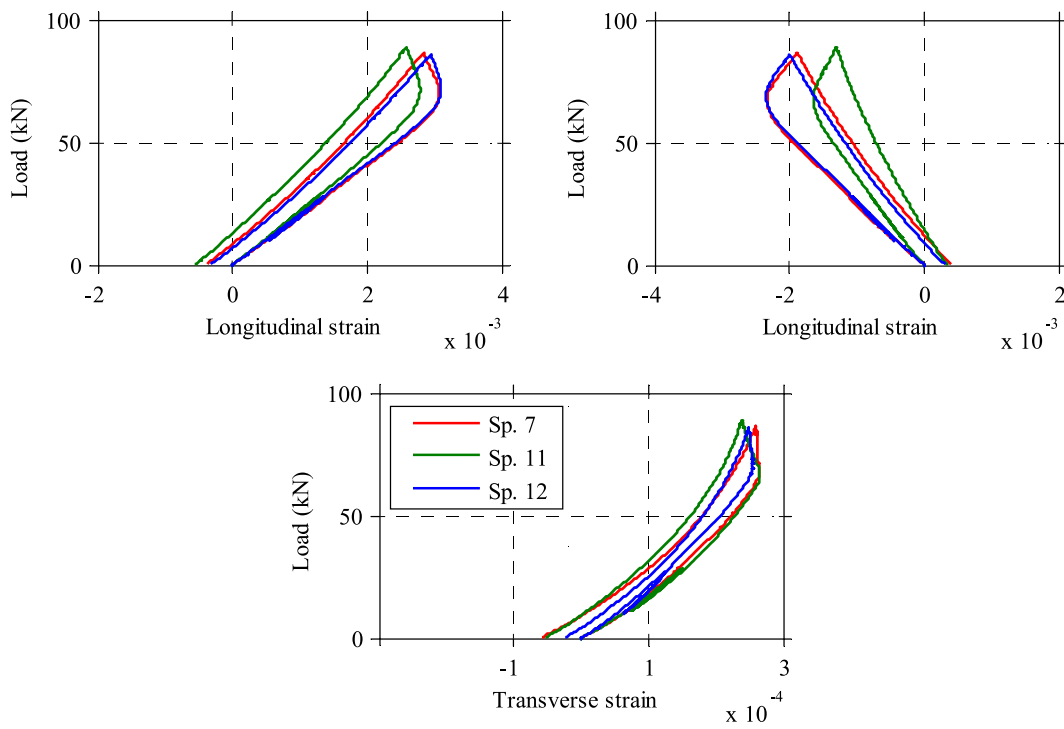


Figure 3-24: Longitudinal strain at the top flange (top-left), the bottom flange (top-right) and transverse strain at the bottom flange (bottom) of shallow arches under tension.

### 3.5 CONCLUSIONS

A state-of-the-art experimental study on the in-plane behavior of roller-bent arches comprising Rectangular-Hollow-Sections was presented in this chapter. Twelve arch specimens, grouped in two sets of curvatures, were tested under tensile and compressive loading. A cold-formed RHS 50x100x5mm was employed in all specimens, which were curved about their weak axis into arch radii of 3.71m (high arches) and 4.10m (shallow arches). Dimension measurements were undertaken in order to evaluate the exact geometric imperfections of the arch specimens; significant deviations from the theoretical shape were observed. The material properties were obtained through tensile coupon tests, machined from specimens prior to the curving process, in order to avoid the effects of roller-bending on the steel properties. The stress-strain curve was found to correspond reasonably to a steel grade S355, exhibiting a smooth transition between the elastic and the plastic domains which is typical of cold-formed sections. Overall, excellent repeatability was observed between the test results, in terms of load-displacement equilibrium paths, developed deformations and failure mechanisms. The arches under compression demonstrated a gradually softening response, even for low levels of loading, in contrast to the arches under tension. Therefore, the loading direction affected significantly the stress-strain response of the material and thus, it was concluded that the roller-bent arches in predominant compression exhibited premature yielding due to the Bauschinger effect. The failure mode of the arches under compression was dominated by yielding at crown due to the developed bending moment, accompanied by the inelastic local buckling of the top flange. On the other hand, an increasing resistance was encountered in the arches under tension, attributed to the steel hardening, as the load was carried in axial tension after yielding of arches at crown.

### REFERENCES

- Di Tommaso, A. & Viola, E. (1976). "An experimental and theoretical research on statics and lateral stability of thin arches." *Giornale del Genio Civile*, vol. 114, pp. 181-204 (in Italian).
- Gardner, L. Æ., Saari, N., and Wang, F. (2010). "Comparative experimental study of hot-rolled and cold-formed rectangular hollow sections." *Thin-Walled Structures*, vol. 48, pp. 495–507.
- Guo, Y., Zhao, S., Pi, Y., Andrew, M., and Dou, C. (2015). "An experimental study on out-of-plane inelastic buckling strength of fixed steel arches." *Engineering Structures*, vol. 98, pp. 118–127.
- Huang, Y., Liu, A., Zhu, C., Lu, H., and Gao, W. (2019). "Experimental and numerical investigations on out-of-plane ultimate resistance of parallel twin-arch under uniform radial load." *Thin-Walled Structures*, vol. 135, pp. 147–159.
- International Organization for Standardization. (2010). *EN ISO 6892.01 - Metallic materials - Tensile testing - Part 1: Method of test at room temperature*. Geneva, Switzerland.
- La Poutré, D. B. La, Spoorenberg, R. C., Snijder, H. H., and Hoenderkamp, J. C. D. (2013). "Out-of-plane stability of roller bent steel arches — An experimental investigation." *Journal of Constructional Steel Research*, vol. 81, pp. 20–34.
- Lu, Y., Cheng, Y., and Han, Q. (2017). "Experimental investigation into the in-plane buckling and ultimate resistance of circular steel arches with elastic horizontal and rotational end restraints." *Thin-Walled Structures*, vol. 118, pp. 164-180.
- Papangelis, J. P., and Trahair, N. S. (1987). "Flexural-Torsional Buckling of Arches." *ASCE J. Struct. Eng.*, vol. 113, pp. 889–906.
- Sakata, T., and Sakimoto, T. (1990). "Experimental study on the out-of-plane buckling strength of steel arches with open cross-section." *Proc. Japan Soc. Civ. Engrs*, vol. 416, pp.101-112.

- Sakimoto, T., Yamao, T., and Komatsu, S. (1979). "Experimental Study on the Ultimate Strength of Steel Arches." *Proc. Jpn. Soc. Civ. Eng.*, No. 286, pp. 139–149.
- Stussi, F. (1943). "Lateral-Buckling and Vibration of Arches." *Proc. Int. Assoc. Bridge Struct. Eng. Publ.*, vol. 7, pp. 327–343 (in German).
- Tokarz, F. J. (1971). "Experimental Study of Lateral Buckling of Arches." *ASCE J. Struct. Div.*, vol. 97, pp. 545–559.





# 4 NUMERICAL SIMULATION OF EXPERIMENTS

## 4.1 INTRODUCTION

Advances in computational engineering have facilitated the use of the Finite Element Method (FEM) in the analysis and design of structures. Nowadays, the research practice is extensively based on finite element models that are calibrated against experimental results, allowing for the execution of a large number of reliable numerical analyses. Several numerical investigations associated with stability tests on arches, are reported in the literature. Komatsu and Sakimoto (1977) as well as Sakimoto and Komatsu (1983) performed finite element analyses on box-section steel arches. Numerical results were compared with the experimental ones presented by Sakimoto et al. (1979) and Sakata and Sakimoto (1990). Pi and Trahair (1996) developed finite element models in order to investigate the spatial stability of I-section steel arches. The accuracy of the proposed models had been validated on the stability tests of Papangelis & Trahair (1987). A comprehensive numerical investigation on roller-bent arches comprising wide-flange sections was performed by Spoorenberg et al. (2012), where numerical results were validated against the experimental tests of La Poutré et al. (2013). More recent numerical studies on the spatial stability of steel arches, along with pertinent experimental results, have been presented by Guo et al. (2015, 2016), Lu et al. (2017) and Huang et al. (2019).

In this chapter, the finite element method (Bathe, 2014) is employed to simulate the pertinent experimental tests of arches presented in Chapter 3. To that end, detailed numerical models of the shallow and high arches are developed, aiming at assessing the effects of roller-bending on the in-plane behavior of RHS arches. The encountered locked-in stress formations, emanating from the curving process of initially straight workpieces, are estimated through explicit roller-bending simulations. Implicit static analyses accounting for geometric and material nonlinearities are carried out to simulate the compression and tension tests, including the loading and support configurations of specimens. Numerical analyses are performed in the general-purpose finite element software ADINA (ADINA, 2017), following the practical aspects of the finite element method presented by Gantes and Fragkopoulos (2009). Experimental and numerical results are compared in terms of load-displacement equilibrium paths, developed deformations and failure mechanisms. Thus, the developed numerical models are validated, and the accuracy of the finite element analyses is verified. Finally, the effects of locked-in stresses on the structural behavior of roller-bent arches are assessed, through the comparison of identical roller-bent and stress-free numerical models, under various loading conditions.

## 4.2 NUMERICAL MODELING

In order to maintain an acceptable level of accuracy and at the same time reduce the computational effort, the finite element modeling is conducted in three successive phases, including the:

- (i) explicit roller-bending formation process,
- (ii) configurations of hinge support and loading cylinders,
- (iii) compressive and tensile loading tests

Detailed finite element models of the roller-bending process are developed first, aiming at estimating the locked-in stress/strain formations in a reliable manner. Initially straight workpieces of RHS 50x100x5mm are modeled using 4-node shell elements of five integration points in the element thickness direction. The Newton-Cotes integration method is employed since it is more effective for capturing the onset and spread of the materially nonlinear conditions, as the integration points are on the boundaries of the elements. Null initial residual stresses are assumed on the straight workpieces, since the final patterns are independent of the initial conditions. Shell elements are employed on the surfaces of bending rollers, which are connected to their center of rotation via rigid links in order to provide rigidity. The interaction between workpieces and rollers is considered by introducing contact elements between their interfaces. The Coulomb friction coefficient of the contacting surfaces is taken equal to 0.3. Implicit static analyses accounting for geometric and material nonlinearities are carried out using the Newton – Raphson solution algorithm. Large displacement and large strain formulations are incorporated, since local or global buckling of the specimens are considered critical and the developed plastic strains due to the curving process are significant. A bilinear material model (Figure 4-1) of Elasticity modulus equal to 205GPa, yield stress 470MPa and strain hardening 0.8GPa, is introduced to the elements of the RHS segment, based on the results of tensile coupon tests (c.f. Section 3.3).

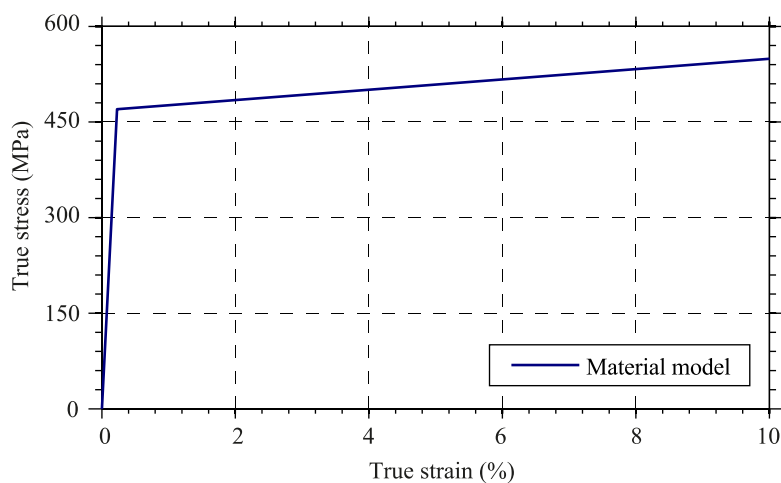
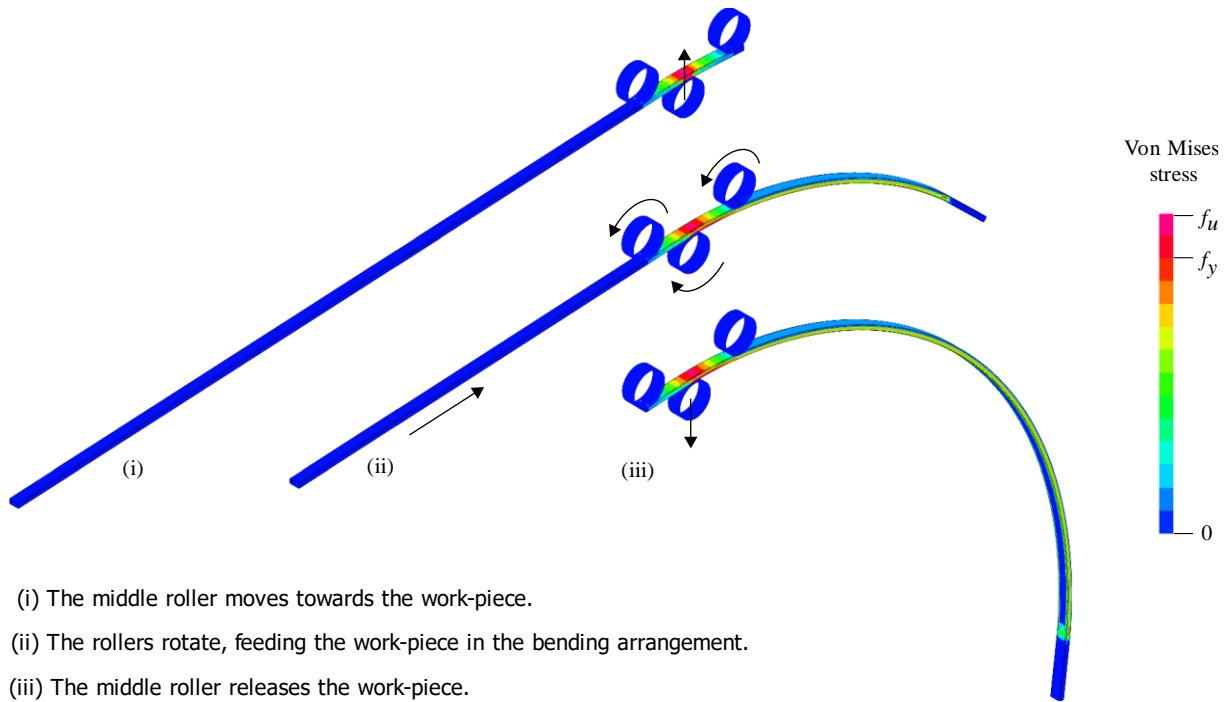


Figure 4-1: Bilinear material model based on the tensile coupon tests.

The analysis sequence is illustrated schematically in Figure 4-2, where a prescribed displacement at the middle roller is applied first towards the beam, followed by a prescribed rotation at the centers of the other two rolls. A sufficiently small load-step magnitude is required to reach uniform plastification along the workpiece. The placement requirements within the three-point-bending restrain bending of the workpiece close to its edges. These regions are trimmed in practice at the end of roller-bending, while they were removed numerically using the element death feature of ADINA. In practice multiple passes are required to roller-bent a workpiece. In numerical simulations only a single forming pass is analyzed, as it is observed that the residual stresses are almost identical for single- and multiple- pass roller-bending.



- (i) The middle roller moves towards the work-piece.
- (ii) The rollers rotate, feeding the work-piece in the bending arrangement.
- (iii) The middle roller releases the work-piece.

Figure 4-2: Numerical simulation of the roller-bending process.

The longitudinal residual stresses and strains along with the accumulated plastic strains of the shallow and high arches at the end of the curving process, are illustrated in Figure 4-3. All distributions are found to be uniform along the arches due to the constant curvature. The encountered longitudinal stresses exhibit a non-symmetrical layout over the cross-sectional width and height differ, differing remarkably from the theoretical distribution of Timoshenko (1956). Significant stress concentrations are found at the edges of the bottom flange, being in agreement with the model proposed by Chiew et al. (2016). The bending curvature is shown to have an insignificant effect on the residual stress formations in contrast to the developed strains. It is worth noting that in both high and shallow arches, the accumulated plastic strains are approximately one order of magnitude larger than the developed longitudinal strains, demonstrating a significant reduction of the material’s ductility.

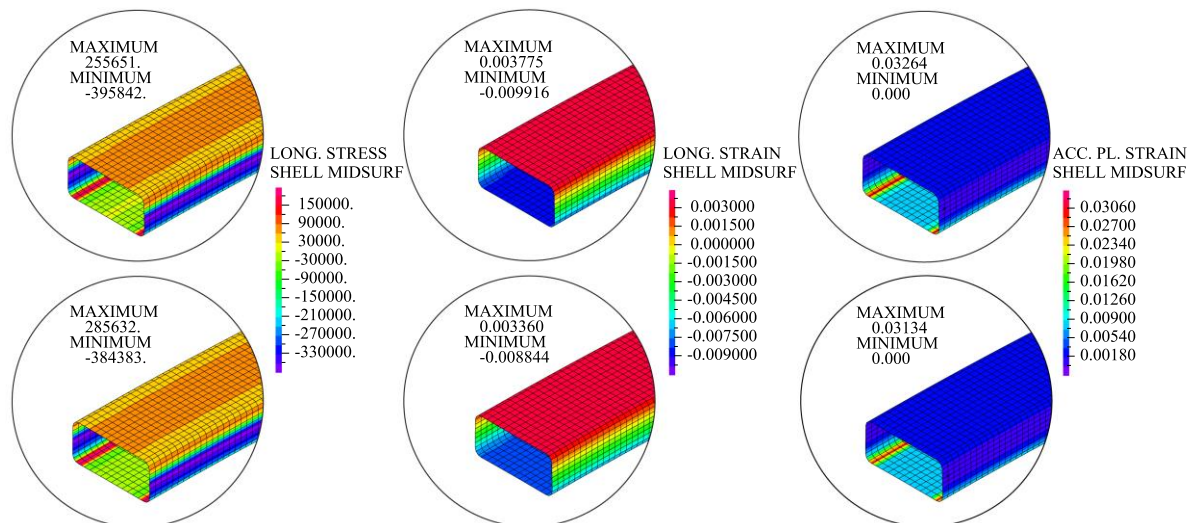


Figure 4-3: Longitudinal residual stresses (kPa), strains and accumulated plastic strains at the shell midsurface of the high (top) and shallow (bottom) arches.

The boundary conditions affect considerably the structural behavior of steel arches, as presented by Dimopoulos and Gantes (2008). Aiming at estimating accurately the translational stiffness of hinge supports, a detailed numerical model of the assembly is developed using 8-node brick elements (Figure 4-4). The numerical model consists of (i) a short part of the RHS 50x100x5mm, (ii) two vertical plates of S355 steel grade, and (iii) a M20 10.9 pin. Elastic – plastic material models are implemented in the finite element analyses, comprising the material model based on tensile coupon tests (Figure 4-1) for the RHS segment, while the characteristic values of mechanical properties are used for the pin and plates in absence of more accurate experimental data. Appropriate contact elements are introduced to the assembly's interfaces of adjacent parts. The Coulomb friction coefficient is typically taken equal to 0.3.

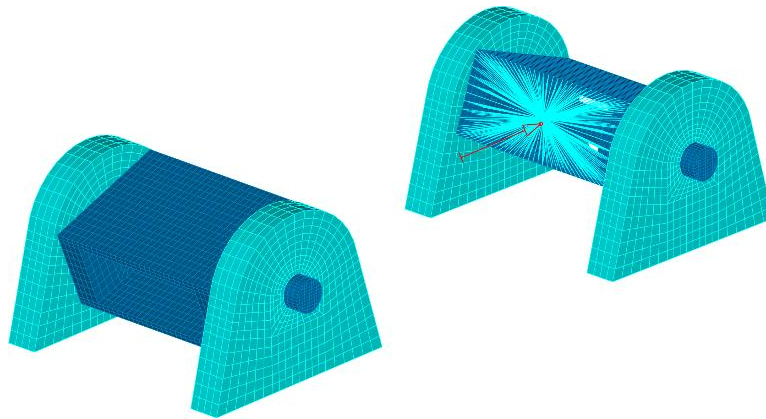


Figure 4-4: Finite element model of hinged support.

The model is fixed at the base and a horizontal force, either compressive (negative) or tensile (positive), is applied on the RHS centroid via the use of rigid links, while the rest degrees of freedom are restrained. Different clearances are considered between the high and shallow arches, since high arches were initially compressed while shallow arches were tensioned, in order to fit to the experimental setup. The horizontal stiffness obtained from nonlinear analyses is presented in Figure 4-5. A similar response is encountered in the vertical direction; however, the support's stiffness and clearances have a less significant effect on the structural behavior in this case.

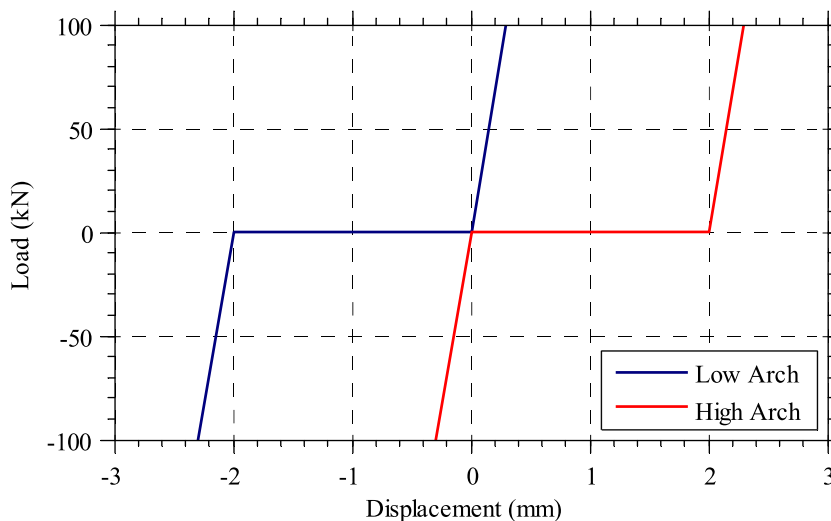


Figure 4-5: Horizontal stiffness of hinged supports.

Computational modeling of residual stresses by introducing appropriate stress values at the integration points of the elements is a rather complicated process. Taking advantage of the explicit roller-bending simulations that have been performed previously, the final state of pertinent analyses is introduced as initial condition for the subsequent simulations of compressive and tensile loading tests, by employing the restart analysis feature of ADINA. The element-death feature is employed for the finite elements that are not needed at this time, such as the bending rollers, the workpiece parts at the edges, and the contact elements. Rigid links are used to connect the nodes of the edged cross-sections to their geometric centroids, in order to prescribe boundary conditions (Figure 4-6). The semi-rigid stiffness of the supports is considered with the use of horizontal spring elements according to Figure 4-5. The rotation is unrestrained for in-plane bending, while rigid supports are considered in the vertical direction. Additional out-of-plane restraints are applied at the positions of the intermediate lateral supports. The induced force from the sliding system is obtained from relevant numerical analyses, equal to 0.40kN and 0.91kN, for imposing an average span shortening at the high arches and lengthening at the shallow arches of 7mm and 13mm, respectively (c.f. Section 3.2.1). Nevertheless, this pre-loading step had a negligible influence on the overall behavior of arches. The loading is applied at the arch's crown similarly to the experiments, through contact with a rigid cylinder (Figure 4-6). Such detailed simulation is appropriate to capture the local buckling of the RHS top flange at the location of the imposed load, which was observed in the experimental tests. A total number of four Geometric and Material Nonlinear Analyses (GMNA) are carried out, including the cases of shallow and high arches, under tensile and compressive loading.

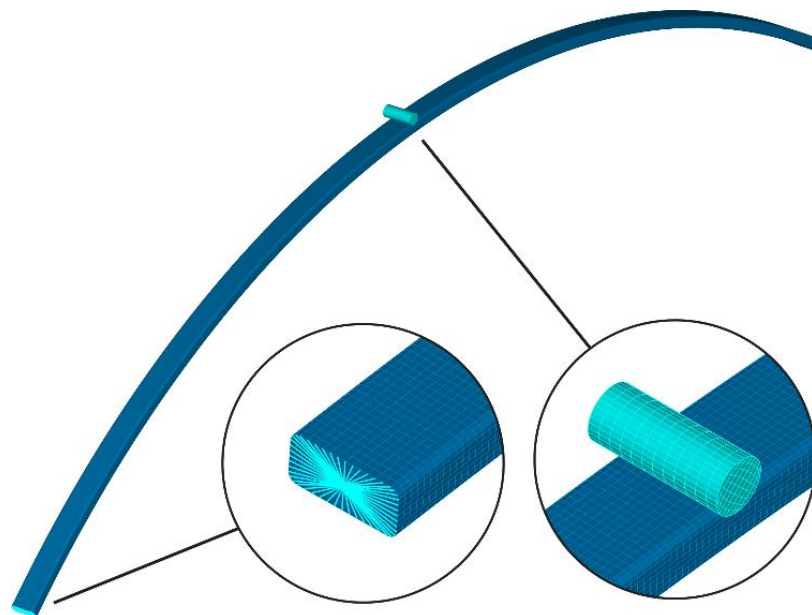


Figure 4-6: Finite element model of experimental tests.

### 4.3 COMPARISON OF EXPERIMENTAL AND NUMERICAL RESULTS

In this section, the experimental results of arch specimens (Sp. 1-12) are compared to the corresponding numerical results obtained from Geometric and Material Nonlinear Analyses (GMNA), in terms of load-displacement equilibrium paths, developed strains and deformed shapes.

### 4.3.1 High arches under compression

Experimental and numerical results of the high arches under compressive loading are compared in terms of equilibrium paths of load with vertical displacement at the crown (Figure 4-7) and transverse displacement at the position of the inclined LVDT (Figure 4-8). The ultimate strength capacity of the arches is well predicted by the numerical model, which is found approximately 48kN. However, a softer response is noticed in the experimental load-displacement curves at the crown compared to the GMNA. The slope of the small unloading cycle is found reasonably parallel to the initial stiffness provided by the numerical model, indicating that the specimens exhibited premature yielding due to the Bauschinger effect (Lange and Grages, 2009), as was explained in Chapter 3.

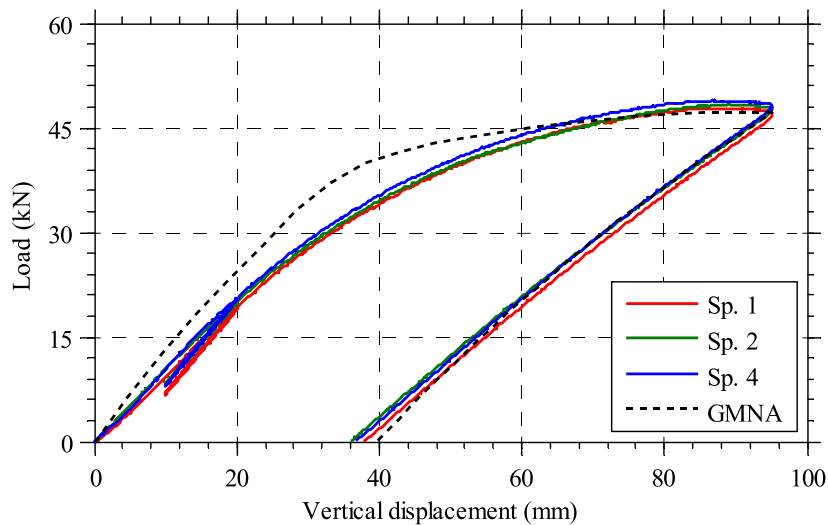


Figure 4-7: Load-displacement curves at the crown of high arches under compression.

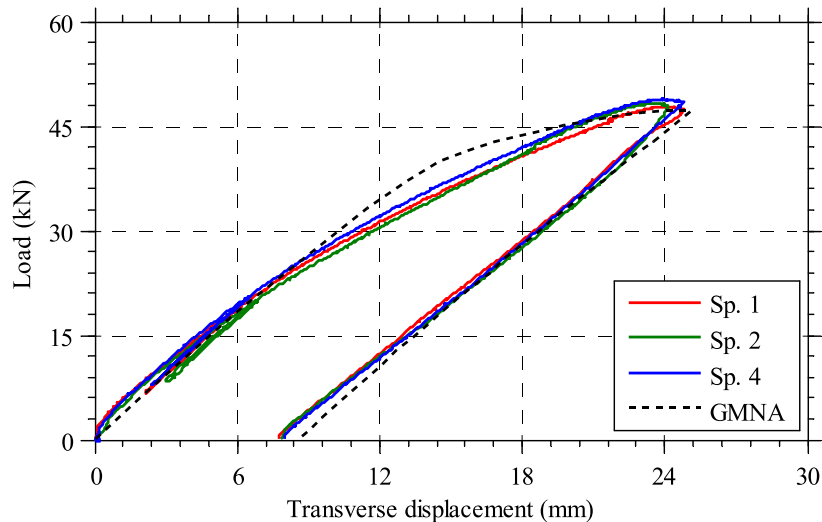


Figure 4-8: Load-displacement curves at the position of inclined LVDT of high arches under compression.

Characteristic strain gauge measurements, including the developed longitudinal strains at the top and bottom flange middle along with the transverse strains at the bottom flange middle, are compared to the corresponding values obtained from GMNA, in Figure 4-9. The softening response is evidenced in all strain gauge measurements and the slope of the small unloading cycle is parallel to the initial slope of the GMNA, supporting the case of premature yielding at the crown due to the Bauschinger effect.

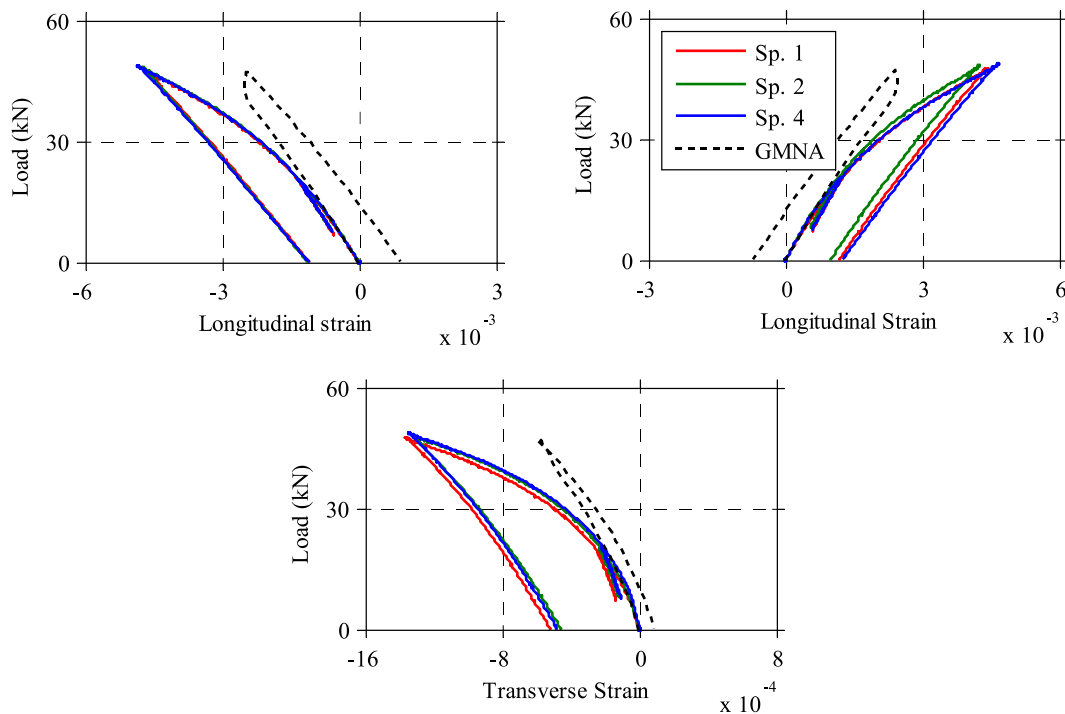


Figure 4-9: Longitudinal strain at the top flange (top-left), the bottom flange (top-right) and transverse strain at the bottom flange (bottom) of high arches under compression.

A characteristic deformed shape at the end of this set of tests (Sp. 1, 2 and 4) as well as the GMNA, is presented in Figure 4-10. The failure mode in both cases is dominated by yielding at the crown accompanied by inelastic local buckling of the RHS top flange.

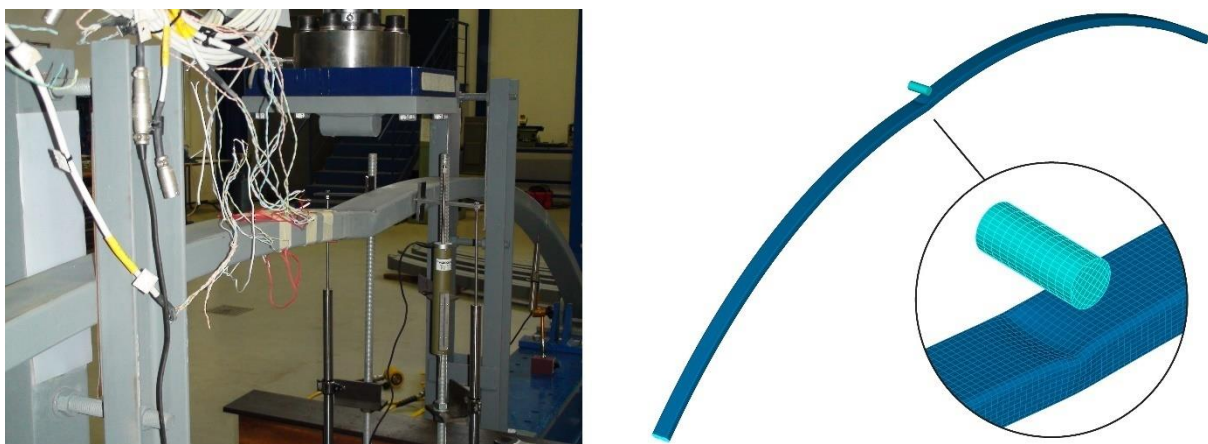


Figure 4-10: Characteristic deformed shape of high arches under compression from tests (left) and GMNA (right).



### 4.3.2 High arches under tension

Experimental and numerical results of the high arches under tensile loading are compared in terms of equilibrium paths of load with vertical displacement at the crown (Figure 4-11) and transverse displacement at the position of the inclined LVDT (Figure 4-12). Very good agreement is found between the test results and the GMNA in this case, where the developed bending moment at the crown is towards the same side as that induced in the bending operation. The load-displacement curves present an initial part of increasing displacement with a small increase of load, attributed to the initial geometric clearances of the support assemblies. An approximately linear behavior is encountered experimentally for imposed load up to 55kN, followed by a gradual diminishing of stiffness due to yielding at the crown before load is carried largely in tension. The plastic yield of GMNA is exhibited for lower imposed load than 55kN. The increased yield strength of test specimens is attributed to the strain aging effect (Chajes et al., 1963), in which a raise of yield/ultimate stress occurs when steel is deformed plastically and then allowed for a period to age in room temperature.

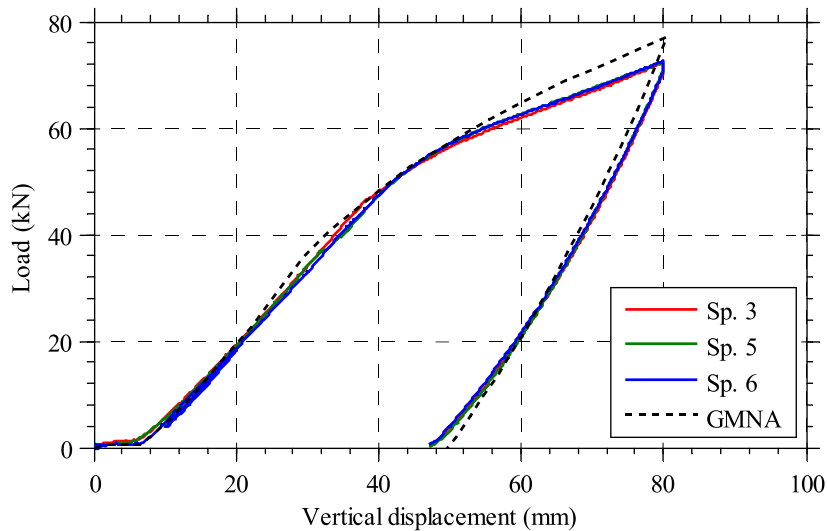


Figure 4-11: Load-displacement curves at the crown of high arches under tension.

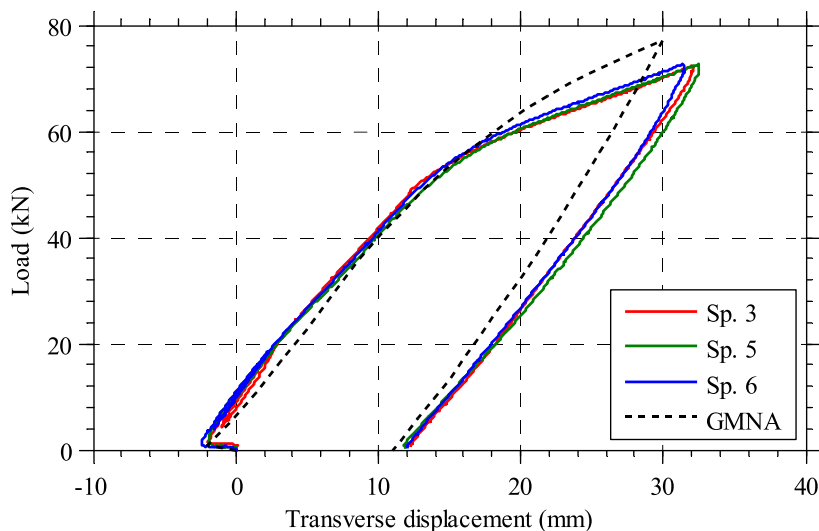


Figure 4-12: Load-displacement curves at the position of inclined LVDT of high arches under tension.



Characteristic strain gauge measurements including the developed longitudinal strains at the top and bottom flange middle along with the transverse strains at the bottom flange middle are compared to the corresponding values obtained from GMNA, in Figure 4-13. Good agreement is observed in the strain-gauge results, which present an initially linear elastic response. The experimentally measured strains exhibit higher yield point than the corresponding numerical ones, confirming the presence of the strain aging effect due to cold-forming process. The developed longitudinal strains at the top and bottom flange middle are found to exhibit similar magnitudes, while transverse strains are also significant. A characteristic deformed shape at the end of this set of tests (Sp. 3, 5 and 6) as well as the GMNA, is presented in Figure 4-14; in both cases, the failure mode is dominated by yielding at the crown accompanied with inelastic local buckling of the bottom flange.

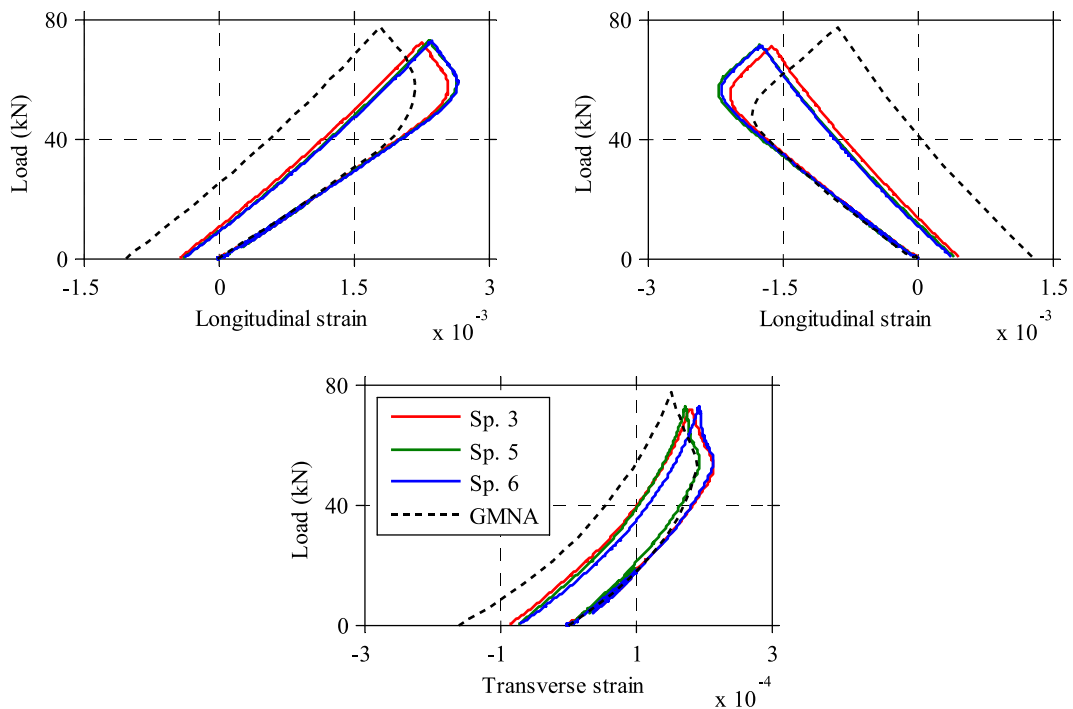


Figure 4-13: Longitudinal strain at the top flange (top-left), the bottom flange (top-right) and transverse strain at the bottom flange (bottom) of high arches under tension.

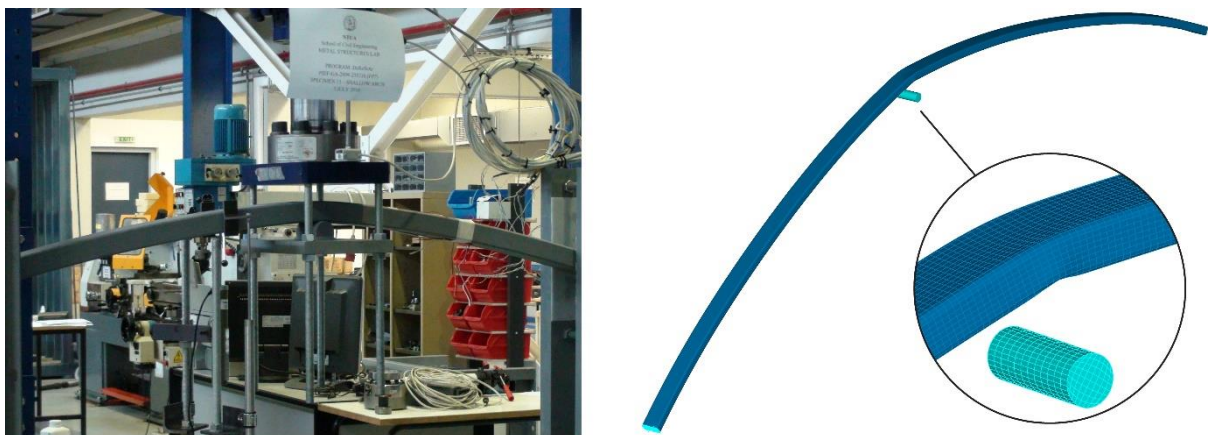


Figure 4-14: Characteristic deformed shape of high arches under tension from tests (left) and GMNA (right).

### 4.3.3 Shallow arches under compression

Experimental and numerical results of the shallow arches under compressive loading are compared in terms of equilibrium paths of load with vertical displacement at the crown (Figure 4-15) and transverse displacement at the position of the inclined LVDT (Figure 4-16). Good agreement is found between the test results and the GMNA; the overall response is almost similar between the shallow and high arches under compression and the softening response is evidenced here as well. In Figure 4-17, characteristic strain gauge measurements including the developed longitudinal strains at the top and bottom flange middle along with the transverse strains at the bottom flange middle are compared to the corresponding values obtained from GMNA; the strain gauge measuring longitudinal strains at the top-flange middle of specimen 8, failed during the test. The failure modes of specimens 8, 10 and the GMNA are similar to the one depicted in Figure 4-10. Testing of specimen 9 was stopped prematurely due to material fracture at the arch's crown, demonstrating the limited ductility of the specimens due to the induced section-forming and roller-bending.

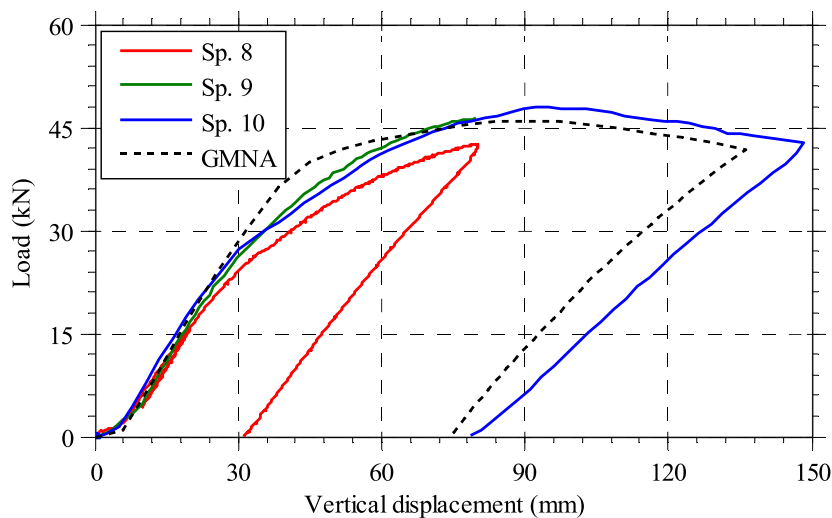


Figure 4-15: Load-displacement curves at the crown of shallow arches under compression.

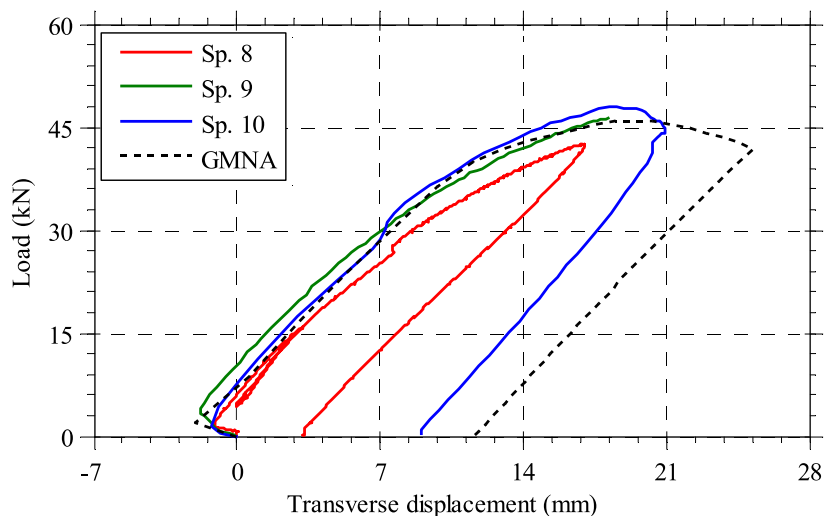


Figure 4-16: Load-displacement curves at the inclined LVDT of shallow arches under compression.

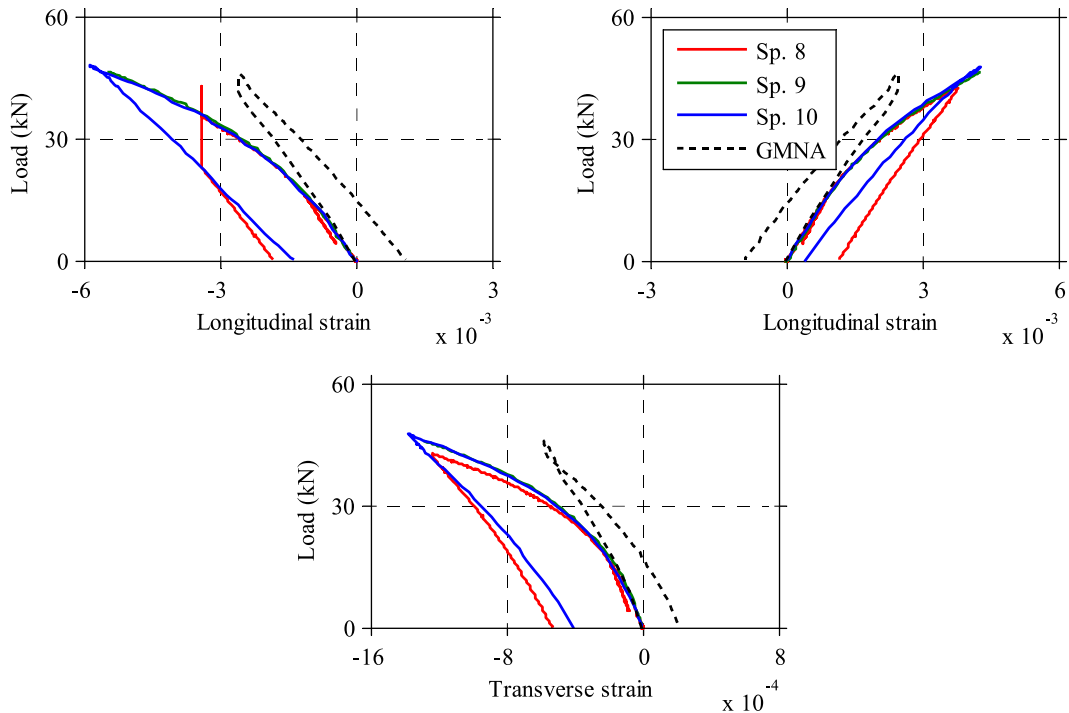


Figure 4-17: Longitudinal strain at the top flange (top-left), the bottom flange (top-right) and transverse strain at the bottom flange (bottom) of shallow arches under compression.

#### 4.3.4 Shallow arches under tension

Experimental and numerical results of the shallow arches under tensile loading are compared in terms of equilibrium paths of load with vertical displacement at the crown (Figure 4-18) and transverse displacement at the position of the inclined LVDT (Figure 4-19). Very good agreement is again observed between the test results and the GMNA. The overall response is very similar between the shallow and high arches under tension. The inclined LVDT of specimen 12 failed to measure accurately the transverse displacement, as friction between the bottom flange and the LVDT introduced a large amount of error.

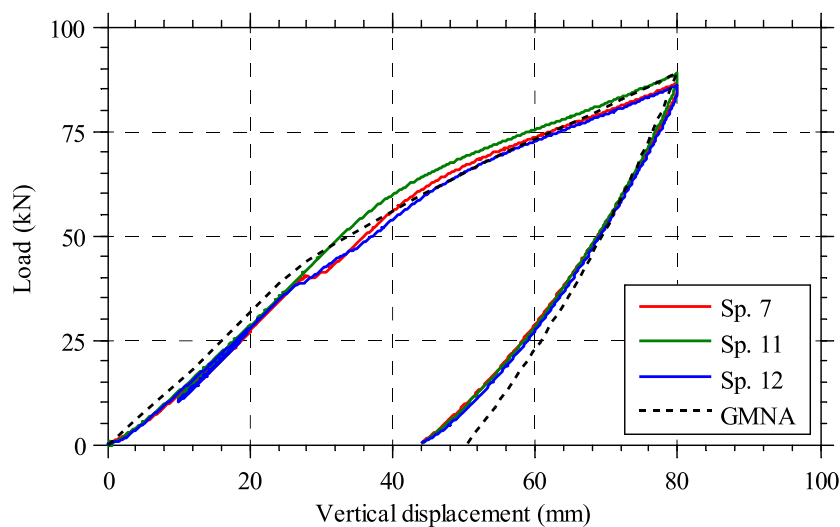


Figure 4-18: Load-displacement curves at the crown of shallow arches under tension.

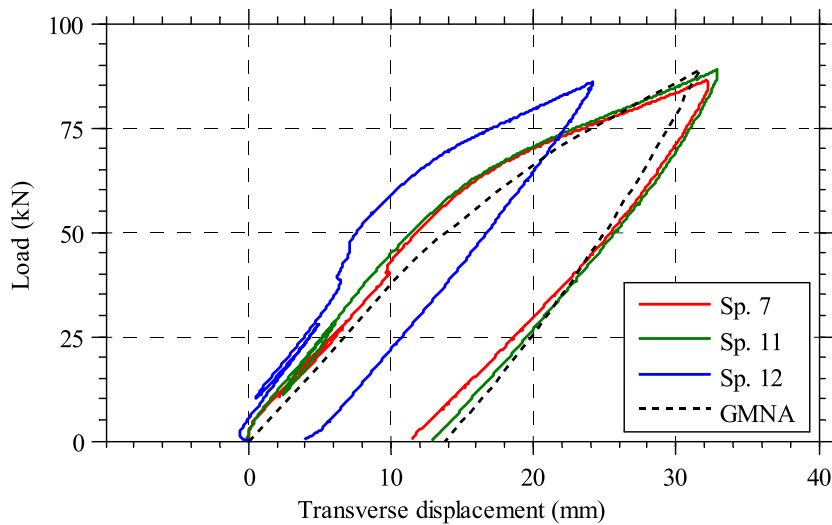


Figure 4-19: Load-displacement curves at the inclined LVDT of shallow arches under tension.

Characteristic strain gauge measurements, including the developed longitudinal strains at the top and bottom flange middles, along with the transverse strains at the bottom flange middle, are compared to the corresponding values obtained from GMNA in Figure 4-20. The increased yield strength of the roller-bent specimens compared to the GMNA is attributed to the strain aging effect. The failure mode at the end of this set of tests (Sp. 7, 11 and 12) as well as the GMNA are similar to the one depicted in Figure 4-14.

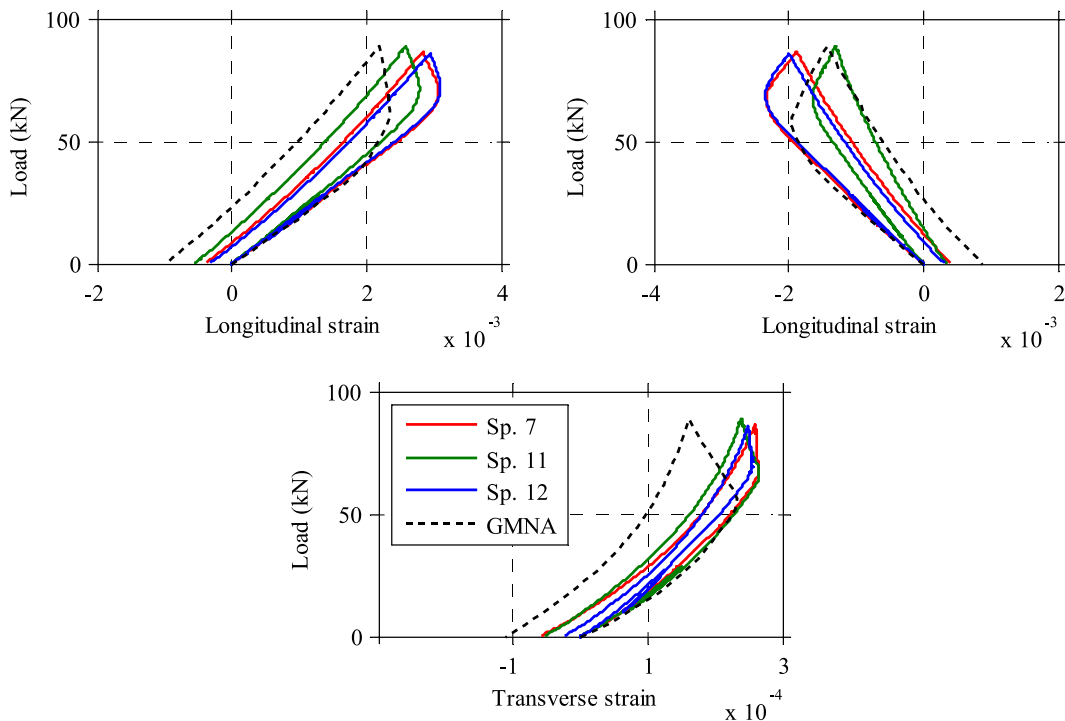


Figure 4-20: Longitudinal strain at the top flange (top-left), the bottom flange (top-right) and transverse strain at the bottom flange (bottom) of shallow arches under tension.

#### 4.4 COMPARISON OF ROLLER-BENT AND STRESS-FREE MODELS

Taking advantage of the computed residual stress distributions, a preliminary assessment of the roller-bending influence on the structural behavior of arches is carried out in this section. To that end, a direct comparison between identical roller-bent and stress-free numerical models of the high and shallow arches is performed. Geometry and material nonlinear analyses are carried out under a concentrated compressive and tensile load at the crown, similarly to the tests. A comparison of the equilibrium paths between roller-bent and stress-free models of high arches under compressive and tensile loading is presented in Figure 4-21 and Figure 4-22, respectively, in terms of imposed load and vertical displacement at the crown. The residual stresses are found to have a negligible effect on the initial stiffness of the arches for the specific loads. Furthermore, the load-bearing capacity under compressive loading is slightly increased due to roller bending ( $\sim 5\%$ ), while the response under tensile loading is almost unaffected. The failure mode of the roller-bent and stress-free arches is dominated by inelastic local buckling at the top and bottom flanges at the crown under compression and tension respectively, same as in the tests. A similar response was encountered in the shallow arches as well.

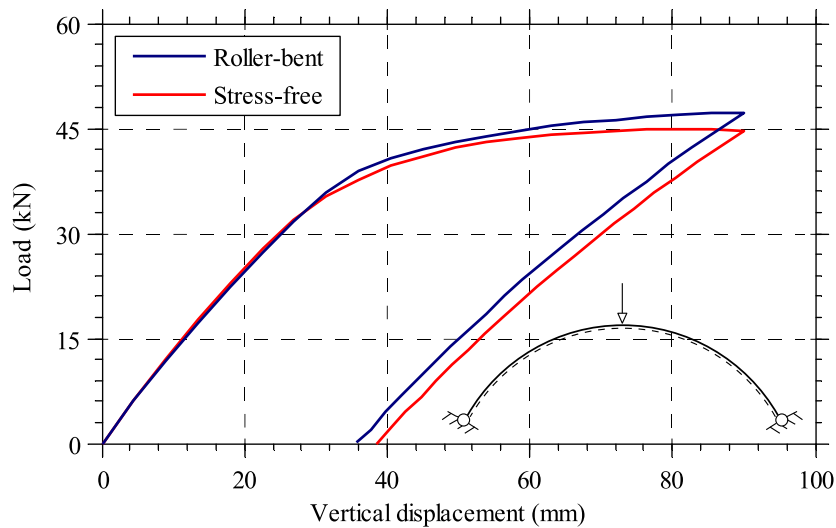


Figure 4-21: Comparison between roller-bent and stress-free model under compressive load.

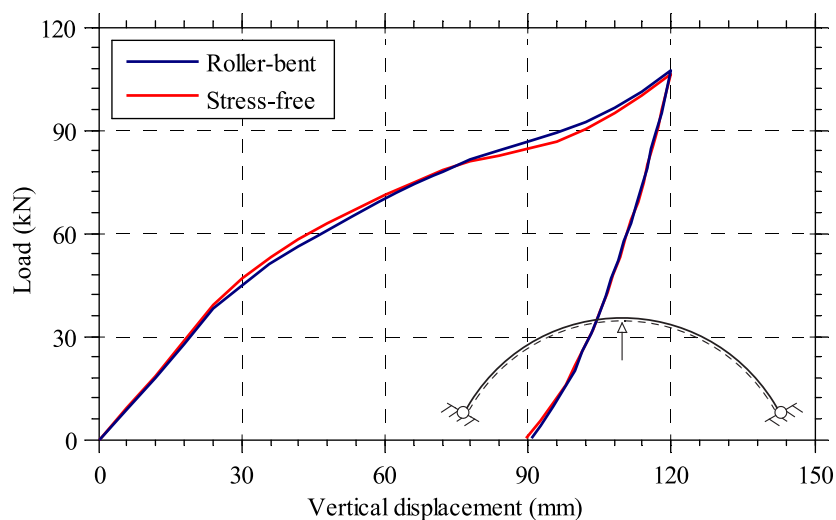
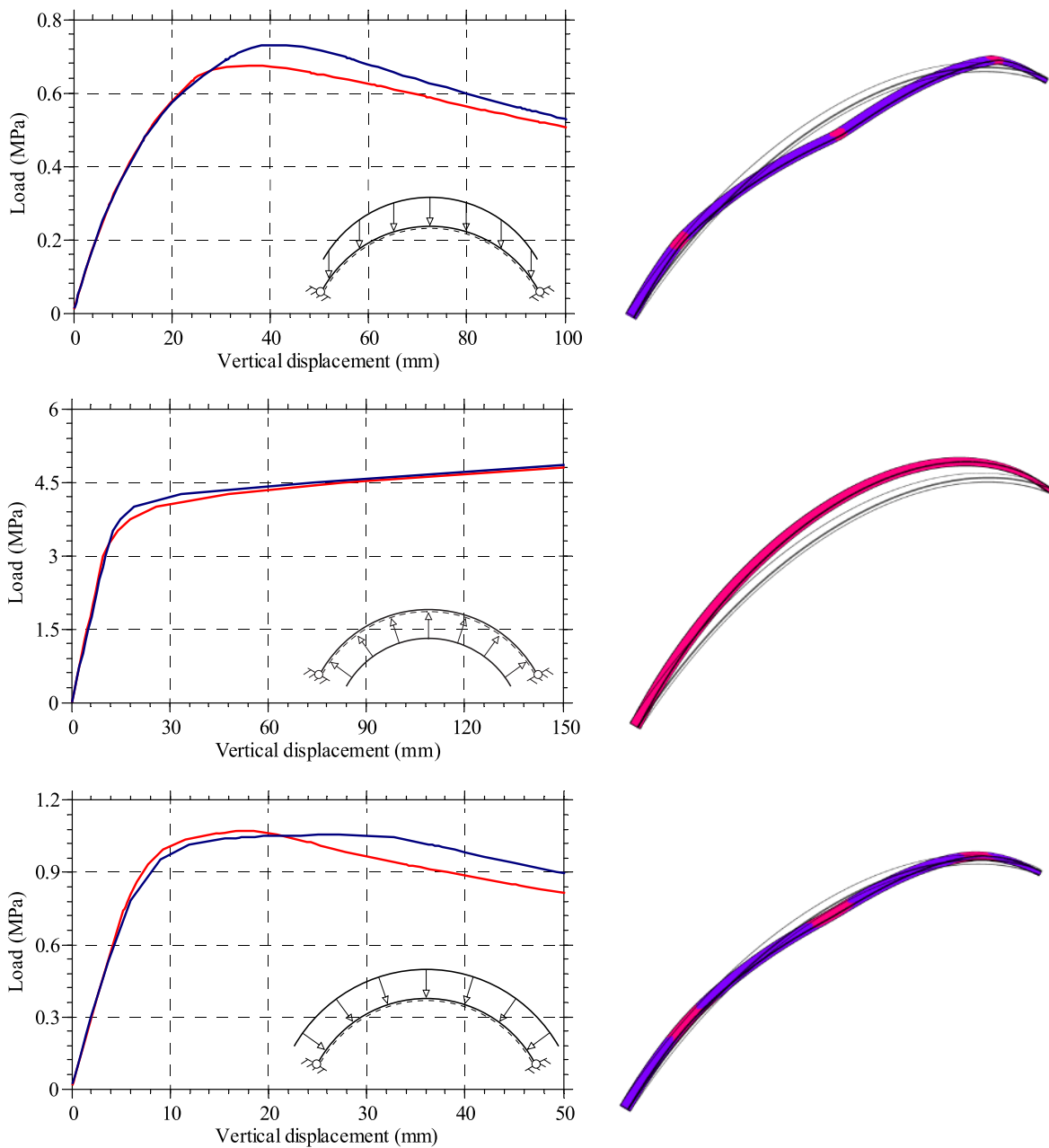


Figure 4-22: Comparison between roller-bent and stress-free model under tensile load.

Moreover, GMNA are performed on the roller-bent and stress-free models under various load conditions that are typically encountered in arched structures. A comparison of the obtained equilibrium paths between the roller-bent and stress-free models is shown in Figure 4-23, in terms of imposed load and vertical displacement at the crown, for uniform compressive loads in the gravity and radial directions, as well as uniform suction and semi suction-pressure loads that correspond to the main actions of the wind. Once again, residual stresses are found to have a negligible effect on the initial stiffness. The load-bearing capacity under uniform gravity loading is increased due to roller bending by approximately 10%, while in the other load cases, residual stresses have a smaller effect. In all cases, the failure modes are similar in both the roller-bent and stress-free models (Figure 4-23).



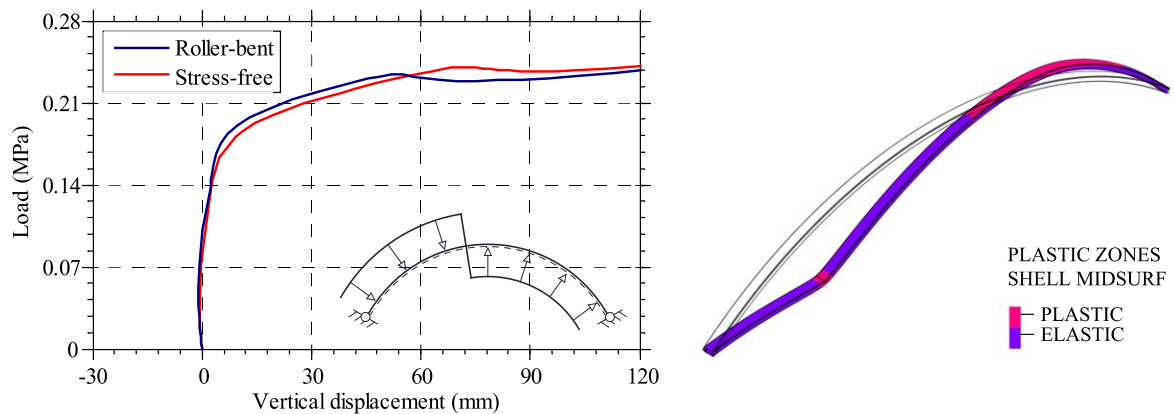


Figure 4-23: Comparison of load-displacement equilibrium paths and failure modes between roller-bent and stress-free arches under various loading conditions.

## 4.5 CONCLUSIONS

In this chapter, finite element simulation of the experimental tests on roller-bent arches comprising Rectangular-Hollow-Sections (c.f. Chapter 3) was presented. In order to maintain an acceptable level of accuracy and at the same time reduce the computational effort, the finite element simulation was conducted in three successive phases, including the explicit roller-bending formation process, the configurations of hinge support and loading cylinders, as well as the compressive and tensile loading tests. A non-symmetrical residual stress layout about the bending axis was obtained, differing significantly from the anti-symmetrical distribution of the theoretical model. Remarkable stress concentrations were located at the edges of the bottom flange, in agreement with the proposed model of Chiew et al. (2016). The bending curvature had an insignificant effect on the residual stress formations, similar to Timoshenko theory. Experimental and numerical results were compared in terms of load-displacement equilibrium paths, strain-gauge measurements and deformed shapes, providing good quantitative and qualitative agreement. The roller-bent arches exhibited increased yield strength compared to GMNA, attributed to the strain aging effect, which is encountered when steel is deformed plastically and then allowed for a period to age in room temperature. A preliminary assessment of the roller-bending influence on the structural behavior of arches was performed through a direct comparison between identical roller-bent and stress-free numerical models under various load conditions. In this context, the effect of residual stresses on the overall response of arches was found quite small, exhibiting a varying effect up to 10% which depends on the developed axial-bending interaction.

## REFERENCES

- ADINA R&D Inc. (2017). *Theory and modeling guide*. Watertown, MA, USA.
- Bathe, K.J. (2014). *Finite Element Procedures*. Prentice Hall, Pearson Education, Inc., Watertown, USA.
- Chajes, A., Britvec, S.J. and Winter, G. (1963). "Effects of Cold-Straining on Structural Sheet Steels." *Journal of the Structural Division*. *ASCE*, vol. 89, pp. 1–32.
- Chiew, S.P., Jin, Y.F. and Lee, C.K. (2016). "Residual Stress Distribution of Roller Bending of Steel Rectangular Structural Hollow Sections." *Journal of Constructional Steel Research*, vol. 119, pp. 85–97.
- Dimopoulos, C. A., and Gantes, C. J. (2008). "Nonlinear in-plane behavior of circular steel arches with hollow circular." *Journal of Constructional Steel Research*, vol. 64, pp. 1436–1445.

- Gantes, C. J., and Fragkopoulos, K. A. (2009). "Strategy for numerical verification of steel structures at the ultimate limit state." *Structure and Infrastructure Engineering*, vol. 6, pp. 1–31.
- Guo, Y., Chen, H., Pi, Y., and Andrew, M. (2016). "In-plane strength of steel arches with a sinusoidal corrugated web under a full-span uniform vertical load: Experimental and numerical investigations." *Engineering Structures*, vol. 110, pp. 105–115.
- Guo, Y., Zhao, S., Pi, Y., Andrew, M., and Dou, C. (2015). "An experimental study on out-of-plane inelastic buckling strength of fixed steel arches." *Engineering Structures*, vol. 98, pp. 118–127.
- Huang, Y., Liu, A., Zhu, C., Lu, H., and Gao, W. (2019). "Experimental and numerical investigations on out-of-plane ultimate resistance of parallel twin-arch under uniform radial load." *Thin Walled Structures*, vol. 135, pp. 147–159.
- Komatsu, S., and Sakimoto, T. (1977). "Ultimate Load Carrying Capacity of Steel Arches." *ASCE J. Struct. Div.*, vol. 103, pp. 2323–2336.
- La Poutré, D. B. La, Spoorenberg, R. C., Snijder, H. H., and Hoenderkamp, J. C. D. (2013). "Out-of-plane stability of roller bent steel arches - An experimental investigation." *Journal of Constructional Steel Research*, vol. 81, pp. 20–34.
- Lange, J. and Grages, H. (2009). "Influence of the Bauschinger Effect on the Deflection Behavior of Cambered Steel and Steel Concrete Composite Beams." *Structural Engineering International*, International Association of Bridge and Structural Engineers.
- Lu, Y., Cheng, Y., and Han, Q. (2017). "Experimental investigation into the in-plane buckling and ultimate resistance of circular steel arches with elastic horizontal and rotational end restraints." *Thin Walled Structures*, vol. 118, pp. 164–180.
- Papangelis, J. P., and Trahair, N. S. (1987). "Flexural–Torsional Buckling of Arches," *ASCE J. Struct. Eng.*, vol. 113, pp. 889–906.
- Pi, Y., Trahair, N.S. (1996). "Three-dimensional nonlinear analysis of elastic arches." *Engineering Structures*, vol. 18, pp. 49–63.
- Sakata, T., and Sakimoto, T. (1990). "Experimental study on the out-of-plane buckling strength of steel arches with open cross-section." *Proc. Japan Soc. Civ. Engrs*, vol. 416, pp. 101–112.
- Sakimoto, T., and Komatsu, S. (1983). "Ultimate Strength Formula for Steel Arches." *ASCE J. Struct. Div.*, vol. 109, pp. 613–627.
- Sakimoto, T., Yamao, T., and Komatsu, S. (1979). "Experimental Study on the Ultimate Strength of Steel Arches." *Proc. Jpn. Soc. Civ. Eng.*, No. 286, pp. 139–149.
- Spoorenberg, R. C., Snijder, H. H., Hoenderkamp, J. C. D., and Beg, D. (2012). "Design rules for out-of-plane stability of roller bent steel arches with FEM." *Journal of Constructional Steel Research*, vol. 79, pp. 9–21.
- Timoshenko, S. P. (1956). *Strength of Materials Part II - Advanced Theory and Problems*, 3rd Ed., D. Van Nostrand Company, New York, NY.



# 5 ROLLER-BENDING SIMULATION OF SHS/RHS ARCHES

## 5.1 INTRODUCTION

Curved constructional steel members have seen much use in modern construction, constituting an attractive solution due to their aesthetic appeal and the variety of forms that can be created. Roller-bending is a typical method of curving constructional steels using a 3-roller bending machine on hot-finished steel sections. Square (SHS) and Rectangular Hollow Sections (RHS) comprise the most challenging cases, as, without the correct machinery to support internally the section's flanges, the process usually results in concavity distortion or even buckling. An example of roller-bending a workpiece of square-hollow-section is depicted in Figure 5-1 (left). Rectangular-hollow-sections can be bent either the "hard way", about the major axis, or the "easy way", about the minor axis, as shown in Figure 5-1 (right). Even though more pressure is required to produce a bend the hard way, the resulting section is less likely to distort precisely because it is more rigid than a section curved the easy way.

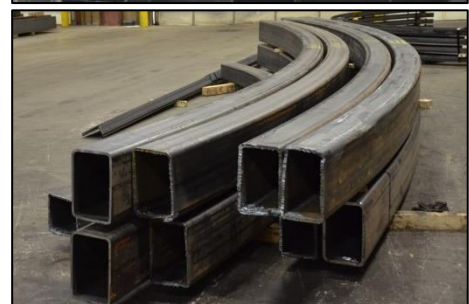
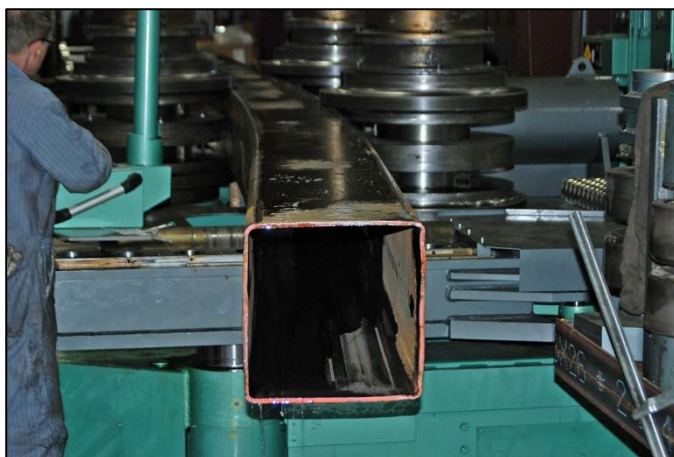


Figure 5-1: Roller-bending of SHS (left) and RHS bent the "hard way" (top-right) and "easy way" (bottom-right).

A classification of SHS/RHS according to their slenderness and steel grade is given in EN1993-1-1 (CEN, 2005). The sections that are classified as Class 1, are able to develop plastic deformations without the occurrence of local buckling, constituting the ones commonly used in roller-bending applications. The minimum allowed radius of curvature is limited by the maximum magnitude of cross-sectional distortion that may take place during bending process. Square and Rectangular hollow sections tend to distort as illustrated in Figure 5-2, exhibiting concave compression of the bottom flange and outward bowing of the webs. The primary sources of distortion are sidewall crippling due to high contact forces from the roller, web local buckling caused by the combined shear and flexural stresses. Another common form of distortion for SHS/RHS is the reduction of the tension flange width, along with the widening of the compression flange, due to the Poisson effect. Sectional distortions are often limited by implementing internal support mechanisms, such as mandrels (smaller sections), or filling hollow cavities with sand.

Curvature tolerances are similar to the standard cambering tolerances of straight members, according to the Code of Standard Practice for Steel Buildings (AISC, 2016); the maximum deviation in curvature measured at the middle ordinate shall be less than the total arc length over 500. The allowable cross-sectional variations for roller-bent square and rectangular hollow-sections are the mill tolerances given in ASTM A500 (ASTM, 2016); for cross-sections larger than 140mm, the tolerance is 1% of the largest outside flat dimension. However, it is impractical to expect post-bending imperfections to meet the ASTM requirements, since the initial geometric imperfections are amplified during the bending process. Post-bending tolerances of 1% to 2% are considered typical (Kennedy, 1988). For cases where the section forms a keystone shape, maximum deformations of approximately  $\pm 5\%$  of the cross-sectional width can be expected. For Architecturally Exposed Structural Steel, the suggested tolerance for all distortion types is one-half of those specified in ASTM A500 (AISC, 2003). Following a limited survey on the available bending capabilities of several roller-benders, records of past projects regarding the minimum radii achieved without appreciable distortion, are given in Table 5-1 (Dowswell, 2018).

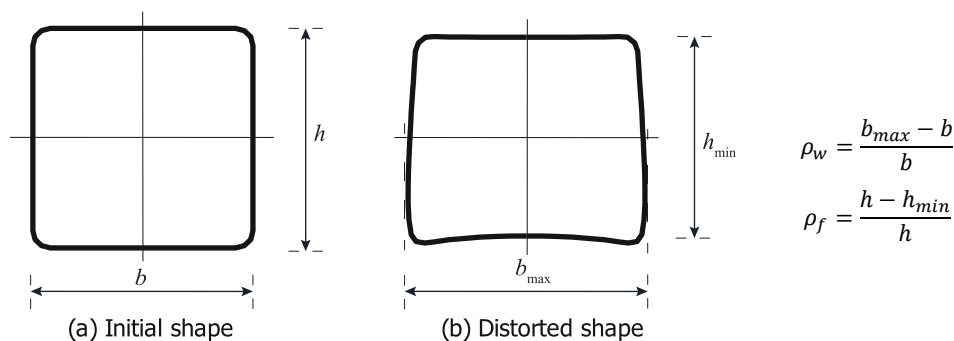


Figure 5-2: Example of SHS distortion due to roller-bending ( $\rho_w = 8\%$  and  $\rho_f = 6\%$ ).

Table 5-1: General guidelines for minimum cold-bending radii of SHS/RHS (Dowswell, 2018).

Member	Minimum Bending Radius, $R_d$ (m)	Minimum $R/h$
<b>Square-Hollow-Sections</b>		
152.4x152.4x12.7	0.9 to 2.3	6.5 to 16
152.4x152.4x6.35	1.4 to 9.1	6.5 to 16
<b>Rectangular-Hollow-Sections</b>		
304.8x152.4x12.7	2.7 to 3.7	9.5 to 13
152.4x304.8x12.7	2.6 to 6.1	18 to 41

Note: The minimum radii listed are for general guidance in the conceptual design stages and smaller radii can often be obtained.

A theoretical model of the residual stress distribution after curving has been proposed by Timoshenko (1956), as a function of the steel's yield stress  $f_y$  and the ratio  $\alpha$  between the plastic and elastic section modulus; the proposed model is based on the Euler-Bernoulli beam theory by aggregating uniaxial stresses from inelastic bending and elastic spring-back, as shown in Figure 5-3. The ratio  $\alpha$  ranges between 1.20 and 1.30 for RHS curved about the major axis, 1.15 to 1.25 for SHS, and 1.10 to 1.20 for RHS curved about the minor axis. Based on the assumptions of the simplified model, the theoretical distribution is generally valid for bending beams exhibiting small shear stresses relative to the bending stresses, as well as uniform bending stresses across the cross-sectional width.

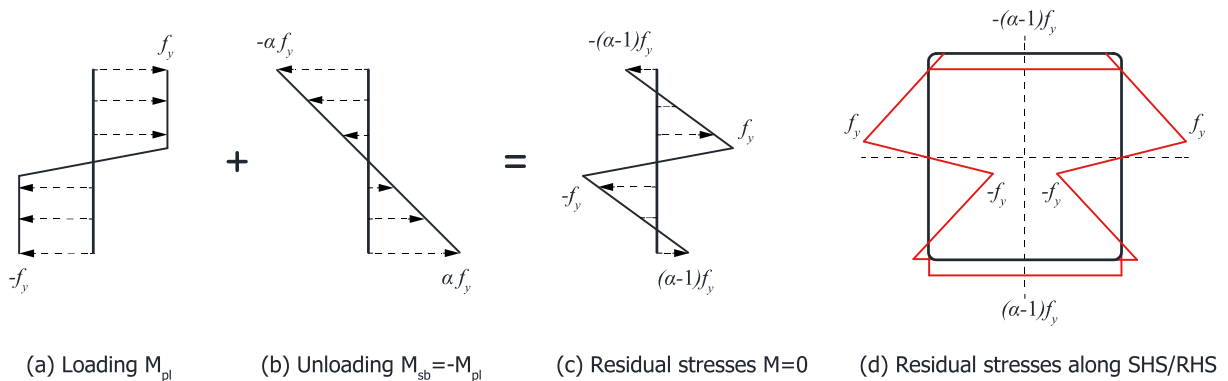


Figure 5-3: Theoretical distribution of residual stresses.

The residual stress distributions of roller-bent RHS have been studied by Chiew et al. (2016), differing significantly from the theoretical distribution. Differences can be interpreted by considering that the classical beam theory is not accurate for bending beams that are deep and short in length, as the beam segment within the three-point-bending length, where shear stresses become large relative to the bending stresses and thus cannot be neglected. Moreover, flanged sections under concentrated bending forces exhibit localized effects of plates (Timoshenko and Woinowsky-Krieger, 1987), including stress concentrations at the web-to-flange junctions (shear-lag effect), which result in non-uniform bending stress distributions over the width. In this chapter, a more in-depth insight on the membrane residual stress and strain formations emanating from the roller-bending process of SHS/RHS workpieces is provided, by means of nonlinear finite element simulations. Similar roller-bending simulations and pertinent residual stresses have been validated in Chapter 4. Mesh sensitivity analyses are first performed to verify the accuracy of the obtained results, followed by parametric investigations in order to assess the effects of the main roller-bending characteristics on the developed stress/strain distributions.

## 5.2 NUMERICAL MODELING

Detailed finite element models of the roller-bending process are developed, aiming at estimating the locked-in stress/strain formations in a reliable manner. Initially straight workpieces of SHS/RHS are modeled with a uniform and sufficiently dense mesh of shell or solid elements, following a mesh convergence study (cf. Section 5.3). Null initial residual stresses are assumed on the straight workpieces, since the final patterns are independent of the initial conditions. Shell elements are employed on the surfaces of bending dies, which are connected to their center of rotation via rigid links in order to provide rigidity. The interaction between workpieces and dies is considered by introducing contact elements between their interfaces. Advantage is taken of symmetry conditions in order to reduce the computational effort and thus, appropriate boundary conditions are applied on the pertinent Degrees of Freedom (DOFs). The numerical model along with the employed boundary conditions are shown in Figure 5-4.

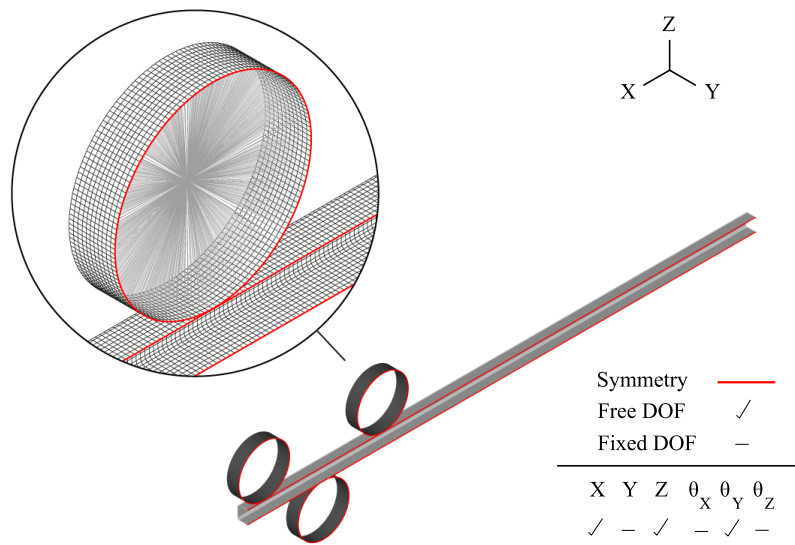


Figure 5-4: Finite element model and boundary conditions.

Geometry and Material Nonlinear Analyses (GMNA) are carried out in the general-purpose finite element software ADINA (ADINA, 2017). Large displacement and strain formulations are employed, since cross-sectional ovalities and distortions are important. An elastic – fully plastic material model is employed in the finite element analyses, comprising a bilinear constitutive law without hardening. The softening response due to the Bauschinger effect, encountered when steel is cyclically yielded in tension and compression, is not taken into account in the analyses. The influence of strain hardening and the Bauschinger effect is considered negligible on the residual stress/strain formations, since the plastic strains that are developed in roller-bending applications are typically small, and the yield direction remains always towards the same side during multi-passes. The plasticity model is characterized by the von Mises yield criterion and the Prandtl–Reuss flow rule. The modulus of elasticity  $E$  is taken equal to 210GPa, while various steel grades are examined. Implicit analyses are carried out using the Newton – Raphson solution algorithm for the geometrically and materially nonlinear equations. The rigid target algorithm, which is mainly used for metal-forming applications, is employed for the solution of the nonlinear contact equations. The Coulomb friction coefficient of the contacting surfaces is taken equal to 0.3.

The analysis sequence is illustrated schematically in Figure 5-5, where a prescribed displacement at the middle roller is applied first towards the beam, followed by a prescribed rotation at the centers of the other two rolls. Through contact traction, the workpiece is fed inside the bending machine. A sufficiently small load-step magnitude is required to reach uniform plastification, leading consequently to a uniform distribution of residual stresses along the workpiece. The placement requirements within the three-point-bending restrain bending of the workpiece close to its edges; these regions are trimmed in practice at the end of roller-bending. Even though multiple passes are practically needed to achieve the desired radius of curvature, a single-forming pass is analyzed, since residual stresses are found to be identical for single- and multiple- pass roller-bending.

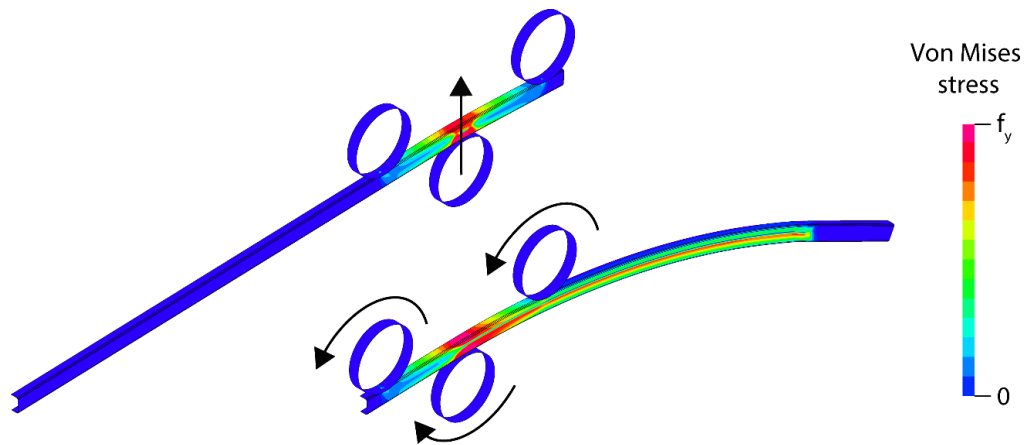


Figure 5-5: Numerical simulation of the roller-bending process.

### 5.3 VALIDATION STUDY

In this section, a validation study is performed in order to verify the accuracy of the stress/strain results obtained from the finite element analyses. To that end, an RHS 50x100 workpiece of thickness 5mm is modeled with either shell or solid elements, and afterwards the mesh is refined. In the first case, 4-node shell elements (Figure 5-6a) with 5 integration points at the element thickness direction are used to model the workpiece. The Newton-Cotes integration method is employed, since it is more effective for capturing the onset and spread of the materially nonlinear conditions, as the integration points are on the boundaries of the elements. Secondly, the workpiece is simulated with 8-node solid elements (Figure 5-6b), exhibiting three integration points in each direction. In the third case, a mesh refinement of the shell element model is performed by subdividing the mesh size one time in both directions (Figure 5-6c). The element aspect ratio ranges between 1.0 and 2.0.

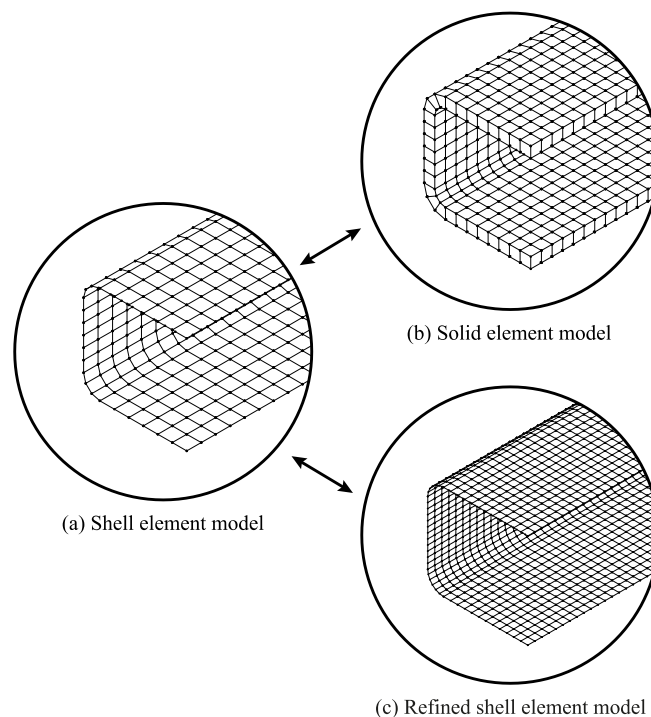


Figure 5-6: Numerical validation models.

For comparison purposes, identical roller-bending characteristics are employed in the mesh sensitivity analyses, regarding the curving radius  $R = 2.50\text{m}$ , the steel yield stress  $f_y = 355\text{MPa}$ , the bending length  $S = 0.90\text{m}$  and the diameter of rolls  $d_r = 0.30\text{m}$ . The convergence study is performed by comparing the membrane residual stress/strain formations at the end of roller-bending. The membrane residual stresses  $\sigma_{memb}$  are calculated by averaging stresses  $\sigma_x$  over the thickness direction, according to Eq. (5-1). The membrane strains  $\epsilon_{memb}$  are calculated from the strains  $\epsilon_x$  respectively. In the case of shell elements,  $\epsilon_{memb}$  is identical to  $\epsilon_x$  at the midsurface, due to the linear distribution of flexural strains over the thickness. Note that section results are extracted with respect to the local Cartesian system of the elements. Indices  $x$  and  $z$  refer respectively to the longitudinal and thickness directions.

$$\sigma_{memb} = \frac{1}{t} \int_{-t/2}^{t/2} \sigma_x dz \quad (5-1)$$

A comparison of the membrane residual stresses and strains between the shell (initial mesh) and solid element models, is shown in Figure 5-7. As it is evidenced, the overall distribution is similar in both cases. The slight discrepancies in membrane stresses are attributed to the different formulations between shell and solid elements. Solid elements tend to lock when they are very thin, making them unsuitable for bending analyses of thin structures. Shell elements are more efficient for modeling thin-walled structures but encounter the limitation that any flexural stress/strain distributions are captured approximately. However, scope of the numerical model is to identify the predominant membrane component of residual stresses, which can be exploited by analysts to assess the structural behavior of roller-bent sections.

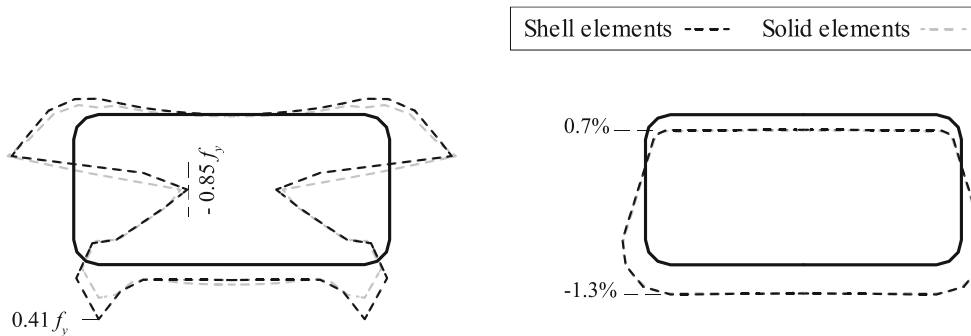


Figure 5-7: Membrane residual stresses (left) and strains (right) of the shell and solid element models.

A comparison of the membrane residual stresses and strains between the initial and refined shell element models, is shown in Figure 5-8. Very good convergence is evidenced in both cases; maximum discrepancies do not exceed  $0.1 f_y$ .

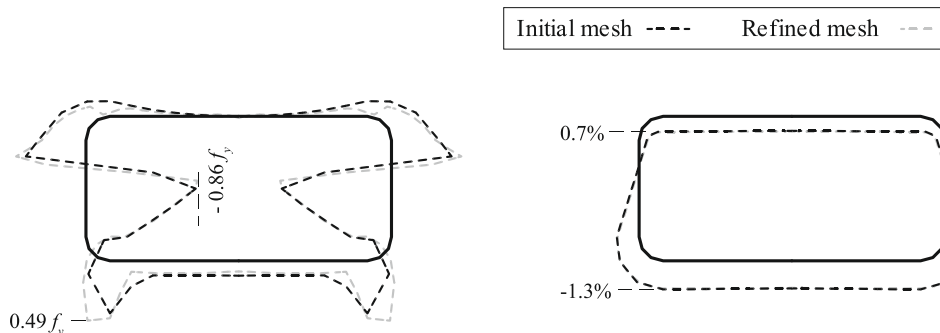


Figure 5-8: Membrane residual stresses (left) and strains (right) of the initial and refined shell element models.



Based on the results of sensitivity analyses, the shell element model employing the initial mesh size is considered to provide sufficiently accurate results in terms of membrane residual stresses and strains for the roller-bent RHS workpiece. Overall, a non-symmetrical residual stress layout about the bending axis is obtained over the cross-sectional width and height, differing significantly from the anti-symmetrical distribution of the simplified theoretical model. More specifically, tensile residual stresses are encountered in both the top- (elongated) and bottom- (shortened) height of the roller-bent RHS, exhibiting stress-concentrations at the web-to-flange junctions of the bottom flange. The magnitude of developed strains in the shortened zone  $\varepsilon_{sh}$  are found slightly higher than the corresponding values of the tensioned zone  $\varepsilon_{el}$ . The strains  $\varepsilon_{sh}$  and  $\varepsilon_{el}$  satisfy the fundamental strain-curvature relationship of Eq. (5-2) .

$$\frac{1}{R} = \frac{\varepsilon_{el} - \varepsilon_{sh}}{d} \quad (5-2)$$

#### 5.4 PARAMETRIC ANALYSES

In this section, parametric analyses are carried out aiming at estimating the quantitative and qualitative effects of the main roller-bending characteristics on the residual stress/strain distributions. The parametric analyses are performed using the shell element model, based on the mesh convergence study of Section 5.3. Three cross-sections of different aspect ratios  $h/b$  are employed in the numerical analyses, namely RHS 80x120, SHS 100x100 and RHS 120x80. The cross-sections remain constant in all cases, while the cross-sectional thickness, the radius of curvature, the steel grade, the bending length and the diameter of rolls are varied within an appropriate range, representing common-in-practice roller-bending cases (Figure 5-9). The parameters are normalized with respect to the cross-sectional height, in order to obtain dimensionless results. Therefore, residual stress/strain results are presented with respect to: (i) the thickness ratio  $h/t$ , (ii) the bending ratio  $R/h$ , (iii) the yield stress  $f_y$ , (iv) the normalized bending length  $S/h$ , and (v) the normalized roll diameter  $d_r/h$ .

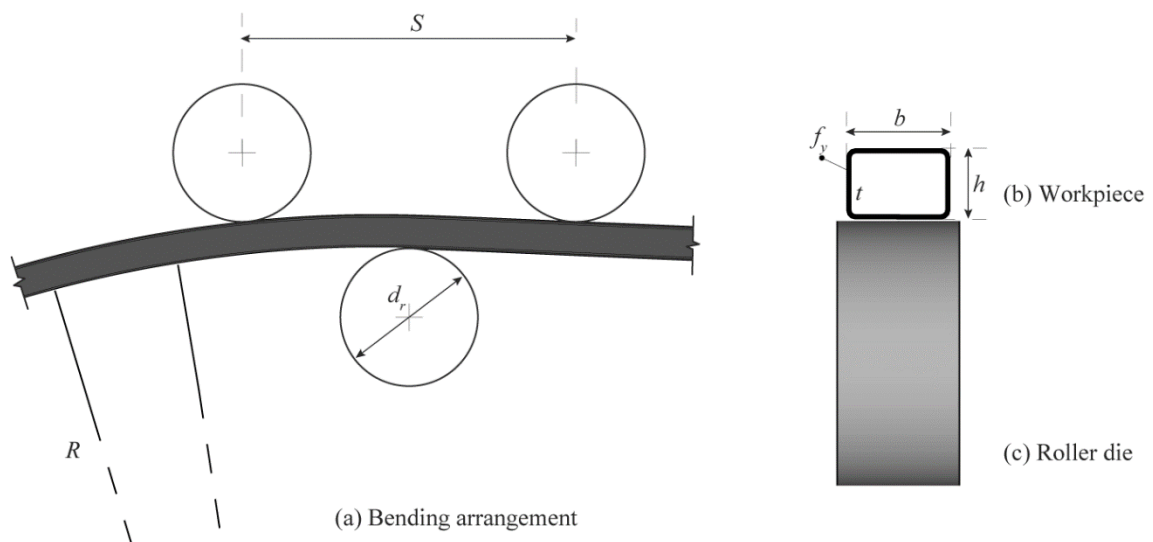


Figure 5-9: Main roller-bending parameters.

### 5.4.1 Thickness ratio $h/t$

The thickness ratio  $h/t$  between the height  $h$  and thickness  $t$  of the section, is associated with the cross-sectional stiffness and slenderness. Parametric analyses are carried out for RHS workpieces roller-bent about the minor axis, exhibiting a cross-sectional aspect ratio  $h/b$  of 0.66 and various  $h/t$ . The examined thickness ratios are equal to 8.0, 10.0 and 13.3, which are typical of Class 1 cross-sections. For comparison purposes, identical roller-bending characteristics are employed in all cases regarding the bending ratio  $R/h = 43.75$ , the yield stress  $f_y = 355\text{MPa}$ , the normalized bending length  $S/h = 11.25$ , and the normalized roll diameter  $d_r/h = 3.75$ . The membrane residual stresses and strains between the examined thickness ratios are compared in Figure 5-10. As it is observed, the locked-in stress formations of roller-bent RHS are correlated with the cross-sectional thickness ratio.

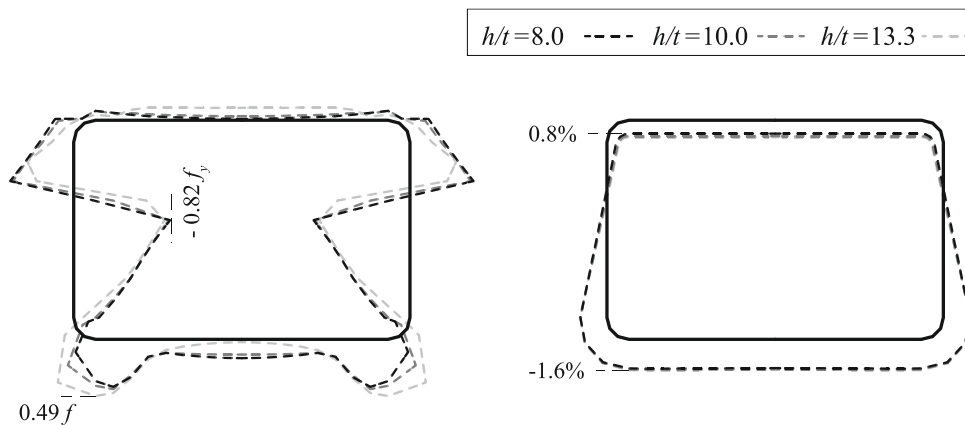


Figure 5-10: Membrane residual stresses (left) and strains (right), for  $h/b = 0.66$ .

Further parametric analyses are carried out for SHS workpieces exhibiting thickness ratios equal to 10.0, 12.5 and 16.6 and employing identical roller-bending characteristics in all cases ( $R/h = 35.00$ ,  $f_y = 355\text{MPa}$ ,  $S/h = 9.00$ , and  $d_r/h = 3.00$ ). A comparison of the membrane residual stresses and strains between the examined thickness ratios is shown in Figure 5-11. Once again, the residual stresses are found to vary significantly with  $h/t$ .

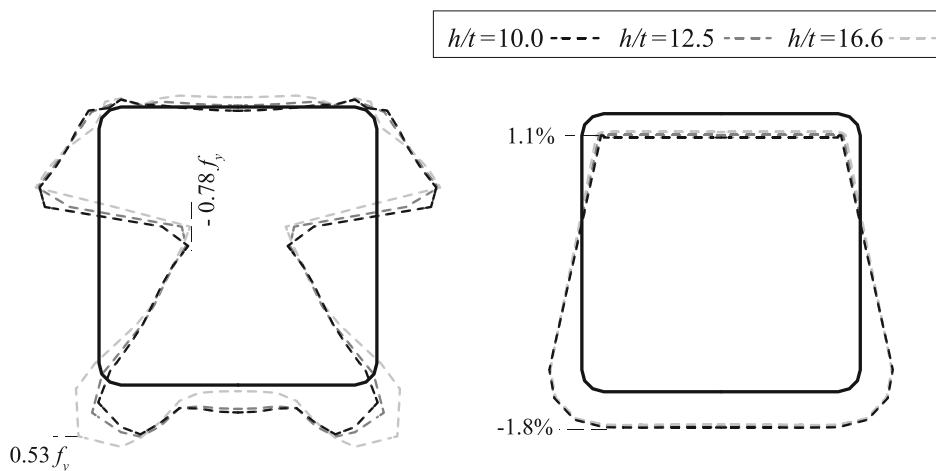


Figure 5-11: Membrane residual stresses (left) and strains (right), for  $h/b = 1.00$ .



Finally, parametric analyses are carried out for RHS workpieces roller-bent about the major axis, exhibiting a cross-sectional aspect ratio  $h/b$  of 1.50 and various  $h/t$ . The examined thickness ratios are equal to 12.0, 15.0 and 20.0, while identical roller-bending characteristics are employed in all cases regarding the bending ratio  $R/h = 29.16$ , the yield stress  $f_y = 355\text{MPa}$ , the normalized bending length  $S/h = 7.50$ , the normalized roll diameter  $d_r/h = 2.50$ . The membrane residual stresses and strains between the examined thickness ratios are compared in Figure 5-12, exhibiting variations in the locked-in stress formations.

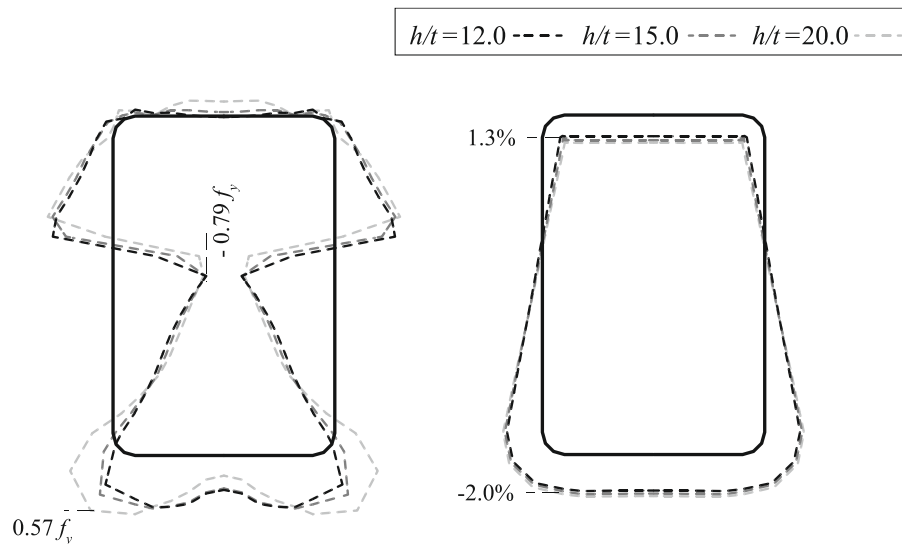


Figure 5-12: Membrane residual stresses (left) and strains (right), for  $h/b = 1.50$ .

The variations in the locked-in formations can be interpreted by considering that short-in-length flanged sections exhibit localized effects of plates, including stress concentrations at the web-to-flange junctions (shear lag effect), which result in non-uniform bending stress distributions over the width under concentrated bending forces. As cross-sections become stockier (i.e. thick-walled SHS/RHS), the stress concentrations at the web-to-flange junctions are reduced. Consequently, the theoretical assumptions of the simplified model hold more accurately in the case of cross-sections exhibiting low  $h/t$ , and pertinent residual stresses tend to the theoretical anti-symmetrical distribution (Timoshenko, 1956).

#### 5.4.2 Bending ratio $R/h$

The bending ratio  $R/h$  defined by the radius of curvature  $R$  with respect to the cross-sectional height  $h$  is related with the amount of required plastic work during roller-bending. Parametric analyses are carried out for SHS roller-bent in a range of bending radii that are commonly met in curved constructional steel members. To that effect, bending ratios equal to 35.0, 50.0 and 70.0 are examined, while typical characteristics are employed regarding the thickness ratio  $h/t = 12.5$ , the yield stress  $f_y = 355\text{MPa}$ , the normalized bending length  $S/h = 9.00$ , and the normalized roll diameter  $d_r/h = 3.00$ . A comparison of the membrane residual stresses and strains between the examined bending ratios is shown in Figure 5-13. It is observed that the radius of curvature has negligible effect on the residual stress formations, in agreement with the theoretical model. The developed strains at the top and bottom height of the section are given in Table 5-2. An approximately linear variation is evidenced between strains and the inverse of bending ratio, in accordance with the fundamental strain-curvature relationship (Eq. (5-2)).

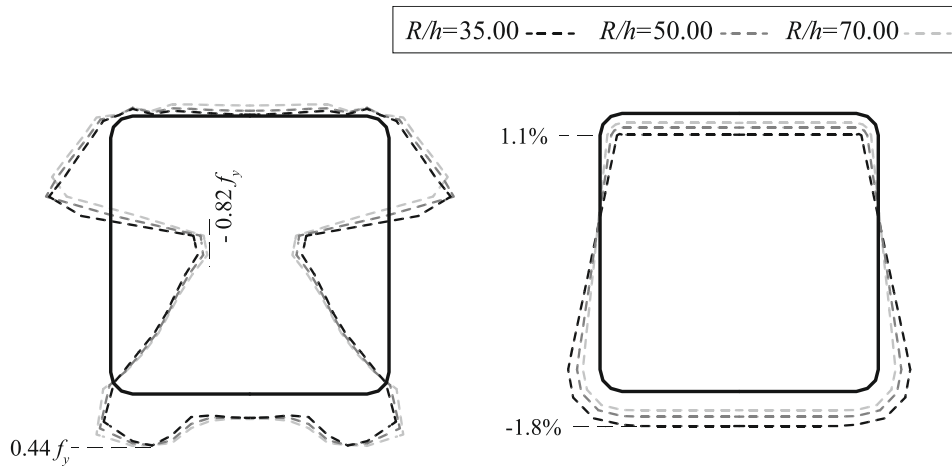


Figure 5-13: Membrane residual stresses (left) and strains (right), for  $h/b = 1.00$ .

Table 5-2: Developed strains in the compression and tension zones of the cross-section.

$h/R$	Compression zone (bottom-height)	Tension zone (top-height)
0.029	-1.8%	1.1%
0.020	-1.1%	0.9%
0.014	-0.9%	0.5%

### 5.4.3 Steel yield stress $f_y$

The yield stress  $f_y$  of steel members is correlated with the magnitude of locked-in stresses, according to the theoretical model of Timoshenko [14]. Parametric analyses are carried out for SHS of yield point equal to 235MPa, 275MPa and 355MPa, which correspond to commonly used steel grades in the constructional industry. For comparison reasons, identical roller-bending characteristics are employed in all cases, including  $h/t = 12.5$ ,  $R/h = 35.00$ ,  $S/h = 9.00$ , and  $d_r/h = 3.00$ . A comparison of the membrane residual stresses and strains between the examined steel grades, is shown in Figure 5-14. It is observed that the yield stress does not affect the residual stress/strain distributions. The magnitude of residual stresses is varied proportionally to  $f_y$ , in all cases, being in accordance with the theoretical model.

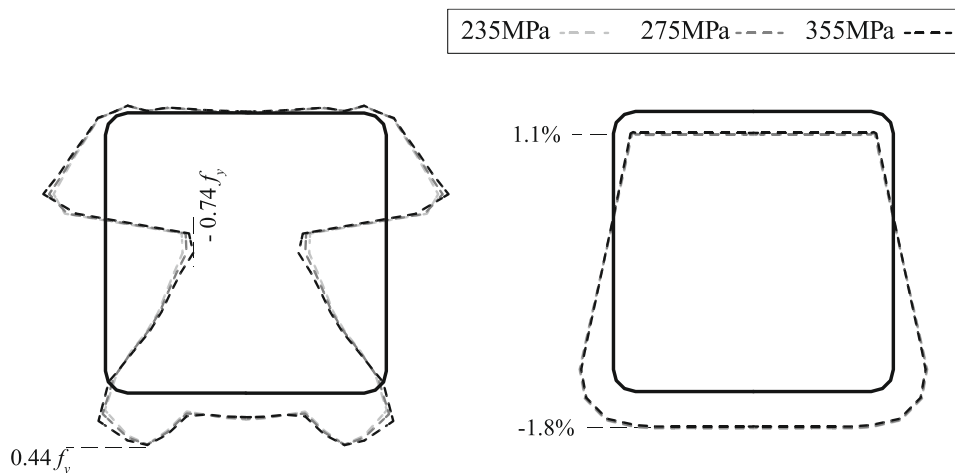


Figure 5-14: Membrane residual stresses (left) and strains (right), for  $h/b = 1.00$ .

#### 5.4.4 Normalized bending length $S/h$

The normalized bending length  $S/h$ , defined by the bending length  $S$  with respect to the cross-sectional height  $h$ , is correlated with the magnitude of the induced shear force during roller-bending. Parametric analyses are carried out for RHS roller-bent about the weak axis, exhibiting a cross-sectional aspect ratio  $h/b$  of 0.66 and a range of  $S/h$ , covering most of the combinations between bending machines and workpieces that are used in the roller-bending practice. To that end, normalized bending lengths equal to 8.75, 11.25 and 13.75 are examined, while typical roller-bending characteristics are employed in all cases, including  $h/t = 10.0$ ,  $R/h = 43.75$ ,  $f_y = 355\text{MPa}$ , and  $d_r/h = 3.75$ . A comparison of the membrane residual stresses and strains between the examined  $S/d$  is presented in Figure 5-15. As it is observed, the locked-in stress formations of roller-bent RHS are correlated with the normalized bending length.

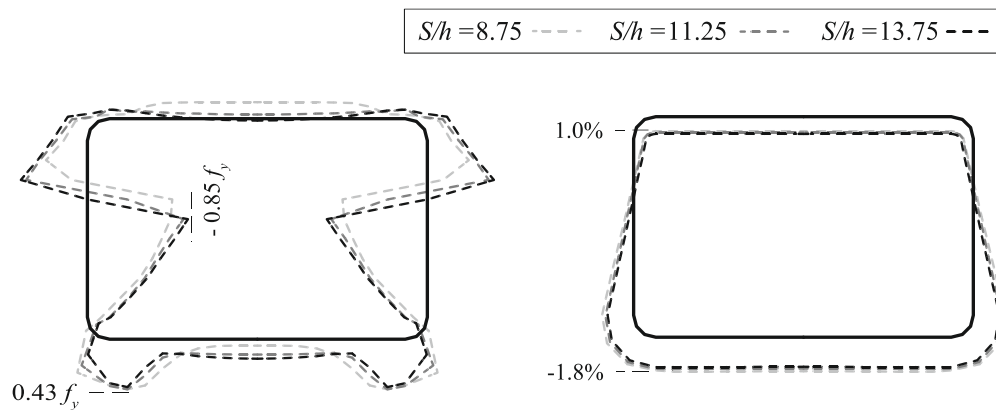


Figure 5-15: Membrane residual stresses (left) and strains (right), for  $h/b = 0.66$ .

Furthermore, parametric analyses are carried out for SHS workpieces employing a range  $S/h$  equal to 7.00, 9.00 and 11.00. For comparison reasons, identical roller-bending characteristics are employed in all cases, including  $h/t = 12.5$ ,  $R/h = 35.00$ ,  $f_y = 355\text{MPa}$ , and  $d_r/h = 3.00$ . A comparison of the membrane residual stresses and strains between the examined  $S/d$  is presented in Figure 5-16. Once again, the residual stresses are found to vary significantly with  $S/h$ .

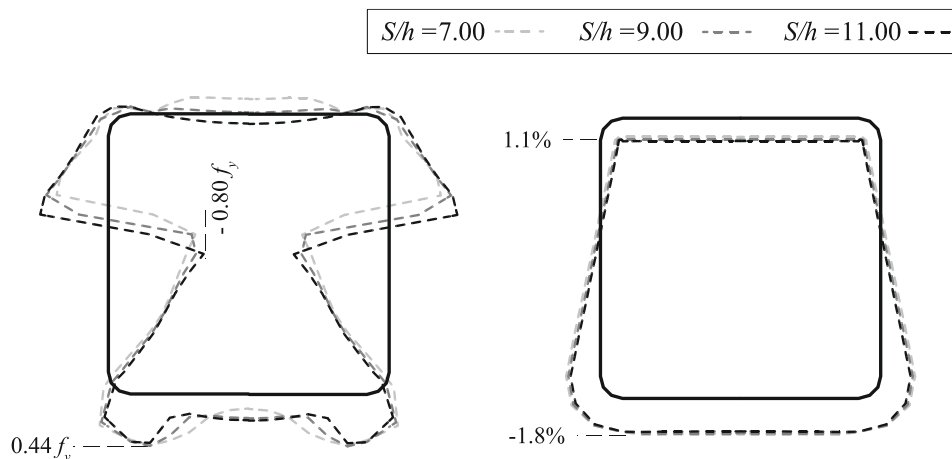


Figure 5-16: Membrane residual stresses (left) and strains (right), for  $h/b = 1.00$ .

Finally, parametric analyses are carried out for RHS roller-bent about the strong axis, exhibiting a cross-sectional aspect ratio  $h/b$  of 1.50 and employing a range of normalized bending lengths equal to 5.83, 7.50 and 9.16. For comparison reasons, identical roller-bending characteristics are employed in all cases, including  $h/t = 15.0$ ,  $R/h = 29.16$ ,  $f_y = 355\text{MPa}$ , and  $d_r/h = 2.50$ . A comparison of the membrane residual stresses and strains between the examined  $S/d$  is presented in Figure 5-17, exhibiting variations in the locked-in stress formations.

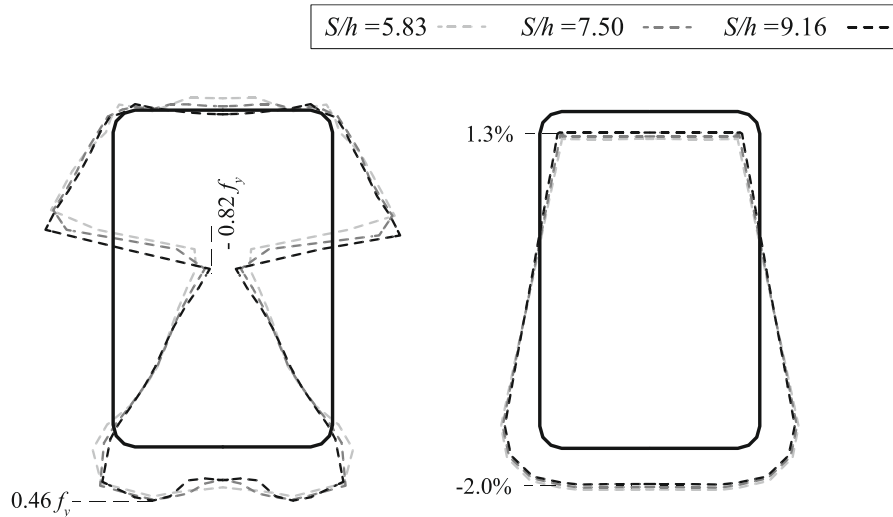


Figure 5-17: Membrane residual stresses (left) and strains (right), for  $h/b = 1.50$ .

The variations in the locked-in formations can be interpreted by considering that the magnitude of the induced shear force varies with bending length. As the normalized bending length increases, lower shear stresses relative to the bending stresses are developed within the three-point-bending length. Consequently, the theoretical assumptions of the simplified model [14] hold more accurately in the case of higher  $S/h$ , and pertinent residual stress distributions tend to the anti-symmetrical distribution.

#### 5.4.5 Normalized roll diameter $d_r/h$

The normalized roll diameter  $d_r/h$  is defined by the diameter of bending rolls  $d_r$  with respect to the cross-sectional height  $h$ . Parametric analyses are carried out for SHS workpieces roller-bent with rollers of normalized roll diameters equal to 2, 3 and 4, which are typically used by steel fabricators. For comparison reasons, identical roller-bending characteristics are employed in all cases, namely  $h/t = 12.5$ ,  $R/h = 35.00$ ,  $f_y = 355\text{MPa}$ , and  $S/h = 9.00$ . A comparison of the membrane residual stresses and strains between the examined  $d_r/h$  ratios is shown in Figure 5-18. As it is observed, the residual stress formations are not affected by the diameter of bending rolls, indicating that a similar roll-workpiece interaction is developed in the examined cases.

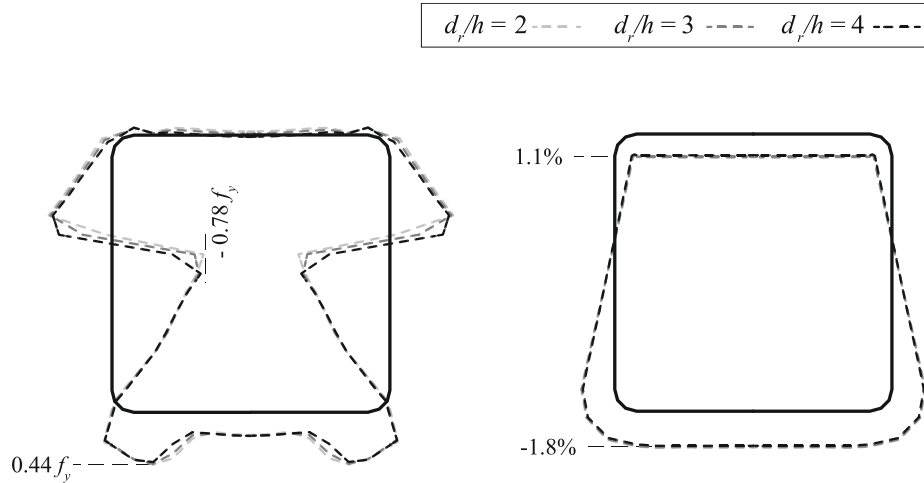


Figure 5-18: Membrane residual stresses (left) and strains (right), for  $h/b = 1.00$ .

## 5.5 RESIDUAL STRESS MODEL

Among the examined parameters, the thickness ratio  $h/t$  and the normalized bending length  $S/h$  are found to mainly affect the residual stress formations within the examined ranges. In the case of very stocky cross-sections that are roller-bent within large bending machines, the residual stress formations are considered to be better approximated by the theoretical model. Representative residual stress distributions can be extracted on the basis of the roller-bending characteristics that are encountered most commonly in practice. To that end, characteristic residual stress formations can be obtained using the mean values of  $h/t$  and  $S/h$ , which are employed within the examined ranges of the parametric study. The proposed numerical distributions are shown in Figure 5-19, Figure 5-20, and Figure 5-21, as well as, pertinent values are given in Table 5-3, Table 5-4, and Table 5-5, for the examined SHS/RHS of aspect ratios 0.66, 1.00 and 1.50, respectively. Finally, the numerical distributions satisfy the internal equilibrium over the cross-sectional area  $A$ , which is expressed by the axial force  $N$  and bending moments  $M_y$ ,  $M_z$  equilibrium equations (5-3), (5-4), and (5-5).

$$N = \int_A \sigma_x dA = 0 \quad (5-3)$$

$$M_y = \int_A \sigma_x \cdot z dA = 0 \quad (5-4)$$

$$M_z = \int_A \sigma_x \cdot y dA = 0 \quad (5-5)$$

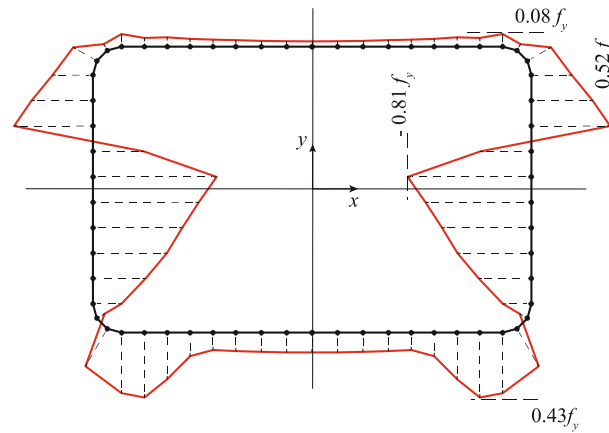
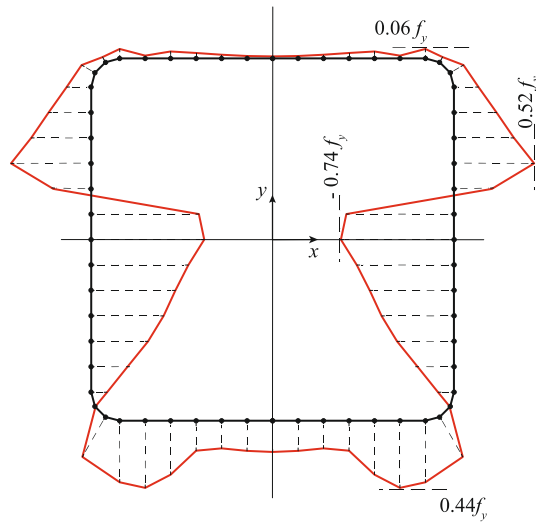


Figure 5-19: Proposed residual stress distribution of roller-bent RHS ( $h/b = 0.66$ ).

Table 5-3: Proposed residual stresses along the semi-perimeter of RHS ( $h/b = 0.66$ ).

No.	Position $x (b)$	Position $y (h)$	Membrane Stress ( $f_y$ )	No.	Position $x (b)$	Position $y (h)$	Membrane Stress ( $f_y$ )
1	0.00	-0.50	0.13	17	0.50	0.04	-0.81
2	0.06	-0.50	0.13	18	0.50	0.13	-0.33
3	0.12	-0.50	0.13	19	0.50	0.22	0.52
4	0.17	-0.50	0.12	20	0.50	0.31	0.40
5	0.23	-0.50	0.11	21	0.50	0.40	0.27
6	0.28	-0.50	0.15	22	0.49	0.45	0.18
7	0.33	-0.50	0.31	23	0.47	0.49	0.05
8	0.38	-0.50	0.43	24	0.43	0.50	0.08
9	0.43	-0.50	0.40	25	0.38	0.50	0.06
10	0.47	-0.49	0.28	26	0.33	0.50	0.06
11	0.49	-0.45	-0.06	27	0.28	0.50	0.05
12	0.50	-0.40	-0.19	28	0.23	0.50	0.05
13	0.50	-0.31	-0.35	29	0.17	0.50	0.04
14	0.50	-0.22	-0.48	30	0.12	0.50	0.04
15	0.50	-0.13	-0.59	31	0.06	0.50	0.03
16	0.50	-0.04	-0.69	32	0.00	0.50	0.03

Figure 5-20: Proposed residual stress distribution of roller-bent SHS ( $h/b = 1.00$ ).Table 5-4: Proposed residual stresses along the semi-perimeter of SHS ( $h/b = 1.00$ ).

No.	Position $x(b)$	Position $y(h)$	Membrane Stress ( $f_y$ )	No.	Position $x(b)$	Position $y(h)$	Membrane Stress ( $f_y$ )
1	0.00	-0.50	0.20	17	0.50	0.07	-0.71
2	0.07	-0.50	0.20	18	0.50	0.14	0.25
3	0.14	-0.50	0.18	19	0.50	0.21	0.52
4	0.21	-0.50	0.20	20	0.50	0.28	0.39
5	0.28	-0.50	0.35	21	0.50	0.35	0.28
6	0.35	-0.50	0.44	22	0.50	0.42	0.16
7	0.42	-0.50	0.40	23	0.49	0.46	0.10
8	0.46	-0.49	0.30	24	0.46	0.49	0.04
9	0.49	-0.46	-0.01	25	0.42	0.50	0.06
10	0.50	-0.42	-0.11	26	0.35	0.50	0.02
11	0.50	-0.35	-0.24	27	0.28	0.50	0.05
12	0.50	-0.28	-0.37	28	0.21	0.50	0.04
13	0.50	-0.21	-0.47	29	0.14	0.50	0.02
14	0.50	-0.14	-0.55	30	0.07	0.50	0.02
15	0.50	-0.07	-0.64	31	0.00	0.50	0.01
16	0.50	0.00	-0.74				

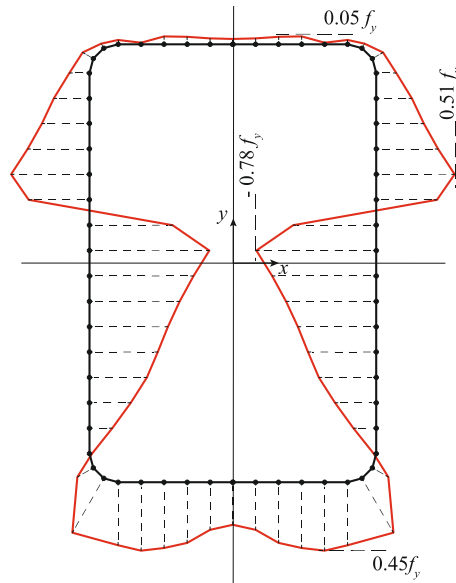


Figure 5-21: Proposed residual stress distribution of roller-bent RHS ( $h/b = 1.50$ ).

Table 5-5: Proposed residual stresses along the semi-perimeter of RHS ( $h/b = 1.50$ ).

No.	Position $x (b)$	Position $y (h)$	Membrane Stress ( $f_y$ )	No.	Position $x (b)$	Position $y (h)$	Membrane Stress ( $f_y$ )
1	0.00	-0.50	0.28	17	0.50	0.03	-0.78
2	0.08	-0.50	0.31	18	0.50	0.09	-0.54
3	0.16	-0.50	0.40	19	0.50	0.14	0.40
4	0.24	-0.50	0.43	20	0.50	0.20	0.51
5	0.32	-0.50	0.45	21	0.50	0.26	0.40
6	0.40	-0.50	0.41	22	0.50	0.32	0.31
7	0.45	-0.49	0.41	23	0.50	0.38	0.23
8	0.49	-0.47	0.12	24	0.50	0.43	0.13
9	0.50	-0.43	-0.02	25	0.49	0.47	0.08
10	0.50	-0.38	-0.15	26	0.45	0.49	0.03
11	0.50	-0.32	-0.27	27	0.40	0.50	0.03
12	0.50	-0.26	-0.37	28	0.32	0.50	0.01
13	0.50	-0.20	-0.45	29	0.24	0.50	0.05
14	0.50	-0.14	-0.51	30	0.16	0.50	0.05
15	0.50	-0.09	-0.59	31	0.08	0.50	0.04
16	0.50	-0.03	-0.68	32	0.00	0.50	0.03



## 5.6 CONCLUSIONS

The membrane residual stress and strain formations of roller-bent SHS/RHS workpieces were assessed in this section, by means of implicit analyses accounting for geometric, contact and material nonlinearities. Mesh sensitivity analyses were first performed to verify the accuracy of the obtained results. The influence of the major curving parameters, such as the cross-sectional dimensions, the yield stress, the bending radius, and the roller-bending configuration have been examined following a comprehensive parametric study. Among the examined parameters, the thickness ratio and the normalized bending length were found to mainly affect the locked-in stress formations. Variations were evidenced between the encountered distributions and the simplified theoretical model, in agreement with pertinent residual stress models in the literature (Chiew et al., 2016). More specifically, tensile residual stresses are encountered in both the top- (elongated) and bottom- (shortened) height of the roller-bent RHS, along with stress-concentrations at the web-to-flange junctions of the bottom flange. The magnitude of developed strains in the shortened zone  $\varepsilon_{sh}$  are found slightly higher than the corresponding values of the tensioned zone  $\varepsilon_{el}$ .

The encountered variations were interpreted by considering that RHS workpieces within the three-point-bending length comprise short in length flanged-sections, in which significant shear and localized effects of plates are developed that cannot be neglected (Timoshenko and Woinowsky-Krieger, 1987), including stress concentrations at the web-to-flange junctions. As cross-sections become stockier and the bending length increases, the residual stress formations are reasonably better approximated by the theoretical model (Timoshenko, 1956). Furthermore, internal supporting of the hollow cross-section with mandrels or other material such as sand, would reasonably lead to residual stress formations closer to the theoretical model. The obtained residual stress distributions were presented for the SHS/RHS of aspect ratios 0.66, 1.00 and 1.50, within the examined range thickness ratios and normalized bending lengths that are commonly encountered in practice. Moreover, characteristic residual stress distributions were proposed for square and rectangular hollow sections. Such membrane residual stress distributions can be exploited from analysts to assess the structural behavior of roller-bent members.

## REFERENCES

- ADINA R&D Inc. (2017). *Theory and modeling guide*. Watertown, MA, USA.
- AISC (2003). "Architecturally Exposed Structural Steel." AESS Supplement, *Modern Steel Construction*, American Institute of Steel Construction, May.
- AISC (2016). *Code of Standard Practice for Steel Buildings and Bridges*. American Institute of Steel Construction, Chicago, IL.
- ASTM (2016). *Selected ASTM Standards for Structural Steel Fabrication*. ASTM International, West Conshohocken, PA.
- CEN (2005). *Eurocode 3: Design of Steel Structures, Part 1-1: General Rules and Rules for Buildings, EN 1993-1-1*. Comité Européen de Normalisation (CEN), European Committee for Standardization Brussels, Belgium.
- Chiew, S.P., Jin, Y.F. and Lee, C.K. (2016). "Residual Stress Distribution of Roller Bending of Steel Rectangular Structural Hollow Sections." *Journal of Constructional Steel Research*, vol. 119, pp. 85–97.
- Dowswell, B. (2018). *Curved Member Design*. American Institute of Steel Construction, Chicago, IL.
- Kennedy, J.B. (1988). *Design Aids - Minimum Bending Radii for Square and Rectangular Hollow Structural Sections Subjected to Cold Bending*. CIDECT Report 11C-88-14-E, CIDECT.

Timoshenko, S. P. (1956). *Strength of Materials Part II - Advanced Theory and Problems*, 3<sup>rd</sup> Ed., D. Van Nostrand Company, New York, NY.

Timoshenko, S. P., and Woinowsky-Krieger, S. (1987). *Theory of Plates and Shells*. 2<sup>nd</sup> Ed., McGraw-Hill Book Company, Inc., United States of America.

# 6 ROLLER-BENDING SIMULATION OF CHS ARCHES

## 6.1 INTRODUCTION

Curved constructional steel members are seen in many architecturally exposed structural steel applications, as a way of expressing the structural integrity of the system and at the same time putting the structural system at the aesthetic forefront. Typical examples of curved steel elements comprising Circular-Hollow-Sections (CHS) are met in large span roofs, bridges, domes, stadiums, atriums etc. Roller-bending comprises the most common and cost-effective process to produce curved CHS elements in the steel industry. In this context, customized sets of dies are adapted to the bending machine in order to fit with the CHS diameter, encapsulating the workpiece. CHS workpieces of diameters up to 600mm can be practically roller-bent, limited by the maximum diameter of bending dies that is available in the fabrication industry. In the case of larger diameters, alternative curving methods, such as incremental bending, are usually employed. An example of roller-bending a workpiece of Circular-Hollow-Section is shown in Figure 6-1.



Figure 6-1: Example of roller-bending a CHS workpiece.

A classification of CHS according to their slenderness and steel grade is given in EN1993-1-1 (CEN, 2005). The sections that are classified as Class 1, are able to develop plastic deformations without the occurrence of local buckling. The magnitude of bending curvature is limited by the induced ovalization that is allowed to take place during roller-bending; ovalization is typically expressed as a percentage of the difference between the major and minor axis dimensions after bending, as shown in Figure 6-2. Generally, CHS workpieces lend themselves well to bending since ovalization is limited due to the cross-sectional encapsulation by the customized sets of dies (Figure 6-1). However, the roller-bent CHS may encounter local buckling at the inner (compression) wall, in a single half-wave or a series of wrinkles. This form of visible waviness, known as oil-canning, can significantly reduce the cross-sectional strength resistance, due to the combined effect of ovalization and local buckling in a single half-wave. Distortion and local buckling can be limited with the use of an internal support mechanisms, such as mandrels (smaller CHS), or filling the CHS cavity with sand.

The curvature tolerances of roller-bent members are similar to the cambering tolerances of straight members, according to the Code of Standard Practice for Steel Buildings (AISC, 2016); the maximum deviation in curvature measured at the middle ordinate shall be less than the total arc length over 500. Standard provisions regarding the allowable cross-sectional variations of roller-bent circular-hollow-sections are not available, and thus the mill tolerances of straight members are generally applied (ASTM, 2016). For curved segments in piping systems, a maximum ovalization tolerance of 8% is specified in ASME B31.1 (ASME, 2016). A tolerance of 5% is usually achievable in most cases of CHS roller-bending. Ovality tolerances of members used in Architecturally Exposed Structural Steel applications, are commonly selected, based on aesthetics. In this context, a 5% tolerance is likely to produce imperceptible ovalization distortions and is usually considered adequate. Following a limited survey on the available bending capabilities of several roller-bending companies, records of past projects regarding the minimum cold-bending radii that have been successfully achieved without appreciable distortion, are summarized in Table 6-1 (Dowswell, 2018).

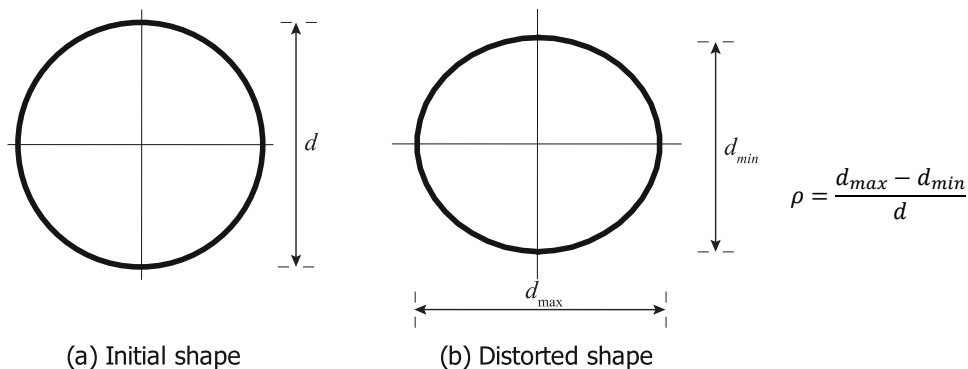


Figure 6-2: Example of CHS distortion due to roller-bending ( $\rho = 13\%$ ).

Table 6-1: General guidelines for minimum cold-bending radii of CHS (Dowswell, 2018).

Member dimensions (mm)	Minimum Bending Radius, $R_d$ (m)	Minimum $R/D$
219.1x12.7	1.1 to 3.0	4.9 to 14
219.1x8.2	1.1 to 4.6	4.9 to 21
219.1x4.8	3.0 to 5.5	14 to 25

Note: The minimum radii listed are for general guidance in the conceptual design stages; smaller radii can often be obtained.

The theoretical distribution of residual stresses (Timoshenko, 1956) is shown along the radial direction of a CHS in Figure 6-3, as function of the steel's yield stress  $f_y$  and the ratio  $\alpha$  between the plastic and elastic section modulus. The ratio  $\alpha$  ranges between 1.30 and 1.40 for circular-hollow-sections. The simplified model is based on the Euler-Bernoulli beam theory by aggregating uniaxial stresses from inelastic bending and elastic spring-back. Based on the assumptions of the simplified model, the theoretical distribution is generally valid for bending beams exhibiting small shear stresses relative to the bending stresses, as well as uniform bending stresses across the cross-sectional width.

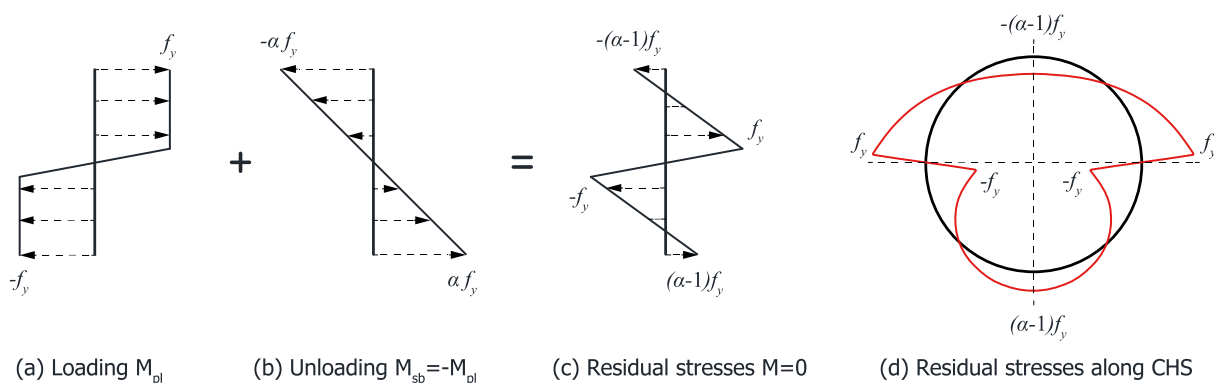


Figure 6-3: Theoretical distribution of residual stresses.

The actual residual stresses emanating from roller-bending are found to differ significantly from the simplified theoretical model for roller-bent wide-flange-sections (Spoorenberg et al., 2011) and rectangular-hollow-sections (Chiew et al., 2016). Neither experimental nor computational studies have been reported in the literature regarding the actual residual stress formations of roller-bent CHS, while their influence on the structural response has not been assessed, mainly due to the lack of reliable stress models. In this chapter, a numerical investigation regarding the membrane residual stress and strain formations of roller-bent CHS workpieces is presented, by means of nonlinear finite element simulations. Similar roller-bending simulations and pertinent residual stresses have been evaluated for members of rectangular-hollow-sections in the previous chapters. Mesh sensitivity analyses are first performed to verify the accuracy of the obtained results, followed by parametric investigations in order to assess the effects of the main roller-bending characteristics on the developed stress/strain distributions. Numerical results are discussed and pertinent residual stress distributions of roller-bent CHS are extracted.

## 6.2 NUMERICAL MODELING

Detailed finite element models of the roller-bending process are developed, aiming at estimating the locked-in stress/strain formations in a reliable manner. Initially straight workpieces of CHS are modeled with a uniform and sufficiently dense mesh of shell or solid elements, following a mesh convergence study (cf. Section 6.3). Null initial residual stresses are assumed on the straight workpieces, since the final patterns are independent of the initial conditions. Shell elements are employed on the surfaces of bending dies, which are connected to their center of rotation via rigid links in order to provide rigidity. The interaction between workpieces and dies is considered by introducing contact elements between their interfaces. The computational effort is reduced by taking advantage of the symmetry conditions and therefore, appropriate boundary conditions are applied on the pertinent Degrees of Freedom (DOFs). The numerical model along with the employed boundary conditions are shown in Figure 6-4.

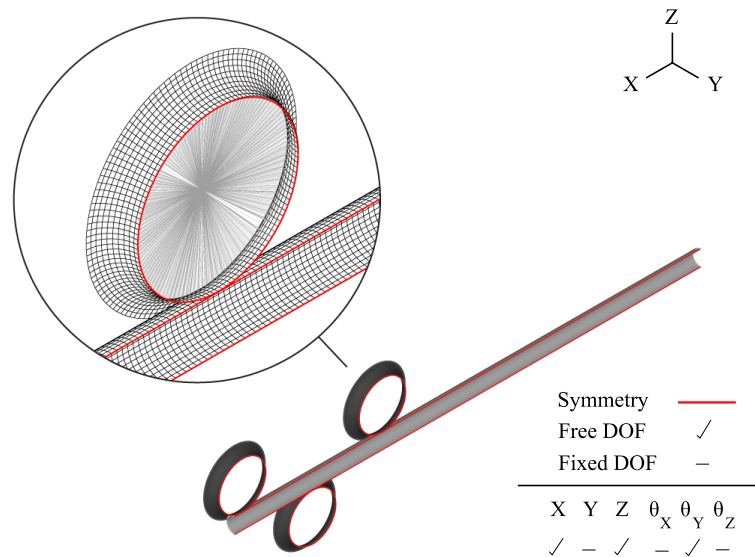


Figure 6-4: Finite element model and boundary conditions.

Geometry and Material Nonlinear Analyses (GMNA) are carried out in the general-purpose finite element software ADINA (ADINA, 2017). Large displacement and strain formulations are employed, since cross-sectional ovalities and distortions are important. An elastic – fully plastic material model is employed in the finite element analyses, comprising a bilinear constitutive law without hardening. The softening response due to the Bauschinger effect, encountered when steel is cyclically yielded in tension and compression, is not taken into account in the analyses. The influence of strain hardening and the Bauschinger effect is considered negligible on the residual stress/strain formations, since the plastic strains that are developed in roller-bending applications are typically small, as well as the yield direction remains always towards the same side during multi-passes. The plasticity model is characterized by the von Mises yield criterion and the Prandtl–Reuss flow rule. The modulus of elasticity  $E$  is taken equal to 210GPa, while various steel grades are examined. Implicit analyses are carried out using the Newton – Raphson solution algorithm for the geometrically and materially nonlinear equations. The rigid target algorithm, which is mainly used for metal-forming applications, is employed for the solution of the nonlinear contact equations. The Coulomb friction coefficient of the contacting surfaces is taken equal to 0.3.

The analysis sequence is illustrated schematically in Figure 6-5. A prescribed displacement of the middle roll is applied towards the workpiece, followed by a prescribed rotation at the centers of the other two rolls. Through contact traction, the workpiece is fed inside the bending machine. A sufficiently small load-step magnitude is required to reach uniform plastification, leading consequently to a uniform distribution of residual stresses along the workpiece. The placement requirements within the three-point-bending restrain bending of the workpiece close to its edges; these regions are trimmed in practice at the end of roller-bending. Even though multiple passes are practically needed to achieve the desired radius of curvature, a single-forming pass is analyzed, since residual stresses are found to be identical for single- and multiple- pass roller-bending.

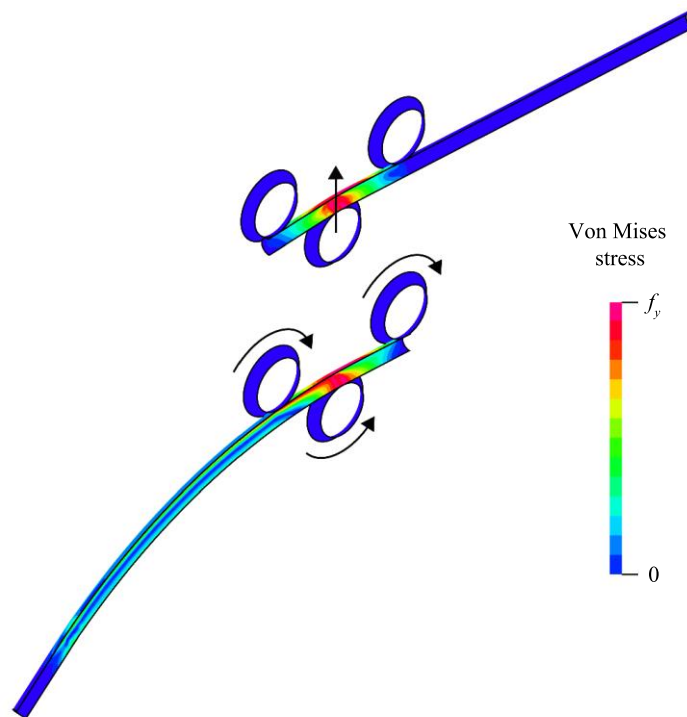


Figure 6-5: Analysis sequence along with von Mises stress.

### 6.3 VALIDATION STUDY

In this section, a validation study is performed in order to verify the accuracy of the stress/strain results obtained from the finite element analyses. To that end, a CHS 100 ( $d = 100\text{mm}$ ) workpiece of thickness 5mm is modeled with either shell or solid elements, and afterwards the mesh is refined. In the first case, 4-node shell elements (Figure 6-6a) with 5 integration points at the element thickness direction are used to model the workpiece. The Newton-Cotes integration method is employed, since it is more effective for capturing the onset and spread of the materially nonlinear conditions, as the integration points are on the boundaries of the elements. Secondly, the workpiece is simulated with 8-node solid elements (Figure 6-6b), exhibiting two integration points in each direction. In both cases, the semi-circle perimeter is divided in 22 subdivisions. In the third case, a mesh refinement of the shell element model is performed by subdividing the mesh size one time in both directions (Figure 6-6c). An aspect ratio close to 1 is employed for shell elements. However, this is computationally unfeasible for solid elements, which exhibit a maximum aspect ratio of approximately 4.

For comparison purposes, identical roller-bending characteristics are employed in the mesh sensitivity analyses, regarding the curving radius  $R = 5.00\text{m}$ , the steel yield stress  $f_y = 355\text{MPa}$ , the bending length  $S = 0.70\text{m}$ , the diameter of rolls  $d_r = 0.30\text{m}$  and the encapsulating angle of dies  $\theta_e = \pi/2$ . The convergence study is performed by comparing the membrane residual stress/strain formations at the end of roller-bending. The membrane residual stresses  $\sigma_{memb}$  are calculated by averaging stresses  $\sigma_x$  over the thickness direction, according to Eq. (5-1). The membrane strains  $\varepsilon_{memb}$  are calculated from the strains  $\varepsilon_x$  respectively. In the case of shell elements,  $\varepsilon_{memb}$  is identical to  $\varepsilon_x$  at the midsurface, due to the linear distribution of flexural strains over the thickness. Note that section results are extracted with respect to the local Cartesian system of the elements. Indices  $x$  and  $z$  refer, respectively, to the longitudinal and thickness directions.

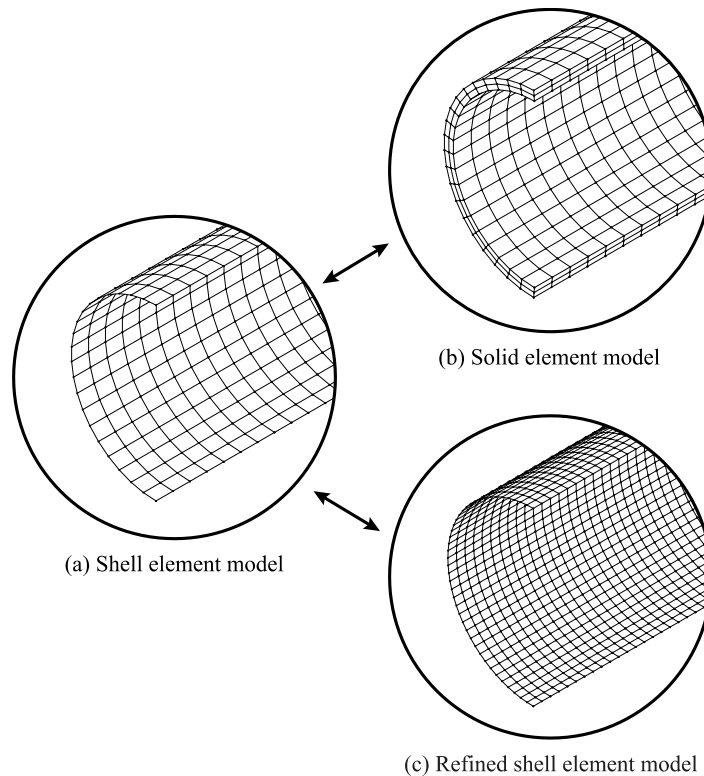


Figure 6-6: Numerical validation models.

A comparison of the membrane residual stresses and strains between the shell (initial mesh) and solid element models, is shown in Figure 6-7. As it is evidenced, the overall distribution is similar in both cases. The slight discrepancies in membrane stresses are attributed to the different formulations between shell and solid elements. Solid elements tend to lock when they are very thin, making them unsuitable for bending analyses of thin structures. Shell elements are more efficient for modeling thin-walled structures but encounter the limitation that any flexural stress/strain distributions are captured approximately. However, scope of the numerical model is to identify the predominant membrane component of residual stresses, which can be exploited by analysts to assess the structural behavior of roller-bent sections.

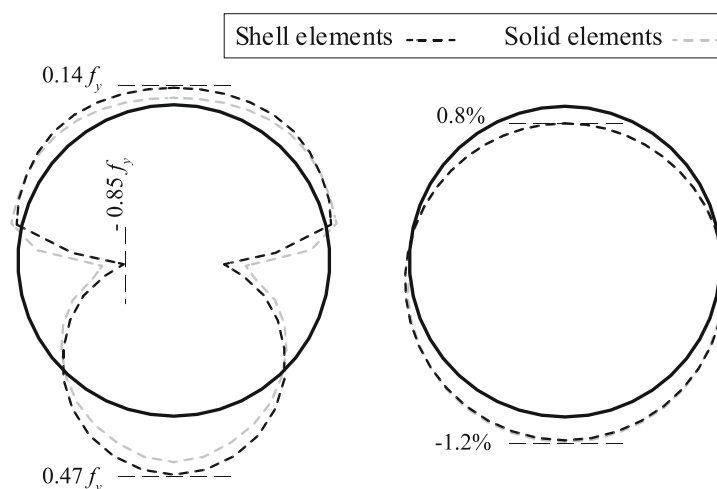


Figure 6-7: Membrane residual stresses (left) and strains (right) of the shell and solid element models.



A comparison of the membrane residual stresses and strains between the initial and refined shell element models, is shown in Figure 6-8. Very good convergence is evidenced in both cases; maximum discrepancies do not exceed 3%.

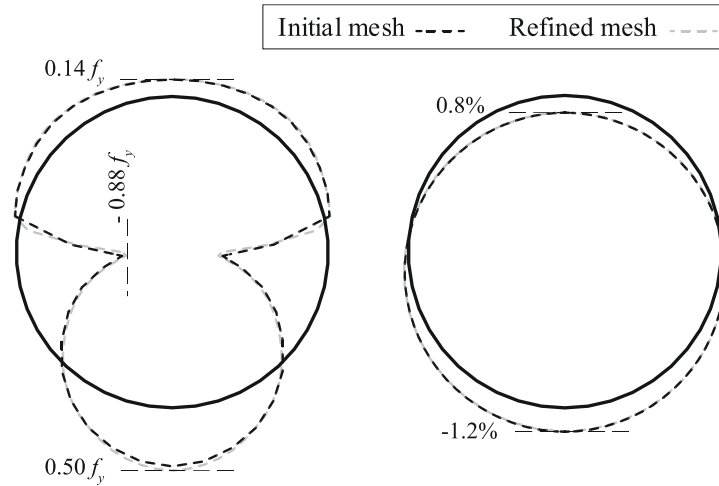


Figure 6-8: Membrane residual stresses (left) and strains (right) of the initial and refined shell element models.

Based on the results of sensitivity analyses, the shell element model employing the initial mesh size is considered to provide sufficiently accurate results in terms of membrane residual stresses and strains for the roller-bent CHS workpiece. Overall, a non-symmetrical residual stress layout about the bending axis is obtained, differing significantly from the distribution of the simplified theoretical model (anti-symmetrical). More specifically, tensile residual stresses are encountered in both the top- (elongated) and bottom- (shortened) height of the roller-bent CHS. The magnitude of developed strains in the shortened zone  $\varepsilon_{sh}$  are found slightly higher than the corresponding values of the tensioned zone  $\varepsilon_{el}$ . The strains  $\varepsilon_{sh}$  and  $\varepsilon_{el}$  satisfy the fundamental strain-curvature relationship of Eq. (5-2).

#### 6.4 PARAMETRIC ANALYSES

In this section, parametric analyses are carried out aiming at estimating the quantitative and qualitative effects of the main roller-bending characteristics on the residual stress/strain distributions. The roller-bending simulations are performed following the modeling considerations of Section 2. Based on the mesh convergence study of Section 3, the verified numerical model of CHS 100 workpiece is adopted for the parametric simulations. The CHS diameter remains constant in all cases, while the cross-sectional thickness, the radius of curvature, the steel grade, the bending length, the diameter of rolls and the encapsulating angle of dies are varied within an appropriate range, representing common-in-practice roller-bending cases. The parameters are normalized with respect to the CHS diameter, in order to obtain dimensionless results. Therefore, residual stress/strain results are presented with respect to: (i) the thickness ratio  $d/t$ , (ii) the bending ratio  $R/d$ , (iii) the yield stress  $f_y$ , (iv) the normalized bending length  $S/d$ , (v) the normalized roll diameter  $d_r/d$  and (vi) the encapsulating angle  $\theta_e$ .

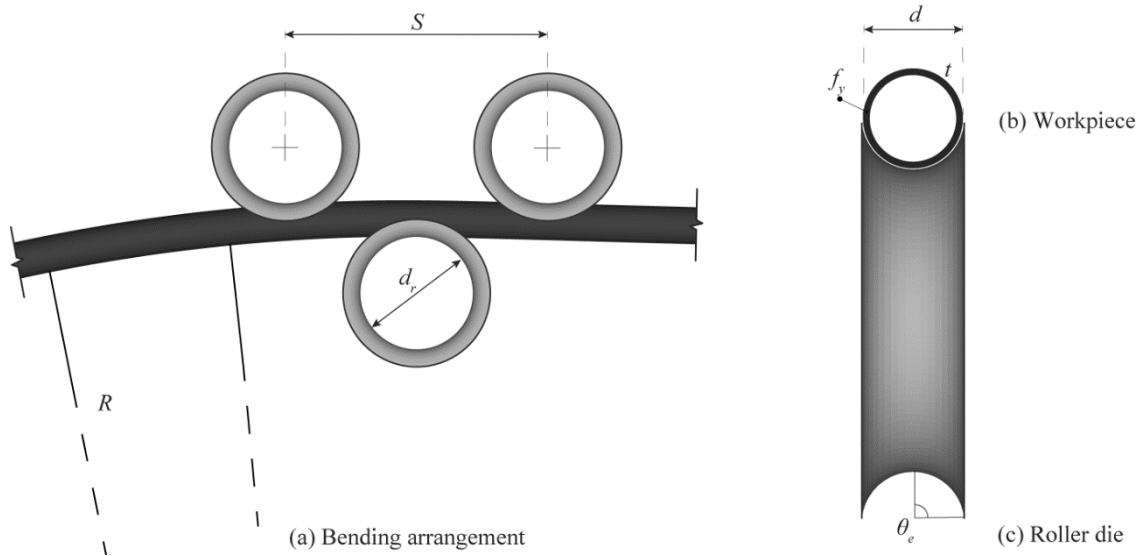


Figure 6-9: Main roller-bending parameters.

**6.4.1 Thickness ratio  $d/t$**

The thickness ratio  $d/t$  between the diameter  $d$  and thickness  $t$  of the CHS, is associated with the cross-sectional stiffness and slenderness. Parametric analyses are carried out for thickness ratios equal to 14, 20 and 33, typical of Class 1 cross-sections. For comparison purposes, identical roller-bending characteristics are employed in all cases, including  $R/d = 50$ ,  $f_y = 355\text{MPa}$ ,  $S/d = 9$ ,  $d_r/d = 3$  and  $\theta_e = \pi/2$ . A comparison of the membrane residual stresses and strains between the examined  $d/t$  ratios is shown in Figure 6-10. The encountered residual stresses at characteristic locations of the section are given in Table 6-2. It is observed that the locked-in stress formations vary considerably with  $d/t$ . The variations can be interpreted by considering that short in length CHS members comprise cylindrical shells, in which transverse stresses are developed apart from the longitudinal ones under concentrated bending forces. As cross-sections become stockier (i.e. thick-walled CHS or solid bars), the longitudinal stresses become more prevalent and uniform over the cross-sectional width. Consequently, the theoretical assumptions of the simplified model hold more accurately in the case of cross-sections exhibiting low  $d/t$ , and pertinent residual stresses tend to the theoretical distribution (anti-symmetrical).

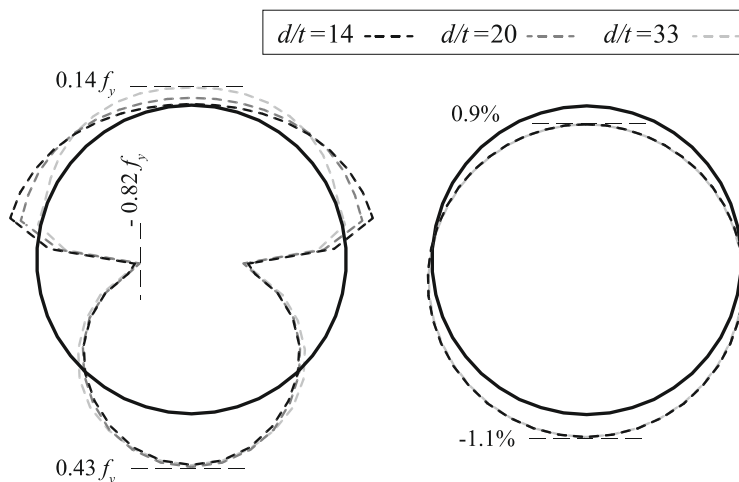


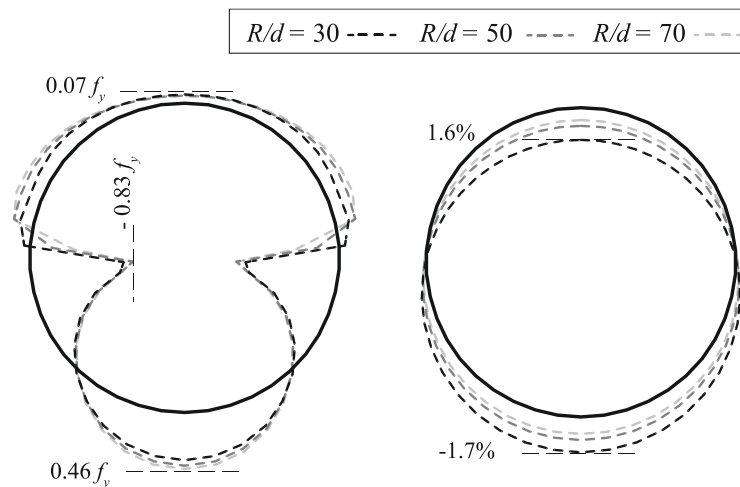
Figure 6-10: Membrane residual stresses (left) and strains (right), for various  $d/t$ .

Table 6-2: Membrane residual stresses of CHS for various  $d/t$ .

$d/t$	Compression zone (bottom-height)	Near neutral axis (mid-height)	Tension zone (top-height)
14	$0.42f_y$	$-0.81f_y$	$0.01f_y$
20	$0.43f_y$	$-0.82f_y$	$0.06f_y$
33	$0.42f_y$	$-0.82f_y$	$0.14f_y$

#### 6.4.2 Bending ratio $R/d$

The bending ratio  $R/d$ , defined by the radius of curvature  $R$  with respect to the CHS diameter  $d$ , is related with the amount of required plastic work during roller-bending. Parametric analyses are carried out for a range of bending radii that are commonly met in curved constructional steel members. To that effect, bending ratios equal to 30, 50 and 70 are examined, while typical characteristics are employed regarding the thickness ratio  $d/t = 20$ , the yield stress  $f_y = 355\text{MPa}$ , the normalized bending length  $S/d = 9$ , the normalized roll diameter  $d_r/d = 3$  and the encapsulating angle of dies  $\theta_e = \pi/2$ . A comparison of the membrane residual stresses and strains between the examined bending ratios is shown in Figure 6-11. It is observed that the radius of curvature has negligible effect on the residual stress formations, which is in agreement with the theoretical model. The developed strains at the top and bottom height of the section are given in Table 6-3. An approximately linear variation is evidenced between strains and the inverse of bending ratio, being in accordance with the fundamental strain-curvature relationship.

Figure 6-11: Membrane residual stresses (left) and strains (right), for various  $R/d$ .Table 6-3: Developed strains of CHS for various  $R/d$ .

$d/R$	Compression zone (bottom-height)	Tension zone (top-height)
0.033	-1.7%	1.6%
0.020	-1.1%	0.9%
0.014	-0.8%	0.6%

### 6.4.3 Steel yield stress $f_y$

The yield stress  $f_y$  of steel members is correlated with the magnitude of locked-in stresses, according to the theoretical model of Timoshenko. Parametric analyses are carried out for yield stresses equal to 235MPa, 275MPa and 355MPa, which correspond to commonly used steel grades in the constructional industry. For comparison reasons, identical roller-bending characteristics are employed in all cases, including  $d/t = 20$ ,  $R/d = 50$ ,  $S/d = 9$ ,  $d_r/d = 3$  and  $\theta_e = \pi/2$ . A comparison of the membrane residual stresses and strains between the examined steel grades, is shown in Figure 6-12. It is observed that the yield stress does not affect the residual stress/strain distributions. The magnitude of residual stresses is varied proportionally to  $f_y$ , in all cases, being in accordance with the theoretical model.

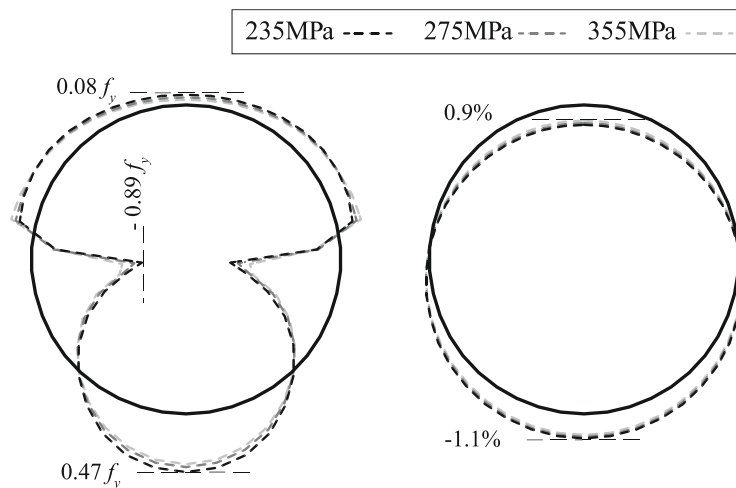
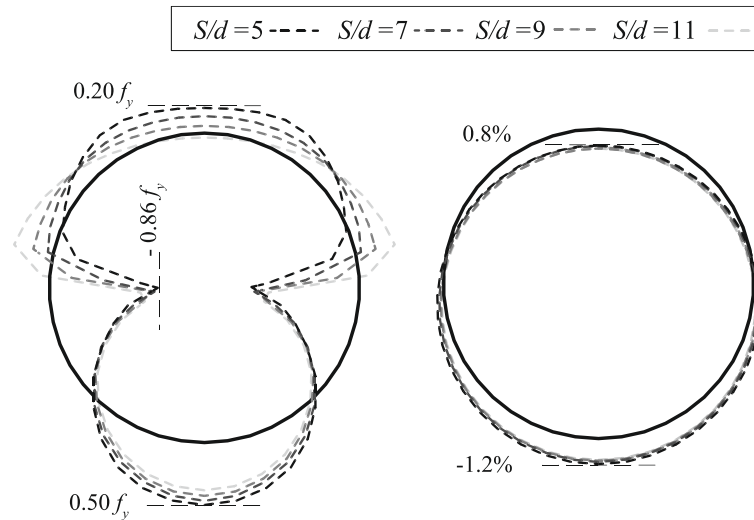


Figure 6-12: Membrane residual stresses (left) and strains (right), for various  $f_y$ .

### 6.4.4 Normalized bending length $S/d$

The normalized bending length  $S/d$ , defined by the bending length  $S$  with respect to the CHS diameter  $d$ , is correlated with the magnitude of the induced shear force during roller-bending. Parametric analyses are carried out for a wide range of  $S/d$ , covering most of the combinations between bending machines and CHS workpieces that are used in the roller-bending practice. To that end, normalized bending lengths equal to 5, 7, 9 and 11 are examined, while typical roller-bending characteristics are employed in all cases, including  $d/t = 20$ ,  $R/d = 50$ ,  $f_y = 355\text{MPa}$ ,  $d_r/d = 3$  and  $\theta_e = \pi/2$ . A comparison of the membrane residual stresses and strains between the examined  $S/d$  is presented in Figure 6-13. The encountered locked-in stresses at characteristic locations of the section are given in Table 6-4. It is observed that the locked-in stress formations vary significantly with  $S/d$ . The variations can be interpreted by considering that the magnitude of the induced shear force varies with bending length. As the normalized bending length increases, lower shear stresses relative to the bending stresses are developed within the three-point-bending length. Consequently, the theoretical assumptions of the simplified model hold more accurately in the case of higher  $S/d$ , and pertinent residual stress distributions approach the anti-symmetrical distribution. Since the locked-in formations are found dependent on both the thickness ratio and the normalized bending length, further parametric analyses are performed for  $d/t$  equal to 14 and 33 (typical of Class 1 cross-sections) within the examined range of  $S/d$ .

Figure 6-13: Membrane residual stresses (left) and strains (right), for various  $S/d$ .Table 6-4: Membrane residual stresses of CHS for various  $S/d$ .

$S/d$	Compression zone (bottom-height)	Near neutral axis (mid-height)	Tension zone (top-height)
5	$0.50f_y$	$-0.86f_y$	$0.20f_y$
7	$0.47f_y$	$-0.85f_y$	$0.14f_y$
9	$0.43f_y$	$-0.82f_y$	$0.06f_y$
11	$0.37f_y$	$-0.73f_y$	$-0.04f_y$

#### 6.4.5 Normalized roll diameter $d_r/d$

The normalized roll diameter  $d_r/d$  is defined by the diameter of bending rolls  $d_r$  with respect to the CHS diameter  $d$ . Parametric analyses are carried out for normalized roll diameters equal to 2, 3 and 4, which are typically used by steel fabricators. For comparison reasons, identical roller-bending characteristics are employed in all cases, namely  $d/t = 20$ ,  $R/d = 50$ ,  $f_y = 355\text{MPa}$ ,  $S/d = 9$  and  $\theta_e = \pi/2$ . A comparison of the membrane residual stresses and strains between the examined  $d_r/d$  ratios is shown in Figure 6-14. As it is observed, the residual stress formations are not affected by the diameter of bending rolls, indicating that a similar roll-workpiece interaction is developed in the examined cases.

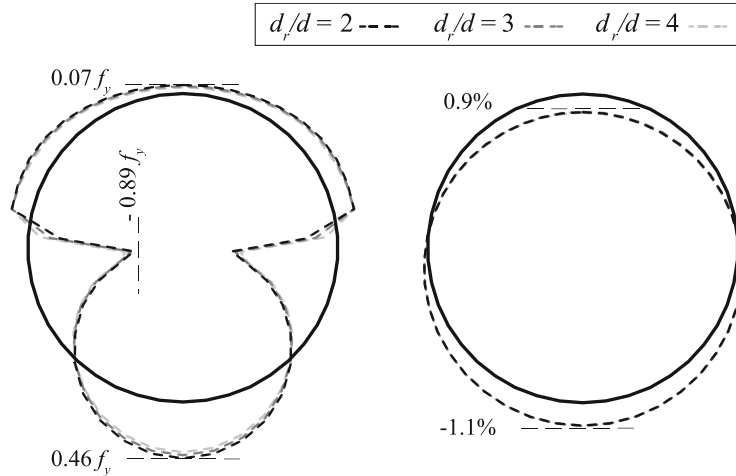


Figure 6-14: Membrane residual stresses (left) and strains (right), for various  $d_r/d$ .

#### 6.4.6 Encapsulating angle $\theta_e$

The encapsulating angle  $\theta_e$  of CHS is normally equal to  $\pi/2$ , so induced ovalities or distortions be minimized. Aiming at assessing the effect of  $\theta_e$  on the residual stress/strain formations, parametric analyses are carried out for various bending dies comprising angles equal to  $\pi/6$ ,  $\pi/3$  and  $\pi/2$ , as shown in Figure 6-15. Identical roller-bending characteristics are employed in all cases, including  $d/t = 20$ ,  $R/d = 50$ ,  $f_y = 355\text{MPa}$  for  $S/d = 9$  and  $d_r/d = 3$ . A comparison of the membrane residual stresses and strains between the examined  $\theta_e$  is shown in Figure 6-16. It is observed that the locked-in formations vary significantly with the encapsulating angle, due to the varying magnitude of transverse stresses that are developed. In the case of inadequately encapsulated sections, significantly higher residual stresses are encountered relative to the well encapsulated ones, which are associated with large cross-sectional ovalization. However, it should be mentioned that CHS workpieces are usually well encapsulated in practice.

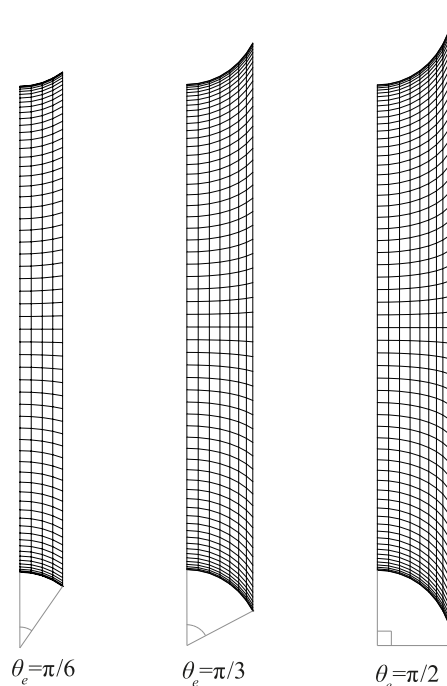


Figure 6-15: Bending dies of encapsulating angles  $\theta_e$  equal to  $\pi/6$ ,  $\pi/3$  and  $\pi/2$ .

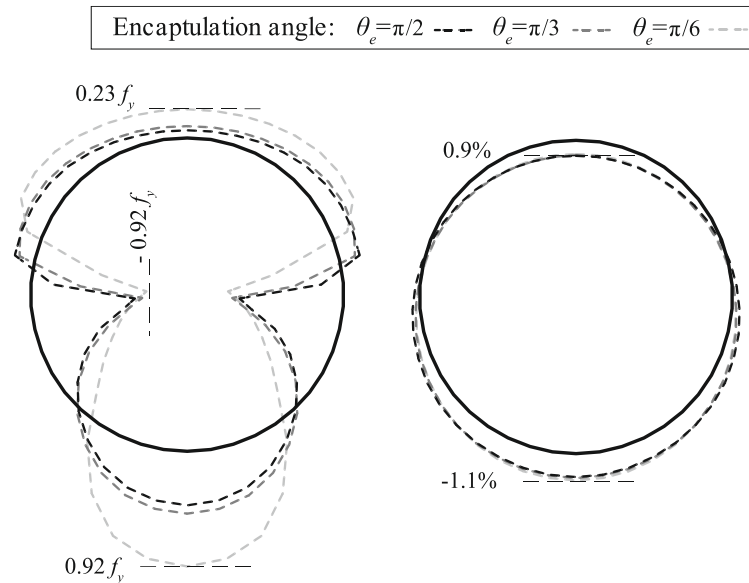


Figure 6-16: Membrane residual stresses (left) and strains (right), for various  $\theta_e$ .

## 6.5 RESIDUAL STRESS MODEL

In this section, results of parametric analyses are summarized, and pertinent residual stress distributions are extracted. Among the examined parameters, the thickness ratio  $d/t$  and the normalized bending length  $S/d$  are found to mainly affect the residual stress formations as long as workpieces are adequately encapsulated. The residual stress distributions, obtained from the numerical analyses within the examined ranges of  $14 \leq d/t \leq 33$  and  $5 \leq S/d \leq 11$ , are summarized in Table 6-5. Results are given along the semi-perimeter of CHS, with respect to the angle  $\varphi$ , which is measured from the shortened zone clock-wisely. Linear interpolation can be employed to calculate residual stresses for intermediate values of  $S/d$  or  $d/t$ . In the case of very stocky cross-sections (i.e.  $d/t \leq 14$ ) that are roller-bent within large bending machines (i.e.  $S/d \geq 11$ ), the residual stress formations are found to be better approximated by the theoretical model (Timoshenko, 1956).

A representative residual stress distribution can be developed on the basis of the roller-bending characteristics that are encountered most commonly in practice, which are usually unknown in advance. By averaging the residual stress formations in the typical range of  $d/t$  and  $S/d$  (Table 6-5), a characteristic distribution is obtained. The average model satisfies the equilibrium requirement, since it comprises a linear combination of self-equilibrated models. The numerically obtained residual stresses (Table 6-5) and the characteristic distribution (Average) are shown expanded in Figure 6-17, with respect to the angle  $\varphi$ , which is measured from the shortened zone of the cross-section clock-wisely. As it is observed, maximum deviations are encountered near the neutral axis of the cross-section. The proposed residual stress model is shown along the CHS in Figure 6-18, and pertinent residual stress values are given in Table 6-6.

Table 6-5: Membrane residual stresses (with respect to  $f_y$ ) for various  $S/d$  and  $d/t$ .

$\varphi$ (rad)	$S/d = 5$			$S/d = 7$			$S/d = 9$			$S/d = 11$		
	$d/t$			$d/t$			$d/t$			$d/t$		
	14	20	33	14	20	33	14	20	33	14	20	33
0.00	0.56	0.50	0.34	0.48	0.47	0.44	0.42	0.43	0.42	0.36	0.37	0.31
0.15	0.53	0.49	0.35	0.45	0.45	0.43	0.40	0.41	0.40	0.36	0.37	0.30
0.30	0.45	0.44	0.36	0.37	0.39	0.40	0.34	0.36	0.35	0.31	0.32	0.28
0.45	0.34	0.36	0.33	0.28	0.31	0.33	0.25	0.28	0.29	0.23	0.24	0.23
0.60	0.18	0.23	0.26	0.16	0.19	0.22	0.14	0.16	0.20	0.12	0.14	0.16
0.75	0.03	0.07	0.13	0.02	0.05	0.09	0.01	0.02	0.08	-0.01	0.00	0.07
0.90	-0.15	-0.11	-0.03	-0.14	-0.12	-0.08	-0.14	-0.13	-0.08	-0.16	-0.15	-0.07
1.05	-0.32	-0.30	-0.21	-0.30	-0.29	-0.27	-0.31	-0.30	-0.26	-0.34	-0.33	-0.24
1.20	-0.47	-0.46	-0.39	-0.48	-0.47	-0.45	-0.50	-0.50	-0.46	-0.54	-0.53	-0.45
1.35	-0.63	-0.64	-0.55	-0.69	-0.68	-0.66	-0.73	-0.72	-0.70	-0.74	-0.76	-0.71
1.50	-0.84	-0.86	-0.81	-0.84	-0.85	-0.82	-0.81	-0.82	-0.82	-0.72	-0.73	-0.73
1.65	-0.70	-0.66	-0.57	-0.34	-0.45	-0.50	-0.08	-0.18	-0.25	0.09	0.08	0.04
1.80	-0.11	-0.19	-0.33	0.14	0.04	-0.10	0.25	0.16	0.02	0.39	0.32	0.19
1.94	0.05	-0.02	-0.09	0.16	0.09	-0.05	0.24	0.17	0.02	0.34	0.28	0.15
2.09	0.10	0.05	0.07	0.16	0.11	0.03	0.21	0.17	0.06	0.27	0.23	0.13
2.24	0.14	0.13	0.14	0.17	0.14	0.11	0.17	0.16	0.11	0.19	0.18	0.12
2.39	0.18	0.19	0.24	0.16	0.16	0.17	0.14	0.15	0.14	0.12	0.12	0.11
2.54	0.20	0.24	0.34	0.14	0.17	0.22	0.10	0.12	0.16	0.05	0.07	0.09
2.69	0.21	0.25	0.31	0.12	0.16	0.23	0.06	0.10	0.16	0.00	0.02	0.07
2.84	0.22	0.23	0.19	0.10	0.15	0.21	0.03	0.08	0.16	-0.04	-0.01	0.05
2.99	0.22	0.21	0.07	0.09	0.14	0.17	0.02	0.06	0.15	-0.07	-0.03	0.04
3.14	0.22	0.20	0.03	0.08	0.14	0.16	0.01	0.06	0.14	-0.07	-0.04	0.04

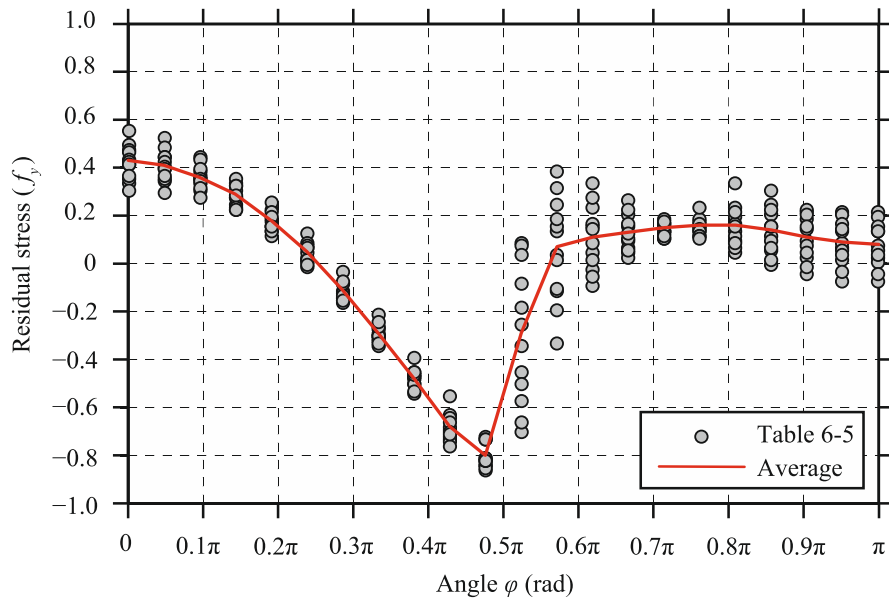


Figure 6-17: Expansion of residual stresses distributions.



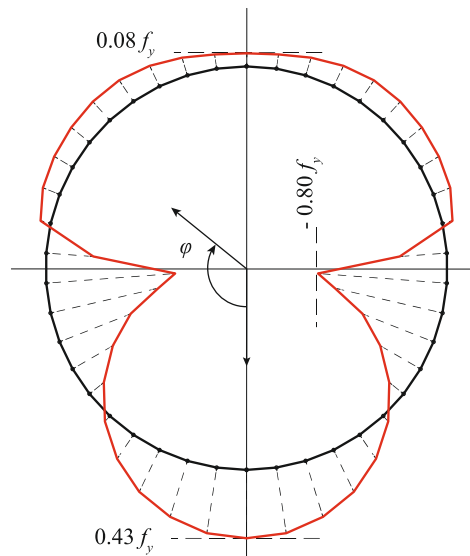


Figure 6-18: Proposed residual stress distributions of roller-bent CHS.

Table 6-6: Proposed residual stresses along the semi-perimeter of CHS.

$\varphi$ (rad)	Membrane stress ( $f_y$ )	$\varphi$ (rad)	Membrane stress ( $f_y$ )
0.00	0.43	1.65	-0.29
0.15	0.41	1.80	0.07
0.30	0.36	1.94	0.11
0.45	0.29	2.09	0.13
0.60	0.18	2.24	0.15
0.75	0.05	2.39	0.16
0.90	-0.11	2.54	0.16
1.05	-0.29	2.69	0.14
1.20	-0.48	2.84	0.11
1.35	-0.68	2.99	0.09
1.50	-0.80	3.14	0.08

## 6.6 CONCLUSIONS

The membrane residual stress and strain formations of roller-bent CHS workpieces were assessed in this section, which had not been investigated until now in the literature. An efficient computational methodology was presented, providing the residual stress/strain formations in a reliable manner, by means of implicit analyses accounting for geometric, contact and material nonlinearities. Similar roller-bending simulations and pertinent residual stresses had been evaluated numerically and experimentally in previous chapters. Mesh sensitivity analyses were first performed to verify the accuracy of the obtained results, followed by parametric investigations aiming at assessing the effects of the main roller-bending characteristics on the developed stress and strain distributions. Among the examined parameters, the thickness ratio and the normalized bending length were found to mainly affect the locked-in stress formations. Variations were evidenced between the encountered distributions and the simplified theoretical model, same as for roller-bent sections of other shapes that have been reported in the literature (Spoorenberg et al., 2011; Chiew et al., 2016)

The encountered variations were interpreted by considering that CHS workpieces within the three-point-bending length comprise short in length cylindrical shells, in which significant shear and transverse stresses are developed that cannot be neglected (Timoshenko and Woinowsky-Krieger, 1987). As cross-sections become stockier and the bending length increases, the residual stress formations are reasonably better approximated by the theoretical model (Timoshenko, 1956). The obtained residual stress distributions were presented within the examined range of section diameter over thickness ratio  $d/t$  and bending length over section diameter ratio  $S/d$  that are commonly encountered in practice, namely  $14 \leq d/t \leq 33$  and  $5 \leq S/d \leq 11$ . Furthermore, internal supporting of the hollow cross-section with mandrels or other material such as sand, would reasonably lead to residual stress formations closer to the theoretical model. Moreover, a characteristic residual stress distribution was extracted. Such membrane residual stress distributions can be exploited from analysts to assess the structural behavior of roller-bent CHS members. Finally, results of the parametric study can be very useful for designing an appropriate experimental testing program of residual stress measurements on roller-bent CHS specimens.

## REFERENCES

- ADINA R&D Inc. (2017). *Theory and modeling guide*. Watertown, MA, USA.
- AISC (2016). *Code of Standard Practice for Steel Buildings and Bridges*. American Institute of Steel Construction, Chicago, IL.
- ASME (2016). *Power Piping-ASME Code for Pressure Piping*. ASME B31.1-2016, American Society of Mechanical Engineers, New York, NY.
- ASTM (2016). *Selected ASTM Standards for Structural Steel Fabrication*. ASTM International, West Conshohocken, PA.
- CEN (2005). *Eurocode 3: Design of Steel Structures, Part 1-1: General Rules and Rules for Buildings, EN 1993-1-1*. Comité Européen de Normalisation (CEN), European Committee for Standardization Brussels, Belgium.
- Chiew, S.P., Jin, Y.F. and Lee, C.K. (2016). "Residual Stress Distribution of Roller Bending of Steel Rectangular Structural Hollow Sections." *Journal of Constructional Steel Research*, vol. 119, pp. 85–97.
- Dowswell, B. (2018). *Curved Member Design*. American Institute of Steel Construction, Chicago, IL.
- Spoorenberg, R.C., Snijder, H.H. and Hoenderkamp, J.C.D. (2011). "Proposed Residual Stress Model for Roller Bent Steel Wide Flange Sections," *Journal of Constructional Steel Research*, vol. 67, pp. 992–1000.
- Timoshenko, S. P. (1956). *Strength of Materials Part II - Advanced Theory and Problems*, 3<sup>rd</sup> Ed., D. Van Nostrand Company, New York, NY.
- Timoshenko, S. P., and Woinowsky-Krieger, S. (1987). *Theory of Plates and Shells*. 2<sup>nd</sup> Ed., McGraw-Hill Book Company, Inc., United States of America.

# 7 EFFECTS OF RESIDUAL STRESSES ON ROLLER-BENT SECTIONS

## 7.1 INTRODUCTION

Metal-forming processes induce, typically, residual stresses and plastic deformations in steel members. Systematic research regarding the effects of residual stresses on strength resistance was initiated in the late 1940s, under the guidance of the Research Committee of the Column Research Council (Osgood, 1951; Yang et al., 1952; Beedle and Tall, 1960). The research work was continued through the early 1970s (Batterman and Johnston, 1967; Kishima et al., 1969; McFalls and Tall, 1970; Alpsten and Tall, 1970; Brozzetti et al., 1970a; Bjorhovde et al., 1972), while a large number of column tests were conducted under the auspices of the European Convention for Constructional Steelwork (ECCS), in order to provide further assurance of the results obtained from computational studies (Sfintesco, 1970; Beer and Schultz, 1970). The presence of residual stresses was considered to affect the elastic domain of the material, causing premature yielding of the cross-section and having considerable effect on the buckling strength of steel members (ECCS, 1976). Based on the results of the aforementioned and supplementary studies, the concept of column formulas was adopted in the normative provisions of most structural steel design standards, which is enjoying popularity up to the present, as the example of the Perry-Robertson formula (Robertson, 1925).

The strength of columns was found to be better represented by more than one column curve, thus introducing the concept of multiple column curves in modern standards. Multiple column curves have been developed in relevant studies of Bjorhovde and Tall (1971), Bjorhovde (1972), Beer and Schultz, (1970), Jacquet (1970), and Sfintesco (1970), in which the buckling resistance of columns is differentiated due to variations in the magnitude and distribution of residual stresses, depending on the type of cross-section, the manufacturing process, and the material properties of steel. The Structural Stability Research Council (SSRC) has suggested the implementation of the column curves, proposed by Bjorhovde and Tall (1971) and Bjorhovde (1972), namely curves 1, 2, 3, 1P, 2P, and 3P. The European Convention for Constructional Steelwork (ECCS, 1976) adopted the column curves of Beer and Schultz (1970), Jacquet (1970), and Sfintesco (1970), comprising now part of the buckling curve formulation of Eurocode 3, part 1-1 (CEN, 2005); this set of buckling curves, namely  $a_0$ , a, b, c, and d, are shown in Figure 7-1. The Canadian Standards Association (CSA, 2009) recommended the use of two column curves, which were based on the SSRC curves 1 and 2. The American Institute of Steel Construction (AISC), adopted the SSRC curve 2P in pertinent provisions of the Specification for Structural Steel Buildings (AISC, 2005).

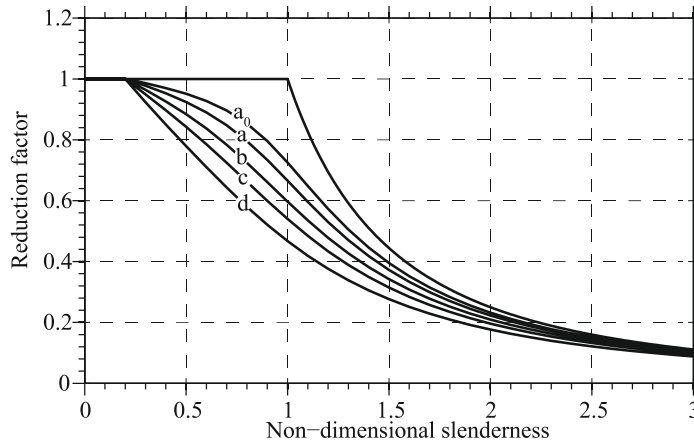


Figure 7-1: Eurocode 3 multiple column curves (CEN, 2005).

In this chapter, the effects of residual stresses on the structural behavior of roller-bent arches are evaluated, using appropriate analytical expressions. To that end, reliable residual stress distributions are implemented (Figure 7-2), emanating from the roller-bending process of Circular-Hollow-Sections (CHS), Square-Hollow-Sections (SHS) and Rectangular-Hollow-Sections (RHS); the employed formations have been thoroughly described in Chapter 5 and Chapter 6. Aiming at defining the elastic domain of roller-bent sections, interaction diagrams of axial force with bending moment are developed for the CHS, SHS, and RHS. Moreover, the effects of locked-in stresses on the inelastic critical loads of roller-bent arches are assessed, following the general methodology of Beedle and Tall (1960). In this context, the critical loads of CHS, SHS, and RHS arches are calculated considering that for a given force, the section may have partly yielded prematurely due to the presence of residual stresses. Finally, the analytical results are discussed, and pertinent conclusions are extracted.

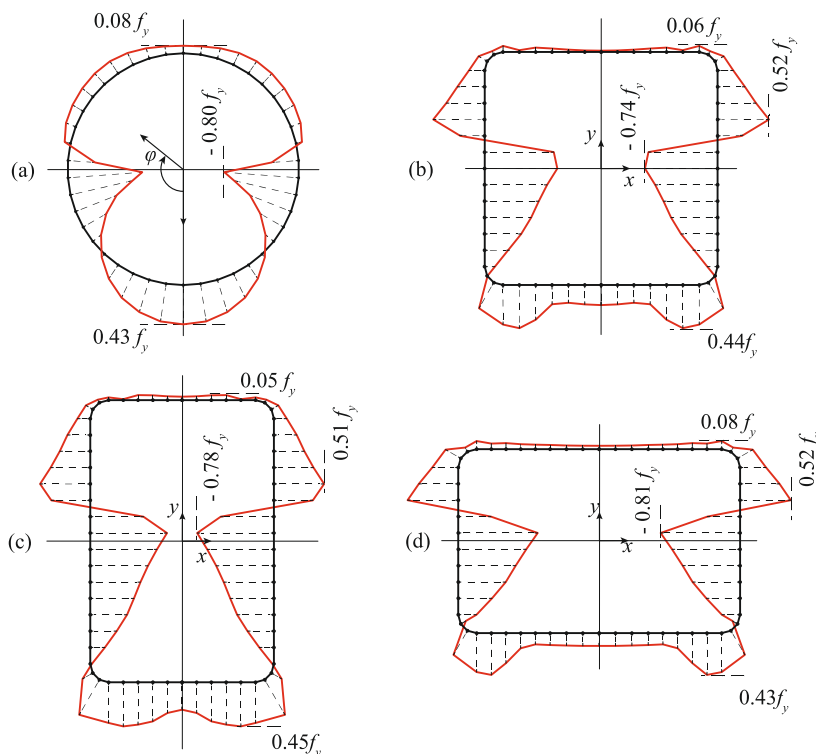


Figure 7-2: Proposed residual stress distributions for roller-bent (a) CHS, (b) SHS, (c) RHS ( $h/b = 1.50$ ) and (d) RHS ( $h/b = 0.66$ ).

## 7.2 ANALYTICAL METHODOLOGY

The effect of residual stresses on the cross-sectional elastic domain can be evaluated by considering that for any combination of normal force  $N$  and bending moment  $M$ , the total stress including locked-in formations  $\sigma_{rs}$ , should be lower than  $f_y$ , as shown in Eq. (7-1). Various residual stress models can be implemented in pertinent calculations, depending on the examined cross-sectional shape and forming process. However, the theoretical residual stress distribution of Timoshenko (1956), yields in a null elastic domain, since stresses at the middle of the web have already reached the yield stress  $f_y$ .

$$\frac{N}{A} + \frac{M}{I}z + \sigma_{rs} \leq f_y \quad (7-1)$$

Where,  $A$ , the cross-sectional area;  $I$ , the cross-sectional moment for in-plane or out-of-plane bending;  $z$ , the distance from the neutral axis;  $\sigma_{rs}$ , the residual stress at position  $z$ .

The effect of residual stresses on the buckling resistance of roller-bent arches can be evaluated through the general methodology proposed by Beedle and Tall (1960). The methodology is based on the calculation of the flexural stiffness of a cross-section considering null rigidity of the yielded parts, as long as an elastic - perfectly plastic material behavior is assumed. Reliable residual stress distributions are employed in the calculations, including the numerical and theoretical residual stress models of roller-bent hollow sections which were presented in the previous chapters. The analytical methodology for obtaining the in-plane and out-of-plane inelastic buckling load of arches is described next.

The axial force  $N$  of circular arches under pure compression is equal to the radial pressure  $q$  times the curvature radius  $R$ , as shown in Figure 7-3. Well-known expressions regarding the in-plane and out-of-plane elastic buckling forces of arches, are given by Timoshenko and Gere (1961). The in-plane buckling load of a circular arch under uniform radial load, which is simply supported and free to rotate at the arch ends, is given in Eq. (7-2). The out-of-plane buckling load of a circular arch under the same load, which is simply supported and free to rotate in the principal in-plane and out-of-plane directions but unable to rotate in torsion at the arch ends, is given in Eq. (7-3).

$$N_{cr}^{in-plane} = \frac{EI_{yy}}{R^2} \left( \frac{\pi^2}{(\alpha/2)^2} - 1 \right) \quad (7-2)$$

$$N_{cr}^{out-of-plane} = \frac{EI_{zz}}{R^2} \cdot \frac{(\pi^2 - \alpha^2)^2}{\alpha^2[\pi^2 + \alpha^2(EI_{zz}/C)]} \quad (7-3)$$

Where,  $EI_{yy}$ , the moment rigidity for in-plane bending;  $EI_{zz}$ , the moment rigidity for out-of-plane bending;  $C$ , the torsional rigidity of the section.

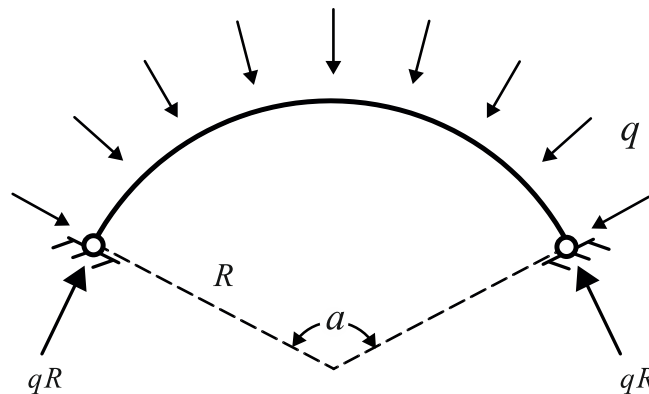


Figure 7-3: Axial force of circular arches under radial compression.

In order to evaluate effective bending stiffness of a cross-section including residual stresses  $\sigma_{rs}$ , a uniform compressive stress  $\sigma_u$  is considered. Thus, the effective stress  $\sigma_{eff}$  for this level of compression is evaluated according to Eq. (7-4).

$$\begin{aligned}\sigma_{eff} &= f_y, & \text{if } \sigma_{rs} + \sigma_u &\geq f_y \\ \sigma_{eff} &= \sigma_{rs} + \sigma_u, & \text{if } \sigma_{rs} + \sigma_u < f_y\end{aligned}\quad (7-4)$$

By integrating the effective stress  $\sigma_{eff}$  over the entire section, the associated normal force  $N_{eff}$  is calculated by Eq. (7-5).

$$N_{eff} = \int_A \sigma_{eff} dA \quad (7-5)$$

The corresponding average stress  $\sigma_{avg}$  is thus given by Eq. (7-6).

$$\sigma_{avg} = \frac{N_{eff}}{A} \quad (7-6)$$

The values of average stress  $\sigma_{avg}$  and normal force  $N_{eff}$  are used as reference levels to characterize the critical inelastic slenderness of the cross-section. Based on the effective stress, the inertia of the elastic parts of the section about the major and minor principal axis are given by Eq. (7-7) and Eq. (7-8), respectively.

$$I_{eff}^{yy} = \int_{A_{el}} z^2 dy dz \quad \text{for } \sigma_{eff}(y, z) \leq f_y \quad (7-7)$$

$$I_{eff}^{zz} = \int_{A_{el}} y^2 dy dz \quad \text{for } \sigma_{eff}(y, z) \leq f_y \quad (7-8)$$

The non-dimensional slenderness  $\bar{\lambda}$  of a steel member is defined by Eq. (7-9). Varying the non-dimensional slenderness within a range between 0 and 4, which is typically met in steel structures, the corresponding buckling loads are obtained.

$$\bar{\lambda} = \sqrt{\frac{N_{pl}}{N_{cr}}} \quad (7-9)$$

The effective critical loads for the in-plane  $N_{cr,eff}^{in-plane}$  and out-of-plane  $N_{cr,eff}^{out-of-plane}$  buckling can be calculated according to Eq. (7-10) and Eq. (7-11), respectively.

$$N_{cr,eff}^{in-plane} = N_{cr}^{in-plane} \cdot \frac{I_{eff}^{yy}}{I_{yy}} \quad (7-10)$$

$$N_{cr,eff}^{out-of-plane} = N_{cr}^{out-of-plane} \cdot \frac{I_{eff}^{zz}}{I_{zz}} \cdot \frac{\pi^2 \cdot C + \alpha^2 (EI_{eff}^{zz})}{\pi^2 \cdot C + \alpha^2 (EI_{zz})} \quad (7-11)$$

The minimum value of  $\bar{\lambda}$  is anticipated, for which the effective buckling load is equal to the supposed normal force. For that  $\bar{\lambda}$ , the reduction factor  $\chi$  of the buckling resistance can be calculated according to Eq. (7-12).

$$\chi = \frac{\sigma_{avg}}{f_y} \quad (7-12)$$

## 7.3 EFFECT ON ELASTIC STRENGTH

### 7.3.1 Circular-Hollow-Sections

The elastic domain of roller-bent and stress-free arches, subjected to combined axial force  $N$  and bending moment  $M$ , is evaluated according to Eq. (7-1). Interaction diagrams  $N$ - $M$ , regarding the in-plane and out-of-plane bending of CHS arches, are shown in Figure 7-4 and Figure 7-5, respectively, employing the proposed residual stress model (c.f. Section 6.5). Results are presented for a CHS 100x5, normalized with respect to the elastic axial/bending capacity. Tensile axial forces, as well as in-plane bending moments that tend to open the arch (increase the radius of curvature), are denoted as positive. Notation of the out-of-plane bending direction is not required, since residual stresses are symmetric in this case. As it is evidenced, the presence of residual stresses reduces significantly the elastic domain. The reduction is more prevalent in the case of out-of-plane bending, since maximum residual stresses are located near the cross-sectional mid-height.

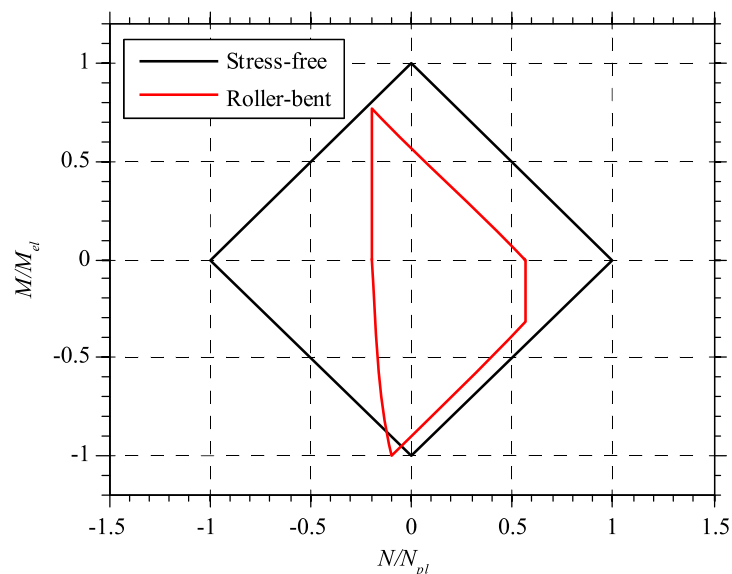


Figure 7-4: Interaction diagram  $N$ - $M$  for the in-plane response of CHS.

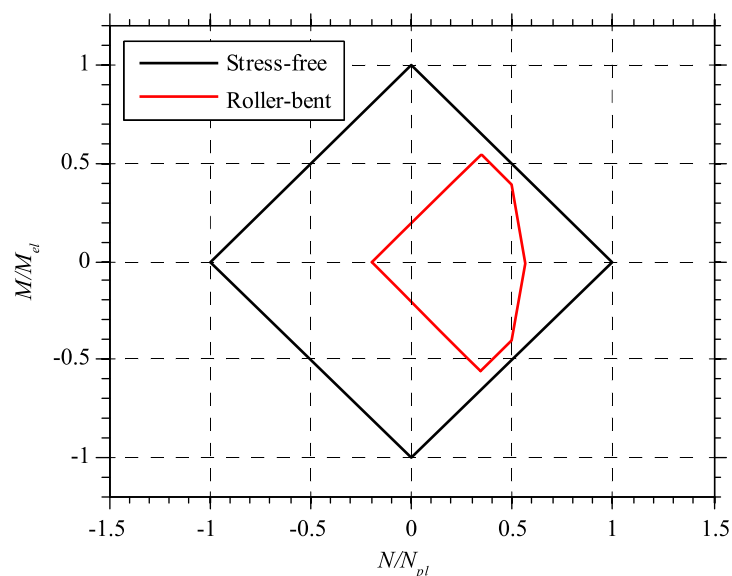


Figure 7-5: Interaction diagram  $N$ - $M$  for the out-of-plane response of CHS.

### 7.3.2 Square-Hollow-Sections

The elastic domain of roller-bent and stress-free SHS arches, subjected to combined axial force  $N$  and bending moment  $M$ , is assessed, employing the proposed model of residual stresses (c.f. Section 5.5). Interaction diagrams  $N$ - $M$ , regarding in-plane and out-of-plane bending of SHS arches, are shown in Figure 7-6 and Figure 7-7, respectively. Results are presented for an SHS 100x100x8, normalized with respect to the elastic axial/bending capacity. The notation is same as in circular-hollow-sections. Once again, the reduction is more prevalent in the case of out-of-plane bending, since maximum residual stresses are located near the mid-height of SHS. The reduction is more pronounced in the case of SHS compared to CHS, since high residual stresses are encountered at the web-to-flange junctions.

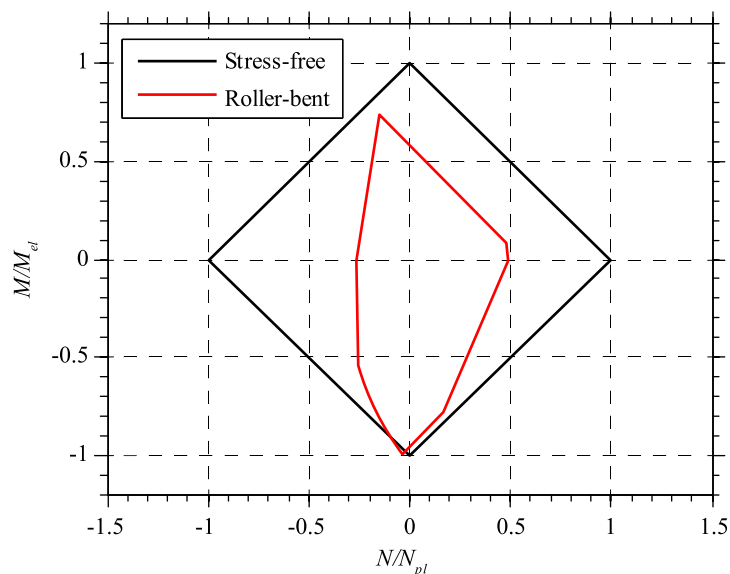


Figure 7-6: Interaction diagram  $N$ - $M$  for the in-plane response of SHS.

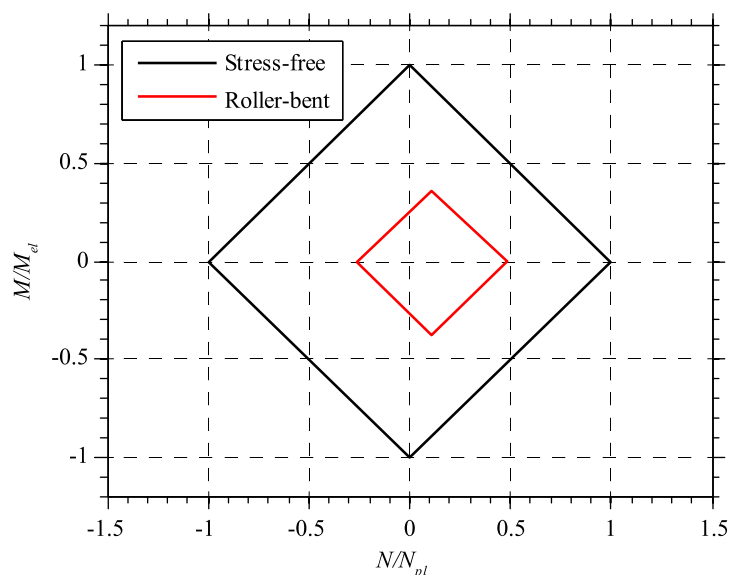


Figure 7-7: Interaction diagram  $N$ - $M$  for the out-of-plane response of SHS.



### 7.3.3 Rectangular-Hollow-Sections

The elastic domain of roller-bent and stress-free RHS arches, subjected to combined axial force  $N$  and bending moment  $M$ , is assessed, employing the proposed residual stress model (c.f. Section 5.5). Interaction diagrams  $N$ - $M$  for the in-plane and out-of-plane bending of RHS arches, comprising aspect ratio of  $h/b = 1.50$ , are shown in Figure 7-8 and Figure 7-9, respectively. Results are presented for an RHS 120x80x8, normalized with respect to the elastic axial/bending capacity. The notation is same as in the previous cases. The overall response is almost similar to the corresponding one of Square-Hollow-Sections.

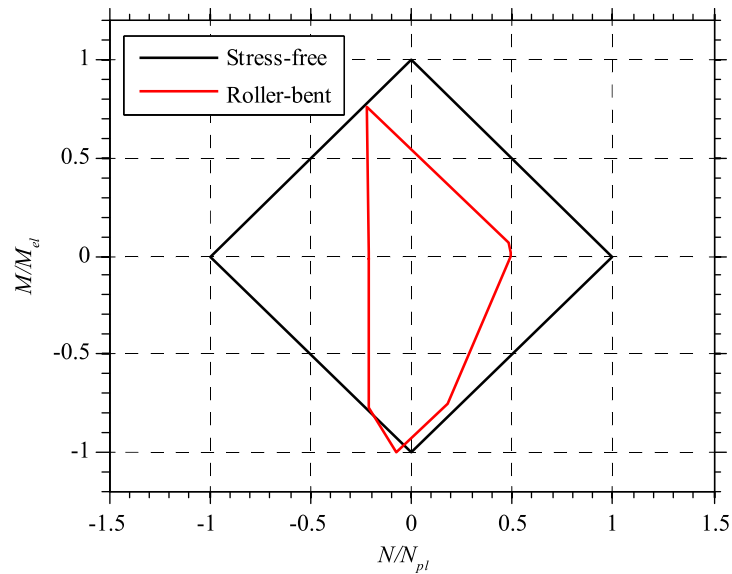


Figure 7-8: Interaction diagram  $N$ - $M$  for the in-plane response of RHS ( $h/b = 1.50$ ).

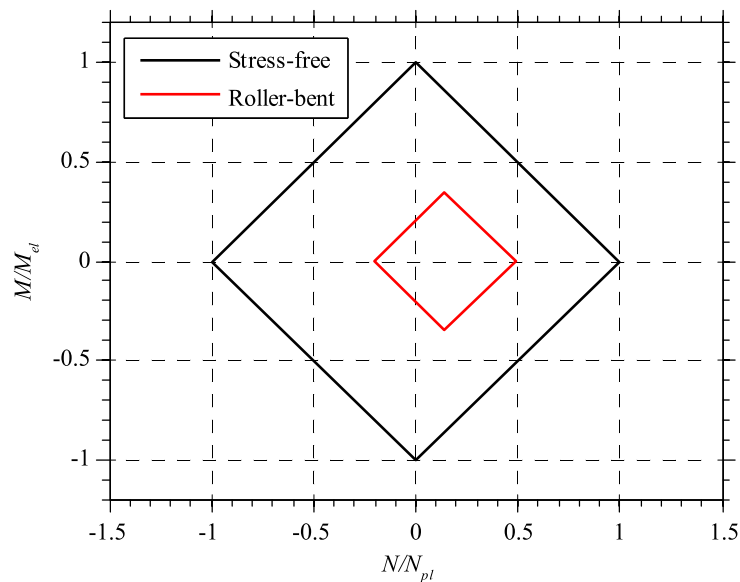


Figure 7-9: Interaction diagram  $N$ - $M$  for the out-of-plane response of RHS ( $h/b = 1.50$ ).

Furthermore, the elastic domain of roller-bent and stress-free RHS arches, comprising an aspect ratio  $h/b = 0.66$ , is evaluated; the characteristic residual stress distribution of roller-bent RHS ( $h/b = 0.66$ ) is employed (c.f. Section 5.5). Interaction diagrams  $N$ - $M$  regarding in-plane and out-of-plane bending are shown in Figure 7-10 and Figure 7-11, respectively. Results are presented for an RHS 80x120x8, normalized with respect to the elastic axial/bending capacity. The overall response is similar to the corresponding one of SHS and RHS comprising an aspect ratio of 1.50. Therefore, the cross-sectional aspect ratio has a negligible effect on the elastic domain.

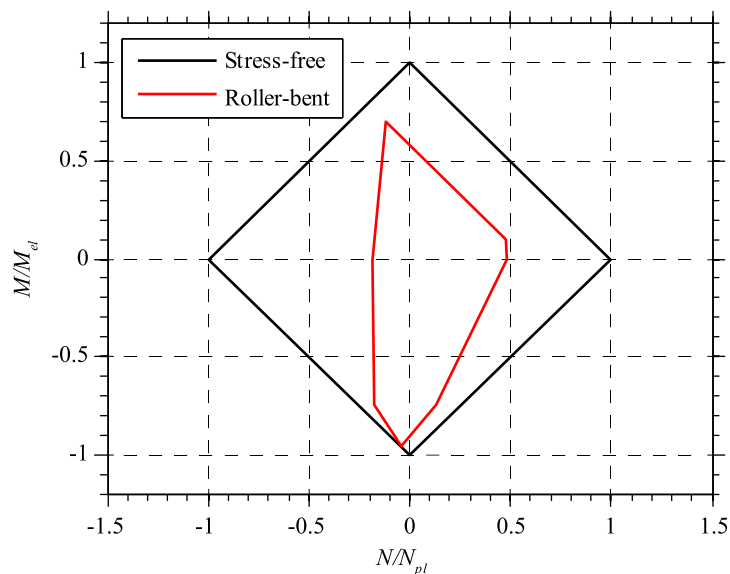


Figure 7-10: Interaction diagram  $N$ - $M$  for the in-plane response of RHS ( $h/b = 0.66$ ).

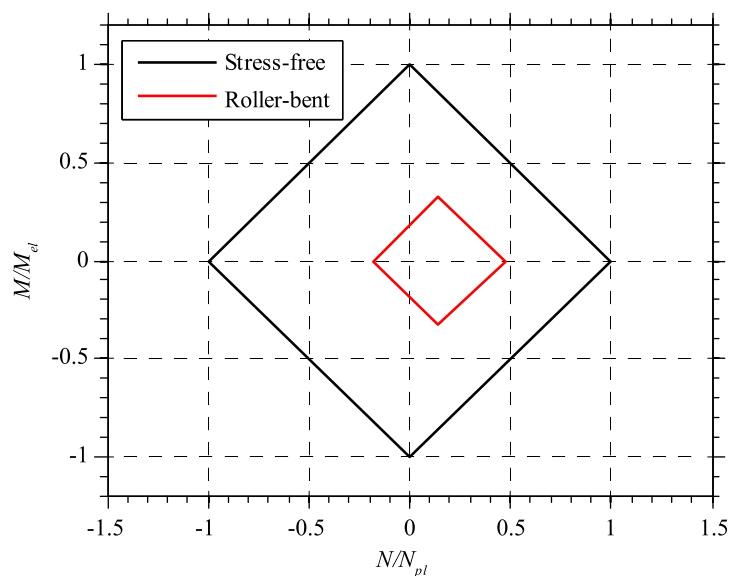


Figure 7-11: Interaction diagram  $N$ - $M$  for the out-of-plane response of RHS ( $h/b = 0.66$ ).

## 7.4 EFFECT ON BUCKLING LOAD

### 7.4.1 Circular-Hollow-Sections

The inelastic buckling resistance of roller-bent arches is assessed in this section, following the methodology of Beedle and Tall (1960). Critical loads for the in-plane and out-of-plane buckling of CHS arches are shown in Figure 7-12 and Figure 7-13 respectively, including the numerical (Section 6.5) and theoretical (Timoshenko, 1956) residual stress distributions. Results are presented for arches of CHS 100x5, steel grade S355, and included angle  $\alpha = \pi/8$ ; relevant investigations, however, have shown that such parameters have negligible influence on the dimensionless buckling curve results. As it is evidenced, the presence of locked-in stresses reduces significantly the critical loads. The theoretical distribution results in lower in-plane buckling resistances than the numerical one, since it comprises compressive values at the CHS top-height. In both cases, the reduction of critical loads is more pronounced for out-of-plane buckling, since the maximum residual stresses are located near the CHS mid-height, which contribute significantly to the out-of-plane flexural resistance.

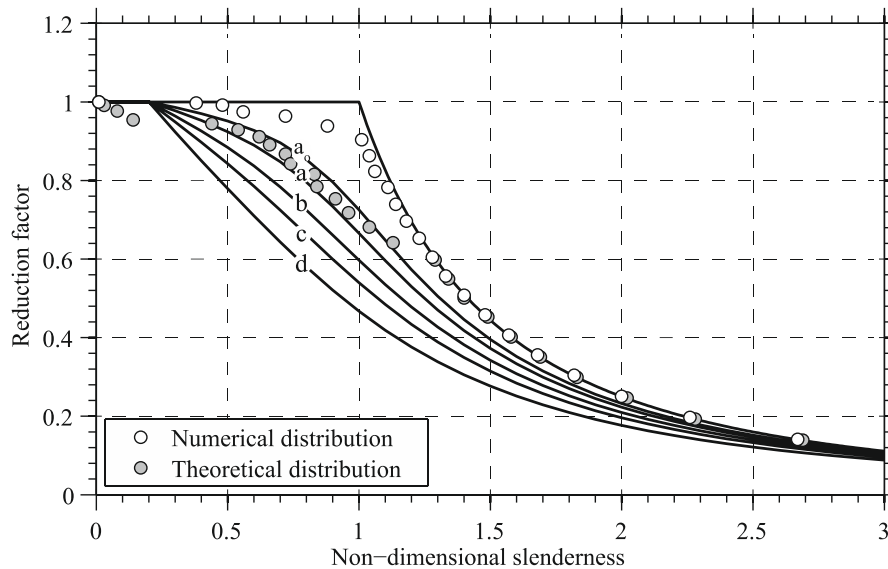


Figure 7-12: In-plane buckling resistance of roller-bent CHS arches.

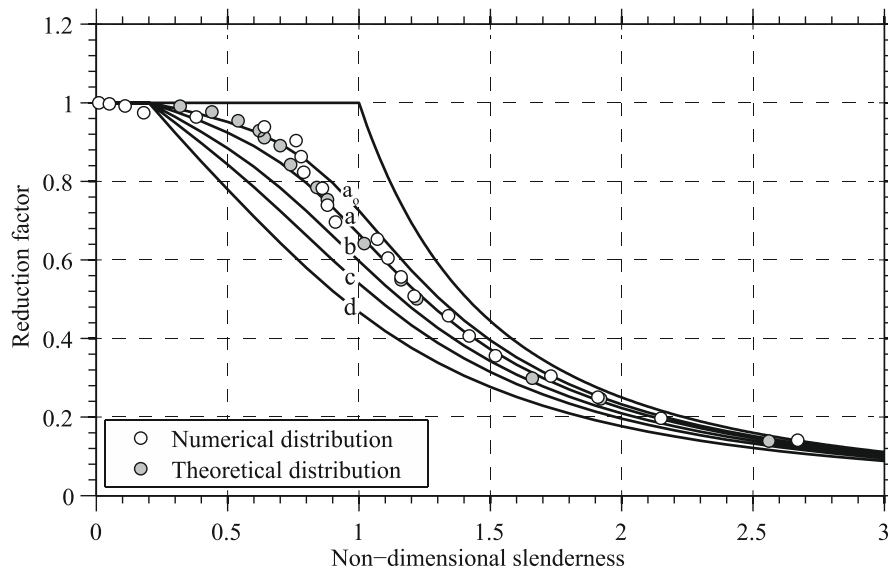


Figure 7-13: Out-of-plane buckling resistance of roller-bent CHS arches.

### 7.4.2 Square-Hollow-Sections

The inelastic buckling resistance of roller-bent SHS arches is evaluated, employing the numerical (c.f. Section 5.5) and theoretical (Timoshenko, 1956) residual stress distributions. Critical loads for the in-plane and out-of-plane buckling of SHS arches are shown in Figure 7-14 and Figure 7-15, respectively. Results are presented for arches of SHS 100x100x8, steel grade S355, and included angle  $\alpha = \pi/8$ , while such parameters have negligible influence on the dimensionless buckling curve results. As it is evidenced, critical loads are remarkably reduced due to the presence of residual stresses, depending on their distribution over the cross-section. Once again, the reduction is more pronounced in the case of out-of-plane buckling, since the maximum residual stresses are located near the SHS mid-height. The in-plane buckling results (theoretical distribution) exhibit two major load jumps, reflecting the loads for which extensive flange yielding takes place, due to the uniform residual stresses along their length.

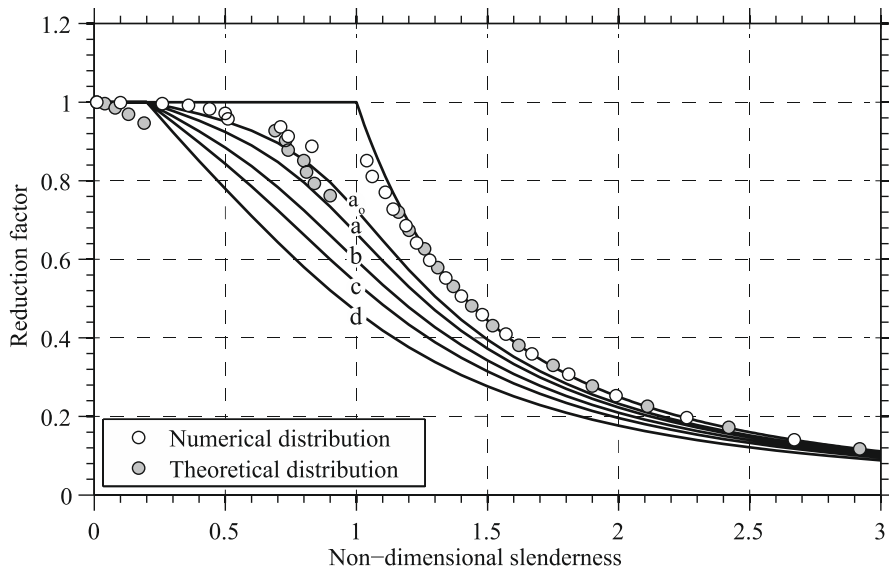


Figure 7-14: In-plane buckling resistance of roller-bent SHS arches.

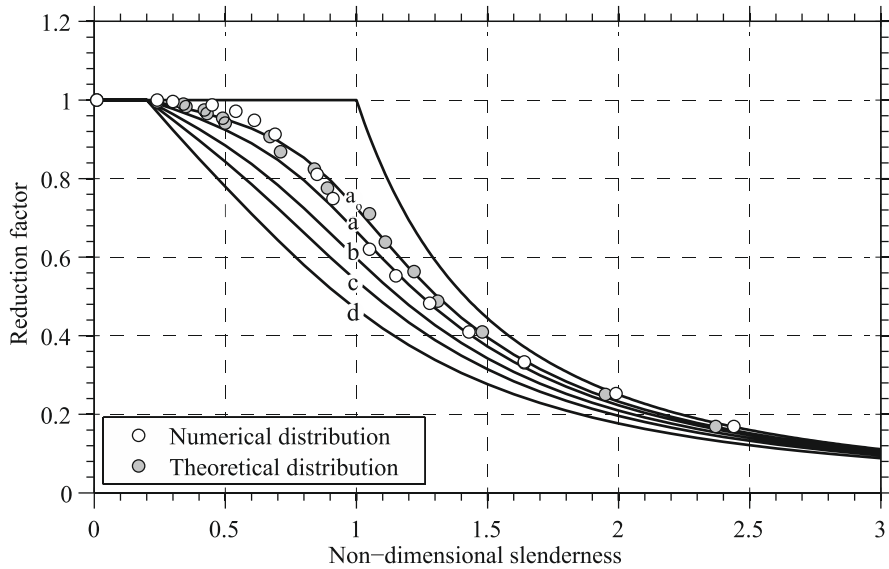


Figure 7-15: Out-of-plane buckling resistance of roller-bent SHS arches.

### 7.4.3 Rectangular-Hollow-Sections

The inelastic buckling resistance of roller-bent arches comprising RHS of aspect ratio 1.50, is evaluated employing the numerical (c.f. Section 5.5) and the theoretical (Timoshenko, 1956) residual stress distributions. Critical loads regarding the in-plane and out-of-plane buckling of RHS arches ( $h/b = 1.50$ ) are shown in Figure 7-16 and Figure 7-17 respectively. Results are presented for arches of RHS 120x80x8, steel grade S355, and included angle  $\alpha = \pi/8$ , while those parameters have negligible influence on the dimensionless buckling curve results. As it is evidenced, the overall response is almost similar to the corresponding one of square-hollow-sections.

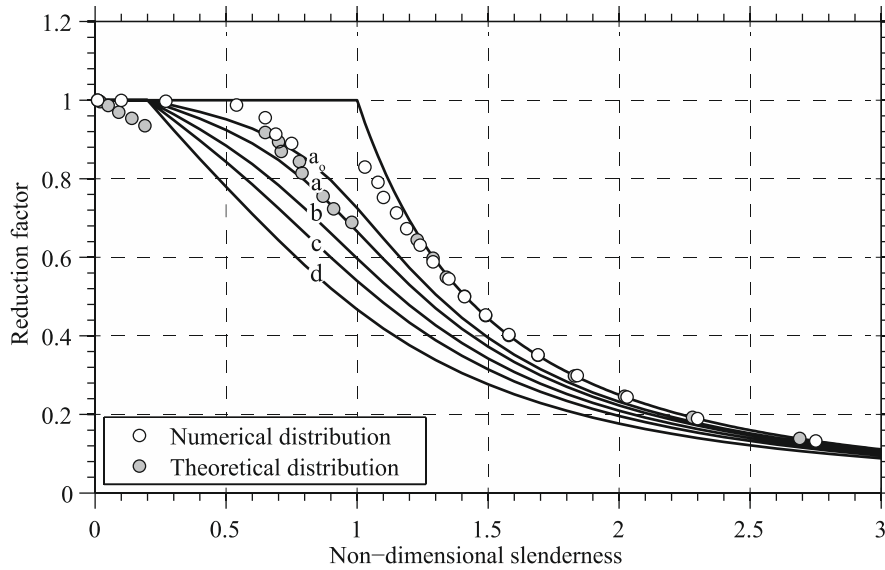


Figure 7-16: In-plane buckling resistance of roller-bent RHS arches ( $h/b = 1.50$ ).

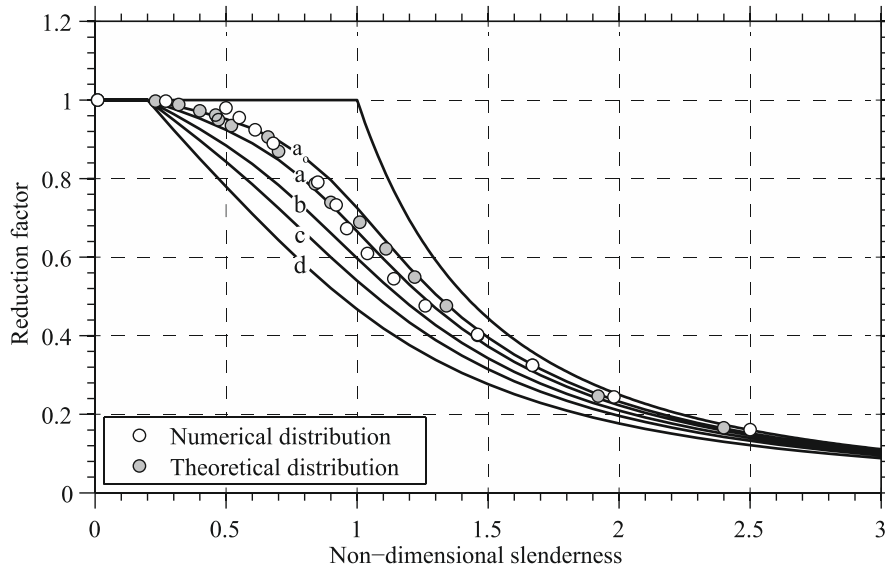


Figure 7-17: Out-of-plane buckling resistance of roller-bent RHS arches ( $h/b = 1.50$ ).

Furthermore, the inelastic buckling resistance of roller-bent arches is evaluated for rectangular-hollow-sections of aspect ratio 0.66. Once again, the corresponding numerical (Section 5.5) and theoretical (Timoshenko, 1956) residual stress distributions of roller-bent RHS are employed. Critical loads for the in-plane and out-of-plane buckling of RHS arches ( $h/b = 0.66$ ) are shown in Figure 7-18 and Figure 7-19 respectively. Results are presented for arches of RHS 80x120x8, steel grade S355, and included angle  $\alpha = \pi/8$ , while those parameters have negligible influence on the dimensionless buckling curve results. The overall response is similar to the corresponding one of RHS comprising aspect ratio 1.50; it is concluded, therefore, that the aspect ratio has a negligible effect on the dimensionless buckling loads.

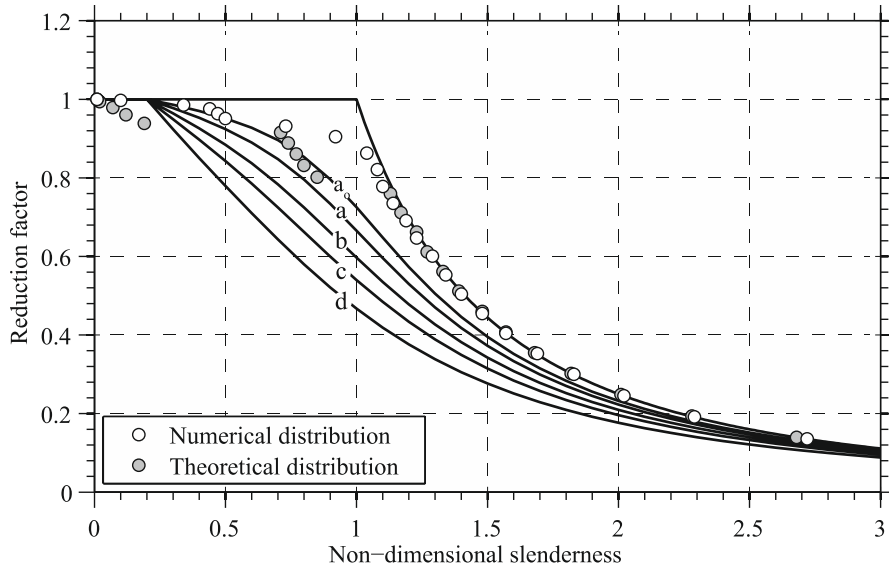


Figure 7-18: In-plane buckling resistance of roller-bent RHS arches ( $h/b = 0.66$ ).

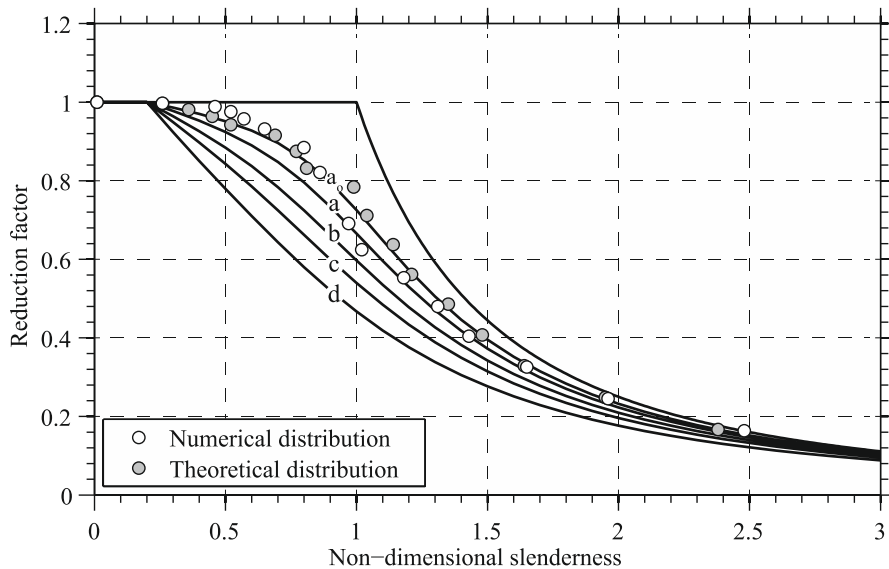


Figure 7-19: Out-of-plane buckling resistance of roller-bent RHS arches ( $h/b = 0.66$ ).

## 7.5 CONCLUSIONS

An analytical investigation regarding the effects of residual stresses on the in-plane and out-of-plane behavior of roller-bent arches was carried out in this chapter, using expressions that rely on linear analysis and employ reliable residual stress distributions. Interaction diagrams of axial force with bending moment were developed for roller-bent hollow sections, in order to define the elastic domain of the cross-sections. It was found that the presence of residual stresses reduces significantly the elastic domain. The reduction is more prevalent in the case of out-of-plane bending, since maximum residual stresses are located near the mid-height of roller-bent sections. In this case, the direction of bending (opening or closing the arch) does not affect the response, as roller-bent residual stresses are symmetric to the arch plane. The elastic domain of roller-bent sections was almost similar in all cases; the reduction was slightly more pronounced in the case of SHS/RHS compared to CHS, since high residual stresses are encountered additionally at the web-to-flange junctions. The cross-sectional aspect ratio of RHS had a negligible effect on the elastic domain. The interaction diagrams can be directly applied in structural engineering design practice to take into consideration the effects of cold bending in the elastic response of arches.

Furthermore, the methodology of Beedle and Tall (1960) was adopted to obtain the inelastic buckling loads of roller-bent arches comprising hollow sections. The calculations were performed employing both the numerical and the theoretical residual stress distributions. The theoretical distribution was found to yield lower in-plane buckling resistances than the numerical one, since it comprises compressive values at the top-height of hollow sections. In both cases, the reduction of buckling strength was more pronounced for out-of-plane buckling, since maximum residual stresses are located near the mid-height of hollow sections. The presence of residual stresses had small effect on the maximum strength of very slender arches, which exhibit buckling strengths approaching the Euler load. The overall response was almost similar between CHS, SHS and RHS; the reduction was slightly more pronounced in the case of SHS/RHS compared to CHS, since high residual stresses are encountered at the web-to-flange junctions. The buckling curve results of this section are very useful to qualitatively assess the effect of residual stresses on the inelastic buckling load of roller-bent arches, while they are not intended to be used for design purposes, since initial imperfections and geometric non-linearities are not taken into account here.

## REFERENCES

- AISC (2005). *Specification for Structural Steel Buildings*. ANSI/AISC Standard 360-05, American Institute of Steel Construction, Chicago, IL.
- Alpsten, G. A. (1970). "Residual Stresses and Strength of Cold-Straightened Wide Flange Shapes." *Jernkontorets Ann.*, pp. 1–9 (in Swedish).
- Batterman, R. H., and Johnston, B. G. (1967). "Behavior and Maximum Strength of Metal Columns." *ASCE J. Struct. Div.*, vol. 93, pp. 205–230.
- Beedle, L. S., and Tall, L. (1960), "Basic Column Strength." *ASCE J. Struct. Div.*, vol. 86, pp. 139–173.
- Beer, H., and Schultz, G. (1970). "Theoretical Basis for the European Column Curves." *Constr. Met.*
- Bjorhovde, R. (1972). "Deterministic and Probabilistic Approaches to the Strength of Steel Columns," Ph.D. dissertation, Lehigh University, Bethlehem, PA.
- Bjorhovde, R., and Tall, L. (1971). "Maximum Column Strength and the Multiple Column Curve Concept," Fritz Eng. Lab. Rep. No. 338.29, Lehigh University, Bethlehem, PA, Oct.

- Brozzetti, J., Alpsten, G. A., and Tall, L. (1970a). "Residual Stresses in a Heavy Rolled Shape 14WF730." Fritz Eng. Lab. Rep. No. 337.1, Lehigh University, Bethlehem, PA, Jan.
- CEN (2005). *Eurocode 3: Design of Steel Structures, Part 1-1: General Rules and Rules for Buildings, EN 1993-1-1*. Comité Européen de Normalisation (CEN), European Committee for Standardization Brussels, Belgium.
- CSA (2009). *Design of Steel Structures*. CSA-S16-09, Canadian Standards Association (CSA), Toronto, Ontario, Canada.
- ECCS (1976). *Manual on Stability of Steel Structures*. European Convention for Constructional Steelwork, Liege, Belgium.
- Jacquet, J. (1970). "Column Tests and Analysis of Their Results." *Constr. Met.*
- Kishima, V., Alpsten, G. A., and Tall, L. (1969). "Residual Stresses in Welded Shapes of Flame-Cut Plates in ASTM A572(50) Steel." Fritz Eng. Lab. Rep. No. 321.2, Lehigh University, Bethlehem, PA, June.
- McFalls, R. K., and Tall, L. (1970). "A Study of Welded Columns Manufactured from Flame-Cut Plates." *AWS Weld. J.*, vol. 49, pp. 141–153.
- Osgood, W. R. (1951). "The Effect of Residual Stress in Column Strength." *Proc. First U.S. Natl. Congr. Appl. Mech.*, June, p. 415.
- Robertson, A. 1925. "The Strength of Struts." *Selected Engineering Papers*, No. 28, The Institution of Civil Engineers, London.
- Sfintesco, D. (1970). "Experimental Basis for the European Column Curves." *Constr. Met.*
- Timoshenko, S. P. (1956). *Strength of Materials Part II - Advanced Theory and Problems*, 3<sup>rd</sup> Ed., D. Van Nostrand Company, New York, NY.
- Timoshenko, S. P., and Gere, J. M. (1961). *Theory of Elastic Stability*. 2<sup>nd</sup> ed., McGraw-Hill, New York.
- Yang, H., Beedle, L. S., and Johnston, B. G. (1952). "Residual Stress and the Yield Strength of Steel Beams." *Weld. J. Res. Suppl.*, vol. 31, pp. 224–225.



# 8 STRUCTURAL STABILITY OF ARCHES

## 8.1 INTRODUCTION

The structural stability of arches may be characterized by snap-through, in-plane, or out-of-plane buckling. Snap-through buckling is usually the prevailing instability mechanism in cases of shallow arches (low height to span ratio), which are restrained against out-of-plane displacements. In this case, the arch stiffness is gradually reduced due to the induced axial shortening, resulting to a limit point in which transition from compressive to tensile action occurs suddenly. The in-plane buckling is predominant in cases of non-shallow arches, which are adequately braced against out-of-plane displacements. In this context, either symmetric or antisymmetric mode shapes can be developed. The out-of-plane buckling occurs in cases of arches exhibiting significant free-standing portions. This type of instability comprises a combination of flexural and lateral-torsional buckling, and therefore is also denoted as flexural-torsional buckling. Residual stresses and geometric imperfections have significant effect on the inelastic stability of members which are subjected mainly to axial compression, as in the case of arches. In practice, pure axial compression without moment cannot exist due to the presence of imperfections, eccentricities, support spreading and unsymmetrical loading.

The effects of geometric imperfections and residual stresses on the stability of steel arches have been reported in early studies conducted by Komatsu and Sakimoto (1977) and Sakimoto et al. (1979). In this context, steel arches comprising welded box and wide-flange sections were examined, revealing that the presence of geometric imperfections and residual stresses can cause a significant reduction on the ultimate resistance load. The in-plane stability of steel arches was studied by Pi and Trahair (1999) and Pi and Bradford (2004), while the out-of-plane stability was studied by Pi and Trahair (1998) and Pi and Bradford (2005). In these studies, circular arches of I-sections were examined, and interaction formulas of axial force with bending moment were proposed. La Poutré et al. (2013) carried out an experimental study on the out-of-plane stability of roller-bent arches comprising wide-flange-sections. Pertinent finite element analyses were carried out by Spoorenberg et al. (2012), and results were extracted in a column curve format that can be easily implemented in the structural design practice. Indicative residual stress models, which were implemented in the studies of Komatsu and Sakimoto (1977), Pi and Bradford (2004), and Spoorenberg et al. (2012), are depicted in Figure 8-1.

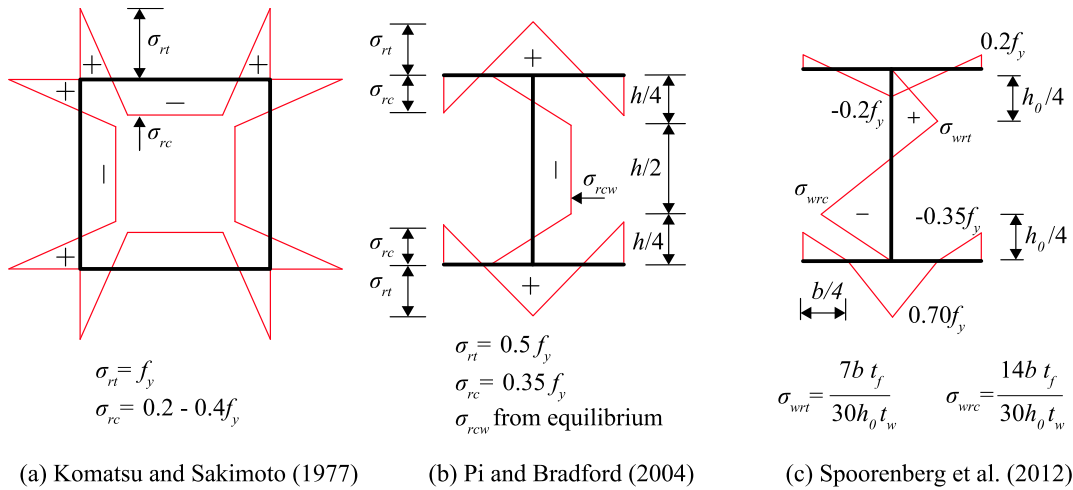


Figure 8-1: Residual stress distributions of steel arches.

State-of-the-art column formulas are based on results of extensive computational studies incorporating residual stresses and geometric imperfections, calibrated against experimental tests (Ziemian, 2010). Appropriate buckling formulas can be developed similarly for steel arches employing the Finite Element Method (FEM). In this context, Material Nonlinear Analyses (MNA) and Linearized Buckling Analysis (LBA) are aimed at providing the plastic strength and the critical buckling loads of steel arches, respectively. The nondimensional slenderness of arches can, thus, be determined for the in-plane and out-of-plane buckling, as the square root of the plastic resistance divided by the corresponding critical buckling load, according to Eq. (8-1). Moreover, Geometric and Material Nonlinear Analyses with Imperfections (GMNIA), are required to obtain the actual strength resistance for in-plane and out-of-plane buckling, including geometric imperfections and residual stresses. Therefore, the reduction factor  $\chi$  of strength can be determined from the actual strength resistance from GMNIA over the plastic strength resistance from MNA, according to Eq. (8-2).

$$\bar{\lambda} = \sqrt{\frac{P_{MNA}}{P_{LBA}}} \tag{8-1}$$

$$\chi = \frac{P_{GMNIA}}{P_{MNA}} \tag{8-2}$$

In this chapter, the structural stability of arches is evaluated by means of finite element analyses, accounting for geometry and material nonlinearities. Appropriate numerical models of arches comprising roller-bent and stress-free Circular-Hollow-Sections (CHS) are developed in the general-purpose finite element software ADINA (ADINA, 2017). The effects of geometric imperfections and residual stresses are included in the developed numerical models, incorporating reliable residual distributions of CHS and appropriate geometric tolerances of arches. Sensitivity analyses are performed, aiming at assessing the separate and combined effects of residual stresses and geometric imperfections on the buckling strength resistance. An extensive parametric study is carried out, in order to assess the spatial stability of arches exhibiting various geometric dimensions. Various dimensions are examined, comprising a wide range of arch non-dimensional slenderness, commonly encountered in practice. The results of parametric analyses are presented in buckling curve diagrams, which are compared to the proposed column curves of EN1993-1-1 (CEN, 2005).

## 8.2 NUMERICAL MODELING

Steel arches of a Circular-Hollow-Sections (CHS) are modeled using 2-node Hermitian beam elements, as shown in Figure 8-2. Appropriate axial force-strain  $N-\varepsilon$  and moment-curvature  $M-C$  diagrams are introduced to the beam elements, representing reliably the cross-sectional properties of roller-bent and stress-free CHS. The methodology of extracting the  $N-\varepsilon$  and  $M-C$  diagrams is based on finite element simulations, accounting for material nonlinearities and the presence of residual stresses. A detailed description of the employed procedure, along with the  $N-\varepsilon$  and  $M-C$  diagrams, are presented in the Appendix A.

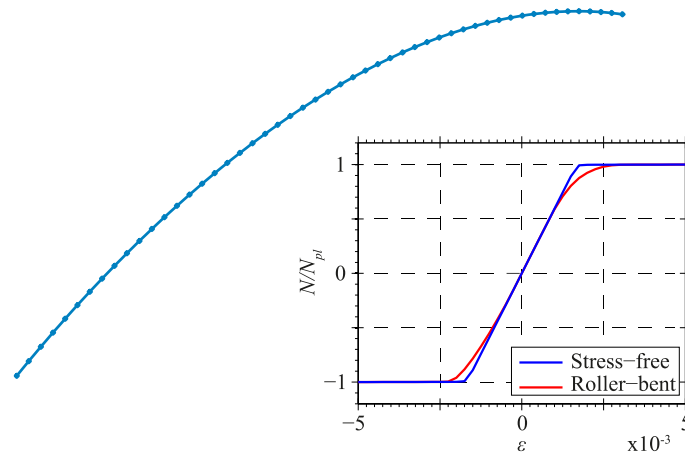


Figure 8-2: Beam element model of arch and  $N-\varepsilon$  diagram of CHS 100x5.

## 8.3 VALIDATION STUDY

In this section, a validation study is performed in order to verify the accuracy of the proposed finite element modeling. To that end, an arch comprising a CHS 100x5, radius of curvature 5.09m, and rise-to-span ratio 0.11, is used as benchmark case to verify pertinent numerical models. In the first case, the arch is modeled using 2-node Hermitian beam elements, following the modeling considerations of Section 8.2. Appropriate  $N-\varepsilon$  and  $M-C$  diagrams of a CHS 100x5 (Appendix A) are introduced to the beam elements, incorporating an elastic-plastic material law without hardening ( $E = 210\text{GPa}$ ,  $f_y = 355\text{MPa}$ ) and the proposed residual stress model of roller-bent CHS. In the second case, the arch is modeled using 4-node shell elements of 5 integration points at the element thickness direction. The Newton-Cotes integration method is employed, since it is more effective for capturing the onset and spread of the materially nonlinear conditions, as the integration points are on the boundaries of the elements. The same material model and residual stress distribution is implemented, as in the case of beam elements. The membrane residual stresses are introduced directly in the integration points of shell elements, at the longitudinal direction of the arch axis. Rigid links are used to connect the nodes of the edged cross-sections to their geometric centroids, in order to prescribe the boundary conditions. Identical boundary conditions are employed in both models. Pinned supports are employed at the arch ends for the in-plane and out-of-plane bending. The torsional degree of freedom is fixed at the arch ends, and a lateral support is applied at the top-height of the arch, in order to increase the out-of-plane buckling load. Numerical analyses are carried out under a uniform compressive load in the gravity direction.

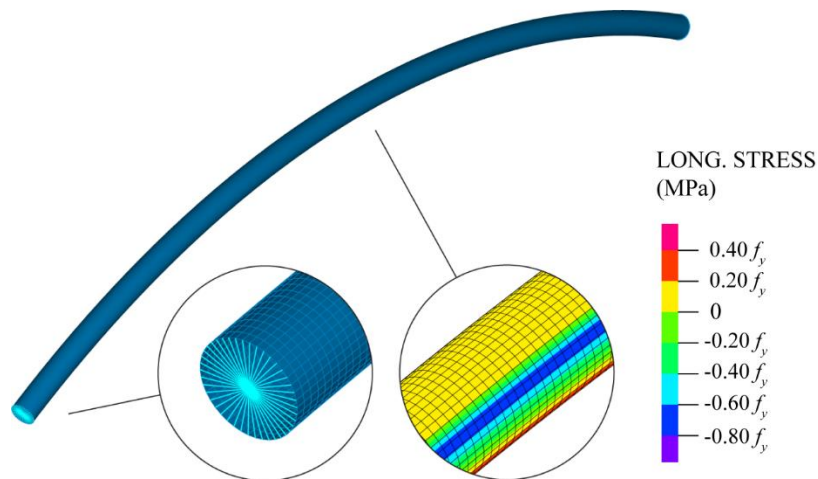


Figure 8-3: Shell element model along with details of the rigid links and the residual stresses.

Material Nonlinear Analyses (MNA) and Linearized Buckling Analyses (LBA) are first performed to obtain the plastic strength and the buckling eigenmodes respectively, using the beam and shell element models. In both cases, the plastic strength ( $P_{MNA}$ ) of the arch is found equal to 102kN, which is identical for the roller-bent and stress-free sections, since the plastic strength is not affected by the presence of residual stresses. The buckling eigenmodes of the arch are shown in Figure 8-4, for the beam and shell element models. The 1<sup>st</sup> critical load ( $P_{cr1}$ ) is found equal to 150kN/m, comprising out-of-plane buckling, and the 2<sup>nd</sup> critical load ( $P_{cr2}$ ) is found equal to 159kN/m, comprising the anti-symmetrical in-plane buckling. The buckling eigenmodes are identical for the roller-bent and stress-free sections, since the initial tangent stiffness of the model is not affected by the presence of residual stresses. The nondimensional slenderness of the arch can be determined as the square root of the plastic load divided by the critical buckling load, which is equal to 0.80 and 0.82, for the out-of-plane and in-plane buckling respectively. It should be noted that LBA provides in most cases an upper bound of the actual strength, whereas Geometric and Material Nonlinear Analyses with Imperfections (GMNIA) are able to provide the actual buckling resistance of steel elements.

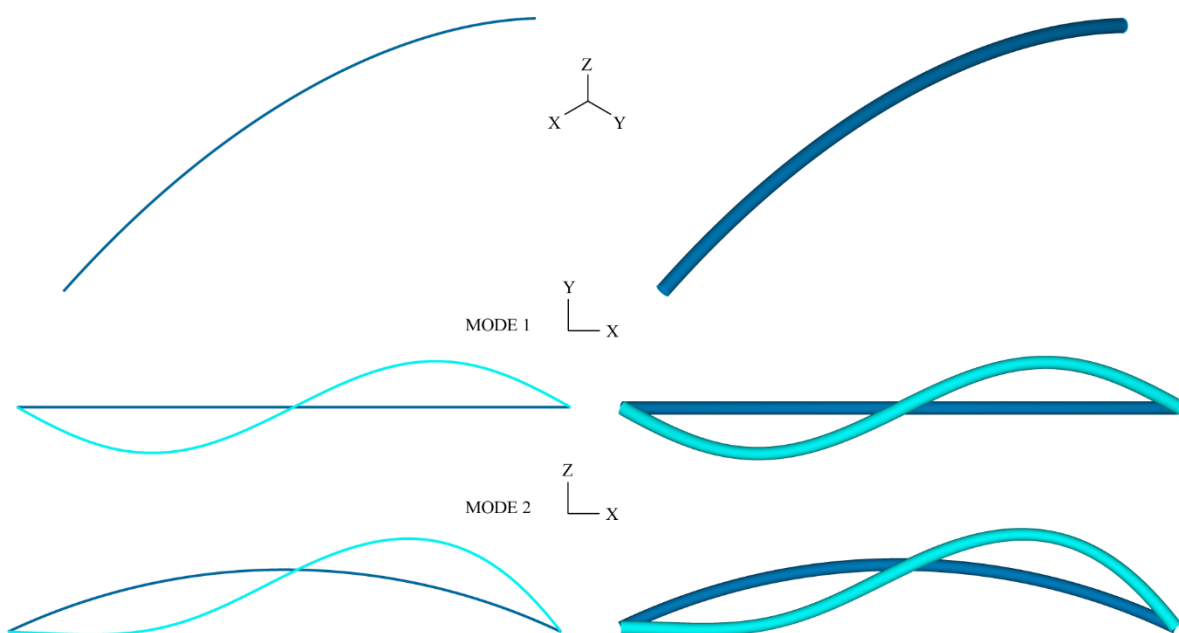


Figure 8-4: Buckling eigenmodes of beam (left) and shell (right) element models.

Geometry and Material Nonlinear Analyses with Imperfections (GMNIA) are carried out to obtain the in-plane and out-of-plane buckling response of roller-bent and stress-free arches using the beam and shell element models. The Newton-Raphson and the Arc-length solution algorithms are implemented in the analyses of beam and shell element models, respectively; the Arc-length solution algorithm is able to provide the post-collapse response. An imperfection magnitude of the arch semi-length  $S$  over 500 is employed, according to shape of the 1<sup>st</sup> or the 2<sup>nd</sup> eigenmode for the out-of-plane and in-plane buckling, respectively. The arch semi-length corresponds to the equivalent buckling length for the in-plane and out-of-plane buckling, while the magnitude of imperfections is taken according to the maximum allowable geometric tolerances of curved members (AISC, 2016). A comparison of the equilibrium paths of the imposed load with the out-of-plane deflection at the crown, between the shell and beam element models of the roller-bent and stress-free CHS is shown in Figure 8-5. Pertinent equilibrium paths of the imposed load with the vertical deflection at the crown, are compared in Figure 8-6. In both diagrams, the imposed load is normalized with respect to the plastic strength of the arch ( $P_{MNA} = 102\text{kN/m}$ ). Excellent agreement is evidenced in both cases, in terms of stiffness and strength capacity.

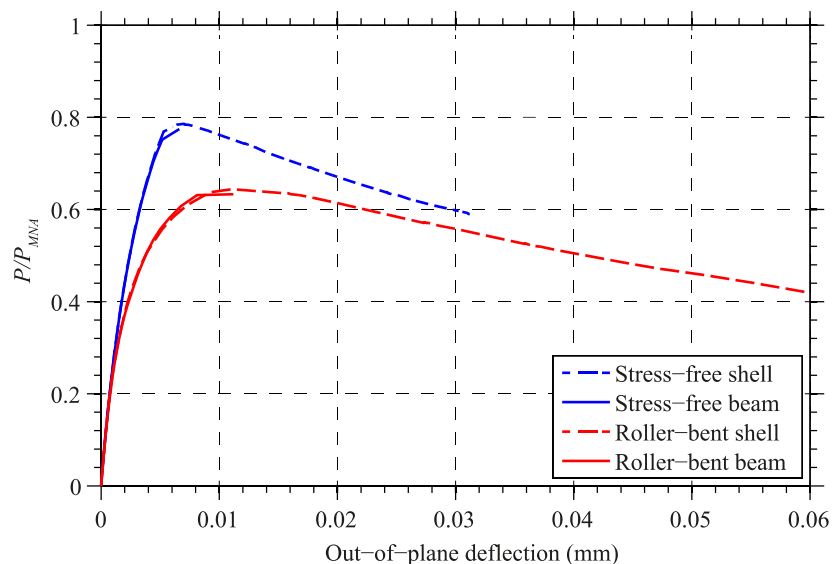


Figure 8-5: Comparison of the out-of-plane buckling response between shell and beam elements.

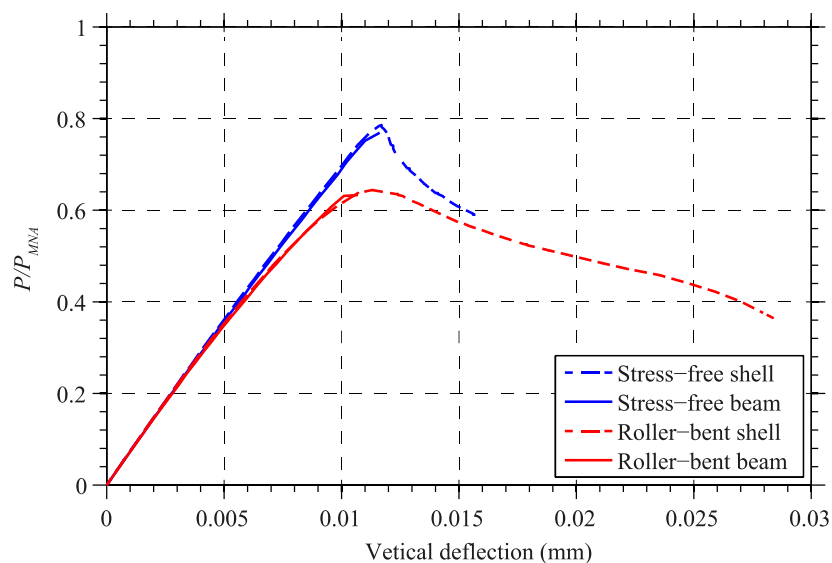


Figure 8-6: Comparison of the out-of-plane buckling response between shell and beam elements.

The equilibrium paths of load with in-plane deflection at the crown are compared between the shell and beam element models of roller-bent and stress-free CHS in Figure 8-7. The imposed load is normalized with respect to the plastic strength of the arch ( $P_{MNA} = 102\text{kN/m}$ ). Excellent agreement is evidenced between the beam and shell element models, in terms of stiffness and strength capacity.

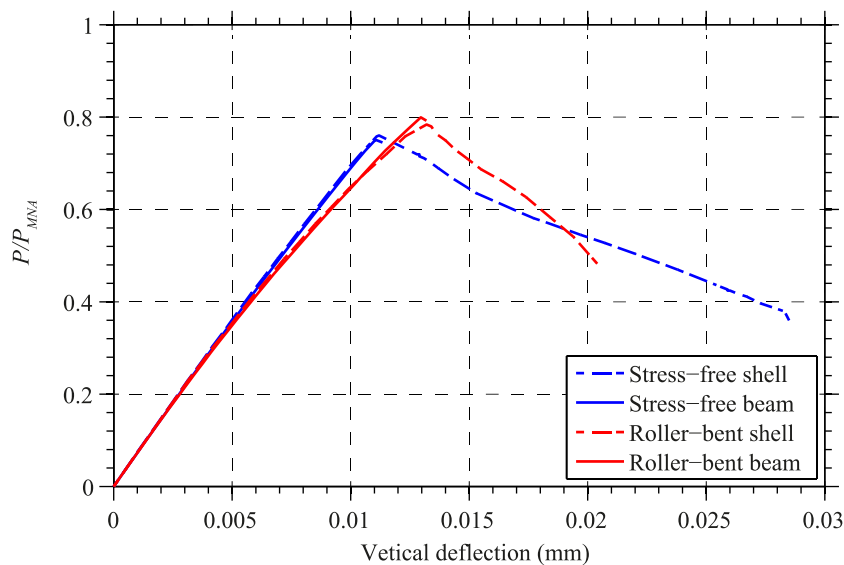


Figure 8-7: Comparison of the in-plane buckling response between shell and beam elements.

## 8.4 SENSITIVITY ANALYSES

In this section, sensitivity analyses are performed in order to assess the effects of geometric imperfections and residual stresses on the inelastic stability of arches, by means of Geometric and Material Nonlinear Analyses with Imperfections (GMNIA). Pertinent analyses are carried out using the shell element model of the benchmark case presented in the validation study. Numerical results are compared in terms of load-displacement equilibrium paths.

### 8.4.1 Effect of geometric imperfections

Aiming at investigating the effect of geometric imperfections on the inelastic stability of roller-bent arches, GMNI analyses are performed for various imperfection magnitudes. The shape of imperfections is taken according to the 1<sup>st</sup> or the 2<sup>nd</sup> eigenmode for the out-of-plane and in-plane buckling respectively, while magnitudes equal to  $S/100$ ,  $S/500$  and  $S/1000$  are examined. A comparison of the pertinent equilibrium paths of imposed load with out-of-plane deflection at the crown is shown in Figure 8-8. The equilibrium path of imposed load with vertical deflection at the crown, for the same imperfection magnitudes, is shown in Figure 8-9. In both diagrams, the load is normalized with respect to the plastic resistance of the arch obtained from MNA ( $P_{MNA} = 102\text{kN/m}$ ). As it is evidenced, the ultimate strength capacity is significantly reduced with increase of the imperfection magnitude.

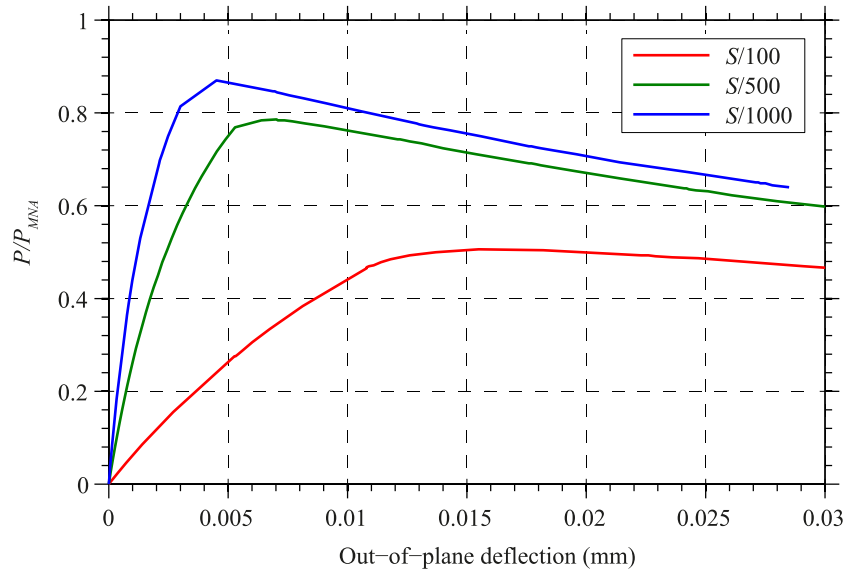


Figure 8-8: Out-of-plane buckling response for various imperfection magnitudes.

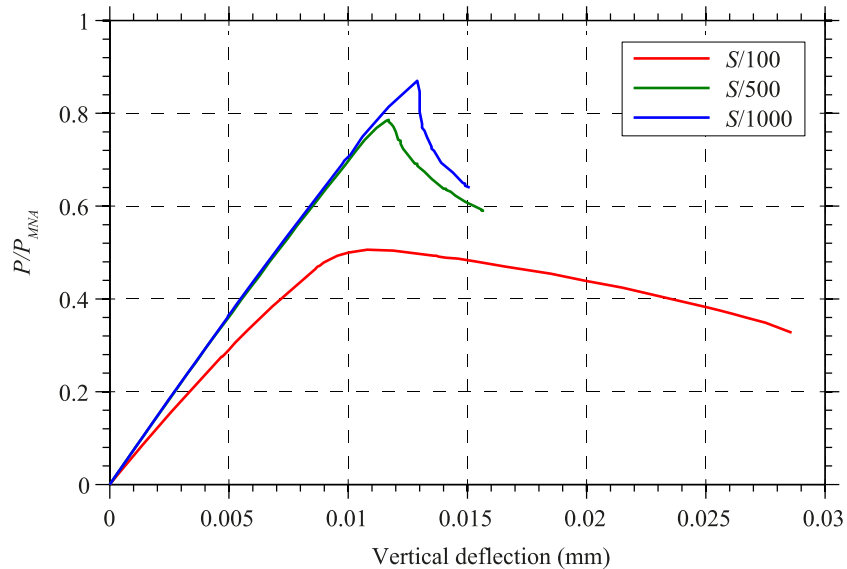


Figure 8-9: Out-of-plane buckling response for various imperfection magnitudes.

The equilibrium paths of load with in-plane deflection at the crown are compared between the same imperfection magnitudes in Figure 8-10. The load is normalized with respect to the plastic resistance obtained from MNA ( $P_{MNA} = 102\text{kN/m}$ ). Once again, the magnitude of imperfections has a significant effect on the overall response of the arch, and especially on the ultimate strength capacity.

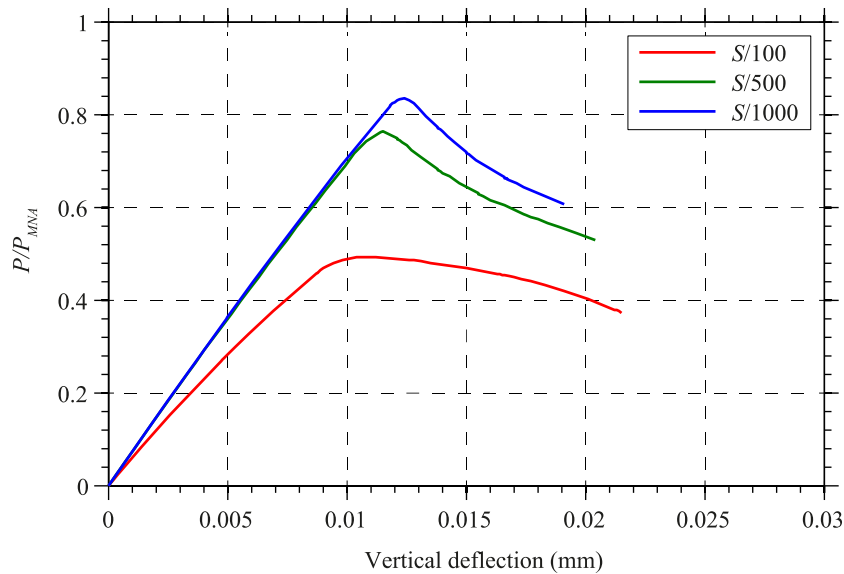


Figure 8-10: In-plane buckling response for various imperfection magnitudes.

#### 8.4.2 Effect of residual stresses

Aiming at investigating the effect of residual stresses on the inelastic stability of arches, GMNI analyses are performed including or not the presence of residual stresses. To that end, the theoretical and numerical residual stress distributions are examined. For comparison purposes the same imperfection magnitude of  $S/500$  is employed in all cases. The shape of imperfections is taken according to the 1<sup>st</sup> or the 2<sup>nd</sup> eigenmode for the out-of-plane and in-plane buckling, respectively. A comparison of the equilibrium paths of imposed load with out-of-plane deflection at the crown between the examined cases, is shown in Figure 8-11. The pertinent equilibrium paths of imposed load with vertical deflection at the crown, are shown in Figure 8-12. In both diagrams, load is normalized with respect to the plastic resistance of the arch obtained from MNA ( $P_{MNA} = 102\text{kN/m}$ ). As it is evidenced, the presence of residual stresses has a significant effect on the out-of-plane buckling response, reducing the buckling strength of the arch.

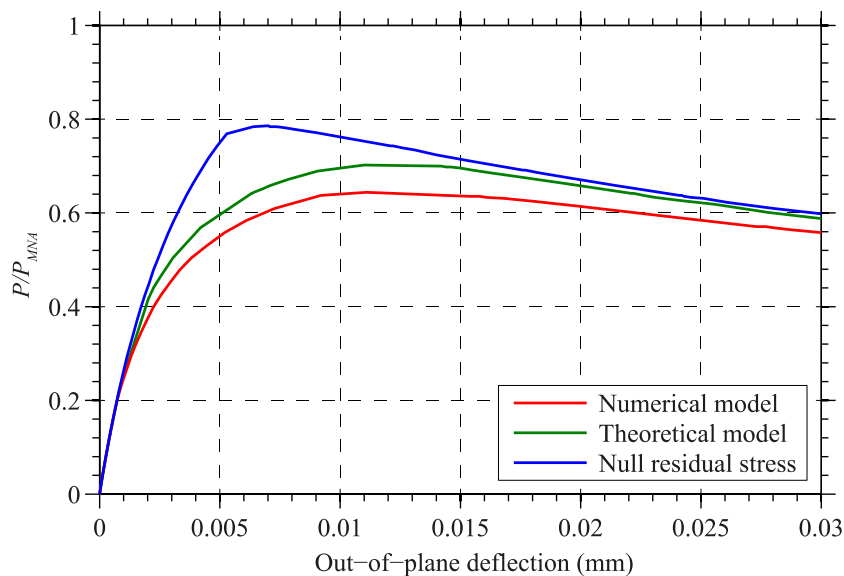


Figure 8-11: Out-of-plane buckling response for various residual stresses.



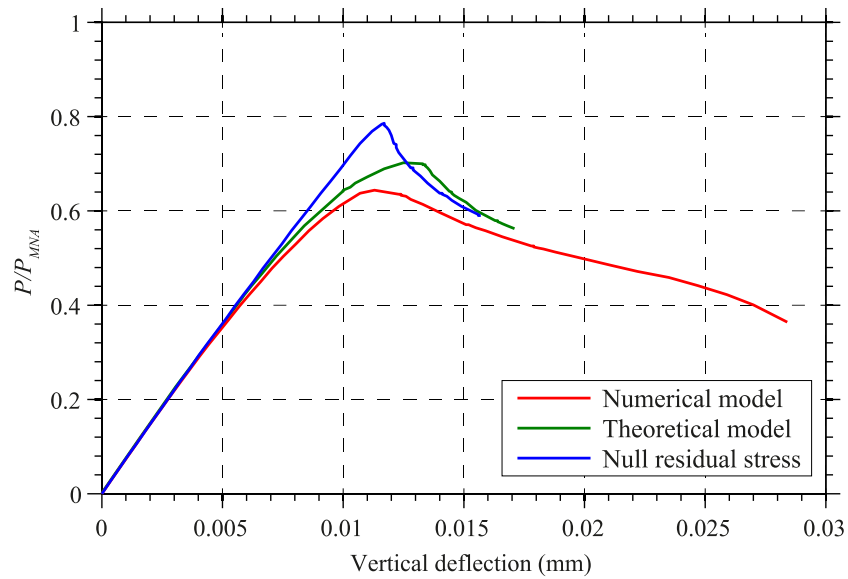


Figure 8-12: Out-of-plane buckling response for various residual stresses.

The equilibrium paths of load with in-plane deflection at the crown for the examined cases are shown in Figure 8-13. The load is normalized with respect to the plastic resistance obtained from MNA ( $P_{MNA} = 102\text{kN/m}$ ). As it is evidenced, the presence of residual stresses has a less significant effect on the in-plane buckling response.

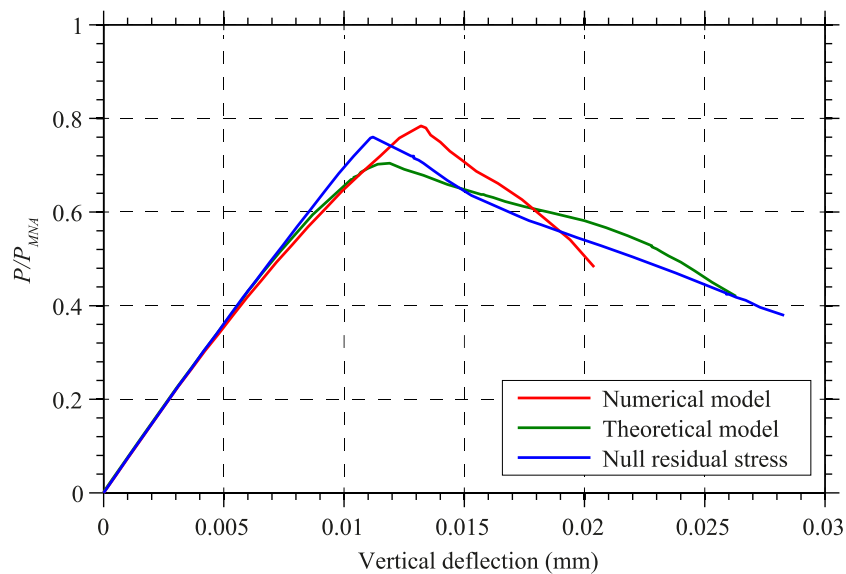


Figure 8-13: In-plane buckling response for various residual stresses.

## 8.5 PARAMETRIC ANALYSES

In this section, a parametric study is conducted, aiming at assessing the inelastic stability of steel arches. Parametric analyses are performed on CHS arches consisting of beam elements, following the modeling aspects of Section 8.2. Various dimensions are examined, covering a wide range of circular arches that are met in civil engineering applications. The cross-sectional properties of a CHS 100x5 ( $d = 100\text{mm}$ ,  $t = 5\text{mm}$ ) remain constant in all cases, while the rise  $f$  and span  $l$  are varied appropriately in order to obtain rise-to-span ratios in the range of  $0.10 \leq f/l \leq 0.30$  and bending ratios in the range of  $10.9 \leq R/d \leq 106.3$ , as shown in Table 8-1. The  $N$ - $\varepsilon$  and  $M$ - $C$  diagrams of a CHS 100x5 (Appendix A) are introduced to the beam elements, incorporating the cross-sectional properties of roller-bent and stress-free CHS. Pinned supports are employed at the arch ends for the in-plane and out-of-plane bending. The torsional degree of freedom is fixed at the arch ends, and a lateral support is applied at the top-height of the arch, in order to increase the out-of-plane buckling load. Material Nonlinear Analyses (MNA) and Linearized Buckling Analyses (LBA) are first performed to obtain the plastic strength and the buckling eigenmodes, respectively. Afterwards, the nondimensional slenderness is determined as the square root of the plastic load divided by the critical buckling load. Geometric and Material Nonlinear Analyses with Imperfections (GMNIA) are carried out to obtain the actual buckling strength for the in-plane and out-of-plane buckling of the roller-bent and stress-free arches. The shape of imperfections is taken according to the 1<sup>st</sup> or the 2<sup>nd</sup> buckling mode for the out-of-plane or the in-plane response respectively, while the magnitude is typically taken equal to  $S/500$ . Parametric analyses are carried out under uniform compressive loads in the radial direction, causing axial compression. Numerical results regarding the out-of-plane and in-plane buckling of the arches are given in Table 8-2 and Table 8-3, respectively.

Table 8-1: Examined arch configurations.

No.	$f$ (m)	$l$ (m)	$R$ (m)	$f/l$	$R/d$
1	3.00	14.00	9.67	0.21	96.7
2	3.00	12.00	7.50	0.25	75.0
3	2.00	11.00	8.56	0.18	85.6
4	2.00	10.00	7.25	0.20	72.5
5	2.50	10.00	6.25	0.25	62.5
6	3.00	10.00	5.67	0.30	56.7
7	1.00	9.00	10.63	0.11	106.3
8	1.50	9.00	7.50	0.17	75.0
9	2.00	9.00	6.06	0.22	60.6
10	2.50	9.00	5.30	0.28	53.0
11	2.00	8.00	5.00	0.25	50.0
12	1.00	8.00	8.50	0.13	85.0
13	2.00	7.00	4.06	0.29	40.6
14	1.00	7.00	6.63	0.14	66.3
15	1.00	6.00	5.00	0.17	50.0
16	1.50	5.00	2.83	0.30	28.3
17	1.00	5.00	3.63	0.20	36.3
18	0.50	5.00	6.50	0.10	65.0
19	0.80	4.00	2.90	0.20	29.0
20	0.49	4.36	5.09	0.11	50.9
21	0.40	4.00	5.20	0.10	52.0
22	0.90	3.00	1.70	0.30	17.0
23	0.50	2.50	1.81	0.20	18.1
24	0.30	2.00	1.82	0.15	18.2
25	0.30	1.50	1.09	0.20	10.9

Table 8-2: Out-of-plane buckling of roller-bent and stress-free arches under uniform radial load.

No.	Roller-bent section					Stress-free section				
	$P_{cr}$ (kN/m)	$P_{MNA}$ (kN/m)	$P_{GMNIA}$ (kN/m)	$\bar{\lambda}$	$\chi$	$P_{cr}$ (kN/m)	$P_{MNA}$ (kN/m)	$P_{GMNIA}$ (kN/m)	$\bar{\lambda}$	$\chi$
1	5.5	57.5	4.7	3.23	0.08	5.5	57.5	5.2	3.23	0.09
2	8.4	74.1	7.1	2.97	0.10	8.4	74.1	7.9	2.97	0.11
3	11.3	64.9	9.0	2.40	0.14	11.3	64.9	10.3	2.40	0.16
4	15.2	76.7	12.0	2.25	0.16	15.2	76.7	13.7	2.25	0.18
5	14.5	89.0	11.8	2.48	0.13	14.5	89.0	13.3	2.48	0.15
6	12.9	98.1	10.8	2.76	0.11	12.9	98.1	12.1	2.76	0.12
7	16.7	52.3	12.0	1.77	0.23	16.7	52.3	14.2	1.77	0.27
8	20.3	74.1	15.2	1.91	0.21	20.3	74.1	17.7	1.91	0.24
9	20.7	91.7	16.1	2.11	0.18	20.7	91.7	18.5	2.11	0.20
10	18.8	104.9	15.2	2.36	0.14	18.8	104.9	17.2	2.36	0.16
11	28.3	111.2	21.9	1.98	0.20	28.3	111.2	25.2	1.98	0.23
12	25.5	65.4	17.8	1.60	0.27	25.5	65.4	21.3	1.60	0.33
13	39.1	136.9	29.9	1.87	0.22	39.1	136.9	34.6	1.87	0.25
14	40.8	83.9	27.2	1.43	0.32	40.8	83.9	32.9	1.43	0.39
15	68.6	111.2	43.1	1.27	0.39	68.6	111.2	52.6	1.27	0.47
16	103.2	196.2	70.1	1.38	0.36	103.2	196.2	84.3	1.38	0.43
17	121.6	153.4	71.1	1.12	0.46	121.6	153.4	87.2	1.12	0.57
18	91.0	85.5	45.8	0.97	0.54	91.0	85.5	55.7	0.97	0.65
19	237.5	191.7	114.7	0.90	0.60	237.5	191.7	137.5	0.90	0.72
20	148.6	109.1	66.6	0.86	0.61	148.6	109.1	79.3	0.86	0.73
21	178.3	106.9	70.8	0.77	0.66	178.3	106.9	82.5	0.77	0.77
22	477.6	327.1	216.3	0.83	0.66	477.6	327.1	253.4	0.83	0.77
23	972.8	306.8	251.0	0.56	0.82	972.8	306.8	269.8	0.56	0.88
24	1803.0	306.1	272.1	0.41	0.89	1803.0	306.1	280.8	0.41	0.92
25	4502.0	511.3	471.5	0.34	0.92	4502.0	511.3	480.5	0.34	0.94

A comparison of the out-of-plane buckling resistance, between the roller-bent and stress-free CHS arches under radial pressure load, is shown in Figure 8-14. As it is evidenced, the geometric imperfections reduce significantly the buckling resistance of steel arches, up to approximately 38%. Moreover, the presence of residual stresses causes an additional reduction up to approximately 12% on the out-of-plane buckling resistance of roller-bent CHS arches.

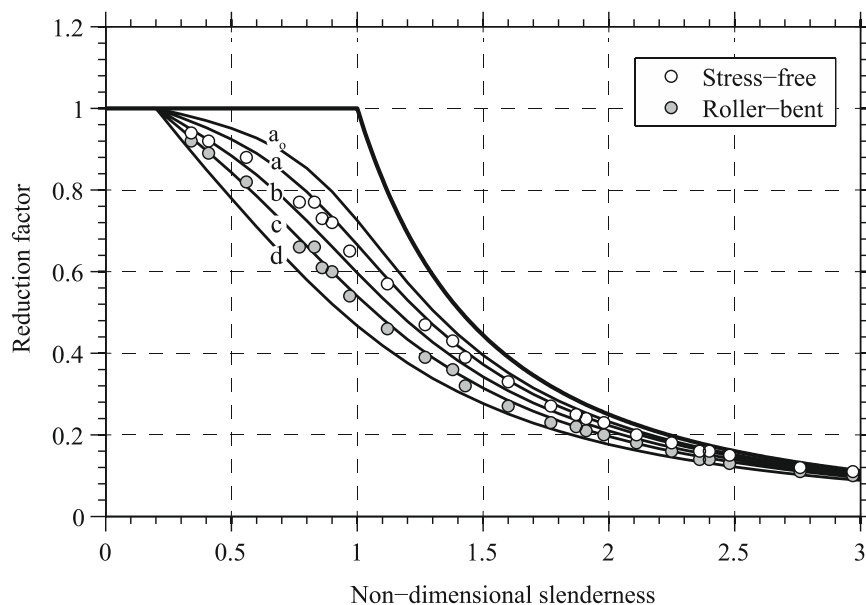


Figure 8-14: Out-of-plane buckling resistance of roller-bent and stress-free CHS arches.

Table 8-3: In-plane buckling of roller-bent and stress-free arches under uniform radial load.

No.	Roller-bent section					Stress-free section				
	$P_{cr}$ (kN/m)	$P_{MNA}$ (kN/m)	$P_{GMNIA}$ (kN/m)	$\bar{\lambda}$	$\chi$	$P_{cr}$ (kN/m)	$P_{cr}$ (kN/m)	$P_{MNA}$ (kN/m)	$\bar{\lambda}$	$\chi$
1	6.8	57.5	6.1	2.90	0.11	6.8	57.5	6.3	2.90	0.11
2	11.0	74.1	9.9	2.59	0.13	11.0	74.1	10.0	2.59	0.14
3	13.3	64.9	11.7	2.21	0.18	13.3	64.9	11.8	2.21	0.18
4	18.4	76.7	16.1	2.04	0.21	18.4	76.7	16.1	2.04	0.21
5	19.1	89.0	16.9	2.16	0.19	19.1	89.0	16.9	2.16	0.19
6	18.6	98.1	16.4	2.30	0.17	18.6	98.1	16.6	2.30	0.17
7	17.9	52.3	15.2	1.71	0.29	17.9	52.3	14.9	1.71	0.28
8	23.4	74.1	20.2	1.78	0.27	23.4	74.1	19.9	1.78	0.27
9	26.0	91.7	22.6	1.88	0.25	26.0	91.7	22.4	1.88	0.24
10	26.1	104.9	22.9	2.01	0.22	26.1	104.9	22.8	2.01	0.22
11	37.4	111.2	32.4	1.72	0.29	37.4	111.2	31.7	1.72	0.29
12	27.8	65.4	23.3	1.53	0.36	27.8	65.4	22.6	1.53	0.34
13	55.0	136.9	47.0	1.58	0.34	55.0	136.9	45.6	1.58	0.33
14	45.5	83.9	36.8	1.36	0.44	45.5	83.9	35.3	1.36	0.42
15	79.0	111.2	60.4	1.19	0.54	79.0	111.2	57.0	1.19	0.51
16	148.9	196.2	112.7	1.15	0.57	148.9	196.2	106.0	1.15	0.54
17	147.6	153.4	102.4	1.02	0.67	147.6	153.4	95.1	1.02	0.62
18	96.4	85.5	59.2	0.94	0.69	96.4	85.5	55.3	0.94	0.65
19	288.5	191.7	152.0	0.82	0.79	288.5	191.7	142.4	0.82	0.74
20	159.7	109.1	82.3	0.83	0.75	159.7	109.1	78.0	0.83	0.71
21	189.3	106.9	81.9	0.75	0.77	189.3	106.9	79.2	0.75	0.74
22	690.0	327.1	277.7	0.69	0.85	690.0	327.1	265.5	0.69	0.81
23	1187.0	306.8	270.5	0.51	0.88	1187.0	306.8	266.3	0.51	0.87
24	2050.0	306.1	275.6	0.39	0.90	2050.0	306.1	273.5	0.39	0.89
25	5561.0	511.3	476.6	0.30	0.93	5561.0	511.3	473.0	0.30	0.93

A comparison of the in-plane buckling resistance, between the roller-bent and stress-free CHS arches under radial pressure load, is shown in Figure 8-15. It can be seen that the presence of residual stresses has negligible effect on the in-plane buckling resistance of roller-bent CHS arches, which is mainly affected by the presence of geometric imperfections.

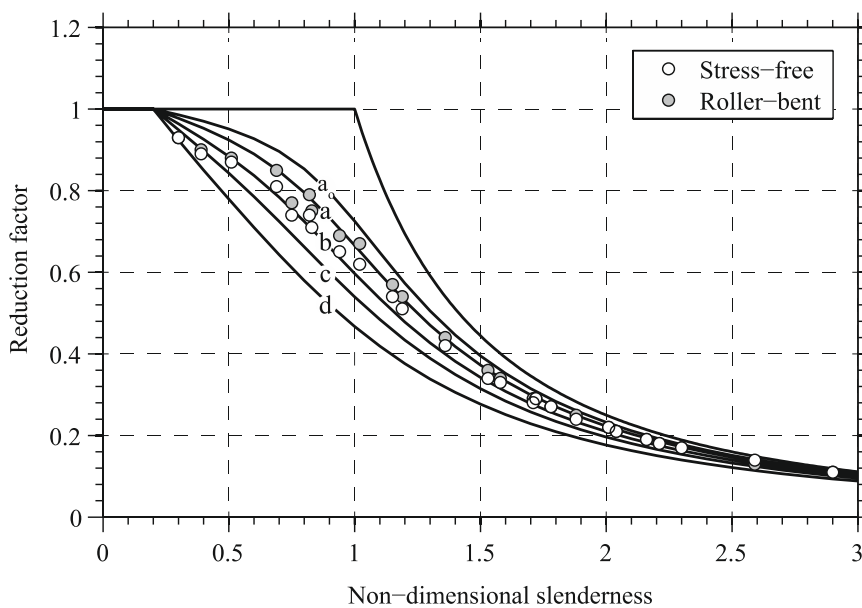


Figure 8-15: In-plane buckling resistance of roller-bent and stress-free CHS arches.

## 8.6 CONCLUSIONS

The structural stability of steel arches was assessed in the present chapter, by means of finite element analyses accounting for geometry and material nonlinearities. The effects of geometric imperfections and residual stresses were included in the developed numerical models, incorporating reliable residual distributions of CHS and appropriate geometric tolerances of arches. A validation study was first performed for a benchmark case of an arch, in order to evaluate the accuracy of the proposed finite element modeling. Sensitivity analyses were subsequently performed, aiming at assessing the separate and combined effects of residual stresses and geometric imperfections on the buckling strength for the aforementioned case. It was found that the magnitude of geometric imperfections and the distribution of residual stresses are crucial for the determination of the in-plane and out-of-plane buckling resistance. The reduction was more pronounced in the case of out-of-plane buckling, since the maximum residual stresses of roller-bent arches are located near the cross-sectional mid-height, which contributes significantly to the out-of-plane flexural resistance.

An extensive parametric study was performed in order to assess the spatial stability of steel arches exhibiting various geometric dimensions. Several arches that are not prone to snap-through buckling were examined, comprising a wide range of rise-to-span ratio  $f/l$  and bending ratio  $R/d$  that are commonly encountered in practice, namely  $0.10 \leq f/l \leq 0.30$  and  $10.9 \leq R/d \leq 85.6$ . A systematic methodology consisting of MNA, LBA and GMNIA was employed to obtain the non-dimensional slenderness  $\bar{\lambda}$  and the normalized buckling resistance  $\chi$  for the in-plane and out-of-plane buckling of both roller-bent and stress-free sections. Results were plotted in a column curve format and compared to the European column curves, namely "a<sub>0</sub>", "a", "b", "c", and "d". It was found that the presence of geometric imperfections reduces significantly the buckling resistance of steel arches (up to 38% for  $\bar{\lambda} = 1.0$ ). Moreover, the presence of residual stresses causes an additional reduction on the out-of-plane buckling resistance of roller-bent CHS arches (up to 12% for  $\bar{\lambda} = 1.0$ ). Finally, the effect of residual stresses on the in-plane buckling resistance of roller-bent CHS arches is found negligible.

## REFERENCES

- ADINA R&D Inc. (2017). *Theory and modeling guide*. Watertown, MA, USA.
- AISC (2016). *Code of Standard Practice for Steel Buildings and Bridges*. American Institute of Steel Construction, Chicago, IL.
- CEN (2005). *Eurocode 3: Design of Steel Structures, Part 1-1: General Rules and Rules for Buildings, EN 1993-1-1*. Comité Européen de Normalisation (CEN), European Committee for Standardization Brussels, Belgium.
- Komatsu, S., and Sakimoto, T. (1977). "Ultimate Load Carrying Capacity of Steel Arches." *ASCE J. Struct. Div.*, vol. 103, pp. 2323–2336.
- La Poutré, D. B. La, Spoorenberg, R. C., Snijder, H. H., and Hoenderkamp, J. C. D. (2013). "Out-of-plane stability of roller bent steel arches - An experimental investigation." *Journal of Constructional Steel Research*, vol. 81, pp. 20–34.
- Pi, Y.-L., and Bradford, M. A. (2004). "In-Plane Strength and Design of Fixed Steel I-Section Arches." *Eng. Struct.*, vol. 26, pp. 291–301.
- Pi, Y.-L., and Bradford, M. A. (2005). "Out-of-Plane Strength Design of Fixed Steel I-Section Arches." *ASCE J. Struct. Eng.*, vol. 131, pp. 560–568.
- Pi, Y.-L., and Trahair, N. S. (1998). "Out-of-Plane Inelastic Buckling and Strength of Steel Arches," *ASCE J. Struct. Eng.*, vol. 124, pp. 174–183.

- Pi, Y.-L., and Trahair, N. S. (1999). "In-Plane Buckling and Design of Steel Arches." *ASCE J. Struct. Eng.*, vol. 125, pp. 1291–1298.
- Sakimoto, T., Yamao, T., and Komatsu, S. (1979). "Experimental Study on the Ultimate Strength of Steel Arches." *Proc. Jpn. Soc. Civ. Eng.*, No. 286, pp. 139–149.
- Spoorenberg, R. C., Snijder, H. H., Hoenderkamp, J. C. D., and Beg, D. (2012). "Design rules for out-of-plane stability of roller bent steel arches with FEM." *Journal of Constructional Steel Research*, vol. 79, pp. 9–21.
- Timoshenko, S. P. (1956). *Strength of Materials Part II - Advanced Theory and Problems*, 3<sup>rd</sup> Ed., D. Van Nostrand Company, New York, NY.
- Ziemian, R. D. (Ed.) (2010). *Guide to Stability Design Criteria for Metal Structures*. John Wiley & Sons, Inc., United States of America.

# 9 DESIGN CRITERIA FOR THE STABILITY OF ARCHES

## 9.1 INTRODUCTION

Several design methods for evaluating the structural adequacy of steel arches are based on normative provisions of straight members. Such methods are very popular in the structural design practice due to their simplicity, as second-order analyses are usually not required. A state-of-the-art design procedure is described in the Curved Member Design (Dowswell, 2018), in which design equations of the Specification for Structural Steel Buildings (AISC, 2016) are employed. A similar design methodology is proposed by King and Brown (2001), based on the requirements of BS 5950–1 (BSI, 2001) with appropriate modifications to account for the effects of curvature. Relevant design formulas are also given in the SSRC Guide (Ziemian, 2010), which were originally developed by Pi and Trahair (1999) and Pi and Bradford (2004) for in-plane strength, and by Pi and Trahair (1998) and Pi and Bradford (2005) for out-of-plane strength. The accuracy of such design methods is mainly dependent on the existence of suitable buckling curves, accounting for reliable residual stress distributions and representative geometric imperfection magnitudes. Pertinent design parameters have been proposed by Spoorenberg et al. (2012), regarding the out-of-plane buckling of arches comprising roller-bent wide-flange-sections.

In the present chapter, suitable buckling curves are developed regarding the spatial stability of steel arches comprising hollow sections. The lateral-torsional buckling is not critical in hollow sections and therefore buckling curves are developed for the flexural in-plane and out-of-plane buckling under axial compressive load. The column curve formulation of EN 1993-1-1 (CEN, 2005) is employed to obtain the appropriate values of imperfection parameters, based on relevant parametric analyses accounting for geometric and material nonlinearities. The effects of residual stresses and geometric imperfections are included in the numerical models, incorporating residual distributions of roller-bent CHS and geometric tolerances of curved members. Circular arches of various geometric dimensions are examined, corresponding to non-dimensional slendernesses that are typically met in structural engineering applications. The examined cases are not prone to snap-through buckling, according to the pertinent criteria of EN 1993-1-1. The structural design of arches can be facilitated by implementing the proposed buckling curves, associated with appropriate interaction equations, in which the axial and flexural strength resistances are calculated independently.

## 9.2 METHODOLOGY

The non-dimensional slenderness  $\bar{\lambda}$  and the normalized buckling strength  $\chi$  of steel arches can be obtained using the Finite Element Method (FEM). To that effect, Material Nonlinear Analyses (MNA) and Linearized Buckling Analyses (LBA) are aimed at providing the plastic strength  $P_{MNA}$  and the critical buckling load  $P_{LBA}$ , respectively; the nondimensional slenderness is determined as the square root of the plastic load  $P_{MNA}$  divided by the critical buckling load  $P_{LBA}$ . Geometric and Material Nonlinear Analyses with Imperfections (GMNIA) are required to obtain the actual buckling strength  $P_{GMNIA}$  for the in-plane and out-of-plane buckling of arches, accounting for reliable residual stress distributions and representative geometric imperfection magnitudes; the normalized buckling strength  $\chi$  is determined as the buckling resistance  $P_{GMNIA}$  normalized with respect to the plastic strength  $P_{MNA}$  of the arch. The European column curve formulation, as described in EN 1993-1-1, can be employed to relate the non-dimensional slenderness  $\bar{\lambda}$  to the normalized buckling strength  $\chi$ , as function of the generalized imperfection parameter  $n$ , according to Eq. (9-1) and Eq. (9-2).

$$\chi = \frac{1}{\phi + \sqrt{\phi^2 - \bar{\lambda}^2}}, \text{ but } \chi \leq 1.0 \quad (9-1)$$

$$\phi = 0.5(1 + n + \bar{\lambda}^2) \quad (9-2)$$

The generalized imperfection  $n$  considers all relevant imperfections, such as geometric tolerances and residual stresses. It can be expressed as function of the non-dimensional slenderness  $\bar{\lambda}$  and the normalized buckling strength  $\chi$ , as shown in Eq. (9-3).

$$n = \chi \left( \frac{1}{\chi^2} + \bar{\lambda}^2 \right) - 1 - \bar{\lambda}^2 \quad (9-3)$$

Aiming at obtaining the generalized imperfection  $n$  based on the results of FEM, Eq. (9-3) is transformed as following:

$$n = \frac{P_{GMNIA}}{P_{MNA}} \left( \left( \frac{P_{MNA}}{P_{GMNIA}} \right)^2 + \frac{P_{MNA}}{P_{LBA}} \right) - 1 - \frac{P_{MNA}}{P_{LBA}} \quad (9-4)$$

A nonlinear expression for the generalized imperfection  $n$ , as function of the imperfection factor  $\alpha$ , the order  $\beta$ , the non-dimensional slenderness  $\bar{\lambda}$ , and the parameters  $\bar{\lambda}_0, \bar{\lambda}_1$ , is given by:

$$n = \alpha [(\bar{\lambda} - \bar{\lambda}_1)^\beta - \bar{\lambda}_0] \geq 0 \quad (9-5)$$

A linear formula of  $n$  is adopted for the column curves of EN1993-1-1, namely "a<sub>0</sub>", "a", "b", "c", and "d", according to Eq. (9-6).

$$n = \alpha(\bar{\lambda} - \bar{\lambda}_0) \geq 0 \quad (9-6)$$

Selection of the appropriate buckling curve depends on the buckling plane and the member's cross-sectional shape and steel grade. Values of the imperfection factor  $\alpha$  for the multiple column curves of EN1993-1-1 are shown in Table 9-1. The parameter  $\bar{\lambda}_0$  corresponds to the value of non-dimensional slenderness below which the presence of imperfections has null effect on the strength resistance. The parameter  $\bar{\lambda}_0$  is set to 0.2 for columns, irrespective of the column curve.

Table 9-1: Imperfection factor  $\alpha$  for column curves according to EN1993-1-1.

Column curve	a <sub>0</sub>	a	b	c	d
Imperfection value $\alpha$	0.13	0.21	0.34	0.49	0.76



### 9.3 BUCKLING CURVES

Following the aforementioned methodology, appropriate buckling curves are developed for steel arches comprising hollow sections. Based on a relevant parametric study (c.f. Chapter 8), circular arches of various geometric dimensions are examined, covering a wide range of rise-to-span ratio  $f/l$  and bending ratio  $R/d$  that are commonly encountered in practice, namely  $0.10 \leq f/l \leq 0.30$  and  $10.9 \leq R/d \leq 106.3$ . Results regarding the out-of-plane buckling are summarized in Table 9-2. The diagram of generalized imperfection  $n$  and non-dimensional slenderness for the roller-bent and stress-free sections is shown in Figure 9-1. A linear correlation is found between  $n$  and  $\bar{\lambda}$  in both cases. Results regarding in-plane buckling are summarized in Table 9-3. The diagram of generalized imperfection  $n$  and non-dimensional slenderness for the roller-bent and stress-free sections is shown in Figure 9-2. The generalized imperfection  $n$  and the non-dimensional slenderness  $\bar{\lambda}$  are linearly correlated regarding the stress-free CHS. On the contrary, a nonlinear correlation is found between  $n$  and  $\bar{\lambda}$  in the case of roller-bent CHS. This can be interpreted by considering that residual stresses induce premature yielding of arches exhibiting low values of  $\bar{\lambda}$  (material yield is critical). This results in axial shortening of the arch that causes additional in-plane bending moments, reducing reasonably the in-plane buckling strength.

Table 9-2: Out-of-plane buckling of roller-bent and stress-free arches under uniform radial load.

No.	Roller-bent section				Stress-free section			
	$\bar{\lambda}$	$\chi$	$n$	$a$	$\bar{\lambda}$	$\chi$	$n$	$a$
1	3.23	0.08	1.75	0.58	3.23	0.09	0.65	0.20
2	2.97	0.10	1.51	0.55	2.97	0.11	0.54	0.18
3	2.40	0.14	1.25	0.57	2.40	0.16	0.47	0.20
4	2.25	0.16	1.14	0.56	2.25	0.18	0.46	0.21
5	2.48	0.13	1.22	0.54	2.48	0.15	0.47	0.19
6	2.76	0.11	1.30	0.51	2.76	0.12	0.47	0.17
7	1.77	0.23	0.93	0.59	1.77	0.27	0.40	0.23
8	1.91	0.21	0.97	0.57	1.91	0.24	0.40	0.21
9	2.11	0.18	1.04	0.54	2.11	0.20	0.42	0.20
10	2.36	0.14	1.13	0.52	2.36	0.16	0.43	0.18
11	1.98	0.20	0.93	0.52	1.98	0.23	0.37	0.19
12	1.60	0.27	0.81	0.58	1.60	0.33	0.35	0.22
13	1.87	0.22	0.85	0.51	1.87	0.25	0.34	0.18
14	1.43	0.32	0.69	0.56	1.43	0.39	0.30	0.21
15	1.27	0.39	0.59	0.55	1.27	0.47	0.26	0.20
16	1.38	0.36	0.58	0.49	1.38	0.43	0.24	0.18
17	1.12	0.46	0.48	0.52	1.12	0.57	0.21	0.19
18	0.97	0.54	0.43	0.56	0.97	0.65	0.21	0.21
19	0.90	0.60	0.35	0.50	0.90	0.72	0.17	0.18
20	0.86	0.61	0.35	0.54	0.86	0.73	0.18	0.20
21	0.77	0.66	0.31	0.53	0.77	0.77	0.16	0.21
22	0.83	0.66	0.28	0.45	0.83	0.77	0.14	0.16
23	0.56	0.82	0.16	0.46	0.56	0.88	0.10	0.18
24	0.41	0.89	0.11	0.50	0.41	0.92	0.08	0.18
25	0.34	0.92	0.08	0.55	0.34	0.94	0.06	0.17

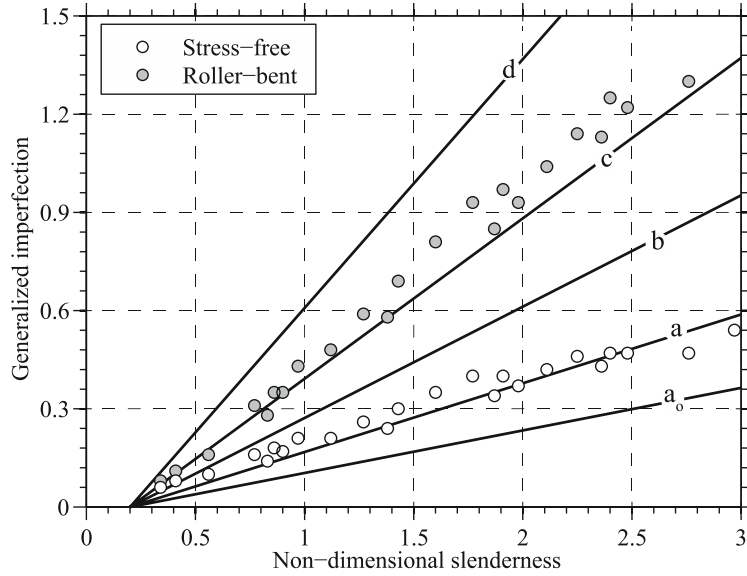


Figure 9-1: Generalized imperfection curves for the out-of-plane buckling.

Table 9-3: In-plane buckling of roller-bent and stress-free arches under uniform radial load.

No.	Roller-bent section				Stress-free section			
	$\bar{\lambda}$	$\chi$	$n$	$a$	$\bar{\lambda}$	$\chi$	$n$	$a$
1	2.90	0.11	0.89	0.11	2.90	0.11	0.71	0.24
2	2.59	0.13	0.69	0.11	2.59	0.14	0.58	0.23
3	2.21	0.18	0.56	0.11	2.21	0.18	0.53	0.24
4	2.04	0.21	0.47	0.11	2.04	0.21	0.47	0.23
5	2.16	0.19	0.49	0.10	2.16	0.19	0.48	0.22
6	2.30	0.17	0.58	0.11	2.30	0.17	0.53	0.23
7	1.71	0.29	0.36	0.11	1.71	0.28	0.42	0.24
8	1.78	0.27	0.36	0.11	1.78	0.27	0.41	0.23
9	1.88	0.25	0.40	0.11	1.88	0.24	0.43	0.23
10	2.01	0.22	0.44	0.11	2.01	0.22	0.45	0.23
11	1.72	0.29	0.33	0.10	1.72	0.29	0.38	0.22
12	1.53	0.36	0.30	0.11	1.53	0.34	0.36	0.23
13	1.58	0.34	0.28	0.10	1.58	0.33	0.34	0.22
14	1.36	0.44	0.24	0.11	1.36	0.42	0.31	0.23
15	1.19	0.54	0.20	0.11	1.19	0.51	0.26	0.22
16	1.15	0.57	0.18	0.10	1.15	0.54	0.25	0.21
17	1.02	0.67	0.15	0.10	1.02	0.62	0.22	0.21
18	0.94	0.69	0.17	0.12	0.94	0.65	0.23	0.25
19	0.82	0.79	0.12	0.10	0.82	0.74	0.18	0.22
20	0.83	0.75	0.16	0.13	0.83	0.71	0.20	0.25
21	0.75	0.77	0.17	0.15	0.75	0.74	0.20	0.27
22	0.69	0.85	0.11	0.10	0.69	0.81	0.14	0.21
23	0.51	0.88	0.10	0.11	0.51	0.87	0.12	0.23
24	0.39	0.90	0.10	0.11	0.39	0.89	0.10	0.27
25	0.30	0.93	0.07	0.08	0.30	0.93	0.07	0.24

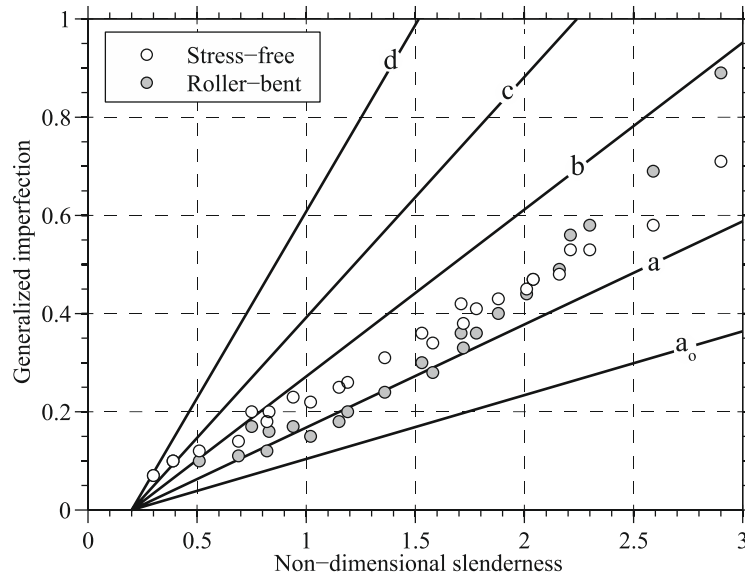


Figure 9-2: Generalized imperfection curves for the in-plane buckling

Aiming at proposing appropriate design formulas of the imperfection parameter  $\eta$ , the obtained results are approximated via regression equations. Linear regression is employed for the out-of-plane buckling of both roller-bent and stress-free sections. A parameter  $\bar{\lambda}_0$  of 0.20 and a mean imperfection factor  $\sigma$  of 0.53 with standard deviation equal to 0.037 are proposed in the former case, while a mean imperfection factor  $\sigma$  of 0.19 with standard deviation 0.016 are proposed in the latter case. Second-order regression is employed for the in-plane buckling of roller-bent CHS, using a parameter  $\bar{\lambda}_0$  of -0.80, a parameter  $\bar{\lambda}_1$  of 0.20 and an imperfection factor  $\sigma$  of 0.11 with standard deviation equal to 0.013. Linear regression is employed for the in-plane buckling of stress-free CHS, using a mean imperfection factor  $\sigma$  of 0.23 with standard deviation equal to 0.016. The proposed design equations for the in-plane and out-of-plane buckling of roller-bent and stress-free sections are summarized in Table 9-4. The proposed imperfection parameter diagrams and pertinent buckling curves are shown in Figure 9-3 and Figure 9-4, respectively.

Table 9-4: Proposed imperfection parameter  $\eta$ .

Section	Out-of-plane buckling	In-plane buckling
Roller-bent	$0.53(\bar{\lambda} - 0.20) \geq 0$	$0.11[(\bar{\lambda} - 0.20)^2 + 0.80] \geq 0$
Stress-free	$0.19\bar{\lambda} \geq 0$	$0.23\bar{\lambda} \geq 0$

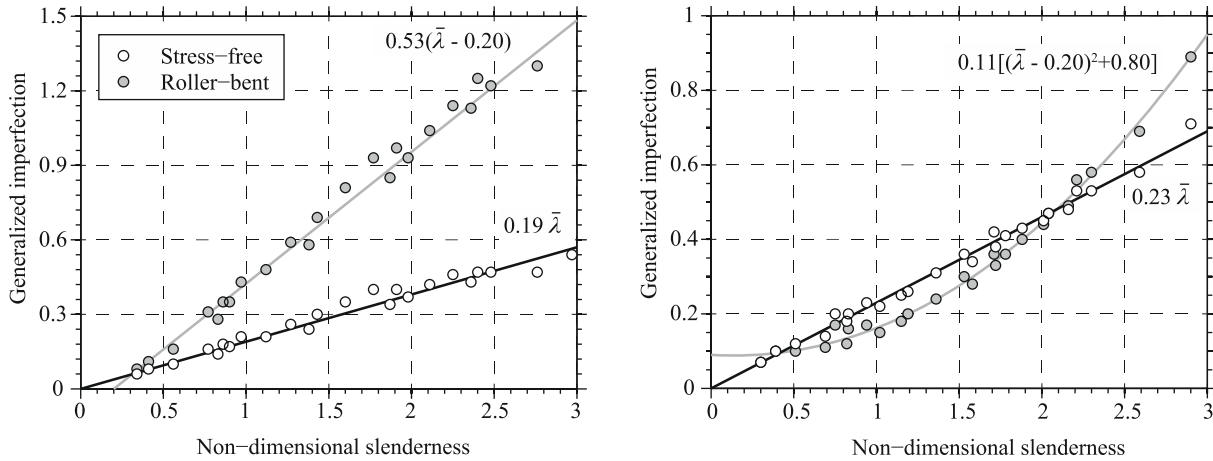


Figure 9-3: Proposed imperfection diagrams for out-of-plane (left) and in-plane (right) buckling.

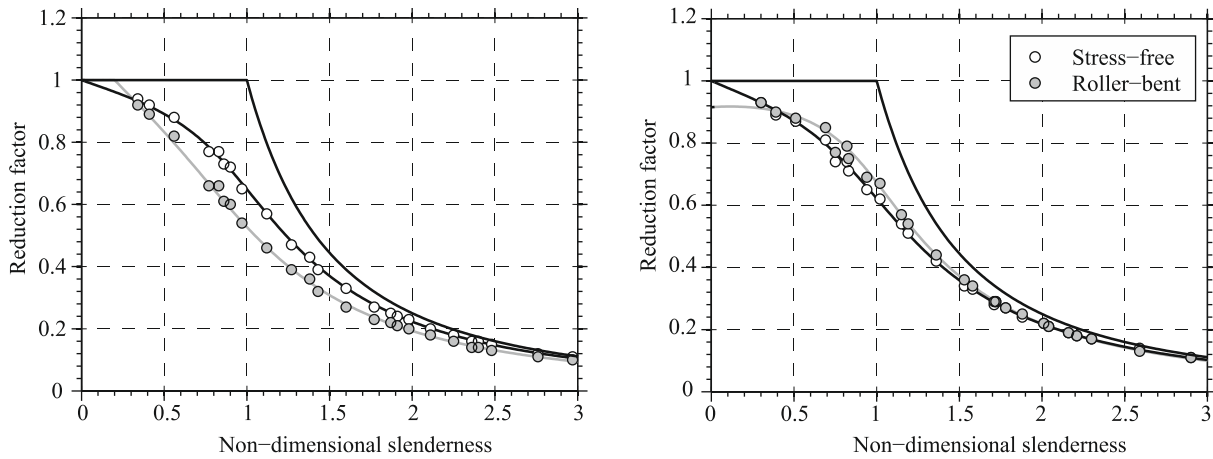


Figure 9-4: Proposed design buckling curves for out-of-plane (left) and in-plane (right) buckling.

### 9.4 CONCLUSIONS

In this chapter, the column curve formulation of EN 1993-1-1 is employed to determine appropriate values of design parameters for the spatial stability of steel arches. Based on the results of a relevant parametric study (c.f. Chapter 8), the generalized imperfection parameter  $n$  is calculated from the non-dimensional slenderness  $\bar{\lambda}$  and the normalized reduction factor  $\chi$  for circular arches of CHS under axial compression loading. Several arches that are not prone to snap-through buckling are examined, comprising a wide range of rise-to-span ratio  $f/l$  and bending ratio  $R/d$  that are commonly encountered in practice, namely  $0.10 \leq f/l \leq 0.30$  and  $10.9 \leq R/d \leq 85.6$ . A linear correlation is found between  $n$  and  $\bar{\lambda}$  regarding the out-of-plane buckling of both roller-bent and stress-free sections. The  $n$  and  $\bar{\lambda}$  are linearly correlated regarding the in-plane buckling of stress-free sections, in contrast to roller-bent sections; in the latter case, residual stresses induce premature yielding of arches exhibiting low values of  $\bar{\lambda}$  (material yield is critical), resulting in axial shortening that causes additional vertical deflections and reduces the in-plane buckling resistance. Appropriate design formulas and pertinent buckling curves are proposed for the in-plane and out-of-plane buckling of roller-bent and stress-free sections. These guidelines can be implemented in the structural design practice of hollow section steel arches, as the effects of residual stresses are similar among them (c.f. Chapter 7).

**REFERENCES**

- AISC (2016). *Code of Standard Practice for Steel Buildings and Bridges*. American Institute of Steel Construction, Chicago, IL.
- BSI (2001). *Code of practice for design: rolled and welded sections, BS 5950-1:2000*. British Standards Institution, London.
- Dowswell, B. (2018). *Curved Member Design*. American Institute of Steel Construction, Chicago, IL.
- King, C., and Brown, D. (2001). *Design of Curved Steel*. The Steel Construction Institute, Berkshire, UK.
- Pi, Y.-L., and Bradford, M. A. (2004). "In-Plane Strength and Design of Fixed Steel I-Section Arches." *Eng. Struct.*, vol. 26, pp. 291–301.
- Pi, Y.-L., and Bradford, M. A. (2005). "Out-of-Plane Strength Design of Fixed Steel I-Section Arches." *ASCE J. Struct. Eng.*, vol. 131, pp. 560–568.
- Pi, Y.-L., and Trahair, N. S. (1998), "Out-of-Plane Inelastic Buckling and Strength of Steel Arches," *ASCE J. Struct. Eng.*, vol. 124, pp. 174–183.
- Pi, Y.-L., and Trahair, N. S. (1999). "In-Plane Buckling and Design of Steel Arches." *ASCE J. Struct. Eng.*, vol. 125, pp. 1291–1298.
- Spoorenberg, R. C., Snijder, H. H., Hoenderkamp, J. C. D., and Beg, D. (2012). "Design rules for out-of-plane stability of roller bent steel arches with FEM." *Journal of Constructional Steel Research*, vol. 79, pp. 9–21.
- Ziemian, R. D. (Ed.) (2010). *Guide to Stability Design Criteria for Metal Structures*. John Wiley & Sons, Inc., United States of America.



# 10 SUMMARY AND CONCLUSIONS

## 10.1 EXTENDED SUMMARY

Objective of the present dissertation is to gain insight in the structural behavior of steel arches comprising hollow cross-sections. Curved steel members are typically manufactured from initially straight members which are subjected to bending in order to meet the desired curvature. The roller-bending process is the most common and cost-effective method for curving constructional steel members in the fabrication industry. It is a cold-forming process, in which a workpiece is passed iteratively through a three-roller-bending machine. Residual stresses, or commonly called "locked-in" stresses, along with significant plastic deformations, are induced to the material during cold-forming. A theoretical distribution of the residual stresses emanating from the inelastic bending of beams is given by Timoshenko, based on simplifications, such as the development of plane stress conditions without shear. Limited research work is found on the residual stresses and the mechanical properties emanating from roller-bending, as well as their effects on the spatial stability of arches. Pertinent research studies were found only for wide-flange-section arches, in which the importance of such parameters was highlighted. The present doctoral thesis aims at bridging this gap, by investigating the structural behavior of roller-bent arches comprising hollow sections. In order to achieve this goal, a combined experimental, numerical and analytical methodology is implemented during the whole research work.

A state-of-the-art experimental study regarding the in-plane behavior of roller-bent arches comprising Rectangular-Hollow-Sections was presented. Twelve roller-bent specimens, grouped in two sets of curvatures, were examined under compression and tension loading. Appropriate dimension measurements were undertaken, aiming at evaluating the encountered geometric imperfections due to roller-bending. The material properties were obtained through tensile coupon tests, machined prior to the curving process, in order to avoid the effects of roller-bending on steel properties. Overall, excellent repeatability was observed between the test results, in terms of load-displacement equilibrium paths, developed deformations and failure mechanisms. The arches under compression demonstrated a gradually softening response, even for low levels of loading, in contrast to the arches under tension. Therefore, the loading direction affected significantly the stress-strain response of the material and thus, it was concluded that the roller-bent arches in predominant compression exhibited premature yielding due to the Bauschinger effect. The failure mode of the arches under compression was dominated by yielding at crown due to the developed bending moment, accompanied by the inelastic local buckling of the top flange. On the other hand, an increasing resistance was encountered in the arches under tension, attributed to the steel hardening effect, as the load was carried in axial tension after yielding of arches at crown.

Subsequently, detailed finite element simulations of the experimental tests were performed. In order to maintain an acceptable level of accuracy and at the same time reduce the computational effort, the finite element simulation was conducted in three successive phases, including the explicit roller-bending formation process, the configurations of hinge support and loading cylinders, as well as the compressive and tensile loading tests. A non-symmetrical residual stress layout about the cross-sectional bending axis was obtained from roller-bending simulations, differing significantly from the anti-symmetrical distribution of the theoretical model. Remarkable stress concentrations were located at the edges of the bottom flange. The bending curvature had an insignificant effect on the residual stress formations, similar to the Timoshenko theory. Experimental and numerical results were compared in terms of load-displacement equilibrium paths, strain-gauge measurements and deformed shapes, providing good quantitative and qualitative agreement. The roller-bent arches exhibited an increased yield strength compared to numerical analyses, attributed to the strain aging effect, which is encountered when steel is deformed plastically and then allowed for a period to age in room temperature. A preliminary assessment of the roller-bending influence on the structural behavior of arches was performed through a direct comparison between identical roller-bent and stress-free numerical models under various loading conditions. In this context, the effect of residual stresses on the overall response of arches was found small, exhibiting a varying effect up to 10% depending on the developed axial-bending interaction.

Since the developed numerical models were validated and the accuracy of the finite element analyses was verified, the effects of the main roller-bending characteristics on the residual stress/strain formations of roller-bent hollow sections were assessed, following a comprehensive parametric study. Among the examined parameters, the thickness ratio and the bending length were found to mainly affect the locked-in stress formations of Circular-Hollow-Sections (CHS), Square-Hollow-Sections (SHS) and Rectangular-Hollow-Sections (RHS). Variations were evidenced between the encountered distributions and the simplified theoretical model, same as for roller-bent wide-flange sections that have been reported in the literature. More specifically, tensile residual stresses were encountered in both the top- (elongated) and bottom- (shortened) height of the roller-bent hollow sections, along with stress-concentrations at the web-to-flange junctions. The magnitude of developed strains in the shortened zone was found slightly higher than the corresponding values of the tensioned zone. The encountered variations were interpreted by considering that workpieces within the three-point-bending length comprise short in length members, in which significant shear and effects of plates/shells are developed, that cannot be neglected. As cross-sections become stockier and the bending length increases, the residual stress formations were reasonably better approximated by the theoretical model. Moreover, characteristic residual stress distributions were proposed for roller-bent circular, square and rectangular hollow sections. Such membrane residual stress distributions can be exploited from analysts to assess the structural behavior of roller-bent members.

An analytical investigation regarding the effects of residuals stresses on the behavior of roller-bent arches was carried out next, using expressions that rely on linear analysis and employ the reliable residual stress distributions that have been assessed previously. Aiming at defining the elastic domain of roller-bent sections, interaction diagrams of axial force with bending moment were developed for the CHS, SHS, and RHS. It was found that the presence of residual stresses reduces significantly the elastic domain of hollow cross-sections. The reduction is more prevalent in the case of out-of-plane bending, since maximum residual stresses are located near the mid-height of roller-bent CHS, SHS, and RHS. The elastic domain of hollow sections was almost similar in all cases; the reduction was slightly more pronounced in the case of SHS/RHS compared to CHS, since high residual stresses were encountered at the web-to-flange junctions. The cross-sectional aspect ratio of rectangular sections had a negligible effect on the elastic domain. The interaction diagrams can be directly applied in structural engineering design practice, in order to take into account the effects of cold bending in the elastic response of the cross-sections.



Furthermore, an analytical methodology was employed to calculate the inelastic buckling loads of roller-bent arches comprising hollow sections. The calculations were performed, implementing comparatively the numerical and theoretical residual stress distributions of roller-bent CHS, SHS and RHS arches. The theoretical distribution was found to yield lower in-plane buckling loads than the numerical one, since the former comprises compressive values at the cross-sectional top-height. In both cases, the reduction of critical load was more pronounced for out-of-plane buckling, since maximum residual stresses are located near the mid-height of roller-bent CHS, SHS and RHS. The presence of residual stresses had small effect on very slender arches, which exhibit buckling loads approaching the Euler load. The overall response was almost similar between CHS, SHS and RHS; the reduction was slightly more pronounced in the case of SHS/RHS compared to CHS, since high residual stresses are encountered at the web-to-flange junctions. The inelastic buckling loads are very useful to qualitatively assess the effect of residual stresses on the stability of roller-bent arches, while they are not intended to be used for design purposes, since initial imperfections and geometric non-linearities are not taken into account.

State-of-the-art design column formulas are based on results of extensive computational studies incorporating residual stresses and geometric imperfections. Appropriate buckling formulas can be developed similarly for steel arches employing the Finite Element Method (FEM). To that end, finite element analyses of circular-hollow-section arches were carried out, accounting for geometry and material non-linearities, as well as, incorporating reliable locked-in distributions and appropriate geometric tolerances. A validation study was first performed for an arch benchmark case in order to evaluate the accuracy of the proposed finite element modeling, followed by sensitivity analyses aiming at assessing the separate and combined effects of residual stresses and geometric imperfections on the strength resistance. It was found that the magnitude of geometric imperfections and the distribution of residual stresses are crucial for determining the in-plane and out-of-plane buckling resistance. The reduction was more pronounced in the case of out-of-plane buckling, since the maximum residual stresses of roller-bent arches are located near the cross-sectional mid-height, which contributes significantly to the out-of-plane flexural resistance. An extensive parametric study was performed in order to assess the spatial stability of steel arches exhibiting various geometric dimensions. Several arches that are not prone to snap-through buckling were examined, comprising a wide range of arch non-dimensional slenderness, commonly encountered in the civil engineering practice.

A systematic methodology was employed to obtain the non-dimensional slenderness and the normalized buckling resistance for the in-plane and out-of-plane buckling of both roller-bent and stress-free arches. Results were plotted in a column curve format and compared to the European column curves. It was found that the presence of geometric imperfections reduces significantly the buckling resistance of steel arches, up to approximately 38%. Moreover, the presence of residual stresses causes an additional reduction on the out-of-plane buckling resistance of roller-bent CHS arches, up to approximately 12%. The effects of residual stresses on the in-plane buckling resistance of roller-bent CHS arches were found negligible. The column curve formulation of EN 1993-1-1 was employed to determine appropriate values of design parameters for the spatial stability of steel arches. Based on the results of parametric analyses, design formulas for the generalized imperfection parameter were developed via regression equations. Linear correlations were found for the out-of-plane imperfection parameter of both roller-bent and stress-free CHS arches, as well as, the in-plane imperfection parameter of stress-free arches, while a non-linear correlation was found for the in-plane buckling of roller-bent arches. Finally, appropriate buckling curves were proposed for the in-plane and out-of-plane buckling of roller-bent and stress-free CHS arches. These guidelines can be reliably implemented in the structural design practice of steel arches comprising hollow sections, since the effects of residual stresses are similar between CHS, SHS and RHS, according to the analytical results.

## 10.2 CONCLUDING REMARKS

The main conclusions, extracted in the frame of the present dissertation, are summarized as following:

- Limited research work is available in the literature, regarding the residual stresses and mechanical properties emanating from roller-bending, as well as their effects on the spatial stability of arches. Pertinent research studies are found only for wide-flange-section arches.
- Roller-bent arches under compression loading exhibit premature yielding, in contrast to the corresponding arches under tensile loading. The loading direction affects significantly the stress-strain response of roller-bent arches due to the Bauschinger effect.
- Roller-bent arches exhibit increased yield strength and decreased ductility, attributed to the strain aging effect. The strain aging effect is encountered when steel is deformed plastically and then allowed for a period to age in room temperature.
- The residual stress formations of roller-bent hollow cross-sections vary from the theoretical distribution. Variations are attributed to the simplifications of the theoretical model, assuming plane stress conditions without shear stresses.
- Tensile residual stresses are encountered in top and bottom height of roller-bent hollow sections, along with stress-concentrations at the web-to-flange junctions. Workpieces within the three-point-bending length comprise short-in-length members, exhibiting large shear and effects of plates/shells.
- The thickness ratio and the bending length affect the locked-in stress formations of roller-bent hollow sections. As cross-sections become stockier or the bending length increases, residual stresses are better approximated by the theoretical model.
- The presence of residual stresses causes a reduction in the elastic domain of hollow cross-sections. The reduction is more prevalent in the case of out-of-plane bending, since maximum residual stresses are located near the mid-height of roller-bent CHS, SHS, and RHS.
- The presence of residual stresses causes a reduction in the inelastic critical loads of hollow-section arches. Once again, the reduction is more prevalent in the case of out-of-plane bending, since maximum residual stresses are located near the mid-height of roller-bent CHS, SHS, and RHS.
- Reduction of the elastic domain and the inelastic critical loads is almost similar between CHS, SHS and RHS. The reduction is slightly more pronounced in the case of SHS/RHS compared to CHS, since high residual stresses are encountered additionally at the web-to-flange junctions.
- The theoretical residual stress model results in lower in-plane buckling loads than the numerical one, since the former comprises compressive values at the cross-sectional top-height. In both cases, buckling loads approach the Euler load for very slender arches.
- State-of-the-art design buckling formulas can be developed for steel arches, based on the results of nonlinear finite element analyses, incorporating reliable locked-in distributions and appropriate geometric tolerances.
- The magnitude of geometric imperfections and the distribution of residual stresses are crucial for determining the appropriate imperfection parameters for the in-plane and out-of-plane buckling resistance of steel arches.
- The presence of geometric imperfections reduces significantly the out-of-plane buckling resistance of steel arches, up to approximately 38%. Moreover, the presence of residual stresses causes an additional reduction on the out-of-plane buckling resistance of roller-bent arches, up to approx. 12%.
- The presence of geometric imperfections reduces significantly the in-plane buckling resistance of steel arches, up to approximately 38%. The presence of residual stresses has a negligible effect on the in-plane buckling resistance of arches.

### 10.3 RESEARCH CONTRIBUTION AND INNOVATION

The innovations and contributions of the present dissertation to the advancement of engineering science and design practice can be summarized as following:

- Results of experimental tests on roller-bent steel arches were presented, providing qualitative understanding and quantitative evaluation of the structural response (Thanasoulas et al., 2018).
- Detailed numerical simulations of the experimental tests were included, demonstrating useful modeling features that can prove beneficial for researchers (Thanasoulas et al., 2018)
- Extensive parametric studies were conducted to evaluate the parameters affecting the residual stress formations of roller-bent hollow sections. Results can be useful for designing appropriate experimental programs of residual stress measurements on roller-bent members.
- Residual stress models were proposed for roller-bent CHS, SHS, and RHS. Pertinent models can be exploited from analysts to assess the structural behavior of roller-bent members (Thanasoulas and Gantes, 2020a; Thanasoulas and Gantes, 2018).
- Interaction diagrams of axial force with bending moment were developed for roller-bent hollow sections. The interaction diagrams can be directly applied in structural engineering design practice to take into consideration the effects of cold bending in the elastic response of arches.
- Inelastic critical buckling loads were provided for roller-bent arches comprising hollow sections. The results are very useful to qualitatively assess the effect of residual stresses on the inelastic buckling load of roller-bent arches, while they are not intended to be used for design purposes.
- Appropriate buckling formulas were proposed for the spatial stability of hollow-section steel arches, via regression equations. The buckling curves can be reliably implemented in the structural design practice according to modern structural design standards (Thanasoulas and Gantes, 2020b).

### 10.4 SUGGESTIONS FOR FUTURE RESEARCH

Based on the present dissertation, some suggestions for future research are summarized next:

- Execution of an appropriate experimental program, including residual stress measurements on roller-bent hollow sections. Relevant locked-in stress measurements are currently available only for roller-bent wide-flange-sections.
- Implementation of more sophisticated material models in the finite element simulations of arches, accounting for a different response under tension and compression, due to the Bauschinger effect. However, such material models usually encounter limitations when residual stresses are introduced.
- Experimental investigation of the material properties encountered in roller-bent hollow sections. Design formulas for calculating a modified non-dimensional slenderness can be provided, considering the premature yielding of the material due to the Bauschinger effect.
- Evaluation of the structural adequacy of steel arches according to normative provisions of straight members. The implementation of pertinent interaction equations should be evaluated through numerical analyses and appropriate experimental tests.
- Assessment of the arch spatial stability, incorporating residual stress distributions from welding or induction-bending manufacturing processes. The hot-forming residual stresses can be obtained accurately through thermomechanical analyses, according to the modeling methodologies presented in Thanasoulas et al. (2015, 2016, 2017, and 2018).

## REFERENCES

- Thanasoulas, I. D., and Gantes, C. J. (2020a). "Numerical investigation on the residual stresses of roller-bent circular-hollow-sections." *Journal of Constructional Steel Research*, vol. 164, 105777.
- Thanasoulas, I. D., and Gantes, C. J. (2020b). "Stability criteria for circular-hollow-section steel arches." Ready for submission in peer-reviewed scientific journal.
- Thanasoulas, I. D., Douthe, C. E., Gantes, C. J., and Lignos, X. A. (2018). "Influence of roller-bending on RHS steel arches: Experimental and numerical investigation." *Thin-Walled Structures*, vol. 131, pp. 668–680.
- Thanasoulas, I. D., and Gantes, C. J. (2018). "Effects of roller bending on curved constructional steels of rectangular hollow section." *Proceedings of the IASS Symposium 2018 Creativity in Structural Design*, Jul. 16-20, MIT, Boston, USA.
- Thanasoulas, I. D., Vardakoulias, I. K., Kolaitis, D. I., Gantes, C. J., and Founti, M. A. (2015). "A preliminary thermal and mechanical simulation study of load-bearing cold-formed steel drywall systems exposed to fire", *2nd IAFSS European Symposium of Fire Safety Science*, Jun. 16-18, Nicosia, Cyprus.
- Thanasoulas, I. D., Vardakoulias, I. K., Kolaitis, D. I., Gantes, C. J., and Founti, M. A. (2016). "Thermal and Mechanical Computational Study of Load-Bearing Cold-Formed Steel Drywall Systems Exposed to Fire." *Fire Technology*, vol. 52(6), pp. 2071–2092.
- Thanasoulas, I. D., Vardakoulias, I. K., Kolaitis, D. I., Gantes, C. J., and Founti, M. A. (2017). "Non-linear numerical simulation of fire-resistance tests for load-bearing cold-formed-steel drywall systems". *9th Greek National Steel Structures Conference*, 5-7 Oct., Larissa, Greece.
- Thanasoulas, I. D., Vardakoulias, I. K., Kolaitis, D. I., Gantes, C. J., and Founti, M. A. (2018). "Coupled thermo-mechanical simulation for the performance-based fire design of CFS drywall systems." *Journal of Constructional Steel Research*, vol. 145, pp. 196–209.

# APPENDIX

Axial force-strain ( $N$ - $\varepsilon$ ) and moment-curvature ( $M$ - $C$ ) diagrams of steel cross-sections can be developed accurately, accounting for material non-linearities and the presence of residual stresses. Such diagrams can be easily implemented in beam element analyses, using the finite element method. A numerical methodology of extracting the  $N$ - $\varepsilon$  and  $M$ - $C$  diagrams for a CHS 100x5 is described next, using the finite element software ADINA. A short CHS member of length equal to 200mm, is modeled using 4-node shell elements of 5 integration points at the element thickness direction. The Newton-Cotes integration method is employed, since it is more effective for capturing the onset and spread of the materially nonlinear conditions, as the integration points are on the boundaries of the elements. An elastic-fully-plastic material law is employed in the numerical model, comprising a bilinear constitutive law without hardening; the modulus of elasticity  $E$  is taken equal to 210GPa and the yield stress  $f_y$  equal to 355MPa. The proposed residual stresses of roller-bent CHS (c.f. Chapter 6) are introduced as initial conditions in the longitudinal direction. The nodes at the edges of CHS are connected to their centers via rigid links, in order to prescribe the load and boundary conditions. Fixed conditions are applied at the one end, while various load combinations of axial force with bending/torsional moment are applied at the other end. Material Nonlinear Analyses (MNA) are carried out using the Newton-Raphson solution algorithm. For comparison reasons, MNA are performed in identical roller-bent and stress-free CHS. The obtained  $N$ - $\varepsilon$  and  $M$ - $C$  diagrams are normalized with respect to the plastic resistances of the cross-section. Tensile axial forces, and moments that tend to open the arch (increase the radius of curvature), are denoted as positive. The employed numerical model, along with the introduced residual stresses, are presented in Figure A-1. A comparison of the axial force-strain response between the roller-bent and stress-free CHS, is shown in Figure A-2.

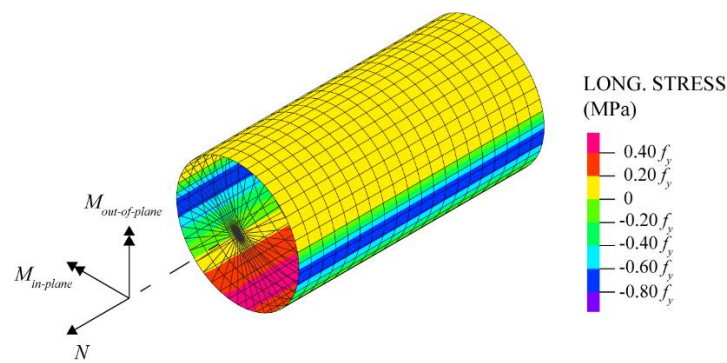


Figure A-1: Finite element model with employed residual stresses.

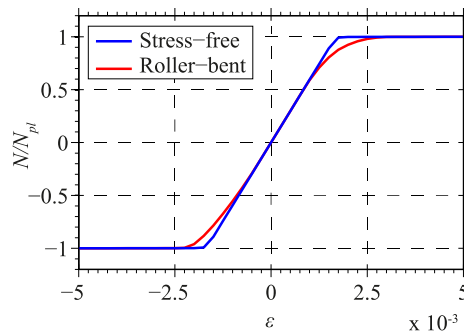


Figure A-2: Axial force-strain response of roller-bent and stress-free CHS.

The axial force-strain values of roller-bent and stress-free CHS are given in Table A-1.

Table A-1: Axial force-strain values of roller-bent and stress-free CHS 100x5.

Roller-bent		Stress-free	
Strain $\varepsilon$	$N$ (kN)	Strain $\varepsilon$	$N$ (kN)
-1.00E-02	-556.12	-1.00E-02	-556.12
-9.50E-03	-556.11	-9.50E-03	-556.11
-9.00E-03	-556.11	-9.00E-03	-556.11
-8.50E-03	-556.10	-8.50E-03	-556.10
-8.00E-03	-556.10	-8.00E-03	-556.10
-7.50E-03	-556.09	-7.50E-03	-556.09
-7.00E-03	-556.08	-7.00E-03	-556.09
-6.50E-03	-556.06	-6.50E-03	-556.07
-6.00E-03	-556.03	-6.00E-03	-556.05
-5.50E-03	-555.99	-5.50E-03	-556.01
-5.00E-03	-555.93	-5.00E-03	-555.96
-4.50E-03	-555.86	-4.50E-03	-555.90
-4.00E-03	-555.77	-4.00E-03	-555.82
-3.50E-03	-555.65	-3.50E-03	-555.72
-3.00E-03	-555.49	-3.00E-03	-555.58
-2.50E-03	-555.25	-2.50E-03	-555.41
-2.00E-03	-534.51	-2.00E-03	-555.03
-1.50E-03	-436.13	-1.50E-03	-495.48
-1.00E-03	-308.71	-1.00E-03	-330.34
-5.00E-04	-162.31	-5.00E-04	-165.17
0.00E+00	0.00	0.00E+00	0.00
5.00E-04	165.49	5.00E-04	165.17
1.00E-03	327.78	1.00E-03	330.34
1.50E-03	447.39	1.50E-03	495.48
2.00E-03	514.01	2.00E-03	555.03
2.50E-03	545.25	2.50E-03	555.41
3.00E-03	555.19	3.00E-03	555.58
3.50E-03	555.57	3.50E-03	555.72
4.00E-03	555.73	4.00E-03	555.82
4.50E-03	555.84	4.50E-03	555.90
5.00E-03	555.91	5.00E-03	555.96
5.50E-03	555.97	5.50E-03	556.01
6.00E-03	556.01	6.00E-03	556.05
6.50E-03	556.04	6.50E-03	556.07
7.00E-03	556.06	7.00E-03	556.09
7.50E-03	556.08	7.50E-03	556.09
8.00E-03	556.09	8.00E-03	556.10
8.50E-03	556.10	8.50E-03	556.10
9.00E-03	556.11	9.00E-03	556.11
9.50E-03	556.11	9.50E-03	556.11
1.00E-02	556.12	1.00E-02	556.12

The moment-curvature diagrams of roller-bent and stress-free CHS for in-plane bending and various levels of axial compression, are compared in Figure A-3.

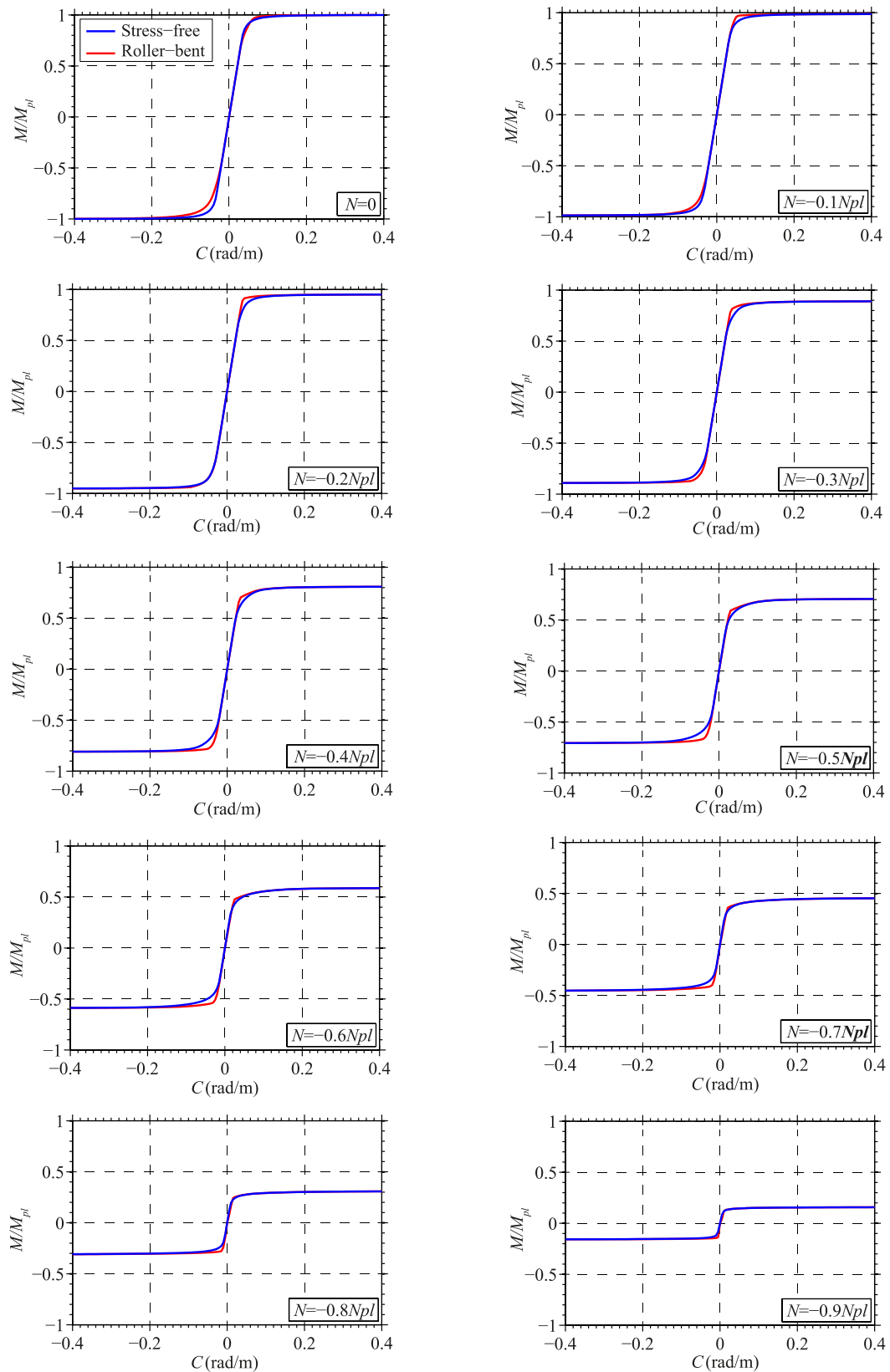


Figure A-3: Moment-curvature diagrams for in-plane bending.

The moment-curvature values of roller-bent CHS for in-plane bending and various levels of axial compression, are given in Table A-2.

Table A-2: Moment-Curvature values for roller-bent CHS 100x5.

Curvature (rad/m)	In-plane bending moment (kN/m), under various levels of axial compression									
	$0N_{pl}$	$-0.1N_{pl}$	$-0.2N_{pl}$	$-0.3N_{pl}$	$-0.4N_{pl}$	$-0.5N_{pl}$	$-0.6N_{pl}$	$-0.7N_{pl}$	$-0.8N_{pl}$	$-0.9N_{pl}$
-0.500	-17.74	-17.53	-16.88	-15.81	-14.36	-12.55	-10.43	-8.06	-5.49	-2.80
-0.460	-17.74	-17.53	-16.88	-15.81	-14.36	-12.55	-10.43	-8.05	-5.48	-2.80
-0.420	-17.73	-17.52	-16.87	-15.81	-14.35	-12.54	-10.42	-8.05	-5.47	-2.80
-0.380	-17.72	-17.52	-16.87	-15.80	-14.35	-12.54	-10.42	-8.04	-5.47	-2.79
-0.340	-17.71	-17.51	-16.86	-15.80	-14.34	-12.53	-10.41	-8.03	-5.46	-2.79
-0.300	-17.69	-17.50	-16.86	-15.79	-14.33	-12.52	-10.40	-8.02	-5.45	-2.78
-0.260	-17.66	-17.49	-16.84	-15.78	-14.32	-12.51	-10.39	-8.00	-5.43	-2.77
-0.220	-17.60	-17.47	-16.83	-15.76	-14.30	-12.49	-10.37	-7.97	-5.41	-2.76
-0.180	-17.51	-17.43	-16.80	-15.74	-14.28	-12.46	-10.33	-7.93	-5.38	-2.75
-0.140	-17.33	-17.31	-16.76	-15.70	-14.24	-12.42	-10.28	-7.86	-5.34	-2.74
-0.100	-16.92	-16.97	-16.67	-15.62	-14.15	-12.33	-10.16	-7.77	-5.29	-2.72
-0.090	-16.74	-16.82	-16.57	-15.59	-14.12	-12.29	-10.11	-7.74	-5.27	-2.71
-0.080	-16.48	-16.61	-16.40	-15.55	-14.08	-12.24	-10.06	-7.70	-5.25	-2.70
-0.070	-16.12	-16.30	-16.14	-15.49	-14.02	-12.18	-9.99	-7.66	-5.23	-2.69
-0.060	-15.59	-15.86	-15.77	-15.29	-13.95	-12.10	-9.91	-7.61	-5.20	-2.68
-0.050	-14.74	-15.14	-15.19	-14.84	-13.85	-11.98	-9.82	-7.55	-5.17	-2.67
-0.040	-13.23	-13.91	-14.16	-13.99	-13.31	-11.79	-9.70	-7.48	-5.13	-2.66
-0.030	-11.05	-11.59	-12.02	-12.20	-11.78	-10.90	-9.47	-7.37	-5.09	-2.63
-0.020	-8.17	-8.28	-8.28	-8.29	-8.32	-8.35	-8.05	-7.06	-5.01	-2.61
-0.010	-4.15	-4.15	-4.15	-4.16	-4.19	-4.23	-4.31	-4.41	-4.33	-2.57
0.000	0.00	0.00	0.00	0.00	0.00	0.00	0.00	0.00	0.00	0.00
0.010	4.10	4.10	4.09	4.07	4.01	3.91	3.73	3.44	2.96	2.08
0.020	8.22	8.22	8.21	8.16	8.04	7.80	7.35	6.37	4.48	2.40
0.030	12.26	12.35	12.30	12.14	11.72	10.49	8.63	6.70	4.68	2.49
0.040	14.53	15.37	15.81	14.49	12.69	10.82	8.90	6.92	4.83	2.55
0.050	15.95	16.99	16.30	14.85	13.01	11.09	9.13	7.10	4.93	2.59
0.060	16.94	17.26	16.42	15.10	13.28	11.35	9.34	7.24	5.00	2.61
0.070	17.33	17.31	16.51	15.24	13.54	11.56	9.51	7.34	5.06	2.64
0.080	17.46	17.35	16.57	15.35	13.73	11.75	9.64	7.43	5.11	2.65
0.090	17.53	17.38	16.62	15.43	13.87	11.91	9.75	7.50	5.15	2.67
0.100	17.57	17.40	16.66	15.49	13.96	12.03	9.85	7.56	5.18	2.68
0.140	17.65	17.45	16.74	15.64	14.16	12.31	10.11	7.73	5.27	2.71
0.180	17.69	17.48	16.79	15.71	14.24	12.41	10.25	7.84	5.33	2.74
0.220	17.71	17.49	16.82	15.74	14.28	12.46	10.32	7.91	5.37	2.75
0.260	17.72	17.50	16.84	15.77	14.31	12.49	10.36	7.96	5.40	2.76
0.300	17.73	17.51	16.85	15.78	14.32	12.51	10.38	7.99	5.42	2.77
0.340	17.73	17.52	16.86	15.79	14.34	12.52	10.40	8.01	5.44	2.78
0.380	17.74	17.52	16.87	15.80	14.34	12.53	10.41	8.02	5.46	2.79
0.420	17.75	17.53	16.87	15.81	14.35	12.54	10.42	8.04	5.47	2.79
0.460	17.75	17.53	16.88	15.81	14.35	12.54	10.42	8.04	5.47	2.80
0.500	17.75	17.53	16.88	15.81	14.36	12.55	10.43	8.05	5.48	2.80



The moment-curvature values of stress-free CHS for in-plane bending and various levels of axial compression, are given in Table A-3.

Table A-3: Moment-Curvature values for stress-free CHS 100x5.

Curvature (rad/m)	In-plane bending moment (kN/m), under various levels of axial compression									
	$0N_{pl}$	$-0.1N_{pl}$	$-0.2N_{pl}$	$-0.3N_{pl}$	$-0.4N_{pl}$	$-0.5N_{pl}$	$-0.6N_{pl}$	$-0.7N_{pl}$	$-0.8N_{pl}$	$-0.9N_{pl}$
-0.500	-17.75	-17.53	-16.88	-15.81	-14.36	-12.55	-10.43	-8.05	-5.48	-2.80
-0.460	-17.75	-17.53	-16.88	-15.81	-14.35	-12.54	-10.42	-8.05	-5.47	-2.80
-0.420	-17.74	-17.52	-16.87	-15.80	-14.35	-12.54	-10.42	-8.04	-5.47	-2.79
-0.380	-17.73	-17.51	-16.86	-15.80	-14.34	-12.53	-10.41	-8.03	-5.46	-2.79
-0.340	-17.72	-17.51	-16.86	-15.79	-14.33	-12.52	-10.40	-8.01	-5.44	-2.78
-0.300	-17.72	-17.50	-16.85	-15.78	-14.32	-12.51	-10.38	-7.99	-5.43	-2.77
-0.260	-17.70	-17.48	-16.83	-15.76	-14.30	-12.49	-10.36	-7.96	-5.40	-2.76
-0.220	-17.68	-17.46	-16.81	-15.74	-14.28	-12.46	-10.32	-7.92	-5.37	-2.75
-0.180	-17.64	-17.42	-16.77	-15.70	-14.23	-12.41	-10.25	-7.85	-5.33	-2.74
-0.140	-17.57	-17.35	-16.69	-15.61	-14.14	-12.30	-10.11	-7.74	-5.28	-2.72
-0.100	-17.39	-17.17	-16.50	-15.41	-13.91	-12.00	-9.83	-7.56	-5.18	-2.68
-0.090	-17.31	-17.08	-16.41	-15.31	-13.79	-11.86	-9.73	-7.50	-5.15	-2.67
-0.080	-17.19	-16.96	-16.29	-15.17	-13.62	-11.69	-9.61	-7.42	-5.11	-2.66
-0.070	-17.01	-16.78	-16.09	-14.96	-13.35	-11.47	-9.46	-7.33	-5.06	-2.64
-0.060	-16.72	-16.49	-15.79	-14.60	-12.97	-11.18	-9.26	-7.21	-5.00	-2.62
-0.050	-16.24	-15.99	-15.24	-13.96	-12.46	-10.81	-9.01	-7.04	-4.91	-2.59
-0.040	-15.26	-14.96	-14.10	-13.00	-11.72	-10.27	-8.64	-6.82	-4.80	-2.55
-0.030	-12.38	-12.37	-12.08	-11.45	-10.56	-9.43	-8.07	-6.47	-4.62	-2.48
-0.020	-8.25	-8.25	-8.25	-8.25	-8.23	-7.85	-7.03	-5.84	-4.30	-2.38
-0.010	-4.13	-4.13	-4.13	-4.13	-4.13	-4.13	-4.13	-4.09	-3.48	-2.12
0.000	0.00	0.00	0.00	0.00	0.00	0.00	0.00	0.00	0.00	0.00
0.010	4.13	4.13	4.13	4.13	4.13	4.13	4.13	4.09	3.48	2.12
0.020	8.25	8.25	8.25	8.25	8.23	7.85	7.03	5.84	4.30	2.38
0.030	12.38	12.37	12.08	11.45	10.56	9.43	8.07	6.47	4.62	2.48
0.040	15.26	14.96	14.10	13.00	11.72	10.27	8.64	6.82	4.80	2.55
0.050	16.24	15.99	15.24	13.96	12.46	10.81	9.01	7.04	4.91	2.59
0.060	16.72	16.49	15.79	14.60	12.97	11.18	9.26	7.21	5.00	2.62
0.070	17.01	16.78	16.09	14.96	13.35	11.47	9.46	7.33	5.06	2.64
0.080	17.19	16.96	16.29	15.17	13.62	11.69	9.61	7.42	5.11	2.66
0.090	17.31	17.08	16.41	15.31	13.79	11.86	9.73	7.50	5.15	2.67
0.100	17.39	17.17	16.50	15.41	13.91	12.00	9.83	7.56	5.18	2.68
0.140	17.57	17.35	16.69	15.61	14.14	12.30	10.11	7.74	5.28	2.72
0.180	17.64	17.42	16.77	15.70	14.23	12.41	10.25	7.85	5.33	2.74
0.220	17.68	17.46	16.81	15.74	14.28	12.46	10.32	7.92	5.37	2.75
0.260	17.70	17.48	16.83	15.76	14.30	12.49	10.36	7.96	5.40	2.76
0.300	17.72	17.50	16.85	15.78	14.32	12.51	10.38	7.99	5.43	2.77
0.340	17.72	17.51	16.86	15.79	14.33	12.52	10.40	8.01	5.44	2.78
0.380	17.73	17.51	16.86	15.80	14.34	12.53	10.41	8.03	5.46	2.79
0.420	17.74	17.52	16.87	15.80	14.35	12.54	10.42	8.04	5.47	2.79
0.460	17.75	17.53	16.88	15.81	14.35	12.54	10.42	8.05	5.47	2.80
0.500	17.75	17.53	16.88	15.81	14.36	12.55	10.43	8.05	5.48	2.80

The moment-curvature diagrams of roller-bent and stress-free CHS for out-of-plane bending and various levels of axial compression, are compared in Figure A-4.

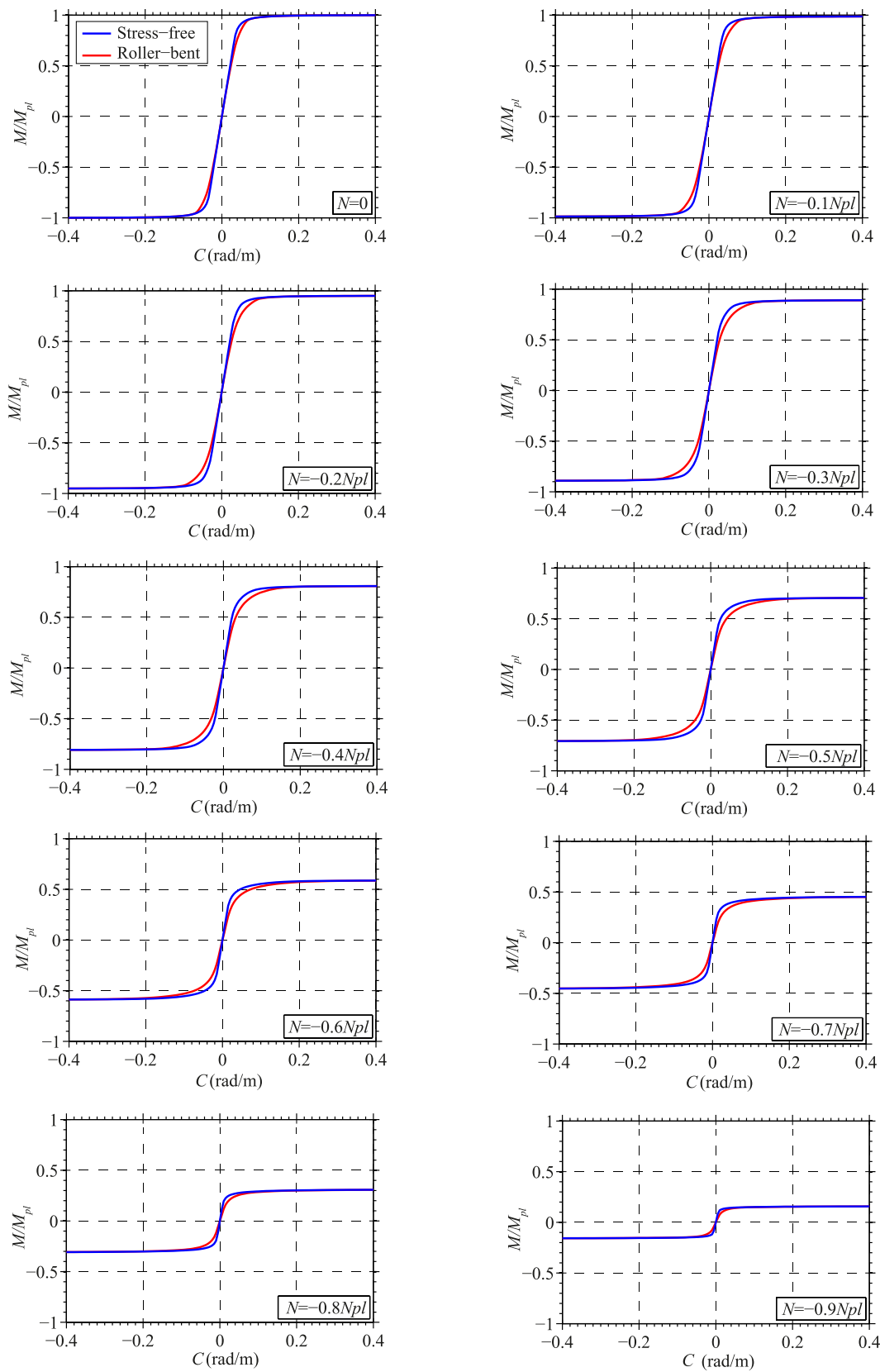


Figure A-4: Moment-curvature diagrams for out-of-plane bending.

The moment-curvature values of roller-bent CHS for out-of-plane bending and various levels of axial compression, are given in Table A-4. The response of stress-free CHS is identical to in-plane bending.

Table A-4: Moment-Curvature values for roller-bent CHS 100x5.

Curvature (rad/m)	Out-of-plane bending moment (kN/m), under various levels of axial compression									
	$0N_{pl}$	$-0.1N_{pl}$	$-0.2N_{pl}$	$-0.3N_{pl}$	$-0.4N_{pl}$	$-0.5N_{pl}$	$-0.6N_{pl}$	$-0.7N_{pl}$	$-0.8N_{pl}$	$-0.9N_{pl}$
-0.500	-17.75	-17.53	-16.88	-15.81	-14.35	-12.54	-10.42	-8.04	-5.47	-2.80
-0.460	-17.74	-17.52	-16.87	-15.81	-14.35	-12.54	-10.42	-8.04	-5.47	-2.79
-0.420	-17.74	-17.52	-16.87	-15.80	-14.34	-12.53	-10.41	-8.02	-5.46	-2.79
-0.380	-17.73	-17.51	-16.86	-15.80	-14.34	-12.53	-10.40	-8.01	-5.44	-2.78
-0.340	-17.72	-17.50	-16.85	-15.79	-14.33	-12.51	-10.38	-7.98	-5.43	-2.77
-0.300	-17.71	-17.50	-16.84	-15.78	-14.31	-12.49	-10.35	-7.95	-5.41	-2.77
-0.260	-17.70	-17.48	-16.83	-15.76	-14.29	-12.46	-10.30	-7.91	-5.38	-2.76
-0.220	-17.68	-17.46	-16.80	-15.73	-14.26	-12.41	-10.22	-7.84	-5.34	-2.74
-0.180	-17.64	-17.42	-16.76	-15.67	-14.18	-12.27	-10.08	-7.73	-5.29	-2.72
-0.140	-17.57	-17.34	-16.66	-15.55	-13.95	-11.98	-9.83	-7.57	-5.21	-2.70
-0.100	-17.39	-17.13	-16.38	-14.97	-13.28	-11.40	-9.39	-7.29	-5.07	-2.66
-0.090	-17.30	-17.02	-16.12	-14.67	-13.02	-11.18	-9.23	-7.18	-5.01	-2.64
-0.080	-17.17	-16.81	-15.70	-14.30	-12.68	-10.91	-9.03	-7.05	-4.94	-2.62
-0.070	-16.96	-16.28	-15.17	-13.82	-12.26	-10.57	-8.78	-6.88	-4.84	-2.60
-0.060	-16.30	-15.51	-14.47	-13.19	-11.71	-10.13	-8.46	-6.66	-4.72	-2.56
-0.050	-15.16	-14.46	-13.51	-12.30	-10.99	-9.57	-8.04	-6.37	-4.55	-2.50
-0.040	-13.55	-12.94	-12.08	-11.10	-10.00	-8.79	-7.46	-5.97	-4.31	-2.41
-0.030	-10.97	-10.55	-10.02	-9.36	-8.56	-7.66	-6.60	-5.37	-3.94	-2.25
-0.020	-7.73	-7.47	-7.15	-6.77	-6.36	-5.86	-5.22	-4.40	-3.34	-1.97
-0.010	-4.07	-3.96	-3.80	-3.58	-3.34	-3.10	-2.85	-2.56	-2.12	-1.37
0.000	0.00	0.00	0.00	0.00	0.00	0.00	0.00	0.00	0.00	0.00
0.010	4.07	3.96	3.80	3.58	3.34	3.10	2.85	2.56	2.12	1.37
0.020	7.73	7.47	7.15	6.77	6.36	5.86	5.22	4.40	3.34	1.97
0.030	10.97	10.55	10.02	9.36	8.56	7.66	6.60	5.37	3.94	2.25
0.040	13.55	12.94	12.08	11.10	10.00	8.79	7.46	5.97	4.31	2.41
0.050	15.16	14.46	13.51	12.30	10.99	9.57	8.04	6.37	4.55	2.50
0.060	16.30	15.51	14.47	13.19	11.71	10.13	8.46	6.66	4.72	2.56
0.070	16.96	16.28	15.17	13.82	12.26	10.57	8.78	6.88	4.84	2.60
0.080	17.17	16.81	15.70	14.30	12.68	10.91	9.03	7.05	4.94	2.62
0.090	17.30	17.02	16.12	14.67	13.02	11.18	9.23	7.18	5.01	2.64
0.100	17.39	17.13	16.38	14.97	13.28	11.40	9.39	7.29	5.07	2.66
0.140	17.57	17.34	16.66	15.55	13.95	11.98	9.83	7.57	5.21	2.70
0.180	17.64	17.42	16.76	15.67	14.18	12.27	10.08	7.73	5.29	2.72
0.220	17.68	17.46	16.80	15.73	14.26	12.41	10.22	7.84	5.34	2.74
0.260	17.70	17.48	16.83	15.76	14.29	12.46	10.30	7.91	5.38	2.76
0.300	17.71	17.50	16.84	15.78	14.31	12.49	10.35	7.95	5.41	2.77
0.340	17.72	17.50	16.85	15.79	14.33	12.51	10.38	7.98	5.43	2.77
0.380	17.73	17.51	16.86	15.80	14.34	12.53	10.40	8.01	5.44	2.78
0.420	17.74	17.52	16.87	15.80	14.34	12.53	10.41	8.02	5.46	2.79
0.460	17.74	17.52	16.87	15.81	14.35	12.54	10.42	8.04	5.47	2.79
0.500	17.75	17.53	16.88	15.81	14.35	12.54	10.42	8.04	5.47	2.80

The torsion-twist diagrams of roller-bent and stress-free CHS for various levels of axial compression, are compared in Figure A-5.

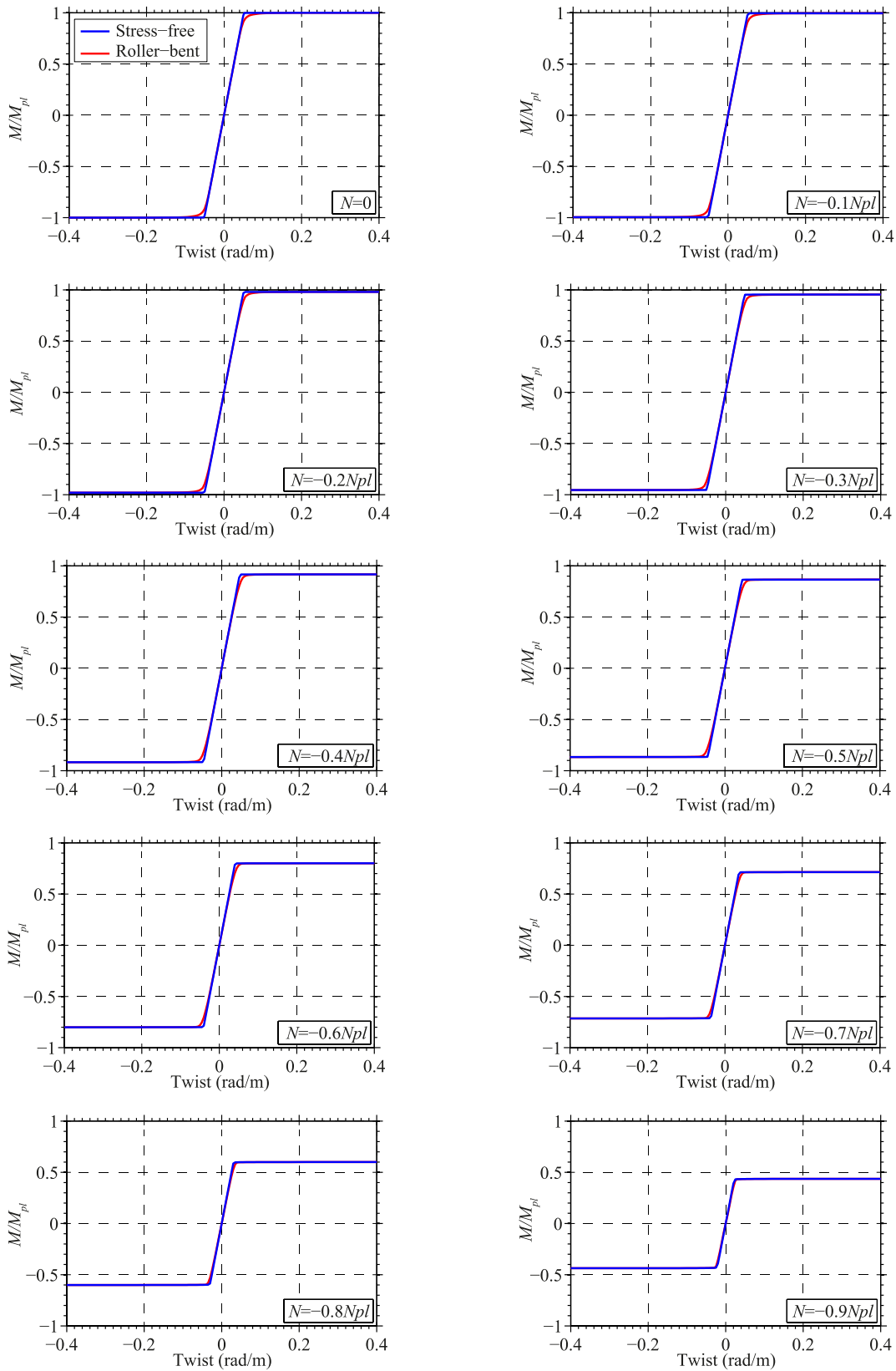


Figure A-5: Torsion-twist diagrams.

The torsion-twist values of roller-bent CHS for various levels of axial compression, are shown in Table A-5. The response is identical regardless the direction of torsion/twist.

Table A-5: Torsion-Twist values for roller-bent CHS 100x5.

Twist (rad/m)	Torsional moment (kN/m), under various levels of axial compression									
	$0N_{pl}$	$-0.1N_{pl}$	$-0.2N_{pl}$	$-0.3N_{pl}$	$-0.4N_{pl}$	$-0.5N_{pl}$	$-0.6N_{pl}$	$-0.7N_{pl}$	$-0.8N_{pl}$	$-0.9N_{pl}$
-0.500	-16.02	-15.94	-15.70	-15.28	-14.68	-13.88	-12.82	-11.44	-9.62	-6.99
-0.460	-16.02	-15.94	-15.70	-15.28	-14.68	-13.88	-12.82	-11.44	-9.62	-6.99
-0.420	-16.02	-15.94	-15.70	-15.28	-14.68	-13.88	-12.82	-11.44	-9.62	-6.99
-0.380	-16.02	-15.94	-15.70	-15.28	-14.68	-13.88	-12.82	-11.44	-9.62	-6.99
-0.340	-16.02	-15.94	-15.70	-15.28	-14.68	-13.88	-12.82	-11.44	-9.62	-6.99
-0.300	-16.02	-15.94	-15.70	-15.28	-14.68	-13.88	-12.82	-11.44	-9.62	-6.99
-0.260	-16.02	-15.94	-15.70	-15.28	-14.68	-13.88	-12.82	-11.44	-9.62	-6.99
-0.220	-16.02	-15.94	-15.70	-15.28	-14.68	-13.88	-12.82	-11.44	-9.61	-6.99
-0.180	-16.02	-15.94	-15.69	-15.28	-14.68	-13.87	-12.82	-11.44	-9.61	-6.98
-0.140	-16.00	-15.92	-15.68	-15.27	-14.68	-13.87	-12.81	-11.44	-9.61	-6.98
-0.100	-15.93	-15.87	-15.64	-15.24	-14.66	-13.86	-12.81	-11.44	-9.61	-6.98
-0.090	-15.88	-15.83	-15.61	-15.22	-14.64	-13.85	-12.80	-11.43	-9.61	-6.98
-0.080	-15.81	-15.76	-15.56	-15.19	-14.62	-13.84	-12.80	-11.43	-9.60	-6.98
-0.070	-15.69	-15.65	-15.46	-15.12	-14.58	-13.82	-12.79	-11.43	-9.60	-6.97
-0.060	-15.41	-15.38	-15.21	-14.91	-14.43	-13.74	-12.77	-11.42	-9.60	-6.97
-0.050	-14.63	-14.56	-14.31	-14.01	-13.66	-13.20	-12.52	-11.39	-9.59	-6.96
-0.040	-12.46	-12.30	-12.14	-11.98	-11.79	-11.56	-11.26	-10.77	-9.56	-6.95
-0.030	-9.47	-9.42	-9.36	-9.27	-9.19	-9.08	-8.95	-8.78	-8.47	-6.93
-0.020	-6.31	-6.31	-6.29	-6.26	-6.23	-6.18	-6.12	-6.05	-5.94	-5.72
-0.010	-3.16	-3.16	-3.15	-3.14	-3.13	-3.10	-3.07	-3.02	-2.96	-2.88
0.000	0.00	0.00	0.00	0.00	0.00	0.00	0.00	0.00	0.00	0.00
0.010	3.16	3.16	3.15	3.14	3.13	3.10	3.07	3.02	2.96	2.88
0.020	6.31	6.31	6.29	6.26	6.23	6.18	6.12	6.05	5.94	5.72
0.030	9.47	9.42	9.36	9.27	9.19	9.08	8.95	8.78	8.47	6.93
0.040	12.46	12.30	12.14	11.98	11.79	11.56	11.26	10.77	9.56	6.95
0.050	14.63	14.56	14.31	14.01	13.66	13.20	12.52	11.39	9.59	6.96
0.060	15.41	15.38	15.21	14.91	14.43	13.74	12.77	11.42	9.60	6.97
0.070	15.69	15.65	15.46	15.12	14.58	13.82	12.79	11.43	9.60	6.97
0.080	15.81	15.76	15.56	15.19	14.62	13.84	12.80	11.43	9.60	6.98
0.090	15.88	15.83	15.61	15.22	14.64	13.85	12.80	11.43	9.61	6.98
0.100	15.93	15.87	15.64	15.24	14.66	13.86	12.81	11.44	9.61	6.98
0.140	16.00	15.92	15.68	15.27	14.68	13.87	12.81	11.44	9.61	6.98
0.180	16.02	15.94	15.69	15.28	14.68	13.87	12.82	11.44	9.61	6.98
0.220	16.02	15.94	15.70	15.28	14.68	13.88	12.82	11.44	9.61	6.99
0.260	16.02	15.94	15.70	15.28	14.68	13.88	12.82	11.44	9.62	6.99
0.300	16.02	15.94	15.70	15.28	14.68	13.88	12.82	11.44	9.62	6.99
0.340	16.02	15.94	15.70	15.28	14.68	13.88	12.82	11.44	9.62	6.99
0.380	16.02	15.94	15.70	15.28	14.68	13.88	12.82	11.44	9.62	6.99
0.420	16.02	15.94	15.70	15.28	14.68	13.88	12.82	11.44	9.62	6.99
0.460	16.02	15.94	15.70	15.28	14.68	13.88	12.82	11.44	9.62	6.99
0.500	16.02	15.94	15.70	15.28	14.68	13.88	12.82	11.44	9.62	6.99

The torsion-twist values of stress-free CHS for various levels of axial compression, are shown in Table A-6. The response is identical regardless the direction of torsion/twist.

Table A-6: Torsion-Twist values for stress-free CHS 100x5.

Curvature (rad/m)	Torsional moment (kN/m), under various levels of axial compression									
	$0N_{pl}$	$-0.1N_{pl}$	$-0.2N_{pl}$	$-0.3N_{pl}$	$-0.4N_{pl}$	$-0.5N_{pl}$	$-0.6N_{pl}$	$-0.7N_{pl}$	$-0.8N_{pl}$	$-0.9N_{pl}$
-0.500	-16.02	-15.94	-15.70	-15.28	-14.68	-13.88	-12.82	-11.44	-9.62	-6.99
-0.460	-16.02	-15.94	-15.70	-15.28	-14.68	-13.88	-12.82	-11.44	-9.62	-6.99
-0.420	-16.02	-15.94	-15.70	-15.28	-14.68	-13.88	-12.82	-11.44	-9.62	-6.99
-0.380	-16.02	-15.94	-15.70	-15.28	-14.68	-13.88	-12.82	-11.44	-9.62	-6.99
-0.340	-16.02	-15.94	-15.70	-15.28	-14.68	-13.88	-12.82	-11.44	-9.62	-6.99
-0.300	-16.02	-15.94	-15.70	-15.28	-14.68	-13.88	-12.82	-11.44	-9.62	-6.99
-0.260	-16.02	-15.94	-15.70	-15.28	-14.68	-13.88	-12.82	-11.44	-9.62	-6.99
-0.220	-16.02	-15.94	-15.70	-15.28	-14.68	-13.88	-12.82	-11.44	-9.61	-6.99
-0.180	-16.02	-15.94	-15.70	-15.28	-14.68	-13.87	-12.82	-11.44	-9.61	-6.98
-0.053	-16.00	-15.94	-15.70	-15.28	-14.68	-13.87	-12.82	-11.44	-9.61	-6.98
-0.050	-15.69	-15.94	-15.70	-15.28	-14.68	-13.87	-12.81	-11.44	-9.61	-6.98
-0.045	-14.20	-15.94	-15.70	-15.28	-14.68	-13.87	-12.81	-11.43	-9.61	-6.98
-0.040	-12.62	-15.94	-15.70	-15.28	-14.68	-13.87	-12.81	-11.43	-9.60	-6.98
-0.035	-11.05	-15.94	-15.70	-15.28	-14.68	-13.87	-12.81	-11.43	-9.60	-6.97
-0.030	-9.47	-15.94	-15.70	-15.28	-14.68	-13.87	-12.81	-11.43	-9.60	-6.97
-0.025	-7.89	-15.65	-15.54	-15.27	-14.67	-13.87	-12.81	-11.43	-9.59	-6.96
-0.020	-6.31	-12.62	-12.62	-12.62	-12.62	-12.62	-12.57	-11.41	-9.59	-6.95
-0.015	-4.73	-9.47	-9.47	-9.47	-9.47	-9.47	-9.47	-9.47	-9.38	-6.94
-0.010	-3.16	-6.31	-6.31	-6.31	-6.31	-6.31	-6.31	-6.31	-6.31	-6.27
-0.005	-1.58	-3.16	-3.16	-3.16	-3.16	-3.16	-3.16	-3.16	-3.16	-3.16
0.000	0.00	0.00	0.00	0.00	0.00	0.00	0.00	0.00	0.00	0.00
0.005	1.58	3.16	3.16	3.16	3.16	3.16	3.16	3.16	3.16	3.16
0.010	3.16	6.31	6.31	6.31	6.31	6.31	6.31	6.31	6.31	6.27
0.015	4.73	9.47	9.47	9.47	9.47	9.47	9.47	9.47	9.38	6.94
0.020	6.31	12.62	12.62	12.62	12.62	12.62	12.57	11.41	9.59	6.95
0.025	7.89	15.65	15.54	15.27	14.67	13.87	12.81	11.43	9.59	6.96
0.030	9.47	15.94	15.70	15.28	14.68	13.87	12.81	11.43	9.60	6.97
0.035	11.05	15.94	15.70	15.28	14.68	13.87	12.81	11.43	9.60	6.97
0.040	12.62	15.94	15.70	15.28	14.68	13.87	12.81	11.43	9.60	6.98
0.045	14.20	15.94	15.70	15.28	14.68	13.87	12.81	11.43	9.61	6.98
0.050	15.69	15.94	15.70	15.28	14.68	13.87	12.81	11.44	9.61	6.98
0.053	16.00	15.94	15.70	15.28	14.68	13.87	12.82	11.44	9.61	6.98
0.180	16.02	15.94	15.70	15.28	14.68	13.87	12.82	11.44	9.61	6.98
0.220	16.02	15.94	15.70	15.28	14.68	13.88	12.82	11.44	9.61	6.99
0.260	16.02	15.94	15.70	15.28	14.68	13.88	12.82	11.44	9.62	6.99
0.300	16.02	15.94	15.70	15.28	14.68	13.88	12.82	11.44	9.62	6.99
0.340	16.02	15.94	15.70	15.28	14.68	13.88	12.82	11.44	9.62	6.99
0.380	16.02	15.94	15.70	15.28	14.68	13.88	12.82	11.44	9.62	6.99
0.420	16.02	15.94	15.70	15.28	14.68	13.88	12.82	11.44	9.62	6.99
0.460	16.02	15.94	15.70	15.28	14.68	13.88	12.82	11.44	9.62	6.99
0.500	16.02	15.94	15.70	15.28	14.68	13.88	12.82	11.44	9.62	6.99







# CURRICULUM VITAE

## Ilias D. Thanasoulas

January 2020

### A. PERSONAL INFORMATION

---

Address 86, Ksanthippou Str., GR-15561 Holargos, Athens, Greece  
E-mail address [ithana@central.ntua.gr](mailto:ithana@central.ntua.gr)  
Date of birth 16.11.1988  
Place of birth Athens, Greece  
Nationality Hellenic

### B. EDUCATION

---

**Doctor of Philosophy** (Jan. 2020) **in Civil Engineering,**  
Institute of Steel Structures, Department of Structural Engineering,  
School of Civil Engineering, National Technical University of Athens, Greece,  
Thesis: **Stability criteria for hollow-section steel arches** (in English).  
Advised by Prof. Charis Gantes.

**Master of Science** (Sep. 2014) **in Interdisciplinary Graduate Program of Studies – "Analysis and Design of Earthquake Resistant Structures",**  
Department of Structural Engineering, School of Civil Engineering,  
National Technical University of Athens, Greece  
Thesis: **"Fatigue analysis of wind turbine tower connections"** (in Greek).  
Advised by Prof. Charis Gantes.

**Diploma** (Sep. 2011) **in Civil Engineering,** with specialisation in Structural Engineering,  
Department of Structural Engineering, School of Civil Engineering,  
National Technical University of Athens, Greece  
Thesis: **"Design and evaluation of the seismic response of steel buildings by means of nonlinear analyses"** (in Greek).  
Advised by: Prof. Ioannis Vayas.

### C. AWARDS AND SCHOLARSHIPS

---

1. "Thomaidis Foundation Award 2016" for the following peer reviewed journal paper:  
**Thanasoulas, I. D.,** Vardakoulis I. K., Kolaitis, D. I., Gantes, C. J., and Founti, M. A. (2016),  
"Thermal and Mechanical Computational Study of Load-Bearing Cold-Formed Steel Drywall Systems  
Exposed to Fire", Fire Technology, 52, 2071-2092. <https://doi.org/10.1007/s10694-016-0604-4>
2. Scholarship awarded by the **State Scholarships Foundation** of Greece (IKY-GR),  
for Ph.D. studies in engineering during the academic years 2015 - 2017.
3. Scholarship awarded by the **State Scholarships Foundation** of Greece (IKY-GR),  
for M.Sc. studies in engineering during the academic year 2012 - 2013.

### D. LANGUAGES

---

Greek Native  
English "Certificate of Proficiency in English, The University of Michigan" (2005)  
French "Diplôme d'Études en Langue Française – Delf 1<sup>er</sup> Degré, Institut Français d'Athènes"  
(2004)

## E. PROFESSIONAL INVOLVEMENT

---

- 07/2018 – **Co-Founder: IST Structural Engineers General Partnership**  
Present Company established in Athens, Greece, offering services in:  
- Engineering consultancy  
- Research and development
- 11/2014 – **Free-lancer engineer**  
07/2018 Specialized in the structural analysis and design of buildings

## F. PARTICIPATION IN RESEARCH PROJECTS

---

1. **"OPTARCH – Optimization Driven Architectural Design of Structures"**, funded by the Marie Skłodowska-Curie Research and Innovation Staff Exchange (1,620,000€), Feb 2016 – Jan 2020. Project coordinator: Assoc. Prof. Nikos Lagaros.
2. **"Structural design of steel and composite structures by means of nonlinear analyses"**, funded by the Research Programs of Excellence IKY/Siemens (50,000€), Sep 2015 – Aug 2017. Project coordinator: Prof. Charis Gantes.
3. **"ELISSA – Energy Efficient Lightweight Sustainable Safe Steel Construction"**, funded by the European Community's Seventh Framework Programme FP7 (5,308,466€), Sep 2013 – Aug 2016. Project coordinator: Prof. Maria Founti.

## G. PARTICIPATION IN WORKING GROUPS

---

1. Member of the Hellenic Organization for Standardization (ELOT) working group, for the discussion and commenting of the next generation Eurocodes (EN1993-1-1 and EN1993-1-14).

## H. TEACHING EXPERIENCE

---

- 2015 - 2019 Teaching assistance for the undergraduate course **"Nonlinear Behaviour of Steel Structures"**, Institute of Steel Structures, School of Civil Engineering, National Technical University of Athens, coordinated by Prof. Charis Gantes.
- 2016 - 2017 Teaching assistance for the postgraduate course **"Design of Cabled and Membraned Structures"**, Institute of Steel Structures, School of Civil Engineering, National Technical University of Athens, coordinated by Prof. Charis Gantes.

## I. STUDENT ADVISING

---

1. Venetis, S.A. (2018), "Numerical investigation of residual stresses in steel arches due to curving process", co-supervised with Prof. Charis Gantes, (Diploma Thesis in Greek).  
<http://dx.doi.org/10.26240/heal.ntua.16134>
2. Korlou, S.K. (2017), "Principles of mechanical behavior and applications of glass and aluminium structural elements", co-supervised with Prof. Charis Gantes (M.Sc. Thesis in Greek).  
<http://dx.doi.org/10.26240/heal.ntua.7431>
3. Kalyvas S.S. (2016), "Comparison of code-based approach and nonlinear analyses for the design of free form steel dome", co-supervised with Prof. Charis Gantes, (Diploma Thesis in Greek).  
<http://dx.doi.org/10.26240/heal.ntua.14036>
4. Vardakoulias I.K. (2015), "Structural behavior of light gauge cold-formed steel frame walls under fire conditions", co-supervised with Prof. Charis Gantes (M.Sc. Thesis in English).  
<http://dx.doi.org/10.26240/heal.ntua.4777>

## **J. MEMBERSHIPS IN ORGANISATIONS**

---

1. Steel Structures Research Society (EEME– <http://eeme.ntua.gr/en>) (since 2015)
2. Technical Chamber of Greece (TEE – [www.tee.gr](http://www.tee.gr)) (since 2014)
3. Society of Civil Engineers (SPME – [www.spme.gr](http://www.spme.gr)) (since 2014)

## **K. SOFTWARE LITERACY**

---

1. Excellent knowledge of various general-purpose FEM software, such as FEMAP, ADINA, SAP2000, ETABS, for performing advanced simulations and validation against experimental results.
2. Very good knowledge of programming language MATLAB.

## **L. PEER REVIEWED JOURNAL PUBLICATIONS**

---

1. **Thanasoulas, I. D.**, Gantes, C. J. (2020), "Stability criteria for circular-hollow-section steel arches", (ready for submission).
2. **Thanasoulas, I. D.**, Gantes, C. J. (2019), "Numerical investigation of the residual stresses of roller-bent circular-hollow-sections", *Journal of Constructional Steel Research* (in-press).  
<https://doi.org/10.1016/j.jcsr.2019.105777>
3. **Thanasoulas, I. D.**, Douthe C. E., Gantes, C. J., Lignos X. A. (2018), "Influence of roller-bending on RHS steel arches: Experimental and numerical investigation", *Thin-Walled Structures*, 131, 668-680. <https://doi.org/10.1016/j.tws.2018.07.027>
4. **Thanasoulas, I. D.**, Vardakoulias I. K., Kolaitis, D. I., Gantes, C. J., and Founti, M. A. (2018), "Coupled Thermo-Mechanical Analyses for the Performance-based Fire Design of Lightweight Steel Drywall Elements", *Journal of Constructional Steel Research*, 145, 196–209.  
<https://doi.org/10.1016/j.jcsr.2018.02.022>
5. **Thanasoulas, I. D.**, Vardakoulias I. K., Kolaitis, D. I., Gantes, C. J., and Founti, M. A. (2016), "Thermal and Mechanical Computational Study of Load-Bearing Cold-Formed Steel Drywall Systems Exposed to Fire", *Fire Technology*, 52, 2071-2092. <https://doi.org/10.1007/s10694-016-0604-4>

## **M. CONFERENCE PUBLICATIONS**

---

1. **Thanasoulas, I. D.**, Gantes, C. J., "Effects of roller-bending on curved constructional steels of rectangular-hollow-section", *IASS 2018 Symposium*, Boston, USA, Jul. 16-20, 2018.
2. Korlou, S.K., **Thanasoulas, I.D.**, Moupatsinoglou K.H. and Gantes, C.J., "Investigation of shear buckling of laminated glass panes", *9th Greek National Steel Structures Conference*, Larissa, 5-7 Oct. 2017.
3. **Thanasoulas I.D.**, Vardakoulias I.K., Kolaitis D.I., Gantes C.J. and Founti M.A., "Nonlinear numerical simulation of fire-resistance tests for load-bearing cold-formed-steel drywall systems", *9th Greek National Steel Structures Conference*, Larissa, 5-7 Oct. 2017.
4. **Thanasoulas I.D.**, Vardakoulias I.K., Kolaitis D.I., Gantes C.J. and Founti M.A., "A preliminary thermal and mechanical simulation study of load-bearing cold-formed steel drywall systems exposed to fire", *2nd IAFSS European Symposium of Fire Safety Science*, Nicosia, Cyprus, 16-18 June, 2015.
5. Koulatsou, K., **Thanasoulas, I.D.**, Margariti, G. and Gantes, C.J., "Generation of Artificial Wind Force Time Histories on Wind Turbine Towers", *8th Greek National Steel Structures Conference*, Tripoli, 2-4 Oct. 2014.
6. **Thanasoulas, I.D.**, Koulatsou, K.G. and Gantes, C.J., "Nonlinear Numerical Simulation of Bolted Ring Flanges in Wind Turbine Towers", *IASS-SLTE 2014 Symposium*, Brasilia, Brazil, Sep. 15-19, 2014.

